NAZARBAYEV
UNIVERSITY

Recent Techniques on Observer Design for Disturbance Estimation and Rejection in Permanent Magnet Synchronous Motors

by

Kanat E. Suleimenov

Submitted in partial fulfillment of the
requirements for the degree of Doctor of
Philosophy in Robotics Engineering

Date of Completion
December, 2023

Recent Techniques on Observer Design for Disturbance Estimation and Rejection in Permanent Magnet Synchronous Motors

by
Kanat E. Suleimenov

Submitted in partial fulfillment of the requirements for the degree of
Doctor of Philosophy in Robotics Engineering

School of Engineering and Digital Sciences
Nazarbayev University

December, 2023

Supervised by
Dr. Ton Duc Do
Dr. Matteo Rubagotti
Dr. Gia Minh Thao Nguyen

Declaration

I, Kanat E. Suleimenov, declare that the research contained in this thesis, unless otherwise formally indicated within the text, is the author's original work. The thesis has not been previously submitted to this or any other university for a degree and does not incorporate any material already submitted for a degree.

Signature:

Date:

BLANK

Abstract

Permanent magnet synchronous machines (PMSMs) (either motor or generator) have attracted attention of research community comparing to other types of AC machines in the recent two decades. PMSMs are preferable than other AC machines in terms of large power-factor, broad speed of operation, compact proportions, and effective operation. Unfortunately, different sources of nonlinearities, model uncertainties, and external perturbations determine severity in a design of accurate speed control scheme for PMSMs. In the era of developing science and technologies, many advanced control solutions are proposed to control PMSMs. Although new solutions show their advantages comparing to traditional methods in terms of performance evaluation, practical realization of those algorithms could require expensive hardware with high computational capabilities. Furthermore, people in industry with less knowledge about the motor control may experience difficulties in using such advanced controllers on their own.

Traditional PI/PID control schemes still work as a major control technique in modern industry, and in motor control as well. Numerous positive facts about the PI/PID schemes make such superiority of these control schemes. Firstly, the PI/PID can be implemented easily on most industrial software and hardware components. Secondly, while its scheme has clear mechanism of operation, most industrial processes could be controlled via the PI/PID scheme. These schemes are good in terms of small number of parameters to tune and tuning process itself could be very straightforward. Finally, implementation of the PI/PID controllers would require smaller time comparing to most proposed complex control solutions.

It is studied that the traditional PI/PID controllers usually cannot deal with unpredictable disturbances, which in turn leads to degraded performance of an overall control system. Inspired by the advantages and widespread application of PI/PID control structure in industry, we propose a disturbance observer based composite control scheme which uses the PI-like controller for the feedback regulation and disturbance observer for estimation of lumped disturbances presented in a PMSM control system. Under this circumstance, this thesis work proposes three different control solutions for PMSM such as High-order disturbance observer-based composite control (HDOBCC), Disturbance rejection PI (DR-PI) control, and Hierarchical optimal disturbance observer-based control (HODOBC). Furthermore, to deeply understand the similarity and difference between the traditional disturbance observer-based control

(DOBC) and active-disturbance rejection control (ADRC) schemes, this thesis also presents results of unification of these two control approaches in the speed control of a PMSM.

The HDOBCC as the first method proposed in this thesis is designed to improve reference speed tracking performance of a PMSM under various operational conditions. A structure of the HDOBCC comprises a fuzzy-PI controller in a feedback stabilization part and novel high-order disturbance observer in a feedforward compensation part of the speed control system. The proposed controller is designed based on the research questions such as: firstly, although a fixed gain traditional PI controller is able to present satisfactory performance at some extent, still it does not guarantee such performance when sudden disturbances occur in a system; secondly, many disturbance observers designed for a PMSM in literature consider only a load torque as a disturbance, neglecting model uncertainties and parameter variations in design stage. Therefore, the HDOBCC is proposed such that it utilizes a fuzzy approach to determine parameters of the PI controller to overcome limitations of the fixed gain PI controller. Furthermore, the proposed scheme includes a high-order disturbance observer, which estimates not only the load torque, but also disturbances due to model uncertainties and parameter variations. Moreover, extended simulation and experimental studies are conducted to affirm performance of the HDOBCC under various form of the load torque. In addition to commonly tested step form of a load torque, severe forms of the load torque such as triangular form and sinusoidal form are tested with the proposed controller. Stability analysis of the closed-loop HDOBCC system is further provided.

The next proposed method, DR-PI control, is designed by seeking answer for questions such as: firstly, although the traditional DOBC scheme applied for PMSM shows reasonable results in a PMSM control, its design can be limited to known actual parameters of the PMSM. In practice, actual parameters are usually not available, hence it could be hard to design the traditional DOBC in the absence of a plant information; secondly, for tuning a PI controller the traditional Ziegler-Nichols tuning approach still remains as one of the popular tuning approaches, however it does not give a rigorous explanation on selection of parameters during its design. Consequently, to answer these questions, the DR-PI control is designed for the PMSM speed control. The DR-PI control is designed such that it has a simple PI-like structure with intrinsic disturbance rejection mechanism determined by the parameters of a filtering element, desired plant model, and desired closed-loop system. Simulation and experimental validations are provided to validate the performance of the DR-PI. Furthermore, gain tuning mechanism and stability analysis of the closed-loop DR-PI-based speed control are also presented.

The HODOBC scheme as a third proposed control scheme targets on the next research questions as: first, parameters of the traditional PI controller are mostly obtained by trial-and-error approach, which in turn may not guarantee satisfactory

results; in a cascaded PMSM control, the outer speed loop performance highly depends on the performance of the inner current loop. The well-tuned speed control loop may degrade in performance, if the inner current loop is not tuned properly. To address these questions, we propose the HODOBC scheme, which consists of optimal PI-like controller in the feedback stabilization part and optimal extended-state observer (ESO) in the disturbance compensation part. The proposed HODOBC showed better performance when it is compared with other traditional controllers via experiments. Stability analysis is provided via the root locus approach.

The study on unification of the DOBC and ADRC schemes has the following research question: the DOBC and ADRC are both used in estimation of total disturbance, but these two schemes are considered differently in literature. Hence, the study of both scheme is conducted to show the condition at which these two schemes show identical performance. The analysis of the traditional DOBC and ADRC schemes concludes that both scheme are equivalent in terms of performance characteristics if the dynamical delays of disturbance observers in each scheme are same. The results of analysis reveal that both scheme can be utilized to design a robust control system for PMSM, i.e. once the gains of disturbance observers can be calculated under the DOBC framework, further the disturbance rejection mechanism can be achieved via the ADRC framework.

The results of PMSM control with the proposed control schemes have been tested on the Lucas-Nuelle DSP-based experimental setup.

BLANK

Acknowledgments

This thesis work is a conclusion of my PhD journey at the Department of Robotics, Nazarbayev University, and research studies were conducted in the Laboratory of Power Conversion and Motion Control (PCMC) at Nazarbayev University (Kazakhstan).

First of all, I would like to express my deep appreciation to my supervisor Dr. Ton Duc Do for his strong and continued support, encouragement, expertise and any advice given during my PhD study. I am incredibly grateful for his patience, mentorship, availability, and guidance. In addition, I deeply appreciate the financial support of Dr. Ton Duc Do's Research project throughout my PhD study.

I am sincere grateful to Dr. Bao-Huy Nguyen and Thanh Vo-Duy for their availability, sincerity, and professionalism during our collaboration.

I want to express my sincere gratitude to Dr. Matteo Rubagotti and Dr. Binh-Minh Nguyen for their valuable comments that helped me to improve my thesis.

I would like to thank my dear friends and colleagues Darkhan Zholtayev and Dr. Bayandy Sarsembayev for their support, cooperation, sincerity, and encouragement.

My deep gratitude is for my loving parents and grandmother, all of whose support, love, and constant motivation always drove me during this exaustive and not straightforward academic way.

I would like to thank my wife for her unselfish love, continuous support, and truthful belief, and lovely daughters Amina and Asiya for their cute childish behavior and pure love.

Contents

List of Tables

List of Figures

Chapter 1

Introduction

1.1 Background

Nowadays, it is hard to imagine a daily life of people without using of electrical drives. Electrical drives play an important role in our domestic life being used in a clock mechanism, a hairdryer, a vacuum cleaner, different types of pumps and etc. Moreover, over the recent decades, its importance has been greatly increased due to electrification of transport systems, i.e. with rapid developing of electrical cars, electrical trains, boats, and so on, and the listed applications are just part of hundred examples of electrical drive popularity [6]. Recently, an active research studies are being conducted in replacing engines powered by traditional power source (gasoline) to electrical drives in order to create clean sustainable society [3]. Since the last decade, the industry of automobile has begun to reform a motor structure and its control to achieve better performance. In the modern electrical vehicle (EV) industry, seven representives of electrical drives such as brushless and brushed DC motors, induction motor (IM), permanent magnet synchronous motor (PMSM), synchronous reluctance motor (SyncRM), axial flux ironless PM motor, and switched reluctance motor (SwRM) are widely used [7]. Permanent magnet synchronous motors become most popular among other types of electrical motors due to properties such that high torque ratio, efficiency, compact size, easy and precise control, and reliable operation [8, 9].

In spite of that PMSMs have superior advantages over other types of motors, accurate control of a PMSM is rather difficult due to its complicated and nonlinear dynamics, furthermore, operation of a PMSM is subject to different sources of external disturbances and indeterminacy. Thanks to its structure, a proportional-integral (PI) control approach is successfully implemented for PMSM control system. Unfortunately, due to nonlinear dynamics of a PMSM, it is hard to guarantee a desireable performance in a wide range of operation of the motor using such linear control schemes. Development of new technologies in microprocessors such as digital signal processor (DSP) and power electronics leads to a birth of new advanced solutions to control a PMSM. Among those control solutions, model-predictive control, adaptive control, robust control, fuzzy control, and neural network control could be utilized to resolve a PMSM control problem in various facets [10].

In general, PMSMs always operate under different disturbances, e.g. disturbance due to frictional force, disturbance due to wrong model dynamics, and disturbance

due to load variations. Traditional feedback controllers are not able to reject such disturbances, hence numerous techniques based on feedforward compensation are proposed as fast and effective approach to eliminate effect of disturbances [10]. Two famous techniques have been proposed to estimate disturbances in PMSMs, since direct measurement of disturbances is not possible in practical applications. One of those technique is the disturbance observer (DO) approach which was initially proposed to improve performance of a DC motor by Ohnishi in 1980s [11]. Based on this method proposed by Ohnishi different disturbance observer-based (DOB) [12–19] methods have been implemented in various applications as motion control, robotic system control, disk drive systems, etc. The second technique named as extended state observer (ESO) is firstly developed by Han in 1990s. Developing of the ESO facilitated introduction of an ESO-based composite control method famous as active disturbance rejection control (ADRC). Due to advantages of the ESO approach in estimation of either states or lumped disturbances, the ADRC method become popular in control of power converters [20–22], electrical motors [23–25], robotic systems [26–29], etc.

Usually, in a diverse number of studies on observer algorithms designed for control electric drives, frictions in mechanical part are taken as unknown, while the other types of friction existed due to Eddy currents, pulling force of flux, internal noises, unmodelling dynamics are ignored or considered as known. Numerous observers based on these preliminary assumptions are proposed in literature, e.g. fuzzy observer [30], H_∞-based observer [31], ADRC [32, 33], nonlinear observer [34], sliding mode observer [35–39], polynomial observer [40], extended state-observer (ESO) [41, 42], etc. Although this proposed solutions show superior results comparing to the results with conventional controllers, due to the made assumptions these methods start to degrade in performance after some point of operation. This happens since unknown frictions and noises are inevitable in practical systems. For instance, a disturbance observer designed in [43] estimates a load torque and cogging torque with assumption of known friction terms.

Moreover, the proposed disturbance-observer based schemes [30–39, 41, 42, 44–50] are designed under the assumption such that disturbance has slow dynamics, i.e. its first-order time derivative equal to zero. In practice, this assumption works for disturbance with constant or piece-wise constant dynamics, and it does not work for disturbances with fast dynamics with shapes such as sinusoidal, triangular, or pulse. To tackle such an issue, studies in [40, 51] consider the high-order time derivatives of disturbance to be zero. Whilst this assumption makes improve to the conventional design approach, the designed observer may show degraded performance under pulse, sinusoidal, or triangular disturbance effect at transient period. An approach to estimate lumped disturbance called fast-integral sliding mode observer and proposed in [52] assumes that the first-order time derivative of the disturbance is not necessary zero,

but bounded with arbitrary positive number. However, due to the limitations in the assumption, this method may not properly estimate disturbances with order higher than two.

In [30], a fuzzy logic based load torque observer is designed to estimate the load torque. In this approach, a linear observer is utilized as a local observer, and its design is based on the conventional assumption about slowly changing load torque. Linear active disturbance rejection (LADRC) scheme is proposed in [32]. In this work, a load torque observer is designed to compensate the influence of load torque variations. The authors designed the LADRC based on the conventional assumption that considers the time derivative of the load torque as equal to zero. This assumption might not work well when a PMSM operates at transient time. Furthermore, according to [32], two observers are required for the control system. Meanwhile, in [40], the high-order disturbance observer is proposed and tested on an IPMSM. The disturbance in [40] is considered to be of a polynomial form and its high-order derivatives to be bounded such that the disturbance is slowly changing over time. Unfortunately, this assumption might not work when the disturbances have a sinusoidal oscillation form.

Observers designed in [31, 34–36, 41] are limited to estimate only a load torque. Studies in [44, 48, 53, 54] proposed disturbance observer considering the first-order derivatives equal to zero or bounded by some positive constant. However, these assumptions may not be feasible in practical applications for control PMSMs.

H_∞-based disturbance observer is proposed for a PMSM in [31]. However, in this work, the observer is designed to estimate only the load torque. Similarly, the authors in [34] propose a nonlinear disturbance observer which estimates a load torque and neglects disturbances due to friction. A generalized proportional integral observer (GPIO) is designed in [55] to estimate lumped disturbance under the assumption that the high-order derivatives of the lumped disturbance are zero.

The ESO is designed to estimate an external disturbance in the speed loop in [41]. According to this work, the external disturbance represents only a load torque. The proposed method might require a detailed performance analysis in case of fast-changing disturbance affects a system. In [53], an extended sliding-mode disturbance observer is proposed to improve speed response of a PMSM. Internal parameter variations and load torque are represented as a disturbance. In this design, the authors assume that a load torque changes with a zero rate, and the disturbance is considered to be bounded. An application of the proposed observer to estimate fast-changing disturbances is not shown. In [35], an advanced second-order sliding mode observer is proposed to estimate only a load torque disturbance in PMSM drives. [36] designed an anti-disturbance speed control scheme for high-torque PMSM based on the sliding mode observer. The proposed design ignores the friction in the mechanical motion and estimates a load torque, which is considered as a constant value. Lumped disturbances in PMSM are

estimated using an extended Kalman filter (EKF) in [44]. However, the time-derivative of the lumped disturbances is taken as zero and this assumption makes the designed observer weak in application for PMSM. Similarly, a proposed nonlinear disturbance observer (NDOB) in [54] estimates disturbances with slow dynamics. [48] shown a disturbance observer based on Super-Twisting Algorithm to estimate unknown external disturbances. The design method takes only the first time-derivative of disturbance term to be bounded.

Precise speed control of PMSM is not easy due to inevitable nonlinear dynamics and potential external and internal disturbances or parameter variations. Disturbances could emerge as a external load torque, frictions of mechanical parts, or as measurement noises [56]. Thanks to a primitive structure, the traditional proportional and integral control (PI) scheme becomes as a popular one in control of electrical machines, particularly, PMSMs. Furthermore, the PI implicitly has a mechanism of disturbance rejection, for instance, in a PMSM's case, the PI gets the reference speed tracking error to find a bias and estimation of disturbance [57, 58]. The cascaded PI controllers are used as main controllers in a technique called as field-oriented control (FOC) (details on the cascaded FOC scheme is presented in Chapter 2).

It is stated that the effect of disturbance negatively affects the output of the speed controller which may generate wrong reference for the i_q^r-current controller, and this results in the degradation of an overall PMSM control system [59]. Furthermore, it is a lack of comprehensive analysis on disturbance attenuation technique in traditional PI schemes [60]. Although the PI scheme is a linear controller with ordinary design, it is not straightforward to obtain universal tuning rules for controller parameters. Major of the existing tuning rules need an exact model of a plant, which in turn inhibits control designers select suitable gains during applications [61].

For control of majority industrial systems, performance analysis on disturbance rejection technique is more important than analysis of just an ideal reference command tracking [58]. Numerous composite control schemes in which the traditional PI is used with disturbance rejection technique [33, 40, 62, 63], [32, 34, 43, 64–68] exist in the literature.

The ESO as a main disturbance rejection technique is used in [33, 67] to construct a linear-nonlinear switching ADRC for both speed and current control of a PMSM. A DOBC scheme is introduced to estimate unmatched disturbance in [62]. In this method, the current constrained PID is used together with a disturbance observer. It is stated in [61] that the current constraint can be slightly violated with the DOBC approach. A fractional-order PID (FOPID) and fractional-order PI (FOPI) are presented for control a PMSM in [34, 65]. The control parameters of the FOPID are selected based on algorithms of optimization, whilst the FOPI's parameters are adjusted online. An ESO-based PID is proposed for PMSMs in [66]. The proposed scheme requires a

mathematical model of a system to be known. Further improvement in the traditional PID can be found in [69], where the parameters of the PID are adapted online by the proposed adaptation laws. Since the adaptation laws are based on the sliding mode dynamics, a solution of chattering problem is not presented in details. Also, the learning rates of the method should be selected properly in order to guarantee satisfactory performance.

In the work of [43], a composite controller is proposed to deal with several disturbances existing in a PMSM. The proposed method in [43] shows satisfactory results in suppression of several disturbances, however the tuning of the controller as well as observer is not shown in details. A method consisting of the feedback linearizing approach and high-gain extended observer is proposed in [68]. This approach shows better results than the traditional PI, but the detailed information on design steps of the observer and its estimation performance are not shown. Disturbance observer-based nonlinear composite speed controller is presented in [70] to speed control of a PMSM. An ESO is utilized to estimated disturbance. Although the method shows promising simulation results, detailed experimental validations should be conducted in order to facilitate its practical application. Fuzzy-logic-based sliding mode controller is presented for speed control of a PMSM. The fuzzy inference is utilized to overcome chattering problem existing in a steady state as well as in the transient period of the speed response.

Optimal control (OC) is one of the important control methods which has a lot of versions and applications. Numerous OC methods [71–77] have been proposed and implemented to get accurate and robust control of a PMSM. In [71], an adaptive OC has been designed to track an error dynamics of the PMSM during transient mode. This method employed an actor-critic neural network to get online solution for the Hamilton-Jacobi-Bellman (HJB) equation to approximate the OC laws by means of adaptive dynamic programming (ADP). Although this method shows satisfactory results in tracking of error dynamics, performance under a sudden disturbance is not shown clearly. A θ-D approximation method is employed for optimal speed control of PMSM in [72]. In this work, solving of an HJB equation is simplified by using the θ-D approximation, and hence complicated HJB equations are reduced to an simpler algebraic Riccati equation (ARE) along with Lyapunov state equations. Fuzzy control theory is integrated with OC design and implemented for a PMSM in [73]. Even though the proposed method with optimal control parameters shows better reference tracking performance than a traditional linear quadratic regulator (LQR), its implementation in practice seems complicated and might need a hardware with high computation capabilities. A model predictive approach for speed control of an interior PMSM (IPMSM) has been applied in [74]. In this work, a traditional PI controller in speed loop is replaced by the proposed model predictive method, where the speed and flux

errors are included in a cost function to track a predefined reference speed and improve quality of stator currents, respectively. However, this method requires complicated calculations to find a reference for a stator flux, and then parameters of a particular machine need to be pre-defined. A neural network (NN)-based optimal controller is designed for a current control loop of a surface-mounted PMSM (SPMSM) in [75]. In general, the method in [75] shows performance with minor difference comparing to a traditional PI controller, except a high-speed region, in which the proposed method is more robust. Another application of an NN-based control is presented in [76]. This work attempted to improve a super-twisting sliding mode control (STSMC) by means of heuristic dynamic programming (HDP) for optimal tuning of parameters of an STSMC. Implementation of the methods in [75, 76] seem complicated and need a hardware with powerful characteristics. In [77], an optimal control has been designed for the reference speed tracking of a PMSM. Although this method gives more accurate outputs compared to the traditional PI, a detailed information on its advantages is not presented clearly.

Among the proposed control solutions a disturbance observer based control (DOBC) approach has been actively studied in the last two decades. A DOBC represents an active anti-disturbance control (AADC) and ensures an effective approach to deal with disturbances and guarantees robustness of a closed-loop system. The DOBC is a composite controller that combines a feedback controller (e.g. PI controller) and disturbance observer-based feedforward controller [10]. A traditional PI controller is widely used as a feedback controller in the DOBC. Despite that the PI controller has only two parameters to tune, in practice, there is no an obvious way to select those parameters unless a systematic approach has been applied [78, 79]. Furthermore, it is shown that tuning of PI control parameters for over the whole operation speed of a PMSM is difficult due to several factors such as position error, current measurement error, time delay in system, parameter variations, etc [79]. The inner current control has a huge impact to the whole system performance [80]. Unfortunately, the traditional PI controllers might show unsatisfactory results due to nonlinearities coming from complicated operating conditions (represented by external disturbances), saturation phenomena in magnetic parts, temperature increase, and possible parameter variations in the current loops as well. Hence, selection of the PI controller parameters for both speed and current control loops by widely used trial-and-error method cannot be feasible in such conditions. Numerous disturbance observer (DOB)-based control schemes for speed-current control of a PMSM are presented in literature. A disturbance observer-based H_∞ speed controller is proposed in [81]. This method is applied only for the speed loop and the traditional PI controllers are utilized in the current loops. Although this method shows the promising results in speed control, the influence of the electrical parameters such as stator resistance and inductance are not considered in

the controller design. In order to show the merits of the linear and nonlinear ADRC schemes, linear-nonlinear switching ADRC (LNSADRC) are designed in the works [33] and [67]. In [33], the LNSADRC serves as speed and current controller for PMSM whereas the switching ADRC method in [67] is designed to control only the speed of a PMSM. Despite the attractive results obtained by the proposed methods, these methods might not be effective in terms of several tuning parameters to achieve satisfactory system performance.

In literature, there are many disturbance observer schemes proposed for robust control of PMSM, however, most of those schemes considered disturbance as a constant value or as a variable with slow dynamics. This kind of assumption might create some limitations on usage of such observer schemes in practical point of view. Therefore, this thesis work attempts to resolve such restrictions on observer design by considering not only dynamics of disturbance but also dynamics of its high-order derivatives. Moreover, this thesis aims to propose practical and straightforward observer design that might be clear to understand not only for researchers but also for control engineers.

This thesis also focuses on improvement of design and tuning approach of traditional PI scheme, which is mainly used in a cascaded FOC scheme. Although the PI schemes presented in literature are widely used in the FOC strategy, its disturbance rejecting mechanism is not stated explicitly. Furthermore, in most research studies, parameters of PI scheme are obtained based on well-known "trial-and-error" approach, which, in turn, can be ineffective if there is no solid knowledge about a plant to be controlled. The thesis work attempts to find explicit formula for PI controller with disturbance rejecting mechanism via using modified disturbance observer-based control.

While most studies utilizing DOBC and ADRC consider these two control schemes as a two different approaches, in this thesis, a first attempt is done to unify these two techniques applied to speed control of PMSM. Based on the obtained results, one can get the following benefits: 1) explicit formulas of dynamic delays in estimated disturbance in both DOBC and ADRC cases are obtained; 2) it is possible to combine the advantages of these two disturbance rejecting schemes such that the ADRC is constructed based on desired delay of estimation of the low-pass filter (LPF) in the DOBC. This, in turn, may help to overcome derivative issue specific to the ADRC. Similarly, one can use superiorities of the ADRC to construct the DOBC.

In the provided literature review, control methods were designed for either surface mounted PMSM (SPMSM) or interior-magnet PMSM (IPMSM). It should be noted that all experiments provided in this thesis work are conducted on particularly type of PMSM, i.e. an SPMSM.

1.2 Main objectives of the current work

The main objectives of this work is the study and design of a disturbance observer-based composite control scheme that can guarantee robust control system for a surface mounted PMSM (SPMSM) (more about SPMSM is discussed in Chapter 2) working under different sources of disturbances. To address stability and robustness of the control of an SPMSM system, uncertainty sources (uncertainties due to parameter mismatch, uncertainties due to external perturbations, uncertainties due to un-modelled dynamics) arising due to different working conditions, load changes, and variations in mechanical as well electrical parameters of the machine are also considered during the design of the control system. A task of the control system is to provide an accurate reference tracking of an SPMSM rotor's speed under the influence of unpredicted disturbance changes.

In order to fulfill the main objectives of the work the following steps have been performed:

- Relatively accurate practical model of a SPMSM was obtained and utilized. The information about the obtained practical model of the SPMSM is discussed in Chapter 2;
- Different disturbance observer-based control schemes were designed and proposed for the speed control of the SPMSM and stability analysis of a closed-loop SPMSM system with those control schemes are presented;
- Rigorous simulation studies were performed to support theoretical evidence resulted from the theory of the proposed control solutions;
- Extended experimental studies were conducted to verify the validity of the proposed control designs in practical applications.

1.3 Main contributions of the current work

This work is devoted to design of novel disturbance observer-based composited controllers for SPMSMs under the field-oriented control (FOC) strategy. The fundamental contributions of the thesis are recapitulated as follows:

1. A high-order disturbance observer-based composite controller (HDOBCC) based on fuzzy-PI controller and generalized high-order disturbance observer (GPHDO) is designed for the speed control of an SPMSM under the FOC strategy. In this control scheme, the fuzzy-PI controller is utilized to guarantee a finite-time stability of speed loop control of the SPMSM system, while the GPHDO is required to estimate lumped disturbances in the speed loop and compensate it via

the feedfoward control. The detailed stability analysis of the speed loop dynamics with the proposed disturbance observer with various orders is investigated. The fuzzy logic is utilized to adjust the gains of the PI controller and improve the speed performance of the motor during the transient dynamics. The current control is achieved via the standard PI controllers. To show the effectiveness and superiority of the HDOBCC over the standard PI controller, comparative experimental studies are performed on an SPMSM working under different types of disturbance load.

2. A novel PI-like scheme called disturbance rejection PI (DR-PI) is proposed for speed regulation of the SPMSM. In this novel design, the standard PI controller is augmented with the pre-filter element and combined with the modified DOBC scheme. In the proposed DR-PI scheme, the disturbance observer and controller are considered as a compact structure. The overshoot problem common to the standard PI controller is eliminated using the pre-filter which is obtained in consequence of design of the modified disturbance observer. The novel PI-like structure has systematic and straightforward gain tuning mechanism. Two standard PI controllers are used to control currents in the current loop. Detailed stability analysis of the closed-loop DR-PI-based speed control system is provided, and the experimental outcomes reveal that the DR-PI is superior over the standard DOBC scheme during the transient operation of the motor.

3. A hierarchical optimal disturbance observer based control (HODOBC) scheme is synthesized for the speed and current control under the FOC strategy. In this control scheme, under the frame of the disturbance observer-based approach, the PI-like control scheme is adopted where the gains of the controller are calculated using the linear-quadratic regulator (LQR) method. Thanks to the LQR approach, the gain tuning mechanism of the PI-like controller becomes simple and experimentally feasible. The proposed HODOBC scheme is implemented to control both outer speed loop as well as two inner current loops. The stability of the HODOBC-based closed loop system is established using the root locus approach and it reveals that with the calculated gains the proposed cascaded HODOBC system is very robust for parameter variations. The performance of the proposed scheme is compared with the performance of the standard PI and DOBC scheme via the experiments, where the SPMSM with the HODOBC-based cascaded scheme shows faster and more robust response under different operation conditions of the motor.

4. A study on unification of the DOBC and ADRC schemes on the basis of speed control of SPMSM is performed. According to the study, the detailed formulas of dynamics delay of disturbance estimation are derived. The transparent

formulas of the disturbance estimation clearly show the following components, i.e. a component indicating external disturbances, a component representing uncertainty terms (parameter variations), and a component indicating dynamical delay of disturbance estimation. During the analysis, it is revealed that unification of dynamical delay of the DO in the DOBC and ESO in the ADRC schemes provides similar estimation performance. The stability analyses of closed-loop speed control of an SPMSM using each disturbance estimation technique are shown via the root locus technique. Comparative experimental studies using the DOBC and ADRC schemes are conducted for analysis of the SPMSM's performance working under the load during the steady-state as well as transient time. This is the first attempt on assessment of dynamical delays of two popular disturbance observer-based schemes like DOBC and ADRC.

1.4 List of publications

1. K. Suleimenov and T. D. Do, "Design and Analysis of a Generalized High-Order Disturbance Observer for PMSMs With a Fuzzy-PI Speed Controller," IEEE Access, vol. 10, pp. 42252-42260, 2022.

2. K. Suleimenov and T. D. Do, "A Practical Disturbance Rejection Control Scheme for Permanent Magnet Synchronous Motors," Symmetry, vol. 14, no. 9, p. 1873, 2022.

3. H. V. Nguyen, K. Suleimenov, B. H. Nguyen, T. Vo-Duy, M. C. Ta, and T. D. Do, "Dynamical Delay Unification of Disturbance Observation Techniques for PMSM Drives Control," IEEE/ASME Transactions on Mechatronics, vol. 27, no. 6, pp. 5560-5571, 2022.

4. A. Kashaganova, K. Suleimenov, S. Sagnaeva, and T. D. Do, "Maximum power tracking for wind energy conversion systems via a high-order optimal disturbance observer-based LQR without a wind speed sensor," Eng. Scien. and Technol., an International Journal, vol. 45, pp. 101472, 2023.

5. B. Sarsembayev, K. Suleimenov, B. Mirzagalikova, and T. D. Do, "SDRE-based integral sliding mode control for wind energy conversion systems," IEEE Access, vol. 8, pp. 51100-51113, 2020.

6. B. Sarsembayev, K. Suleimenov, and T. D. Do, "High-Order disturbance observer-based discrete-time PI-PI control system with anti-windup for PMSMs," IEEE Access, 2021.

1.5 Thesis outline

Most parts of the thesis are based on the published or submitted to peer-review work, therefore repetitive background theory and explanations may exist. The outline of the current thesis can be shown in Fig. 1.1. The structure of the thesis is based on two parts such as theory and applications. The chapters on the theoretical part describe modelling of an SPMSM and disturbance observers. The chapters describing applications respectively refer to the chapters on theory of disturbance observers. The detailed information of each chapter are presented as follows:

Chapter 2: Initially, theoretical basis of the SPMSM models in the stator and rotor reference frames is presented. Further, a three-phase inverter and two pulse width modulation (PWM) techniques used in AC drive control, i.e. sinusoidal PWM and space vector PWM techniques, are introduced. Common types of uncertainties existing in SPMSMs such as parameter variations, external disturbances, un-modelled dynamics are reviewed. Expressions for power and electromagnetic torque generated in SPMSMs are given further. After reviewing of the common uncertainties in SPMSMs, the practical system of the motor including such uncertainties is obtained. After this, the fundamentals of the field-oriented control (FOC) strategy for the SPMSMs have been presented shortly. Common constraints belong to AC drive systems, i.e. voltage and current constraints, are reviewed for the SPMSM operation. Finally, the brief information on description of hardware and software equipment used in experiments is presented.

Chapter 3: In this chapter, theory on disturbance observers, i.e. conventional disturbance observer (DOB), modified disturbance observer, extended state observer (ESO), and high-order disturbance observer is briefly presented. Specifically, the conventional DOB design is formulated in time and frequency domains. Further, based on the conventional DOB scheme, the modified version of the DOB is shown. Under the framework of the modified DOBC scheme, a disturbance rejection control theory is derived. Advantages of the ESO over the conventional DOB are discussed and presented based on a general second-order dynamic system. Finally, theory of design of high-order disturbance observer is presented in details.

Chapter 4: A comprehensive design and stability analysis of the generalized high-order disturbance observer-based composite control (HDOBCC) are presented for speed control of the SPMSM. Based on the practical model of the current dynamics, two conventional PI controllers are utilized in the inner loop of the cascaded FOC strategy of the SPMSM. The experimental comparative results between the traditional PI-PI based cascaded FOC strategy and proposed HDOBCC-based FOC strategy are analyzed and presented.

Chapter 5: This chapter presents a disturbance rejection PI (DR-PI) control based on a modified DOBC scheme. The proposed DR-PI is applied to control a rotor's speed

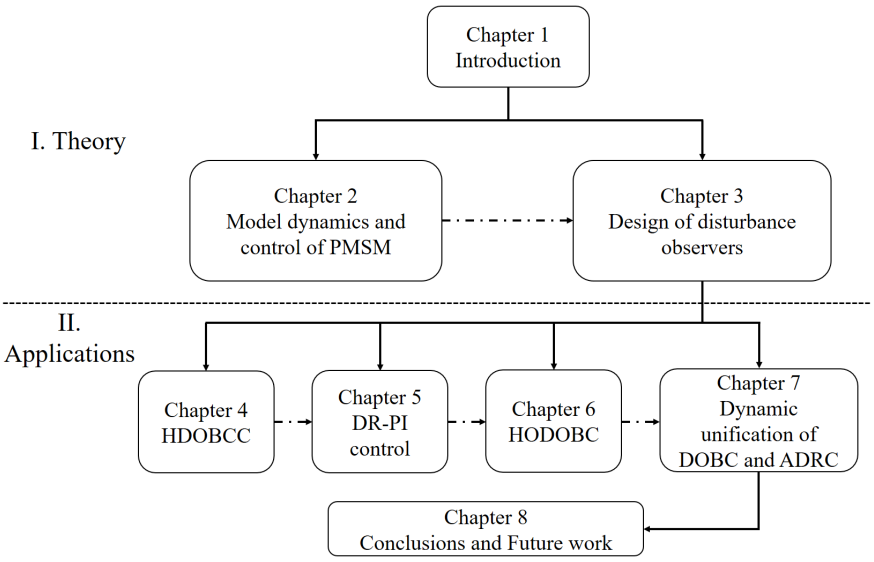

Figure 1.1: Outline of the current thesis

of the SPMSM. A stability and gain tuning mechanism in the proposed method are discussed in a straightforward manner. The comparison of the experimental results of the proposed DR-PI-based cascaded FOC with the traditional PI-PI cascaded FOC and DOBC-based cascaded FOC are presented and discussed.

Chapter 6: A comprehensive design and stability analysis of the hierarchical optimal disturbance observer-based control (HODOBC) for a SPMSM are introduced. Specifically, the HODOBC is designed for the speed control loop as well as for two current control loops under the cascaded FOC strategy. The comparative experimental results among the methods implemented under the FOC strategy, i.e. traditional cascaded PI-PI, traditional DOBC, HODOBC designed for only speed control loop, and HODOBC designed for both speed and current control loops are provided and discussed.

Chapter 7: In this chapter, two popular disturbance observer-based control schemes, i.e. DOBC and ADRC, are considered and explicit formulas of dynamical delays of estimated disturbances are presented. Comparative simulation and experimental studies between the DOBC and ADRC schemes are performed. Stability analysis of two disturbance observer-based closed-loop speed control schemes are presented and discussed.

Chapter 8: This chapter concludes the thesis and presents about future perspectives for control SPMSMs.

Part I

Theory

BLANK

Chapter 2

Model dynamics and control of PMSM

2.1 Structural description and principle of operation

The main difference of permanent magnet synchronous motors (PMSMs) from other electrical drives is in the configuration of the rotor. Locations of magnets on the rotor define different categories of the PMSMs. In literature, based on the location of magnetic elements on the rotor, the categories such as surface-mounted PMSM (SPMSM), interior magnet PMSM (IPMSM), and inset magnet PMSM can be distinguished. In terms of control perspectives, the PMSM can be considered as salient and non-salient motors [1]. The SPMSM belongs to a non-salient type of motor, whereas the IPMSM and inset magnet PMSM are representatives of a salient PMSM. In the SPMSM, due to the locations of magnets on the surface of the rotor, the equal reluctance is created, this phenomenon in turn creates a non-uniform air-gap resulting in a loss and noise. Unlike the SPMSM, inset magnet and interior types of PMSM have different reluctance, hence air-gap might be non-uniform or uniform in these types of motor based on how the magnetic poles are located. Each type of the PMSM has own advantages as well as drawbacks defined in terms of permanent magnets location, way of permanent magnets fixing, type of permanent magnets, generated harmonics, saliency, reluctance torque, speed range, and power density [3]. For instance, an SPMSM, usually, is not applicable for applications with speed more than 3000 rpm, but negligible difference in reluctance simplify the operation and control of this motor. An IPMSM has a robust mechanical structure and, due to this, it is widely used in applications with high range of speed, however, production of this type of the motor is complicated in terms of manufacturing comparing to the SPMSM or inset magnet PMSM. It should be noted that PMSMs have less possibilities of overheating due to the absence of copper loss and magnetizing current in the rotor. This factor leads to extended lifetime of a motor and reduced cost of maintenance [1].

A torque in a PMSM is produced according to similar principal of wound rotor synchronous motors (WRSM), but in the PMSM case, an excitation magnetic field is developed by permanent magnets not by windings as in the WRSM [1, 82]. A magnetomotive force (mmf) created in the stator and flux of the rotor are important

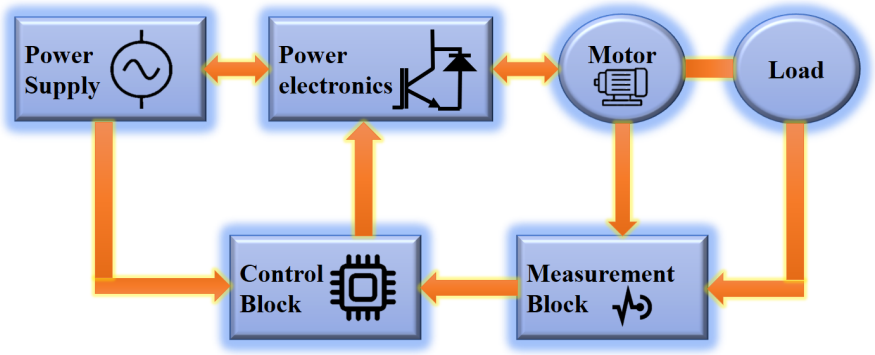

Figure 2.1: A general VSD diagram.

components in developing of electromagnetic torque. The mmf in the stator is generated by the stator currents, whereas the flux is created by the permanent magnets of the rotor. As it is known, three stator windings shifted from each other by 120^0 and conducting the currents (also shifted by 120^0) develop a rotational magnetic field with a constant magnitude and frequency equal to the frequency of the injected currents. When stator and rotor fields have the same rotational speed, interaction of these fields create a constant torque called as an alignment torque. At steady-state mode, motor torque and rotor speed are determined by the magnitude of the stator current and its frequency. However, during the transient mode, the rotor's magnetic field may be asynchronous with magnetic field produced by the stator. These two fields can be synchronized during the transient time by proper design of a control system.

Motors play a crucial role in conversion of electrical energy into mechanical energy and they are necessary in all economic needs and casual lives. Majority part of motors is aimed to run at invariable speed and produce constant productiveness, but the modern industry requires operation of motors at different range of speed. Variable speed drive (VSD) system is used to control both the speed and electromagnetic torque of the motor and it is an important part in regulation of electrical pumps, electrical vehicles, elevators, robotics, air conditioning systems, etc [83]. A VSD system serves as a main part in conversion of electrical energy from DC or AC electrical power supply into the mechanical energy. General diagram of the VSD system can be summarized as in Figure 2.1. The VSD system comprises of six components such as power supply unit, power electronics unit, DC or AC motor, external load, measurement block, and control block.

Power supply is utilized to satisfy different electrical power requirements of power electronics unit and motor drives in various usage. The power supply can receive electrical power from different power sources such as renewable energy sources, hydro power stations, etc.

The power electronics unit in the VSD system is based on the semiconductor components which can include diodes, MOSFETs, and IGBTs. Thanks to high switching

frequency of semiconductor components, power electronics unit is able to convert an energy from the power supply into corresponding forms of voltage or current. Many topologies of power electronics unit are available for various applications, but most commonly utilized topologies in variable speed drive systems are rectifiers represented by AC/DC converters, DC/AC inverters, and DC/DC converters. A diode rectifier which is placed between the power supply unit and DC terminals of the DC/AC inverter does not permit electrical power to go back into the power supply [6]. The inverter is used to invert the rectified DC power into the AC power. Depending on the energy type stored in the DC-link, the inverters can be categorized into voltage-source inverters (VSIs) and current-source inverters (CSIs). The VSIs are more popular comparing to CSIs due to the low cost and straightforward control [1]. Details about the VSIs are presented in the following section.

An electrical motor serves as a heart of the variable speed drive system and it is responsible for conversion of electromechanical energy. Furthermore, the electrical motor can also convert a mechanical energy into the electrical energy by delivering it to power supply during a regenerative mode of motor running [1, 6]. Actually, the primary purpose of the control block and power electronics unit in the VSD system is to provide high-performance motor operation.

An external load as a part of the VSD system is characterized by different applications. Satisfying to the demand of the external load in terms of power and torque capabilities is a main goal of making the VSD system. Consequently, it is recommended to determine parameters of an external load in advance in order to avoid potential issues of the VSD system due to overloading as well as overheating.

The fundamental aim of the measurement block is to measure all of the required information to send to the control block. The measurement signals are generally obtained via the mechanical and electrical sensors. In the VSD system, voltage, current, flux, position, and speed sensors are commonly used.

The control block as a part of the variable speed drive system is represented by hardware equipment such as digital signal processor (DSP), field programmable gate arrays (FPGAs), and microprocessors. It serves as a brain of the VSD system. The control block receives the information required for its implementation from the measurement block. Further, it generates the switching commands for the VSI in the power electronics unit to meet the requirements of the motor response and characteristics of the external load [84].

Satisfactory operation characteristics of the VSD system can be guaranteed by the highly effective control strategy carried out in the control block. Quick progress in design of hardware components leads to the wide use of vector-based closed-loop control strategies in the VSD systems. Vector control or field-oriented control (FOC) and direct torque control (DTC) strategies are the most popular representatives of

vector-based closed-loop control strategies. These two control strategies are formed in a cascaded structure consisting of two loops, i.e. inner loop and outer loop. In the inner loop, the FOC method performs control of current signals, whereas the DTC method controls the flux linkage of the stator and electromagnetic torque. In the outer loop, both FOC and DTC methods control the speed of the rotor [6].

2.2 Permanent magnet brushless DC vs PMSM

Among the existing AC motors, PMSMs have been confused in the literature with permanent magnet brushless DC (PMBLDC) motors, because these two motors have similarities in terms of used material and structure of the rotor [7, 85]. Unlike the PMSMs, the PMBLDC motors have different principle of operation, i.e. the PMBLDC motors operate due to the principle similar to those of traditional DC motors. In both motors, the excitation field is created by permanent magnets on the rotor [1, 85]. These two motors have different patterns of the back electromotive force (EMF), i.e. PMSMs generate a sinusoidal form of the back EMF, whereas the PMBLDC is characterised by the trapezoidal (square) form of the back EMF. Different patterns of the back EMF is obtained due to the difference in arrangements of magnets and cavities as well as a structure of coil winding. Due to high performance, durability, quiet operation, and accurate torque control, a PMBLDC is considered as one of the high-efficient motors and promising one in industry of electrical motors. However, a control of the PMBLDC at low speeds is still not stable and its module of drive control remains to be expensive. Furthermore, due to the speed-torque relationships, the application of the PMBLDC in the EV industry is limited by cars with power less than 30 kW [83]. Comparing to the PMBLDC, the PMSMs are preferable in terms of accurate position and speed control. Moreover, the PMSMs do not generate much torque ripples as PMBLDC motors [3]. There are other types of electrical motors that can have similarities with PMSMs, e.g. line-start PM motors and synchronous reluctance motors [1].

2.3 PMSM models in the stator and rotor reference frames

Transformation of coordinate system from one reference frame to another one is a required step in developing of the FOC technique. Usually, reference frame transformations are carried out from the three-axis stator's reference frame to the two-axis rotor's frame. Generally, transformations of reference frames can be made in three different types as (i) the reference transformation from the three-axis stationary frame to the two-axis stationary frame; (ii) the reference transformation from the two-

axis stationary frame to the two-axis rotational frame; (iii) the reference transformation from the three-axis stationary frame to the two-axis rotational frame [1, 2, 6].

2.3.1 Three-axis stationary stator frame: a-b-c frame

In AC drives, three phase windings are located such that to have an angle of 120^0 between each pair of the phases. A rotational mmf is created due to the injection of three-phase alternative current into a terminal of each winding. At the same time, the injected alternative current should be balanced in order to have a zero sum of the current components during the operation. This constraint on the alternative currents helps to define a flux vector in the complex plane and hence makes an easy mapping principle of the reference transformation. Reference frame transformations can be performed using matrix manipulations. Comparing to a WRSM, voltage equations of the PMSMs are determined only by equations of the stator. Therefore, the voltage equations of the PMSMs are given in the three-axis $a-b-c$ stator frame as below [1, 6]

$$\begin{bmatrix} v_a^s \\ v_b^s \\ v_c^s \end{bmatrix} = \begin{bmatrix} R_s & 0 & 0 \\ 0 & R_s & 0 \\ 0 & 0 & R_s \end{bmatrix} \begin{bmatrix} i_a^s \\ i_b^s \\ i_c^s \end{bmatrix} + \delta \begin{bmatrix} \gamma_a \\ \gamma_b \\ \gamma_c \end{bmatrix} \tag{2.1}$$

where R_s is a resistance of the stator windings, v_a^s, v_b^s; and v_c^s are voltages in the stator windings, i_a^s, i_b^s, and i_c^s are currents in the stator windings; γ_a, γ_b, and γ_c are flux linkages; δ is an operator of a time-derivative.

As known, the currents in the stator windings and permanent magnets on the rotor surface create two separate origins of the flux, as a result, three phase flux linkages are produced. The equations of the flux linkages can be represented in a compact matrix form as

$$\begin{bmatrix} \gamma_a \\ \gamma_b \\ \gamma_c \end{bmatrix} = \begin{bmatrix} L^{a-a} & L^{a-b} & L^{a-c} \\ L^{b-a} & L^{b-b} & L^{b-c} \\ L^{c-a} & L^{c-b} & L^{c-c} \end{bmatrix} \begin{bmatrix} i_a^s \\ i_b^s \\ i_c^s \end{bmatrix} + \gamma_{pm} \begin{bmatrix} \cos(\phi_r) \\ \cos(\phi_r - \frac{2\pi}{3}) \\ \cos(\phi_r + \frac{2\pi}{3}) \end{bmatrix} \tag{2.2}$$

where L^{a-a}, L^{b-b} and L^{c-c} - self-inductions of the stator's coil in each phase; L^{a-b}, L^{a-c}, L^{b-a}, L^{b-c}, L^{c-a}, and L^{c-b} - mutual inductions created between the stator's windings; ϕ_r - an electrical angle between an axis of the rotor's pole and an axis of the stator winding in the phase a; γ_{pm} - a magnetic flux linkage created by poles of the permanent magnets, this parameter is defined by properties of permanent magnets and a structure of a motor. The equations of the inductances (self and mutual) presented in

2.2 can be expressed by

$$\begin{aligned}
L^{a-a} &= L_{comp_1} + L_{comp_2}\cos(2\phi_r) \\
L^{b-b} &= L_{comp_1} + L_{comp_2}\cos(2\phi_r + \frac{2\pi}{3}) \\
L^{c-c} &= L_{comp_1} + L_{comp_2}\cos(2\phi_r - \frac{2\pi}{3}) \\
L^{a-b} &= -\frac{1}{2}L_{comp_1} + L_{comp_2}\cos(2\phi_r - \frac{2\pi}{3}) \\
L^{b-c} &= -\frac{1}{2}L_{comp_1} + L_{comp_2}\cos(2\phi_r) \\
L^{a-c} &= -\frac{1}{2}L_{comp_1} + L_{comp_2}\cos(2\phi_r + \frac{2\pi}{3})
\end{aligned} \tag{2.3}$$

in which L_{comp_1} and L_{comp_2} are the components of inductance due to flux linkages defined by air gap and position of the rotor, respectively.

2.3.2 Two-axis stator reference frame: α-β frame

In the two-axis stator reference frame, a model of an equivalent AC drive is designed based on two fictitious stator windings with sinusoidal distribution and ninety degrees apart reference frame axes. We denote the axes of the new reference frame as α- and β-axis, respectively. The α-axis is taken such that it is coincided with the axis a. Using matrix operations voltage equations in the three-axis stator frame (2.1) can be transformed into the two-axis stator reference frame as

$$\begin{bmatrix} v^s_\alpha \\ v^s_\beta \\ v_0 \end{bmatrix} = \frac{2}{3}\begin{bmatrix} 1 & -\frac{1}{2} & -\frac{1}{2} \\ 0 & \frac{\sqrt{3}}{2} & -\frac{\sqrt{3}}{2} \\ \frac{1}{\sqrt{2}} & \frac{1}{\sqrt{2}} & \frac{1}{\sqrt{2}} \end{bmatrix}\begin{bmatrix} v^s_a \\ v^s_b \\ v^s_c \end{bmatrix} \tag{2.4}$$

Similarly, we can represent three-phase currents and flux linkages in the two-axis stator reference frame

$$\begin{aligned}
\begin{bmatrix} i^s_\alpha \\ i^s_\beta \\ i_0 \end{bmatrix} &= \frac{2}{3}\begin{bmatrix} 1 & -\frac{1}{2} & -\frac{1}{2} \\ 0 & \frac{\sqrt{3}}{2} & -\frac{\sqrt{3}}{2} \\ \frac{1}{\sqrt{2}} & \frac{1}{\sqrt{2}} & \frac{1}{\sqrt{2}} \end{bmatrix}\begin{bmatrix} i^s_a \\ i^s_b \\ i^s_c \end{bmatrix} \\
\begin{bmatrix} \gamma_\alpha \\ \gamma_\beta \\ \gamma_0 \end{bmatrix} &= \frac{2}{3}\begin{bmatrix} 1 & -\frac{1}{2} & -\frac{1}{2} \\ 0 & \frac{\sqrt{3}}{2} & -\frac{\sqrt{3}}{2} \\ \frac{1}{\sqrt{2}} & \frac{1}{\sqrt{2}} & \frac{1}{\sqrt{2}} \end{bmatrix}\begin{bmatrix} \gamma_a \\ \gamma_b \\ \gamma_c \end{bmatrix}
\end{aligned} \tag{2.5}$$

where v^s_α, v^s_β, i^s_α, and i^s_β are the stator voltages and currents in the $\alpha - \beta$-frame, accordingly; γ_α and γ_β are the flux linkages represented in the $\alpha - \beta$-frame. In literature, the transformation from the three-axis stator frame into the two-axis stator frame is known as the *Clarke transformation*. A term v^s_0 in (2.4) is a fictitious term

introduced to have the *Clarke transformation matrix* $T_{Clarke} = \frac{2}{3}\begin{bmatrix} 1 & -\frac{1}{2} & -\frac{1}{2} \\ 0 & \frac{\sqrt{3}}{2} & -\frac{\sqrt{3}}{2} \\ \frac{1}{\sqrt{2}} & \frac{1}{\sqrt{2}} & \frac{1}{\sqrt{2}} \end{bmatrix}$ to be invertible. This term usually called as a zero component, and it is zero when the following relationship of three phase variables is kept

$$p_a^s + p_b^s + p_c^s = 0 \tag{2.6}$$

where p_a^s, p_b^s, and p_c^s represent one of the three-phase variables such as voltage, current or flux. We note that the relationship in (2.6) arises from the balanced three-phase PMSM, in which a net sum of variables such as voltages, currents, and flux linkages in each phase winding is zero. When a PMSM operates in a steady-state, phase voltages and phase currents are balanced and sinusoidal with 120^0 angle difference in phase, i.e.

$$\begin{aligned} v_a^s &= V_{abc}\cos\Omega t \\ v_b^s &= V_{abc}\cos(\Omega t - \frac{2\pi}{3}) \\ v_c^s &= V_{abc}\cos(\Omega t + \frac{2\pi}{3}) \\ i_a^s &= I_{abc}\cos\Omega t \\ i_b^s &= I_{abc}\cos(\Omega t - \frac{2\pi}{3}) \\ i_c^s &= I_{abc}\cos(\Omega t + \frac{2\pi}{3}) \end{aligned} \tag{2.7}$$

where V_{abc} and I_{abc} are amplitudes of the three-phase voltages and currents, accordingly; Ω is an angular frequency of the three-phase voltages delivered into the stator windings. Hence, in the α-β stationary frame, three-axis stator voltages and currents in (2.7) have a form

$$\begin{aligned} v_\alpha^s &= V_{abc}\cos\Omega t \\ v_\beta^s &= -V_{abc}\sin\Omega t \\ i_\alpha^s &= I_{abc}\cos\Omega t \\ i_\beta^s &= -I_{abc}\sin\Omega t \end{aligned} \tag{2.8}$$

From (2.8), we point out that in the two-phase stator frame, only two sinusoidal components 90^0 apart are introduced.

In order to get a three-phase voltages based on the $\alpha-$ and $\beta-$ voltages in the two-axis stator frame, an inverse transformation, i.e. *inverse Clarke transformation*, is used

$$\begin{bmatrix} v_a^s \\ v_b^s \\ v_c^s \end{bmatrix} = T_{Clarke}^{-1}\begin{bmatrix} v_\alpha^s \\ v_\beta^s \\ v_0 \end{bmatrix} \tag{2.9}$$

where T^{-1}_{Clarke} is an inverse Clarke transformation matrix defined as

$$T^{-1}_{Clarke} = \frac{2}{3}\begin{bmatrix} 1 & 0 & \frac{1}{\sqrt{2}} \\ -\frac{1}{\sqrt{2}} & \frac{\sqrt{3}}{2} & \frac{1}{\sqrt{2}} \\ -\frac{1}{\sqrt{2}} & -\frac{\sqrt{3}}{2} & \frac{1}{\sqrt{2}} \end{bmatrix} \tag{2.10}$$

Likewise, the currents and flux linkages can be transformed respectively into the initial $a-b-c$ reference frame just by multiplication both sides of (2.5) by the inverse transformation matrix in (2.10).

2.3.3 Two-axis rotational frame: d - q frame

Since in the two-axis stator frame, the α- and β- components are time-varying, a control system designed based on this transformation turns out to be complicated. To simplify a design of a control system, a transformation in which a motor model is described in a rotating rotor's reference frame is introduced. This rotating rotor's frame is usually called as a $d-q$ frame in the literature. The $d-q$ reference frame consists of a direct axis (d-axis) which placed to coincide with the rotor's magnet axis and a quadrature axis (q-axis) which is perpendicular to the d-axis. The initial angle between the α-axis of the $\alpha-\beta$ frame and d-axis is defined as ϕ_d.

The voltages in the $\alpha-\beta$-frame can be transformed to the voltages in the $d-q$-frame as

$$\begin{bmatrix} v^r_d \\ v^r_q \end{bmatrix} = \begin{bmatrix} \cos\phi_d & \sin\phi_d \\ -\sin\phi_d & \cos\phi_d \end{bmatrix} \begin{bmatrix} v^s_\alpha \\ v^s_\beta \end{bmatrix} \tag{2.11}$$

Similarly, the currents and flux linkages in the $\alpha-\beta$ frame are represented in the $d-q$ frame

$$\begin{aligned} \begin{bmatrix} i^r_d \\ i^r_q \end{bmatrix} &= \begin{bmatrix} \cos\phi_d & \sin\phi_d \\ -\sin\phi_d & \cos\phi_d \end{bmatrix} \begin{bmatrix} i^s_\alpha \\ i^s_\beta \end{bmatrix} \\ \begin{bmatrix} \gamma_d \\ \gamma_q \end{bmatrix} &= \begin{bmatrix} \cos\phi_d & \sin\phi_d \\ -\sin\phi_d & \cos\phi_d \end{bmatrix} \begin{bmatrix} \gamma_\alpha \\ \gamma_\beta \end{bmatrix} \end{aligned} \tag{2.12}$$

This transformation is well-known as the *Park transformation* with the transformation matrix as

$$T_{Park} = \begin{bmatrix} \cos\phi_d & \sin\phi_d \\ -\sin\phi_d & \cos\phi_d \end{bmatrix} \tag{2.13}$$

Furthermore, the rotating quantities in the $d-q$ frame can be transformed into the stationary quantities in the $\alpha-\beta$ frame via the *inverse Park transformation*

$$\begin{aligned} \begin{bmatrix} v^s_\alpha \\ v^s_\beta \end{bmatrix} &= \begin{bmatrix} \cos\phi_d & -\sin\phi_d \\ \sin\phi_d & \cos\phi_d \end{bmatrix} \begin{bmatrix} v^r_d \\ v^r_q \end{bmatrix} \\ \begin{bmatrix} i^s_\alpha \\ i^s_\beta \end{bmatrix} &= \begin{bmatrix} \cos\phi_d & -\sin\phi_d \\ \sin\phi_d & \cos\phi_d \end{bmatrix} \begin{bmatrix} i^r_d \\ i^r_q \end{bmatrix} \end{aligned}$$

$$\begin{bmatrix} \gamma_\alpha \\ \gamma_\beta \end{bmatrix} = \begin{bmatrix} \cos\phi_d & -\sin\phi_d \\ \sin\phi_d & \cos\phi_d \end{bmatrix} \begin{bmatrix} \gamma_d \\ \gamma_q \end{bmatrix} \tag{2.14}$$

The *inverse Park* transformation matrix is denoted as

$$T_{Park}^{-1} = \begin{bmatrix} \cos\phi_d & -\sin\phi_d \\ \sin\phi_d & \cos\phi_d \end{bmatrix} \tag{2.15}$$

The Clarke and Park transformations are used together to represent three-phase voltages in the stationary $a-b-c$-frame in the rotational $d-q$-frame via the following relationship

$$\begin{bmatrix} v_d^r \\ v_q^r \\ v_0 \end{bmatrix} = \frac{2}{3} \begin{bmatrix} \cos\phi_r & \cos(\phi_r - \frac{2\pi}{3}) & \cos(\phi_r + \frac{2\pi}{3}) \\ -\sin\phi_r & -\sin(\phi_r - \frac{2\pi}{3}) & -\sin(\phi_r + \frac{2\pi}{3}) \\ \frac{1}{2} & \frac{1}{2} & \frac{1}{2} \end{bmatrix} \begin{bmatrix} v_a^s \\ v_b^s \\ v_c^s \end{bmatrix} \tag{2.16}$$

The same way, three-phase alternative currents and flux linkages in the $a-b-c$-frame can be represented in the $d-q$-frame as

$$\begin{aligned} \begin{bmatrix} i_d^r \\ i_q^r \\ i_0 \end{bmatrix} &= \frac{2}{3} \begin{bmatrix} \cos\phi_r & \cos(\phi_r - \frac{2\pi}{3}) & \cos(\phi_r + \frac{2\pi}{3}) \\ -\sin\phi_r & -\sin(\phi_r - \frac{2\pi}{3}) & -\sin(\phi_r + \frac{2\pi}{3}) \\ \frac{1}{2} & \frac{1}{2} & \frac{1}{2} \end{bmatrix} \begin{bmatrix} i_a^s \\ i_b^s \\ i_c^s \end{bmatrix} \\ \begin{bmatrix} \gamma_d \\ \gamma_q \\ \gamma_0 \end{bmatrix} &= \frac{2}{3} \begin{bmatrix} \cos\phi_r & \cos(\phi_r - \frac{2\pi}{3}) & \cos(\phi_r + \frac{2\pi}{3}) \\ -\sin\phi_r & -\sin(\phi_r - \frac{2\pi}{3}) & -\sin(\phi_r + \frac{2\pi}{3}) \\ \frac{1}{2} & \frac{1}{2} & \frac{1}{2} \end{bmatrix} \begin{bmatrix} \gamma_a \\ \gamma_b \\ \gamma_c \end{bmatrix} \end{aligned} \tag{2.17}$$

where v_d^r, v_q^r, i_d^r, and i_q^r are the d-axis and q-axis components of the three-phase voltages and currents, respectively; γ_d and γ_q are the flux linkages obtained in the $d-q$-frame. The electrical angle ϕ_r determines an angle between the a-axis of the $a-b-c$-frame and the d-axis of the two-axis $d-q$-frame. The electrical angle is determined through the rotor's speed ω_e and initial electrical angle value ϕ_{r0} as below [1]

$$\phi_r = \int_0^t \omega_e \, dt + \phi_{r0} \tag{2.18}$$

This electrical angle or flux angle in another call is essential to know, and its value is measured by sensors such as resolver or position sensor [3].

A transformation from the $a-b-c$ frame into the $d-q$ frame is called as the *dq0-transformation* or *Clarke-Park transformation* and its transformation matrix is denoted as

$$T_{dq0} = \frac{2}{3} \begin{bmatrix} \cos\phi_r & \cos(\phi_r - \frac{2\pi}{3}) & \cos(\phi_r + \frac{2\pi}{3}) \\ -\sin\phi_r & -\sin(\phi_r - \frac{2\pi}{3}) & -\sin(\phi_r + \frac{2\pi}{3}) \\ \frac{1}{2} & \frac{1}{2} & \frac{1}{2} \end{bmatrix} \tag{2.19}$$

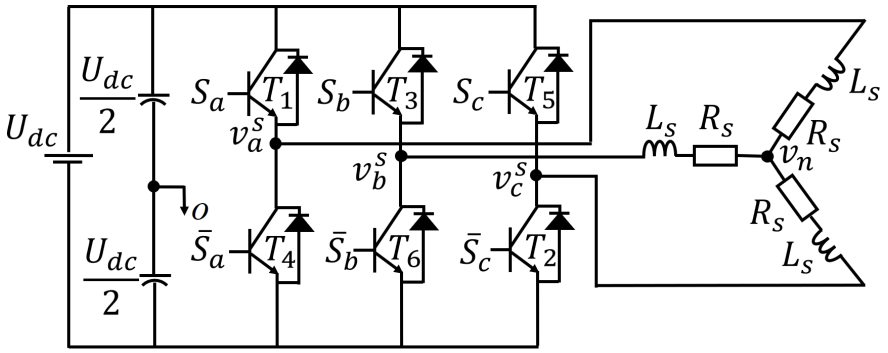

Figure 2.2: A VSI with six-step switching with a star-connected three-phase load [1, 2].

Using the *inverse dq0 transformation* one can obtain the three-phase variables from the variables given in the rotating $d-q$-frame. So, three-phase voltages can be transformed from the $d-q$-frame into the $a-b-c$-frame as follows

$$\begin{bmatrix} v_a^s \\ v_b^s \\ v_c^s \end{bmatrix} = T_{dq0}^{-1} \begin{bmatrix} v_d^r \\ v_q^r \\ v_0 \end{bmatrix} \tag{2.20}$$

where the inverse transformation matrix T_{dq0}^{-1} is defined as

$$T_{dq0}^{-1} = \begin{bmatrix} \cos\phi_r & -\sin\phi_r & 1 \\ \cos(\phi_r - \frac{2\pi}{3}) & -\sin(\phi_r - \frac{2\pi}{3}) & 1 \\ \cos(\phi_r + \frac{2\pi}{3}) & -\sin(\phi_r + \frac{2\pi}{3}) & 1 \end{bmatrix} \tag{2.21}$$

Also, three-phase currents i_a^s, i_b^s, and i_c^s are obtained based on the i_d^r and i_q^r via the inverse Clarke-Park transformation

$$\begin{bmatrix} i_a^s \\ i_b^s \\ i_c^s \end{bmatrix} = T_{dq0}^{-1} \begin{bmatrix} i_d^r \\ i_q^r \\ i_0 \end{bmatrix} \tag{2.22}$$

It should be noted that the zero component used in the transformations is non-zero when a motor system has faults (unbalanced motor system), otherwise, in the balanced system, this component is disregarded in the analysis.

2.4 Three-phase inverter and pulse-width modulation

2.4.1 An IGBT-based three-phase inverter

Three-phase inverters are devices that convert a DC power source to a three-phase variable amplitude/frequency AC voltage or AC current. The inverters based on the type of source of input could be voltage-source inverter (VSI) or current source inverter (CSI) [1, 2]. Since CSIs are commonly used in applications of motors with power

Table 2.1: Switching states of the inverter [1]

$S_a = 1, \bar{S}_a = 0$	T_1 ON	T_4 OFF
$S_a = 0, \bar{S}_a = 1$	T_1 OFF	T_4 ON
$S_b = 1, \bar{S}_b = 0$	T_3 ON	T_6 OFF
$S_b = 0, \bar{S}_b = 1$	T_3 OFF	T_6 ON
$S_c = 1, \bar{S}_c = 0$	T_5 ON	T_2 OFF
$S_c = 0, \bar{S}_c = 1$	T_5 OFF	T_2 ON

measured in megawatts, an application of VSIs is wider than that of CSIs [1]. A typical scheme of the three-phase VSI is depicted in Figure 2.2. Generally, depending on characteristics of switching and power requirements of an inverter, a circuit of the VSI could be implemented using various types of semiconductor-based switches. However, the most common type of switches are based on the insulated gate bipolar transistors (IGBT) [2]. The VSI shown in Figure 2.2 includes three parallel half-bridge inverters, which are used to generate output voltages with 120^0 difference in phases.

The IGBTs are able to conduct a current in only one direction, therefore diodes are used in parallel in order to allow a flow of the current in the reverse direction. In Figure 2.2, each leg of the VSI has two IGBT switches. In each leg, to avoid a short circuit issue, only one switch is required to be "ON", whereas the other switch is "OFF" at each time. Consequently, one can identify the states of the switches by only knowing the states of switches in the upper part of the inverter [4]. The states of the inverter's switches are summarized in Table 2.1. The output of each phase leg is determined as follows: when a *j-th* switch in the upper part is "ON", i.e. $S_j = 1$ and $\bar{S}_j = 0$, the output of the corresponding leg is linked to the upper part of the voltage supply, and hence, $v_j^s = \frac{U_{dc}}{2}$, where $j = a, b, c$ is a corresponding phase; on the contrary, the output is linked to the lower part of the voltage supply when a *j-th* switch in the lower part is "ON", i.e. $S_j = 0$ and $\bar{S}_j = 1$, which results in $v_j^s = -\frac{U_{dc}}{2}$. The following equation describes a connection between the voltage in the output and states of the switches in the inverter

$$v_j^s = U_{dc} S_j - \frac{U_{dc}}{2} \tag{2.23}$$

Recall that the voltages in each phase are related to the neutral point of a load in a star-connection as below

$$\begin{aligned} v_{a-n}^s &= v_a^s - v_n \\ v_{b-n}^s &= v_b^s - v_n \\ v_{c-n}^s &= v_c^s - v_n \end{aligned} \tag{2.24}$$

where v_{a-n}^s, v_{b-n}^s, and v_{c-n}^s are the phase-to-neutral voltages in the phase a, b, and c, respectively; v_n is a voltage in the neutral point of the load. At this stage, the VSI generates v_a^s, v_b^s, and v_c^s signals in a rectangular shape with amplitude alternating between $\pm\frac{U_{dc}}{2}$.

2.4.2 Sinusoidal PWM technique to control the switching states of the inverter

Theory of modulation has been under the active research in the power electronics since from the 70s of the past century. In general, the aim of modulation way is to create switching pulses that have identical fundamental components as a reference signal. In most cases, the created switching pulses comprise unwanted harmonics and there are two steps in the operation of a PWM technique. In the first step, it is required to calculate "ON"-states of the switches, which is an important to generating the necessary voltage (current) in the output. The second step is to obtain the most effective solution to diminish unwanted harmonics, losses due to switching, etc [86]. The most popular PWM techniques such as sinusoidal PWM (SPWM) and space-vector PWM (SVPWM) are briefly presented in the following part.

Before going to present the SPWM and SVPWM, it worse to mention about a PWM technique called six-step mode to control the inverter's switches. The six-step mode approach is one of the oldest technologies used in power electronics to control the switches of the inverter. Despite that this approach is convenient in terms of its implementation, unwanted harmonics related to the fundamental component of the voltage in the output are hard to eliminate. These unwanted harmonics could be a part of potential disturbances and noises in a control system. Hence, to solve issue with unwanted harmonics, methods of the SPWM and SVPWM are implemented.

Sinusoidal PWM technique is a method based on comparison of a carrier signal with an voltage in the input. In the carrier-based PWM, a repeating triangular signal with frequency f_{cr} is utilized. In practice, the frequency of a carrier signal is commonly selected to have a value much greater than the value of the frequency of the input voltage, f_{inp} [4]. The carrier-based PWM works according to the principle shown below

$$\begin{cases} \text{if } \bar{v}_j(t) \geq m(t), S_j = 1 \\ \text{otherwise } S_j = 0 \end{cases} \tag{2.25}$$

where $\bar{v}_j(t)$ and $m(t)$ are a voltage signal in the input and a signal used in the carrier, respectively; S_j is a switching signal, where $j = a, b, c$. Hence, the actual voltage in the output of the inverter is obtained based on the relationship provided in (2.23). As noted previously, the output voltages in the inverter have a rectangular shape and defined based on (2.23), further the fundamental components of those signals of the rectangular shape are derived using the Fourier series. Usually, the modulated signals have characteristics identical to the original input signal to the inverter. Sinusoidal PWM as the most popular carrier-based type has limitation such that the peak amplitude of the sinusoidal input signal is required to be less than $\frac{U_{dc}}{2}$, since in case of exceeding this limitation the inverter will not work properly. Working principle of the sinusoidal PWM is illustrated in Figure 2.3. This drawback of the sinusoidal PWM can be solved

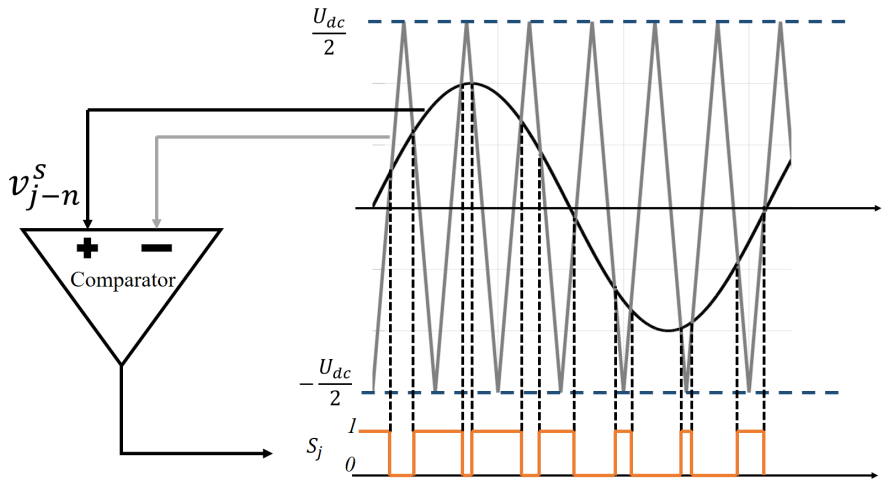

Figure 2.3: Sinusoidal PWM technique with a triangular carrier signal [3].

by injection of zero-sequence. Let us consider a three phase voltage signals described as follows

$$\begin{aligned} v_a^{des} &= v_p \sin \omega_e t \\ v_b^{des} &= v_p \sin(\omega_e t - \frac{2\pi}{3}) \\ v_c^{des} &= v_p \sin(\omega_e t + \frac{2\pi}{3}) \end{aligned} \tag{2.26}$$

where v_p is a peak value of the input voltage signals. From Figure 2.2, it can be derived that the voltage on the neutral point regarding the ground is defined as

$$v_n = \frac{v_a^{des} + v_b^{des} + v_c^{des}}{3} \tag{2.27}$$

This relationship is based on the assumption that in the case of balanced three-phase voltages, the voltage on the neutral point is zero. From the assumption about the balanced three-phase system, it is possible to add a non-zero voltage to v_n to modify the desired three-phase signals in (2.26)

$$\begin{aligned} v_a^{mod} &= v_a^{des} + v_n \\ v_b^{mod} &= v_b^{des} + v_n \\ v_c^{mod} &= v_c^{des} + v_n \end{aligned} \tag{2.28}$$

This approach of adding of a non-zero voltage to v_n is called as "zero-sequence injection", and its principle of work is briefly summarized in Figure 2.4.

Among various methods of selection of zero-sequence signal, a method so called third harmonic injection PWM (THIPWM) is widely used [4]. This method uses a third order harmonic component of the desired voltage signal v_a^{des} to inject as a zero-sequence signal. It should be noted that the injection of the third order harmonic reduces the maximum amplitude of the desired input signal.

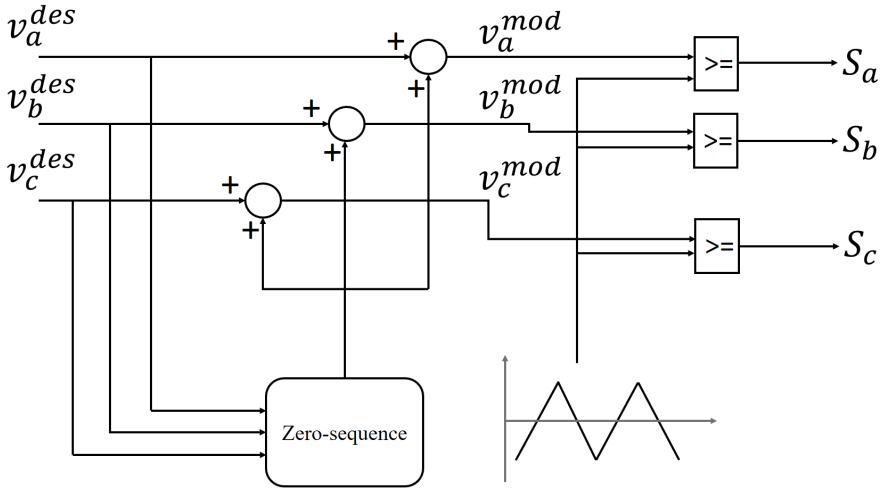

Figure 2.4: Carrier signal-based PWM with zero-sequence injection technique [4].

2.4.3 Space Vector PWM technique to control the switching states of the inverter

A principle of work of the SVPWM method is realized in the concept of geometrical interpretations of space vectors. A spatial representation of a three-phase desired voltage can be written as [1, 4]

$$\vec{U}_s^{des} = \frac{2}{3}(v_{a-n}^{des} + v_{b-n}^{des} e^{j\frac{2\pi}{3}} + v_{c-n}^{des} e^{j\frac{4\pi}{3}}) \tag{2.29}$$

This equation shows that the resulting space vector $\vec{U}_s^{des}$ rotates with an electrical speed ω_e in a three-phase balanced system. The terms $e^{j\frac{2\pi}{3}}$ and $e^{j\frac{4\pi}{3}}$ are vector with unit size and their directions are aligned with b- and c- phase axes, respectively, where the a-phase axis serves as a base. Hence, each term in (2.29) are vectors having magnitudes of each phase voltage, i.e. v_a^s, v_b^s, and v_c^s. Based on this idea, the desired voltage vector is revealed in terms of the DC-link voltage and the inverter's states as following

$$\vec{U}_s^{des} = \frac{2}{3}U_{dc}(S_a + S_b e^{j\frac{2\pi}{3}} + S_c e^{j\frac{4\pi}{3}}) \tag{2.30}$$

Since the values of the switches S_a, S_b, and S_c could be either 0 or 1, using (2.30) eight spatial voltage vectors are defined. Among these eight voltage vectors, six vectors are called as active voltage vectors ($\vec{U}_1$, $\vec{U}_2$, $\vec{U}_3$, $\vec{U}_4$, $\vec{U}_5$, $\vec{U}_6$), whereas other two vectors ($\vec{U}_0$, $\vec{U}_7$) are called zero voltage vectors.

Each active voltage vector is 60^0 apart from other two neighboring vectors, and two zero voltage vectors are positioned at the center of the coordinate system as shown in Figure 2.5. Two zero voltage vectors are emerged when the switches in the upper part are all "ON" or "OFF", in this case, the motor terminals will have U_{dc} or 0, accordingly. Thus, these listed vectors create six different sectors of modulation as in Figure 2.5.

Based on the eight voltage vectors, one can define a desired voltage vector at any position. This actually happens using the vectors adjacent to the desired voltage vector

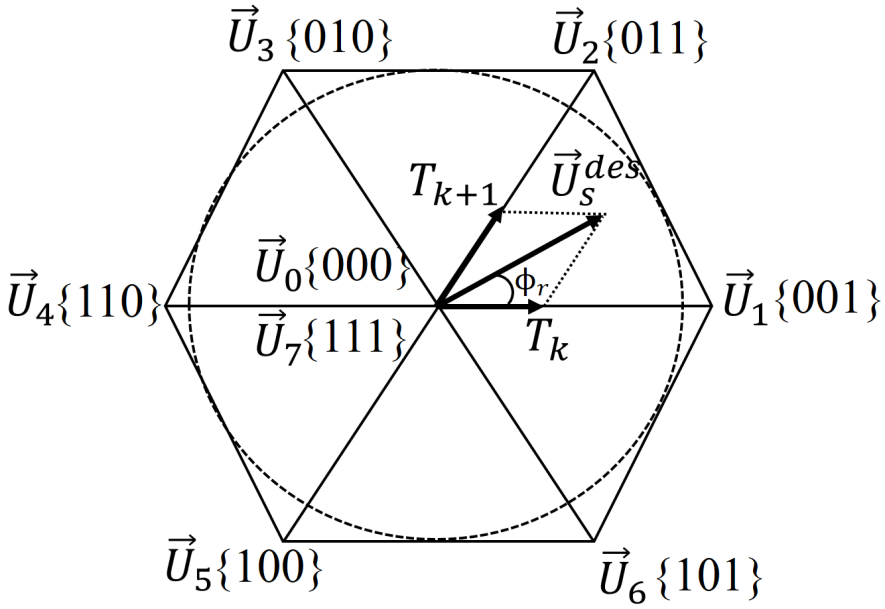

Figure 2.5: Six inverter's voltage vectors in SVPWM [4].

and one of the zero vectors. For instance, the desired voltage vector can be determined in terms adjacent voltage vectors as

$$T_{sample}\vec{U}_s^{des} = T_k\vec{U}_k + T_{k+1}\vec{U}_{k+1} \tag{2.31}$$

in which T_k and T_{k+1} are the time duration when $\vec{U}_k$ and $\vec{U}_{k+1}$ are "ON", accordingly; $\vec{U}_k$ and $\vec{U}_{k+1}$ are two adjacent voltage vectors; $k = 0, 1, \ldots, 7$. Note that a sum of T_k and T_{k+1} gives a value of a sampling period T_s, i.e.

$$T_{sample} = T_k + T_{k+1} \tag{2.32}$$

Next from Figure 2.5, the following relationship can be derived based on the geometric point of view

$$\begin{aligned} \frac{T_{sample}|\vec{U}_s^{des}|}{\sin\frac{2\pi}{3}} &= \frac{T_k|\vec{U}_k|}{\sin(\frac{\pi}{3}-\phi_r)} \\ \frac{T_{sample}|\vec{U}_s^{des}|}{\sin\frac{2\pi}{3}} &= \frac{T_{k+1}|\vec{U}_{k+1}|}{\sin\phi_r} \end{aligned} \tag{2.33}$$

From (2.33), a relations of the ratio of duty cycle of $\vec{U}_k$ and $\vec{U}_{k+1}$ are derived

$$\begin{aligned} \frac{T_k}{T_{sample}} &= \frac{\sqrt{3}|\vec{U}_s^{des}|}{U_{dc}}\sin(\frac{\pi}{3}-\phi_r) \\ \frac{T_{k+1}}{T_{sample}} &= \frac{\sqrt{3}|\vec{U}_s^{des}|}{U_{dc}}\sin\phi_r \end{aligned} \tag{2.34}$$

Note that a value of length of every active voltage vector is $\frac{2}{3}U_{dc}$. The zero voltage vectors U_0 and U_7 are utilized in the remaining part of the sampling time by the following expression

$$\vec{U}_s = \vec{U}_kT_k + \vec{U}_{k+1}T_{k+1} + \vec{U}_{zv}T_{zv} \tag{2.35}$$

where $\vec{U}_{zv}$ could be either $\vec{U}_0$ or $\vec{U}_7$ depending on the sequence of the switching states of the vectors; then the sampling time period would be $T_{sample} = T_k + T_{k+1} + T_{zv}$, T_{zv} is a time duration of either $\vec{U}_0$ or $\vec{U}_7$. In general, the inverter generates a sinusoidal voltages in the output when a tip of the voltage vectors is inside of the hexagon and rotates at constant speed, otherwise an over-modulation issue of the inverter could happen [1]. The sequence of realization of each vector is chosen such that only one pair of transistors is switched in each sampling period, i.e. $\vec{U}_0 \Rightarrow \vec{U}_1 \Rightarrow \vec{U}_2 \Rightarrow \vec{U}_7$ when $\vec{U}_0$ is a last state of switching, $\vec{U}_7 \Rightarrow \vec{U}_2 \Rightarrow \vec{U}_1 \Rightarrow \vec{U}_0$ when $\vec{U}_7$ is a last state of switching [87]. This switching strategy of the vectors helps to minimize switching losses of the inverter, also it provides a constant switching frequency and reduced harmonics. In order to meet a linear modulation requirement, the voltages in $\alpha - \beta$ and $d - q$- frames need to fulfill the next constraints

$$\begin{aligned} \sqrt{v_\alpha^{s^2} + v_\beta^{s^2}} &\leq \frac{1}{\sqrt{3}} U_{dc} \\ \sqrt{v_d^{r^2} + v_q^{r^2}} &\leq \frac{1}{\sqrt{3}} U_{dc} \end{aligned} \tag{2.36}$$

These constraints are used in the design of control system and its practical implementation. Note that when the linear modulation requirement is met, the IGBT inverter results in an approximated values of the desired voltages, i.e. $v_a^{des} \approx v_a^s$, $v_b^{des} \approx v_b^s$, and $v_c^{des} \approx v_c^s$, hence $v_d^{r^*} \approx v_d^r$ and $v_q^{r^*} \approx v_q^r$ [4].

2.5 Common uncertainties of a PMSM

AC machines are characterized by disturbances (uncertainties) with various features, these uncertainties are generally created by different sources such as load changes, working conditions, and changes in mechanical as well as electrical components of the machine. There are three common categories of uncertainties such as uncertainties due to parameter mismatch, uncertainties due to external perturbations, and uncertainties due to un-modelled dynamics [11, 88]. This chapter briefly reviews the listed categories of uncertainties which play a crucial role in control of PMSMs.

2.5.1 Uncertainty due to variations in parameter

The stator of the PMSM is mostly manufactured using a copper wire, and it is known that the resistance of the copper wire is depending on the temperature coefficient of the copper wire as below [5, 11]

$$R_s = R_{s_0} \frac{(235 + \tau)}{(235 + \tau_0)} \tag{2.37}$$

where R_{s_0} is a nominal value of the resistance when the temperature is τ_0. Due to existence of unwanted harmonics a phenomenon called *skin effect* always presents. This

effect produces crowding of the current on the surface of the copper wire, the current crowding rises the resistance and reduces the leakage inductance [89]. In PMSMs, the skin effect is negligible on the windings of the stator, hence it can be neglected in most cases [5]. So, it is hard to claim that the motor parameters in the obtained equivalent circuit are constant during the operation. Furthermore, the inductance of the motor also varies nonlinearly under different load types. In general, the control system may potentially become unstable in case of variations of resistance and inductance. These two electrical parameters of the PMSM can be described in terms of nominal and variation values as

$$\begin{aligned} R_s &= R_{s_0} + \Delta R_s \\ L_s &= L_{s_0} + \Delta L_s \end{aligned} \tag{2.38}$$

where L_{s_0} is a nominal value of the stator inductance; ΔR_s and ΔL_s are amount of variations in the stator resistance and inductance, respectively. Note that in the SPMSMs stator inductance is equal to its components in the $d-q$-frame, i.e. $L_{ds} = L_{qs} = L_s$.

The mechanical parameters in AC drives, a rotor's inertia J_m is also changing during the operation of the AC drive. The value of the inertia is mostly obtained experimentally and it is shown that the variation in the moment of inertia highly affects the overall performance of a drive system [90]. This parameter can be defined in terms of its nominal and variation values as follows

$$J_m = J_{m_0} + \Delta J_m \tag{2.39}$$

where J_{m_0} is a nominal value of the inertia, ΔJ_m is a variation amount of the inertia value.

2.5.2 Uncertainty due to external disturbance

The external disturbances mainly come from the effects of load torque, mechanical reasons, and existing friction. A load torque is considered as one of the most serious type of disturbances which could negatively affect to a mechanical system of the motor. Under the sudden load changes a speed of the motor might change inevitably. Also, the load torque change might lead to the parameter variations during motor's operation. As known, friction is created due to the exising of tangential force between two contacting surfaces. Static models of friction as Coulomb model, Karnopp model, and Stribeck model as well as the dynamic models of friction known as Bristle model, Dahl model, and LuGre model could be found in the literature. Twisting vibrations, wrong rotor's shaft position, disturbed shaft are reasons of mechanical issues in the motor system. These mechanical issues also may restrict the improvement of the system performance. For instance, it is revealed that, in industry, over 70% of vibration issues are due to the

wrong rotor's shaft position [11]. Models of torque generated due to the friction, flux, and Eddy current losses are given below

$$\begin{aligned} T_{fr} &= (\eta_{hys} + \eta_{fr}) sign(\omega_m) \\ T_v &= (\eta_e + D_v)\omega_m \\ T_{mfl} &= D_e \frac{\dot{\gamma}_{pm} \times \gamma_{pm}}{|\Psi|^2} \end{aligned} \tag{2.40}$$

where T_{fr} is a torque due to the friction; T_v is a pulling force due to the viscous as well as Eddy current; T_{flux} is a torque generated due to flux; η_{hys} is a coefficient of a hysteresis loss; η_{fr} is a coefficient of static friction; η_e is a coefficient of the Eddy current; D_v is a damping coefficient of viscosity; D_e is a damping coefficient of the Eddy current.

2.5.3 Uncertainty due to un-modelled dynamics

In the PMSMs, due to interaction of the magnets with stator slots a torque called cogging torque is created. As a disturbance, the cogging torque may negatively affect the speed controller performance when the motor runs at low speed, hence this disturbance limits the operating range of the PMSM. The cogging torque also limits the performance of a disturbance observer in practical applications. The model for the cogging torque is given as follows [91]

$$T_{cog}(\phi_r) = \sum_{m=1}^{\infty} (C_m) \sin(m N_c \phi_r) \tag{2.41}$$

where N_c is least-common multiplier of stator slot's number and poles number of the rotor; C_m is a peak value of the m-th harmonic. Demagnetization property of a magnetic material due to increase of temperature has considerable impact on the PMSM's torque facilities and effectiveness. A prolonged operation of the PMSM leads to increase of temperature and high temperature provides demagnetization phenomena of the permanent magnets. In general, the flux linkage between the stator and rotor magnets of the PMSM can be expressed via components of the 6k-th harmonics as

$$\gamma_{s-r} = \sum_{k=0}^{\infty} \gamma_{max} \cos(6k\phi_r) \tag{2.42}$$

where γ_{max} is a peak value of the 6k-th harmonic component of the flux. Similar to (2.53), the disturbance torque created by the flux harmonics is defined as

$$T_{flux} = \frac{3}{2} p i_q^r \sum_{k=0}^{\infty} \gamma_{max} \cos(6k\phi_r) \tag{2.43}$$

Moreover, un-modelled dynamics could exist based on dead-time issues of the inverter as well as issues of inaccurate measurement. The issues related to the dead-time of the inverter distort the voltage in the output and consequently decrease its peak value. The

resulted distortion in voltage and possible harmonic components might be severe at low frequencies. The equations of the dead-time issue can be written as follows [89]

$$T_{U_d}^{dead} = \sum_{k=0}^{\infty} C_d^k \sin(6k\phi_r)$$
$$T_{U_q}^{dead} = \sum_{k=0}^{\infty} C_q^k \sin(6k\phi_r) \tag{2.44}$$

in which C_d^k and C_q^k are peak values of the 6k-th component of $T_{U_d}^{dead}$ and $T_{U_q}^{dead}$, accordingly. When the dead-time effect happens, the current also deteriorate by creating ripples in the dynamics of the electromagnetic torque. Furthermore, error in current measurement can also produce ripples in the current dynamics, which in turn leads to unwanted ripples in the torque. Uncertainties due to current measurement error can be derived as shown

$$T_d^{offset} = C^{offset} \sin(\phi_r + \beta)$$
$$T_q^{offset} = C^{offset} \sin(\phi_r + \beta) \tag{2.45}$$

where C^{offset} is a peak value of the offset; β is an angular displacement [88, 89].

2.6 Dynamic model of the SPMSM

2.6.1 Power and electromagnetic torque

In AC drives, particularly in a PMSM, calculation of power and electromagnetic torque have a great importance in machine applications. In general, the input power in either $a-b-c$ or $d-q$-frame is equal and this is imporant fact in the analysis and modelling of AC drives. By taking three-phase voltages and currents in the vector form as $v_{abc}^s = \begin{bmatrix} v_a^s \\ v_b^s \\ v_c^s \end{bmatrix}$ and $i_{abc}^s = \begin{bmatrix} i_a^s \\ i_b^s \\ i_c^s \end{bmatrix}$, the input power of a machine model in the $a-b-c$ frame can be calculated as

$$P_i^{abc} = (v_{abc}^s)^T i_{abc}^s \tag{2.46}$$

Since $P_i^{abc} = P_i^{dq}$, using the inverse Park transformation in (2.20) and (2.22), one can substitute the three-phase signals in (2.46) by the two-phase signals in the $d-q$-frame, and obtain the input power as follows

$$P_i^{dq} = (v_{dq0}^r)^T (T_{dq}^{-1})^T T_{dq}^{-1} i_{dq0}^r \tag{2.47}$$

where $v_{dq0}^r = \begin{bmatrix} v_d^r \\ v_q^r \\ v_0 \end{bmatrix}$ and $i_{dq0}^r = \begin{bmatrix} i_d^r \\ i_q^r \\ i_0 \end{bmatrix}$ are voltage and current vectors in the $d-q$-frame. After developing the right-hand part of (2.47) and some algebraic operations, an

expression for the input power in the $d-q$-frame can be derived [1, 82]

$$P_i^{dq} = \frac{3}{2}(v_d^r i_d^r + v_q^r i_q^r + 2v_0 i_0) \tag{2.48}$$

As stated previously, the zero components v_0 and i_0 are neglected under the condition of (2.6). Consequently, the power equation in (2.48) can be simplified as

$$P_i^{dq} = \frac{3}{2}(v_d^r i_d^r + v_q^r i_q^r) \tag{2.49}$$

Alternatively, the input power can be expressed in terms of copper loss in the stator P_{copper}, electromagnetic power P_{em}, and change rate of stored magnetic energy P_{mgn}

$$P_i^{dq} = \frac{3}{2}(P_{copper} + P_{em} + P_{mgn}) \tag{2.50}$$

where $P_{copper} = R_s\left[(i_d^r)^2 + (i_q^r)^2\right]$, $P_{em} = \omega_e i_q^r\left[(L_{ds} - L_{qs})i_d^r + \gamma_{pm}\right]$, and $P_{mgn} = L_{ds} i_d^r \delta i_d^r + L_{qs} i_q^r \delta i_q^r$.

The electromagnetic power P_{em} is defined as a product of the electromagnetic torque and the mechanical speed of the motor, i.e.

$$P_{em} = T_{em}\omega_m \tag{2.51}$$

The mechanical speed ω_m and electrical speed ω_e of a motor relate each other via the following equation

$$\omega_e = p\omega_m \tag{2.52}$$

where p is a number of pole-pairs of the motor. Using (2.50), (2.51), and (2.52) one can obtain the electromagnetic torque of the motor

$$T_{em} = \frac{3}{2}p i_q^r\left[(L_{ds} - L_{qs})i_d^r + \gamma_{pm}\right] \tag{2.53}$$

In general, the electromagnetic torque in a PMSM has two components such as magnetic torque and reluctance torque. From (2.53), the magnetic torque has a form

$$T_{mgn} = \frac{3}{2}p\gamma_{pm} i_q^r \tag{2.54}$$

whereas the reluctance torque is

$$T_{rel} = \frac{3}{2}p\left[L_{ds} - L_{qs}\right] i_d^r i_q^r \tag{2.55}$$

From (2.54), it is revealed that the magnetic torque linearly depends on the q-axis current and does not depend on any inductances in the $d-q$-frame. As opposed to the magnetic torque, the reluctance torque represents a nonlinear function which simultaneously depends on both d- and q- axis currents. Furthermore, the reluctance torque is proportional to the difference between L_{ds} and L_{qs}. The reluctance torque component plays a crucial role in generating of the electromagnetic torque in a motor,

thus this torque component is positive when the q-axis inductance is greater than the d-axis inductance given the i_d^r current is negative. As a design parameter of a motor, a saliency ratio is defined as an important index of the motor's performance [82]

$$\rho_{sal} = \frac{L_{qs}}{L_{ds}} \tag{2.56}$$

A large saliency ratio indicates the large reluctance torque. In practice, a positive value of the d-axis current is not effective, and hence negative i_d^r is usually set for a regular operation of the salient motor [1]. The SPMSM as a non-salient motor has an electromagnetic torque represented only by the magnetic torque

$$T_e = \frac{3}{2} p \gamma_{pm} i_q^r = K_T i_q^r \tag{2.57}$$

where $K_T = \frac{3}{2} p \gamma_{pm}$ is a torque constant.

2.6.2 Practical system of the SPMSM

Using the Park transformation, the equations of the voltages in the rotating $d-q$-frame can be derived [1, 2]

$$v_d^r = R_s i_d^r + \delta \gamma_d - \omega_e \gamma_q \tag{2.58}$$

$$v_q^r = R_s i_q^r + \delta \gamma_q + \omega_e \gamma_d \tag{2.59}$$

and the equations for the flux linkages are obtained

$$\gamma_d = L_{ds} i_d^r + \gamma_{pm} \tag{2.60}$$

$$\gamma_q = L_{qs} i_q^r \tag{2.61}$$

where the inductances in the $d-q$-frame are expressed through the inductance components $L_{comp_1 1}$ and L_{comp_2} as

$$L_{ds} = \frac{3}{2}(L_{comp_1} + L_{comp_2}) \tag{2.62}$$

$$L_{qs} = \frac{3}{2}(L_{comp_1} - L_{comp_2}) \tag{2.63}$$

Finally, after substitution of (2.60) and (2.61) into (2.58) and (2.59) and taking $L_{ds} = L_{qs} = L_s$, it yields the voltage equations in the $d-q$-frame based on the i_d^r and i_q^r currents

$$v_d^r = R_s i_d^r + L_s \frac{di_d^r}{dt} - \omega_e L_s i_q^r \tag{2.64}$$

$$v_q^r = R_s i_q^r + L_s \frac{di_q^r}{dt} + \omega_e L_s i_d^r + \omega_e \gamma_{pm} \tag{2.65}$$

The mechanical motion of the rotor of the PMSM is derived based on the first principles of rotational motion of the rotor

$$J_m \dot{\omega}_m = T_m - T_L \tag{2.66}$$

where T_m and T_L are a mechanical torque and load torque applied to the motor, respectively. After combining (2.57)-(2.66) and using relationship in (2.52), the equations describing dynamics of the SPMSM are derived

$$\begin{cases} \dot{\omega}_e = \frac{p}{J_m}(T_m - T_L) \\ \dot{i}_d^r = \frac{1}{L_s}(v_d^r - R_s i_d^r + \omega_e L_s i_q^r) \\ \dot{i}_q^r = \frac{1}{L_s}(v_q^r - R_s i_q^r - \omega_e L_s i_d^r - \omega_e \phi_{pm}) \end{cases} \tag{2.67}$$

In most research work, this model of the SPMSM is considered to design a controller, in which the uncertainties due the parameters, external disturbances, and un-modelled dynamics discussed in previous section are not taken into account. Neglecting these types of uncertainties during control design may lead to poor tracking performance of the SPMSM control system and thus it is important to design a control system based on the model including the most common types of the uncertainties provided in the previous section. Moreover, selected controller parameters are mainly dependent on the frontier of the obtained lumped disturbance presenting in the speed or current dynamics [6]. Therefore, we shall modify (2.64), (2.65), and (2.66), in order to derive a dynamic equations of the SPMSM described in terms of parametric uncertainties, un-modelled dynamics, and external disturbances. The voltage equations given in (2.64)-(2.65) can be modified as

$$\begin{aligned} \dot{i}_d^r &= \frac{1}{L_{s_0}} v_d^r - \frac{R_{s_0}}{L_{s_0}} i_d^r + \frac{1}{L_{s_0}} \omega_e L_s i_q^r + z_d \\ \dot{i}_q^r &= \frac{1}{L_{s_0}} v_q^r - \frac{R_{s_0}}{L_{s_0}} i_q^r - \frac{1}{L_{s_0}} \omega_e L_s i_d^r - \frac{1}{L_{s_0}} \omega_e \gamma_{pm} + z_q \end{aligned} \tag{2.68}$$

where $z_d = -\frac{\Delta R_s}{L_{s_0}} i_d^r - \frac{\Delta L_s}{L_{s_0}} \dot{i}_d^r$ and $z_q = -\frac{\Delta R_s}{L_{s_0}} i_q^r - \frac{\Delta L_s}{L_{s_0}} \dot{i}_q^r$ are lumped disturbance terms in the i_d^r and i_q^r dynamics, respectively.

Noting that $T_m = T_e - T_{fr} - T_v - T_{flux}$, the mechanical dynamics of the rotor in (2.66) can be rewritten as

$$J_m \dot{\omega}_m = T_e - T_{fr} - T_v - T_{flux} - T_L \tag{2.69}$$

Considering variations in the inertia as $J_m = J_{m_0} + \Delta J_m$, (2.69) is modified as

$$\dot{\omega}_m = \frac{1}{J_{m_0}}(T_e - T_{fr} - T_v - T_{flux} - T_L - \Delta J_m \dot{\omega}_m) \tag{2.70}$$

Note that in the practical model of the SPMSM we use the electrical speed of the motor, which relates to the mechanical speed of the motor as $\omega_e = p\omega_m$. Therefore, the modified equation of the rotor's motion considering the variations in the inertia value and expressed in terms of the electrical speed will be

$$\dot{\omega}_e = \frac{p}{J_{m_0}} T_e - z_m \tag{2.71}$$

where $z_m = \frac{p}{J_{m_0}}(T_{fr} + T_v + T_{flux} + T_L + \Delta J_m \dot{\omega}_e)$ represents the lumped disturbance that includes the friction torque, torque due to flux's pulling force, and torque due to the Eddy current's pulling force affecting the mechanical dynamics of the motor, and variation in the inertia. Finally, the practical model of the SPMSM's dynamics is derived based on ω_e, i_d^r, and i_q^r

$$\begin{cases} \dot{\omega}_e = \frac{p}{J_{m_0}} T_e - z_m \\ \dot{i}_d^r = \frac{1}{L_{s_0}} v_d^r - \frac{R_0}{L_{s_0}} i_d^r + \frac{1}{L_{s_0}} \omega_e L_s i_q^r + z_d \\ \dot{i}_q^r = \frac{1}{L_{s_0}} v_q^r - \frac{R_0}{L_{s_0}} i_q^r - \frac{1}{L_{s_0}} \omega_e L_s i_d^r - \frac{1}{L_{s_0}} \omega_e \gamma_{pm} + z_q \end{cases} \tag{2.72}$$

2.6.3 Field-oriented control

PMSMs are preferable than induction motors thanks to its flexibility in application of advanced control schemes providing high performance operation. This advantage is due to the usage of permanent magnets instead of winding in the rotor, which in turn makes the dynamics of the PMSM primitive than other types of AC drives. This means that, during design, control engineers mostly pay attention on stator dynamic equations rather than rotor dynamics [1, 82]. In this section, a commonly used high performance control method known as vector control or field-oriented control (FOC) is presented. First introduction of the FOC approach in an AC drive control is dated to the late of 60s of XX century. A torque in AC drives is determined by the outer product of vectors of currents and flux, i.e. two vectors creating the magnetic flux linkage. Since a control of DC motors is a good example of superior independent control of the torque and flux, the main purpose of the FOC is to transform the dynamics of an AC drive to be equivalent to the dynamics of a DC motor. Once two magnetic fields are decoupled by the FOC, a performance of the AC drive control system becomes very fast, and accuracy in speed and flux control under the dynamic and static operational conditions is increased [1, 2, 6, 82]. In general, the FOC is more about the control of the inner current loop, and the speed control loop could be either scalar control or other related control method. Usually, we pay attention to the speed control since it plays an important role in generating of the reference to the current control loop designed by the FOC strategy [1]. In the FOC of the PMSM, the control system comprises two transformations of reference frame. The first transformation, i.e. *the inverse Park's transformation*, is required to transform the voltage commands in the $d-q$-frame into the phase voltages in the $a-b-c$-frame. The second one, i.e. *the Park's transformation*, is used to obtain the i_d^r and i_q^r currents from the real phase currents i_a^s, i_b^s, and i_c^s. In both transformations, the angular position of the rotor measured by the incremental optical encoder is used.

As mentioned before, the FOC strategy is possible to design when the d-axis current and q-axis current are decoupled from each other in the PMSMs. A detailed view on the

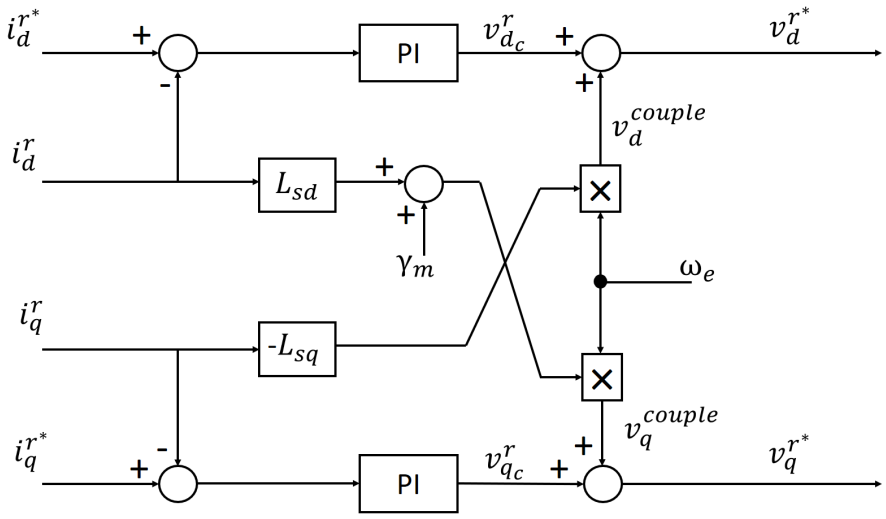

Figure 2.6: Decoupling scheme in the current controller [1].

equations (2.64) and (2.65) reveals that there are cross-coupled terms, i.e. $\omega_e L_{qs} i_q^r$ and $\omega_e L_{ds} i_d^r$, in the v_d^r and v_q^r voltage equations, respectively. To solve the cross-coupling effect, a decoupling scheme for the current controller has been suggested as in Figure 2.6. According to Figure 2.6, the voltage commands to the inverter $v_d^{r^*}$ and $v_q^{r^*}$ are composed as

$$\begin{aligned} v_d^{r^*} &= v_{d_c}^r + v_d^{couple} \\ v_q^{r^*} &= v_{q_c}^r + v_q^{couple} \end{aligned} \tag{2.73}$$

where $v_{d_c}^r$ and $v_{q_c}^r$ are the outputs of the two PI current controllers; v_d^{couple} and v_q^{couple} are nonlinear terms used to compensate the cross-coupling terms in v_d^r and v_q^r and defined as

$$\begin{aligned} v_d^{couple} &= -\omega_e L_{qs} i_q^{r^*} \\ v_q^{couple} &= \omega_e L_{ds} i_d^{r^*} + \omega_e \gamma_{pm} \end{aligned} \tag{2.74}$$

2.7 Current and voltage limits in the SPMSM operation

The operation of an SPMSM being at steady-state should meet specific limits on voltage and current in order to satisfy design characteristics of the motor. An inverter as a main source of the power with variable voltage and frequency supplied to the SPMSM determines limits to the voltage and current values due to the characteristics of the inverter's components and inverter's input voltage. As a rule, a rated voltage of the inverter is chosen to be equal to a rated voltage of the SPMSM, whereas the rated value of the current is usually set to be higher much more times than the rated current of the SPMSM [1, 5].

As it is shown in Section 2.4.3, the peak value of the phase voltage is determined based on the voltage of the inverter's DC-link, i.e. U_{dc}. However, if we consider the

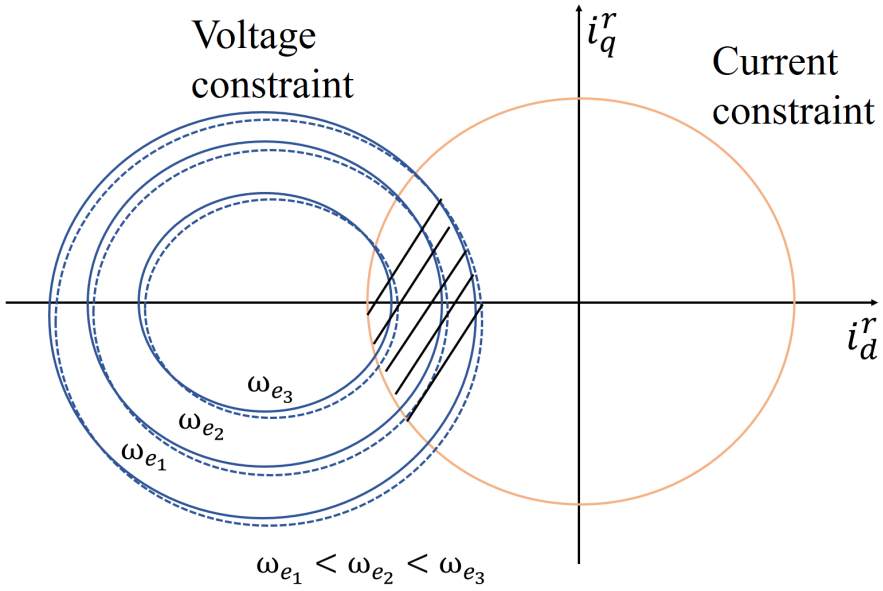

Figure 2.7: A current plane depicting the voltage and current constraints of the SPMSM [5].

dead time effect of the inverter and current regulation, the peak voltage for the phase would be [5]

$$v_s^{max} = \frac{U_{dc}}{\sqrt{3}}\mu \tag{2.75}$$

where μ an adjustment parameter which can be in the range $[0.9; 0.95]$. The maximum voltage decided by the inverter's parameters should meet the inequality given below

$$v_d^{r^{*^2}} + v_q^{r^{*^2}} \leq v_s^{max^2} \tag{2.76}$$

In general, the current limits in the SPMSM can be determined by the thermal parameters of either the inverter or the motor itself. In case of the inverter's thermal limits, the current constraint condition is revealed based on dissipation in the heat during the conduction losses in the inverter's components as well as switching periods. Iron and copper losses are taken into account when the motor's thermal limitations are considered to obtain the maximum limit of the stator current. Once the peak current value, i_s^{max}, is determined, the stator currents in the $d-q$-frame should satisfy to the next inequality

$$i_d^{r^{*^2}} + i_q^{r^{*^2}} \leq i_s^{max^2} \tag{2.77}$$

In order to consider the constraints given in (2.76) and (2.77) simultaneously, the stator voltage equations (2.64) and (2.65) are used and the both constraints are viewed on the current plane since the current plane is a better choice in terms of control design [5]. Considering the slowly oscillating currents or the steady-state condition the constraint of the voltage equation is derived

$$(i_d^r + \frac{\omega_e^2 L_s \gamma_{pm}}{R_s^2 + \omega_e^2 L_s^2})^2 + (i_q^r + \frac{\omega_e R_s \gamma_{pm}}{R_s^2 + \omega_e^2 L_s^2})^2 \leq \frac{U_s^{max^2}}{R_s^2 + \omega_e^2 L_s^2} \tag{2.78}$$

Table 2.2: Technical parameters of the SPMSM

Parameters	**Values**	**Units**
Rated power	300	W
Rated speed	2500	rpm
Nominal torque	0.97	$N{\cdot}m$
Pole pairs	4	-
Nominal stator resistance	2.37	Ω
Nominal stator inductance	4.3	mH
Magnetic flux linkage	0.0623	$V{\cdot}sec/rad$
Nominal inertia	0.0033	$kg{\cdot}m^2$

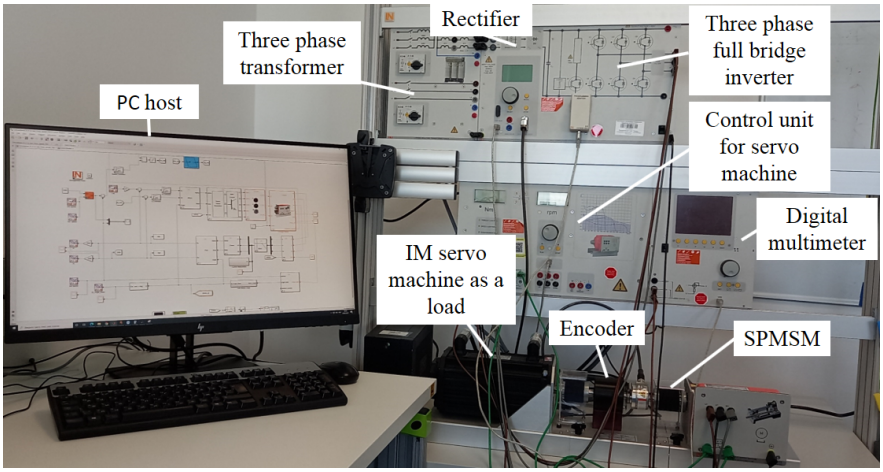

Figure 2.8: Description of the experimental stand.

Consequently, the area related to (2.78) is depicted in Figure 2.7, where the current constraint is an inner area of the circle with the center at the origin, while the voltage constraint is depicted as inner area of the circle located left to the current constraint circle. Figure 2.7 shows that when the stator's resistance voltage drop is negligible, the main axis of the circle showing voltage constraint remains on the d-axis of the current plane (solid lines), whereas when the stator's resistance voltage drop is sensible then the main axis of that circle does not coincide with the d-axis of the current plane (dashed lines) and its center also changes depending on the speed. From Figure 2.7, it is shown that the operation area of the motor is the crossing part between the two constraint circles. When the speed of the motor increases the area of the voltage constraint decreases and hence the area of the common part also decreases, which means that at specific speed the electric motor stops its operation under such current and voltage constraints [5].

2.8 Experimental stand

The experimental validations of the proposed composite control schemes for an SPMSM are conducted on the experimental stand assembled by Lucas-Nuelle. The experimental stand presented in Figure 2.8 is a compact-size, effective platform for real-time testing of control algorithms for the SPMSM. The experimental stand consists of a three-phase transformer, a full-bridge rectifier, an IGBT-based inverter, an analog/digital multimeter, an incremental encoder, a load motor, and a target motor. In this stand, a three-phase induction motor and the SPMSM are coupled mechanically. The induction motor operates as the load machine, whereas the SPMSM is the target motor. Both motors are controlled through the servo machine control block. The positions of the rotors of two motors are measured by 1024 pulses per rotation incremental encoder, which is installed between the load and target motors. A PWM switching frequency is chosen as 8 kHz and sampling time is set to 125 μs. A Code Composer Studio is used as a software to perform a real-time data collection and graphical visualization. MATLAB/Simulink 2019a is used for modelling an SPMSM control system.

2.9 Summary

This chapter provides information about the main parts of the modelling of the SPMSM. Three reference frames such as stationary $a-b-c$, stationary $\alpha-\beta$, and rotational $d-q$ frames are reviewed in order to design a dynamic model of the SPMSM. Moreover, the most popular techniques of the PWM such as sinusoidal PWM and space-vector PWM are presented. Also, a brief review of an IGBT-based three-phase inverter has been provided. Next, the uncertainty types existing in a PMSM drive are discussed prior of deriving of the dynamic equations of the SPMSM. Afterwards, practical dynamic equations including parametric uncertainties are derived for the SPMSM. The constraints based on current and voltage limits during the SPMSM's operation are briefly discussed. In the end, a brief description of the experimental test stand used for experimental validations of controllers proposed in this thesis is reported.

BLANK

Chapter 3

Design of disturbance observers

3.1 Introduction

Disturbances as an integral part of most modern control systems can negatively affect to the overall performance of the systems. Consequently, rejection of disturbances plays an important role in design of a control system. A term disturbance does not mean only external type disturbance, but it also refers to un-modelled dynamics, variations in parameters, and nonlinear coupling terms in a system's dynamics. All these components of the disturbance are not easy to handle in practice [10]. A question on disturbance rejection becomes a regular research concern since the early beginning of control theory and its use. Disturbance rejection is an important in control theory, since the controllers such as conventional PID or linear-quadratic regulator (LQR) cannot guarantee to sustain high-performance control requirements under strong disturbances and parametric uncertainties. The main cause is that the conventional control methods do not consider any disturbance or parametric uncertainty effects during their design [10].

Feedforward control is one of the oldest disturbance rejection mechanism which uses a measured disturbance and reject it further. Difficulty in measuring of disturbance or high cost of sensors result in limitation of using of the feedforward control. In general, except the high-cost, sensors may create additional issues due to wiring, difficulty in measuring of impractical signals, bad responsiveness as well as sensor noise. An alternative method called disturbance observer (DO) become popular approach since its first implementation to solve the issues existing in the feedforward control. Disturbance observer is usually used as an augmented component or alternative to sensors in a control system to obtain observed signals. The observed data may be more secure, more exact, cheaper to get [92]. Based on the disturbance observer's application a composite controller named as disturbance observer based composite control (DOBCC) has emerged as a method highly attracted a research community. In this chapter, we discuss about design of the conventional disturbance observer (DOB), modified disturbance observer (DOB), extended state observer (ESO), and high-order disturbance observer.

3.2 Problem formulation

Let us consider a SISO system with uncertainty as follows [6]

$$\begin{cases} \dot{\chi} = a + bu \\ y = \chi \end{cases} \tag{3.1}$$

where χ is a system state variable; u represents a control input; y is an output of the system; a, b are unknown parameters of the system. Further, let us rewrite the unknown parameters in terms of nominal and variation parts as below

$$\begin{aligned} a &= a_0 + \Delta a \\ b &= b_0 + \Delta b \end{aligned} \tag{3.2}$$

in which a_0, b_0 positive nominal part of a and b, respectively; Δa and Δb are variations due to uncertainties in the system. Substitution of (3.2) into (3.1) expresses the given system in terms of the nominal and uncertain parts as

$$\begin{aligned} \dot{\chi} &= (a_0 + \Delta a) + (b_0 + \Delta b)u \\ y &= \chi \end{aligned} \tag{3.3}$$

Denoting a lumped disturbance as $\epsilon = a_0 + \Delta a + \Delta b u$ gives a system expressed in terms of the lumped disturbance term and control input

$$\dot{\chi} = \epsilon + b_0 u \tag{3.4}$$

Remark 3.2.1. *We note that a, b, Δa, Δb are the functions of the state χ and time t. We omit the state and time dependence to simplify the derivation process provided above.*

Assumption 3.2.1. *The lumped disturbance ϵ is assumed to be bounded in the upper side, i.e. $|\epsilon| \leq \Lambda$, where $\Lambda > 0$ is a constant.*

Hence, the main purpose of using the DO is to get estimation of the lumped disturbance ϵ.

3.3 Design of a standard DOB

A conventional disturbance observer (DOB) is considered and analyzed in this section. DOB-based control is able to provide an effective and active solution to estimate disturbances and enhance the robustness of the whole closed-loop system. It is shown in [10] that the DOBC approach can estimate not only disturbances of constant type, but also it may give good estimation of harmonic disturbances. However, harmonic disturbances cannot be compensated by the proportional and integral control.

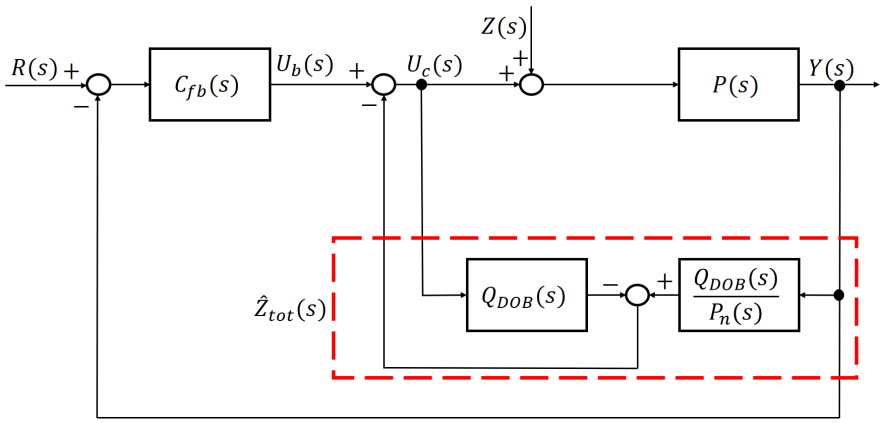

Figure 3.1: Traditional DOBC scheme in the frequency domain.

3.3.1 DOBC formulation in frequency domain

To start, let us consider the following linear minimum phase SISO system given in the frequency domain representation

$$Y(s) = P(s)(U_c(s) + Z(s)) \tag{3.5}$$

where $Y(s)$ is a system output, $U_c(s)$ is a the control input, $P(s)$ is a model of the controlled system, $Z(s)$ represents a disturbance term. The DOBCC is designed based on a feedback and feedforward control parts. In the feedback control, a baseline controller (usually a PI/PID controller) is utilized in order to track the reference command and stabilize a nominal system's dynamics. At the same, time a DOB is designed in the feedforward part in order to estimate lumped disturbances and compensate them in the feedforward loop.

A block scheme of the DOBCC shown in Figure 3.1 presents a basic implementation of the conventional DOBCC in the frequency domain. It consists from the nominal plant model $P_n(s)$, disturbance observer filter $Q_{DOB}(s)$, and the baseline controller $C_{fb}(s)$. Then the the output signal of the system $Y(s)$ can be described in terms of the inputs $R(s)$ and $Z(s)$ as below

$$Y(s) = T_1(s)Z(s) + T_2(s)R(s) \tag{3.6}$$

where $T_1(s)$ and $T_2(s)$ are the sensitivity and co-sensitivity transfer functions, respectively. Since we assume that $N(s) = 1$, we consider only T_1 and T_2, which can be derived from Figure 3.1 as

$$\begin{aligned} T_1(s) &= \frac{P_n(s)(1 - Q_{DOB}(s)) + P(s)Q_{DOB}(s)}{P_n(s)(1 + C_{fb}(s)P(s)) + Q_{DOB}(s)(P(s) - P_n(s))} \\ T_2(s) &= \frac{P_n(s)P(s)C_{fb}(s)}{P_n(s)(1 + C_{fb}(s)P(s)) + Q_{DOB}(s)(P(s) - P_n(s))} \end{aligned} \tag{3.7}$$

Robustness of a disturbance observer-based control system which usually defines the robust stability and robust performance of the overall control system can be analyzed

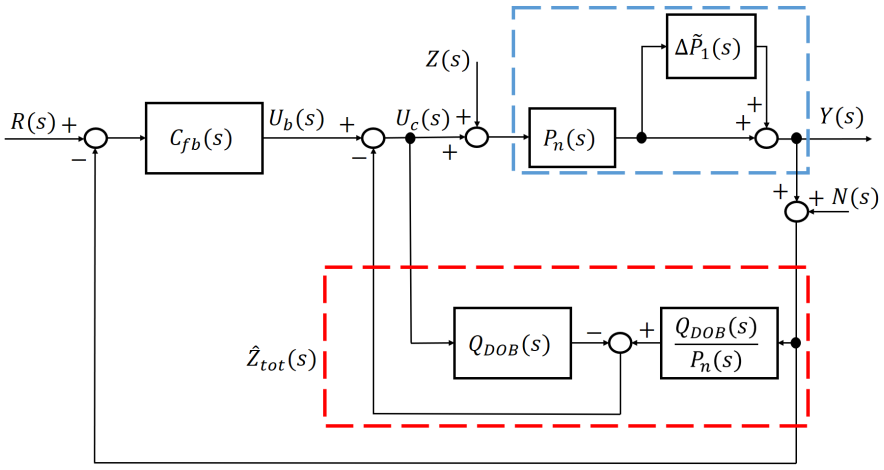

Figure 3.2: Traditional DOBC scheme in frequency domain when an uncertain plant is defined via multiplicative unstructured uncertainty.

using methods such as Small Gain theorem, Nyquist criteria, or μ-analysis. Figure 3.2 shows a DOBCC scheme in which the plant is given in terms of a nominal value and multiplicative unstructured uncertainty. In this scheme, $N(s)$ defines external noise input, $\tilde{P}_1(s)$ and $\tilde{P}_2(s)$ represent weighting functions for robust stability and performance, accordingly. The Δ function called as a complex perturbation is determined by any stable transfer function which satisfies to the condition as $\| \Delta \|_\infty \leq 1$. For the robust stability the following criteria is required [93]

$$\| \Delta\tilde{P}_1(\omega)T_2(\omega) \|_\infty < 1, \forall\omega \tag{3.8}$$

whereas for the robust performance the following criteria should be met

$$\| \Delta\tilde{P}_2(\omega)T_1(\omega) \|_\infty < 1, \forall\omega \tag{3.9}$$

In general, from the equation of the co-sensitivity transfer function in (3.7), it is shown that the bandwidth of the DOB is limited by the dynamics of $\tilde{P}_1(s)$. This means that if the bandwidth of the DOB is much larger than the frequency at which the nominal system $P_n(s)$ cannot sufficiently replicate the dynamics of the actual plant, then the overall system loses its robust stability. Furthermore, it can be seen that the bandwidth of the DOB is also limited by the dynamics of $\tilde{P}_2(s)$.

Furthermore, the equations in (3.7) show that a mechanism of rejecting disturbance relies on the proper design of the filter $Q_{DOB}(s)$. For instance, for disturbances with low frequencies, $Q_{DOB} \cong 1$, then from (3.7) one can observe that [94]

$$\begin{aligned} \lim_{s\to 0} T_1(s) &= \lim_{\omega\to 0} \frac{P(s)}{P(s) + P(s)P_n(s)C_{fb}(s)} \\ \lim_{s\to 0} T_2(s) &= \frac{P(s)P_n(s)C_{fb}(s)}{P(s) + P(s)P_n(s)C_{fb}(s)} \end{aligned} \tag{3.10}$$

From (3.10), it is observed that at low frequencies the robustness of the closed-loop system can be changed by the feedback stabilizing controller $C_{fb}(s)$.

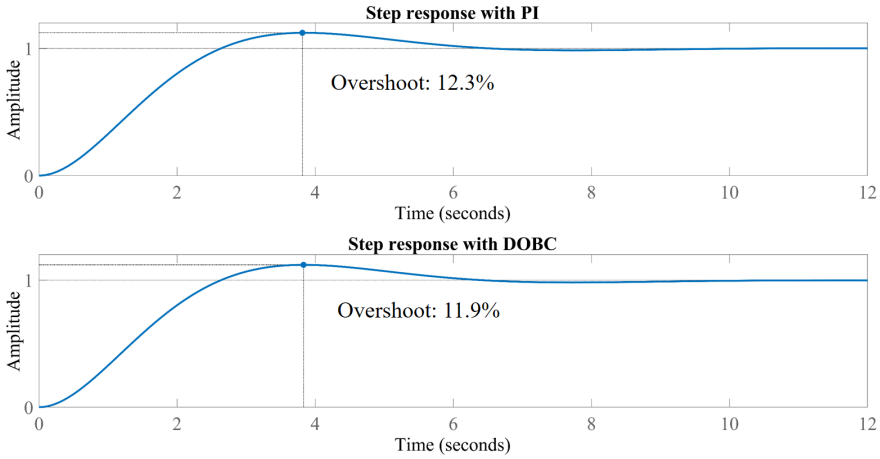

Figure 3.3: Step response of the closed-loop DC motor control system with the traditional PI and DOBC schemes.

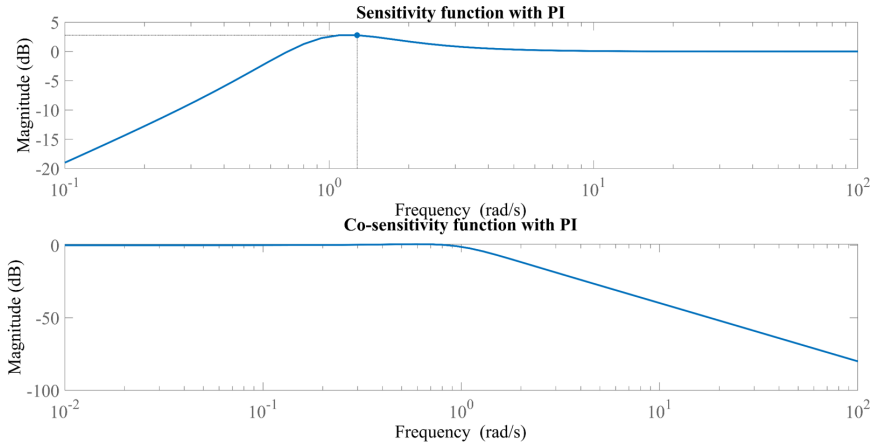

Figure 3.4: Bode analysis of the closed-loop DC motor control system the traditional PI.

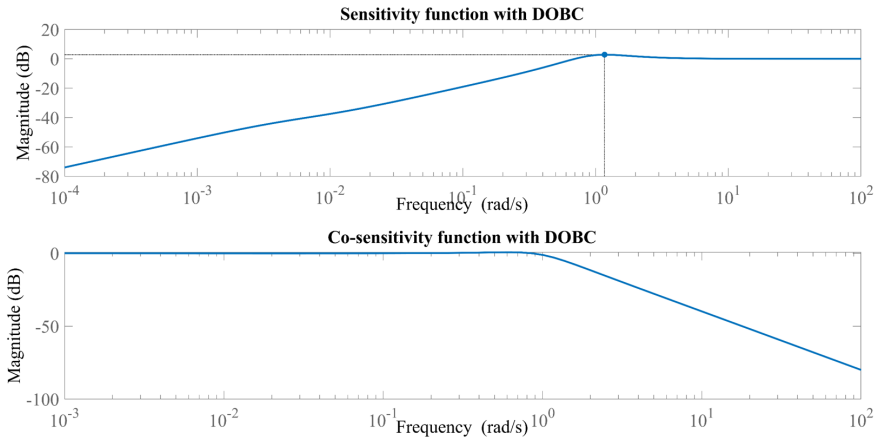

Figure 3.5: Bode analysis of the closed-loop DC motor control system the traditional DOBC.

To see the advantages of the DOBC scheme over the traditional PI scheme, consider an example with DC motor control system. Let the nominal plant of the DC motor is

given as

$$P_n(s) = \frac{0.01}{0.005s^2 + 0.06s + 0.1001}$$

Assume that there is an multiplicative uncertainty with perturbation and weighting function determined as

$$\Delta = \frac{1}{s+1}, \qquad \tilde{P}_1(s) = \frac{1.5s + 29.81}{s + 37.27} \tag{3.11}$$

Hence the actual plant defined as $P(s) = P_n(1 + \Delta\tilde{P}_1(s))$ will have a transfer function

$$P(s) = \frac{2s^2 + 79.54s + 134.2}{s^4 + 50.27s^3 + 516.5s^2 + 1213s + 746.1}$$

The PI controller is used as a feedback stabilizing controller and it has a form

$$C_{fb}(s) = \frac{0.5s + 5}{s}$$

Figure 3.3 shows that both control scheme have similar step response with overshoot level about 12.3%. However, from the sensitivity plots shown in Figures 3.4 and 3.5 one can observe that the DOBC scheme is better in terms of disturbance suppression. This example reveals that the DOBC can guarantee better robustness comparing to the PI controller, even if both controller have same tracking performance.

3.3.2 DOBC formulation in time domain

Let a linear system of MIMO type has a state-form representation as

$$\begin{cases} \dot{\chi} = A\chi + Bu + Bz \\ y = C\chi \end{cases} \tag{3.12}$$

where χ is a state vector, u is a control signal vector, y is a output signal vector, and z is a disturbance vector; A, B, and C are system matrices. Hence, the disturbance observer in the time domain can be constructed as follows [10]

$$\begin{cases} \dot{w} = -L_oB(w + L_o\chi) - L_o(A\chi + Bu) \\ \hat{z} = w + L_o\chi \end{cases} \tag{3.13}$$

where $\hat{z}$ is an estimation of the disturbance vector, w is a vector of intermediate variables of the observer, L_o is a matrix gain of the designed observer. The schematic diagram of the DOBC in the time domain is shown in Figure 3.6. From Figure 3.6, the control algorithm for the given system in (3.12) will have a form

$$u = K_c\chi - \hat{z} \tag{3.14}$$

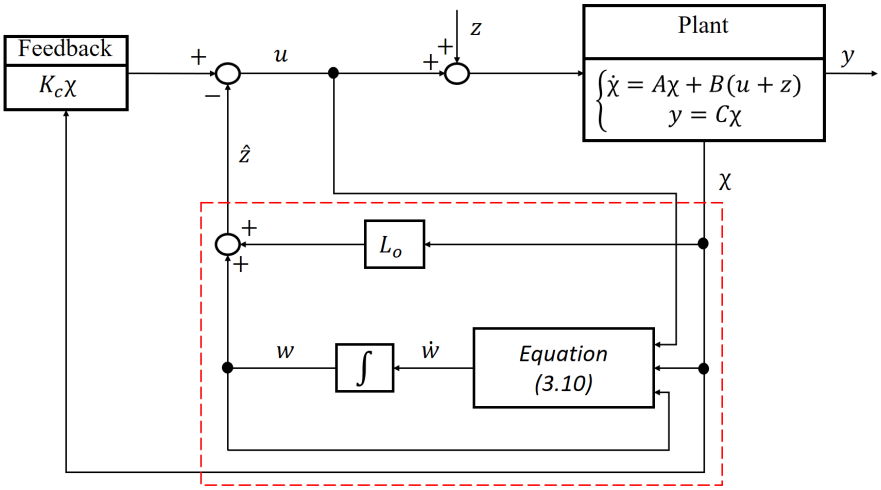

Figure 3.6: Traditional DOBC scheme in the time domain.

with K_c as a gain of the feedback controller to be obtained.

By introducing the observer's error dynamics as $e_z = \hat{z} - z$ and exploiting equations (3.12) - (3.14), the closed-loop DOBC system is designed as

$$\begin{cases} \dot{\chi} = (A - BK_c)\chi - Be_z \\ \dot{e}_z = -L_oBe_z - \dot{z} \end{cases} \tag{3.15}$$

From the obtained estimation error-based system, it concludes that the closed-loop DOBC system is bounded-input-bounded-output (BIBO) stable when the selected K_c makes $A - BK_c$ stable by Hurwitz criterion, and the selected observer gain L_o makes $-L_oB$ stable by Hurwitz criterion.

3.4 Design of a modified DOB

The standard scheme of the DOBC functions only when a system is under the effect of lumped disturbance, this means that the nominal performance of the system can be kept. Unfortunately, the standard DOBC design requires an existence of information of the nominal model and suitable design of a filtering element.

3.4.1 Disturbance Rejection Control

The standard DOBC is designed to estimate disturbance and compensate it in the feedforward loop. Different modifications of the DOBC exist. A modification used in this work is shown in Figure 3.7, where $R(s)$ is a reference command, $P(s)$ is a plant model, $Y(s)$ is an output of the system, $Q_{DOB}(s)$ is a filtering element to be designed, $\bar{W}_r(s)$ is a desired model, $Z(s)$ is a disturbance term, and $K(s)$ is a compensator. Actually, $\bar{W}_r(s)$ is used to replace the inverse of the nominal plant model, $P_n(s)$, which is included in the design of the standard DOBC [95]. Hence, the modified

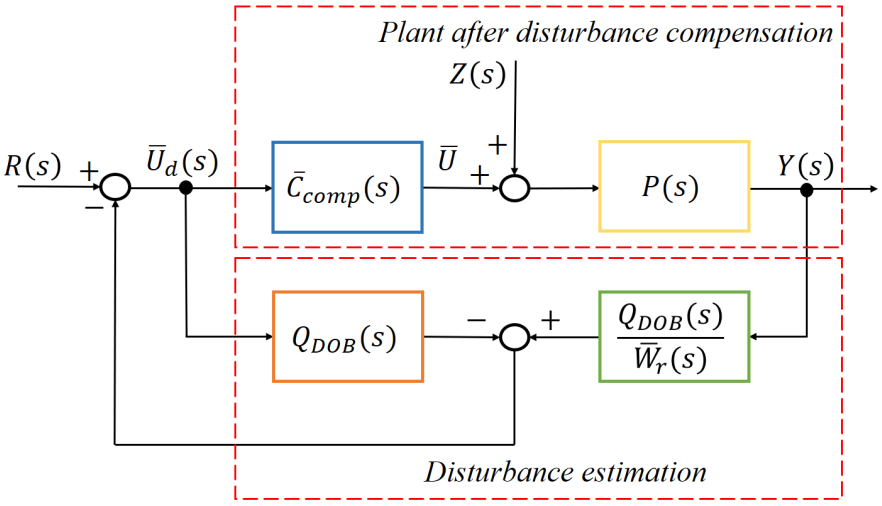

Figure 3.7: DOBC scheme with modification.

DOBC scheme does not require an information about the nominal plant. By doing such modification it is possible to avoid issues with cancellation of unstable poles and zeros. Let us modify the equation of the system in (3.5) as below

$$Y(s) = P(s)(U_c(s) + Z(s)) = P_n(s)U_c(s) + (P(s) - P_n(s))U_c(s) + P(s)Z(s) = P_n(s)(U_c(s) + \epsilon_0(s)) \quad (3.16)$$

where $\epsilon_0(s) = P_n^{-1}(s)\left[(P(s) - P_n(s))U_c(s) + P(s)Z(s)\right]$ represents a lumped disturbance which includes $Z(s)$ and discrepancy between the actual plant $P(s)$ and nominal plant $P_n(s)$.

Remark 3.4.1. *It is assumed that the actual plant $P(s)$ and nominal plant $P_n(s)$ belong to a set of plants with uncertain parameters*

$$\bar{\Omega} = \left\{ \begin{array}{c} P(s) = \frac{\lambda_{m-p}s^{m-p} + \lambda_{m-p-1}s^{m-p-1} + \cdots + \lambda_0}{\rho_m s^m + \rho_{m-1}s^{m-1} + \cdots + \rho_0} \\ : \rho_i \in \left[\rho_i^-, \rho_i^+\right], \lambda_i \in \left[\lambda_i^-, \lambda_i^+\right] \end{array} \right\}$$

in which m, p are defined as positive integers and $m \geq p$; ρ_i^-, ρ_i^+, λ_i^-, λ_i^+ are known constants which define the intervals $[\rho_n^-, \rho_n^+]$ and $\left[\lambda_{n-k}^-, \lambda_{n-k}^+\right]$ such that neither number in the intervals could not be zero, hence the relative order of $P(s)$ is not changed. Note that the relative order $\bar{l}$ of a transfer function $\bar{G}(s) = \frac{\bar{n}(s)}{\bar{d}(s)}$ is found as $\bar{l} = deg(\bar{d}) - deg(\bar{n})$ and $\bar{\Omega}$ determines a sufficiently large set with bounded parametric uncertainties. $deg(\cdots)$ means a degree of a polynomial.

It is obvious that after the compensation of the lumped disturbance, the relation of the output and control input should be described as following

$$Y(s) = P_n(s)U_b(s) \quad (3.17)$$

where $U_b(s)$ is a baseline controller. The main drawback of the standard DOBC scheme's implementation is that an inverse of the nominal plant model is required

during the design. However, nominal plant model is subject to change when a system operates. Furthermore, sometimes nominal parameters might not be known for control system designer. To resolve these limitations, in this section, a modification of the standard DOBC scheme is presented. Let us define a compensator $\bar{C}_{comp}(s)$ which is used to design a controller such that $\bar{U}_c(s) = \bar{C}_{comp}(s)\bar{U}_d(s)$, hence the modification of (3.5) can be written as

$$Y = \bar{W}_r(s)\bar{U}_d(s) + (P(s)\bar{C}_{comp}(s) - \bar{W}_r(s))\bar{U}_d(s) + P(s)Z(s) = \bar{W}_r(s)(\bar{U}_d(s) + \epsilon) \tag{3.18}$$

where $\epsilon(s) = \epsilon_1(s) + \epsilon_2(s)$, $\epsilon_1(s) = \bar{W}_r^{-1}(s)(P(s)\bar{C}_{comp}(s) - \bar{W}_r(s))\bar{U}_d(s)$, and $\epsilon_2(s) = \bar{W}_r^{-1}(s)P(s)Z(s)$. Here, the lumped disturbance is defined as ϵ, which has similar components as ϵ_0 in (3.16), but the nominal plant model, $P_n(s)$, is replaced by the desired model $\bar{W}_r(s)$ and $P(s)$ is changed to $P(s)\bar{W}_r(s)$. The first component of the lumped disturbance ϵ, i.e. ϵ_1, determines the internal disturbance, whereas the second component, i.e. ϵ_2, defines the external disturbances. As shown, ϵ_1 appears due to the difference $P(s)\bar{C}_{comp}(s) - \bar{W}_r(s)$, larger the difference means larger the internal disturbance. The large internal disturbance negatively affect to transient control performance and overall stability of the system.

Remark 3.4.2. *The implementation of the standard DOBC needs an actual plant model to be known, however, in practice the actual parameters of a system are hard to determine. Hence, it could be difficult to calculate the inverse of the actual plant model during design of the standard DOBC. In this work, we refer to the idea presented in [61, 95] to overcome the limitations existing in the standard DOBC design, thus a disturbance rejection control scheme is proposed for minimum-phase as well as non-minimum phase systems, particularly, for speed control of a PMSM.*

The general transfer function of the filtering element in the proposed scheme is taken in the form

$$Q_{DOB}(s) = \frac{\bar{a}_{k-m}(\bar{\tau}s)^r + \bar{a}_{k-m-1}(\bar{\tau}s)^{r-1} + \cdots + \bar{a}_0}{(\bar{\tau}s)^k + \bar{b}_{k-1}(\bar{\tau}s)^{k-1} + \cdots + \bar{b}_0} \tag{3.19}$$

where $\bar{\tau} > 0$ is a positive parameter of the filtering element that responsible for a bandwidth of the filter. $r \geq 0$ and $k \geq 0$ are non-negative integers with relation $r \leq k - rel.deg(\bar{W}_r)$, and these integers are selected to make $Q_{DOB}\bar{W}_r$ feasible, while the parameters $\bar{b}_j$ are determined such that the characteristic equation $(\bar{\tau}s)^k + \bar{b}_{k-1}(\bar{\tau}s)^{k-1} + \cdots + \bar{b}_0$ is Hurwitz stable and DC gain of the filter is one, i.e. $\frac{\bar{a}_0}{\bar{b}_0} = 1$.

Remark 3.4.3. *The proposed method is suitable for systems with the highest relative order two. In the SPMSM, the relative order of the speed loop is one. Hence, the compensator $\bar{C}_{comp}(s)$ can be selected to have the relative order of $P(s)\bar{C}_{comp}(s)$ equal to one. Considering the fact that the internal disturbance may appear due to*

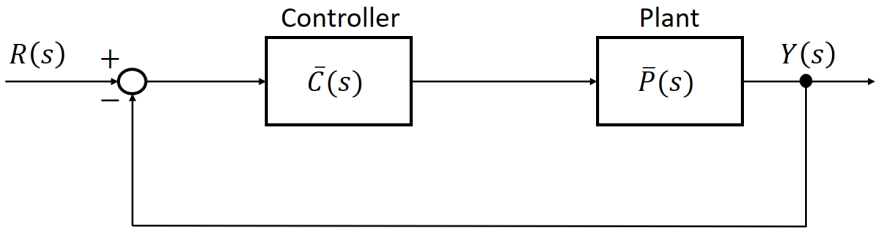

Figure 3.8: Unity feedback closed-loop system.

$P(s)\bar{C}_{comp}(s) - \bar{W}_r(s)$, *to make this difference proper, the relative order of the desired model* $\bar{W}_r(s)$ *is selected to match the relative order of* $P(s)\bar{C}_{comp}(s)$.

Based on Remark 3.4.3, the desired model is chosen as a first-order low-pass filter

$$\bar{W}_r = \frac{\bar{\beta}}{\bar{\alpha}s + \bar{\beta}} \tag{3.20}$$

where $\bar{\beta}$ is a parameter responsible for solving an overshoot problem. The compensator $\bar{C}_{comp}(s)$ is selected based on the relative order of the plant to be controlled

$$\begin{aligned} &\text{For systems with } \bar{l} = 1\text{: } \bar{C}_{comp}(s) = \bar{k}_c \\ &\text{For systems with } \bar{l} = 2\text{: } \bar{C}_{comp}(s) = \bar{k}_c(1 + \bar{k}_d s) \end{aligned} \tag{3.21}$$

in which, for systems with a relative order two, the compensator is chosen in the proportional-derivate (PD) form, which is used for phase-lead compensation of the plant $P(s)$, $\bar{k}_c > 0$ and $\bar{k}_d \geq 0$ are the parameters of the compensator. For the SPMSM control, we use the proportional controller as a compensator, i.e. $\bar{C}_{comp}(s) = \bar{k}_c$. The gain parameter $\bar{k}_c$ of the compensator is tuned such that $P(s)\bar{C}_{comp}(s)$ has stable poles. Based on the conditions whether the system has RHP zeros or RHP poles, the gain of the compensator can be determined

$$\begin{cases} \bar{k}_c = \frac{\rho_m}{\lambda_{m-p}\bar{\alpha}}, \text{ if no zeros on the RHP} \\ \bar{k}_c = \frac{\rho_0}{\lambda_0}, \text{ if no poles on the RHP} \end{cases} \tag{3.22}$$

Remark 3.4.4. *In (3.20), large* $\bar{\beta}$ *is set for systems with slow dynamics and large* $\bar{\alpha}$. *Alternatively, small* $\bar{\beta}$ *is set for systems with fast dynamics and small* $\bar{\alpha}$.

Based on the modified DOBC in Figure 3.7, a closed-loop transfer function for the control system is derived as

$$G_{CL}(s) = \frac{\bar{C}_{comp}(s)\bar{W}_r(s)P(s)}{\bar{C}_{comp}(s)Q_{DOB}(s)P(s) + \bar{W}_r(s) - \bar{W}_r(s)Q_{DOB}(s)} \tag{3.23}$$

Let us consider a general scheme of a closed-loop system with a negative unity-feedback shown in Figure 3.8. The closed-loop transfer function of the negative unity-feedback system can be derived as

$$G'(s) = \frac{\bar{P}(s)\bar{C}(s)}{1 + \bar{P}(s)\bar{C}(s)} \tag{3.24}$$

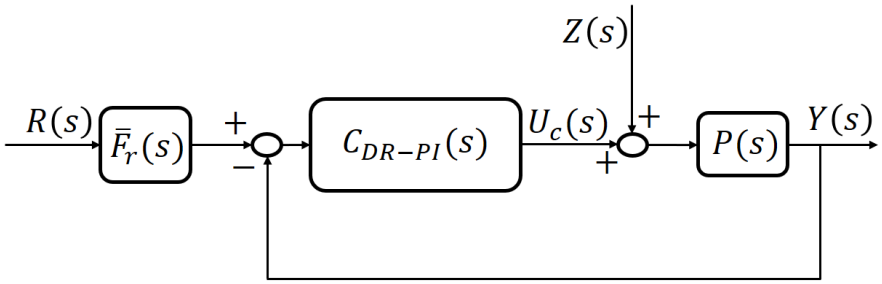

Figure 3.9: Proposed DR-PI scheme.

A transfer function given in (3.24) is a general formula for closed-loop systems with negative unity-feedback. To represent the closed-loop transfer function in (3.23) in the general form similar to (3.24), let us make a modification as follows

$$G_{CL}(s) = \frac{\frac{\bar{W}_r(s)}{Q_{DOB}(s)}}{1 + \frac{\bar{W}_r(s)}{\bar{C}_{comp}(s)Q_{DOB}(s)P(s)} - \frac{\bar{W}_r(s)}{\bar{C}_{comp}(s)P(s)}} = \frac{\frac{\bar{W}_r(s)}{Q_{DOB}(s)}}{1 + \frac{\bar{W}_r(s) - \bar{W}_r(s)Q_{DOB}(s)}{\bar{C}_{comp}(s)Q_{DOB}(s)P(s)}} \tag{3.25}$$

After simplification of (3.25), the closed-loop transfer function will be

$$G_{CL}(s) = \frac{\frac{\bar{W}_r(s)}{Q_{DOB}(s)} \frac{\bar{C}_{comp}(s)Q_{DOB}(s)P(s)}{\bar{W}_r(s) - \bar{W}_r(s)Q_{DOB}(s)}}{1 + \frac{\bar{C}_{comp}(s)Q_{DOB}(s)P(s)}{\bar{W}_r(s) - \bar{W}_r(s)Q_{DOB}(s)}} \tag{3.26}$$

Given that $G_{CL}(s) = \frac{Y(s)}{R(s)}$, (3.26) is modified as

$$\frac{Y(s)}{R(s)\frac{\bar{W}_r(s)}{Q_{DOB}(s)}} = \frac{\frac{\bar{C}_{comp}(s)Q_{DOB}(s)P(s)}{\bar{W}_r(s) - \bar{W}_r(s)Q_{DOB}(s)}}{1 + \frac{\bar{C}_{comp}(s)Q_{DOB}(s)P(s)}{\bar{W}_r(s) - \bar{W}_r(s)Q_{DOB}(s)}} \tag{3.27}$$

Then, from (3.24) and (3.27), the proposed DR-PI scheme should be

$$\bar{C}_{DR-PI} = \frac{\bar{C}_{comp}(s)Q_{DOB}(s)}{\bar{W}_r(s)(1 - Q_{DOB}(s))} \tag{3.28}$$

$\bar{F}_r(s) = \frac{\bar{W}_r(s)}{Q_{DOB}(s)}$ appeared in (3.27) plays a role of a pre-filter applied to the reference signal. The proposed DR-PI is schematically presented in Figure 3.9. The filtering element in (3.19) is designed as a first-order low-pass filter

$$Q_{DOB}(s) = \frac{1}{\bar{\tau}s + 1} \tag{3.29}$$

After substitution $\bar{W}_r(s)$, $Q_{DOB}(s)$, and $\bar{C}_{comp}(s)$ into (3.28), the DR-PI is designed

$$\begin{cases} \bar{C}_{DR-PI} = \frac{\rho_m}{\lambda_{m-p}\bar{\tau}} + \frac{\rho_m}{\lambda_{m-p}\bar{\tau}\bar{\alpha}s}, \text{ if no zeros on the RHP} \\ \bar{C}_{DR-PI=\frac{\rho_0}{\lambda_0\bar{\tau}\bar{\alpha}}+\frac{\rho_0}{\lambda_0\bar{\tau}s}}, \text{ if no poles on the RHP} \end{cases} \tag{3.30}$$

3.5 Design of an ESO

In this section, another type of a disturbance observer called the extended state observer (ESO) is introduced. Comparing to the DOBC, the ESO method's implementation

requires less information, i.e. only a relative degree of a system should be available [96].

Consider a system given in (3.1) and let us take $\chi_1 = y$, $\chi_2 = \dot{y}$, $\chi_3 = \ddot{y}$, ..., $\chi_k = y^{(k-1)}$, then the given system with uncertainty terms can be represented in the form

$$\begin{cases} \dot{\chi_1} = \chi_2 \\ \dot{\chi_2} = \chi_3 \\ \vdots \\ \dot{\chi}_{k-1} = \chi_k \\ \dot{\chi}_k = f(\chi_1, \chi_2, \chi_3, \ldots, \chi_k, \bar{d}, t) + bu \\ y = \chi_1 \end{cases} \tag{3.31}$$

where the lumped disturbance ϵ defined in (3.1) is shown based on the system states χ_1, χ_2, ..., χ_k, and external disturbance $\bar{d}$, b is a nonsingular control vector. Let us consider a known nonsingular vector $\hat{b}$ as an estimation for b. Hence, a canonical form of a system in terms of cascaded integrators can be obtained [97]

$$\begin{cases} \dot{\chi}_1 = \chi_2 \\ \dot{\chi}_2 = \chi_3 \\ \vdots \\ \dot{\chi}_{k-1} = \chi_k \\ \dot{\chi}_k = \hat{b}u \end{cases} \tag{3.32}$$

So, a part of the system in (3.31) which differs from the its canonical form is introduced as an augmented variable under the concept of the ESO design, i.e.

$$\chi_{k+1} = f(\chi_1, \chi_2, \chi_3, \ldots, \chi_k, \bar{d}, t) + (b - \hat{b})u \tag{3.33}$$

Thus combination of equations (3.31) and (3.33) gives an extended-state space equation of the system with the augmented variable

$$\begin{cases} \dot{\chi_1} = \chi_2 \\ \dot{\chi_2} = \chi_3 \\ \vdots \\ \dot{\chi}_{k-1} = \chi_k \\ \dot{\chi}_k = \chi_{k+1} + \hat{b}u \\ y = \chi_1 \end{cases} \tag{3.34}$$

Based on (3.34), an ESO is constructed to estimate the lumped disturbance defined as an augmented state

$$\begin{cases} \dot{\hat{\chi}}_1 = \hat{\chi}_2 + l_1(y - \hat{\chi}_1) \\ \dot{\hat{\chi}}_2 = \hat{\chi}_3 + l_2(y - \hat{\chi}_1) \\ \dot{\hat{\chi}}_3 = \hat{\chi}_4 + l_3(y - \hat{\chi}_1) \\ \vdots \\ \dot{\hat{\chi}}_k = \hat{\chi}_{k+1} + l_k(y - \hat{\chi}_1) + bu \\ \dot{\hat{\chi}}_{k+1} = l_{k+1}(y - \hat{\chi}_1) \end{cases} \tag{3.35}$$

where the estimated values of the states $\chi_1, \chi_2, \ldots, \chi_{k+1}$ are denoted as $\hat{\chi}_1, \hat{\chi}_2, \ldots, \hat{\chi}_{k+1}$, respectively; $l_1, l_2, \ldots, l_{k+1}$ are the gains of the ESO to be designed.

Remark 3.5.1. *Note that the estimation of the control parameter $\hat{b}$ in (3.32) is a function of time and does not depend on the system states, whereas the actual control parameter b is a function of both time and states.*

Based on the ESO design, a method named as an active-disturbance rejection control (ADRC) is proposed by Han in the 90s. Since that time the ADRC method has been popular in research community, and this is due to its simple structure, original concept, excellent performance, and many more [97]. The ADRC method can guarantee a robust operation of a system under matched and unmatched conditions. To show the ability of the ADRC method in suppressing unmatched disturbance, let us consider an example below.

Example 1. Consider a second-order dynamic system given as

$$\begin{cases} \dot{\bar{x}}_1 = \bar{f}_1(t, \bar{x}_1, \bar{x}_2, \bar{d}) \\ \dot{\bar{x}}_2 = \bar{f}_2(t, \bar{x}_1, \bar{x}_2, \bar{d}) + b'(t, \bar{x}_1, \bar{x}_2)\mu \\ y = \bar{x}_1 \end{cases} \tag{3.36}$$

where $\bar{x}_1$ and $\bar{x}_2$ are the system states, $y(t)$ is an output of the given system, μ is a control input, y is an output of the system, $\bar{d}$ is an undefined external disturbance, $\bar{f}_1(t, \bar{x}_1, \bar{x}_2, \bar{d})$, $\bar{f}_2(t, \bar{x}_1, \bar{x}_2, \bar{d})$ are unknown nonlinear functions. Most systems in industry have nonlinear behaviour, and disturbance can come in from multiple channels. As we see from Example 1, the system has unmatched disturbance term affecting the first state's dynamics. To design an ADRC scheme for the given system, let us write the system in a canonical form as

$$\begin{cases} \dot{\bar{\bar{x}}}_1 = \bar{\bar{x}}_2 \\ \dot{\bar{\bar{x}}}_2 = \frac{\partial \bar{f}_1}{\partial t} + \frac{\partial \bar{f}_1}{\partial \bar{x}_1}\bar{f}_1(t, \bar{x}_1, \bar{x}_2, \bar{d}) + \frac{\partial \bar{f}_1}{\partial \bar{d}}\dot{\bar{d}} + \frac{\partial \bar{f}_1}{\partial \bar{x}_2}\bar{f}_2(t, \bar{x}_1, \bar{x}_2, \bar{d}) + \frac{\partial \bar{f}_1}{\partial \bar{x}_2}b'(t, \bar{x}_1, \bar{x}_2)\mu \\ y = \bar{\bar{x}}_1 \end{cases} \tag{3.37}$$

where the newly defined state variables are taken as $\bar{\bar{x}}_1 = y_1$ and $\bar{\bar{x}}_2 = \bar{f}_1(t, \bar{x}_1, \bar{x}_2, \bar{d})$. Following the condition such that $\frac{\partial \bar{f}_1}{\partial x_2} \neq 0$, the following system of a canonical form is obtained

$$\begin{cases} \dot{\bar{\bar{x}}}_1 = \bar{\bar{x}}_2 \\ \dot{\bar{\bar{x}}}_2 = \hat{b}'\mu \end{cases} \tag{3.38}$$

where $\hat{b}' \neq 0$ serves as an estimation of $\frac{\partial \bar{f}_1}{\partial \bar{x}_2} b'(t, \bar{x}_1, \bar{x}_2)$. Then the extended state denoted as $\bar{\bar{x}}_3$ will be defined as

$$\dot{\bar{\bar{x}}}_3 = \frac{\partial \bar{f}_1}{\partial t} + \frac{\partial \bar{f}_1}{\partial \bar{x}_1}\bar{f}_1(t, \bar{x}_1, \bar{x}_2, \bar{d}) + \frac{\partial \bar{f}_1}{\partial \bar{d}}\dot{\bar{d}} + \frac{\partial \bar{f}_1}{\partial \bar{x}_2}\bar{f}_2(t, \bar{x}_1, \bar{x}_2, \bar{d}) + (\frac{\partial \bar{f}_1}{\partial \bar{x}_2} b'(t, \bar{x}_1, \bar{x}_2) - \hat{b}')\mu \tag{3.39}$$

$\bar{\bar{x}}_3$ is revealed as a total disturbance existing in the system (3.37). Finally, one can apply the ADRC approach for the system in (3.37) as below

$$\begin{cases} \dot{\hat{\bar{\bar{x}}}}_1 = \hat{\bar{\bar{x}}}_2 - \bar{g}_1(\hat{\bar{\bar{x}}}_1 - y) \\ \dot{\hat{\bar{\bar{x}}}}_2 = \hat{\bar{\bar{x}}}_3 - \bar{g}_2(\hat{\bar{\bar{x}}}_1 - y) + \hat{b}'\mu \\ \dot{\hat{\bar{\bar{x}}}}_3 = \bar{g}_3(\hat{\bar{\bar{x}}}_1 - y) \end{cases} \tag{3.40}$$

where $\bar{g}_1$, $\bar{g}_2$, $\bar{g}_3$ are the gains of the ESO to be designed. The control law is then designed such that

$$\mu = -\frac{1}{\hat{b}'}\hat{\bar{\bar{x}}}_3 + \mu_0 \tag{3.41}$$

in which μ_0 is a control law that can stabilize the system of the canonical form in (3.38). This example demonstrates a power of the ADRC method in rejection of not only matched disturbances, but also unmatched disturbances without requiring its exact values. Hence, the ADRC is able to estimate a total disturbance of a system which may include both the matched and unmatched disturbances. Furthermore, the total disturbance is observable at anytime [97].

3.6 Design of a high-order disturbance observer

Commonly, the traditional disturbance observers are designed based on appropriate bounded conditions and assumption that requires disturbances to be slow compared to the dynamics of an observer. Once these requirements are met, the stability and convergence are guaranteed. However, during the transient time period, the traditional observers may not precisely estimate disturbances with fast-changing dynamics which usually exist in electrical part of the PMSMs. Let us modify the system given in (3.12) as follows

$$\begin{cases} \dot{\chi} = A\chi + Bu + Dz \\ y = C\chi \end{cases} \tag{3.42}$$

where χ is a $m \times 1$ state vector, u is a $l \times 1$ control input vector, y is a $1 \times s$ output vector, A, B, C, and D are system matrices, z represents a lumped disturbance. Hence, we introduce the following assumption to design a high-order observer.

Assumption 3.6.1. *The lumped disturbance z is a continuous function and its high-order derivatives are upper-bounded, i.e. $z_k^{(n)} \leq \eta$, where η is undefined positive upper-bound of the disturbance, $k = 0, 1, 2, \ldots, r$. The notation $(\cdot)^{(n)}$ defines the n^{th}-order time-derivative of a given function.*

This assumption makes generalization for disturbance observer design, hence if we take $\eta = 0$ and $n = 1$, a conventional DO is designed. When $\eta = 1$ and $n = 1$, an assumption in [98] is revealed. For the case with $\eta = 0$ and $n \geq 2$, the traditional assumption is loosen, since the variation level of the disturbance is determined by the value of n through the degree of the time-dependent polynomial. However, this case does not work for oscillating disturbances having sinusoidal, triangular, or sawtooth form, it means that η cannot be considered as zero. Hence, for high-order disturbances a requirement in Assumption 3.6.1 about existing of an upper-bound for the disturbance itself and its subsequent derivatives is reasonable.

Using Assumption 3.6.1, the next system with high-order disturbances is designed

$$\begin{cases} \dot{\psi} = \bar{S}\psi + \bar{M}z^{(n+1)} \\ z = \bar{N}\psi \end{cases} \tag{3.43}$$

in which $\psi = \begin{bmatrix} z & z^{(1)} & \ldots & z^{(n)} \end{bmatrix}$ is a vector of disturbance and its high-order derivatives, $\bar{S}$, $\bar{M}$, and $\bar{N}$ are design matrices with the next structures

$$\begin{aligned} \bar{S} &= \begin{bmatrix} 0_{r(n)\times r} & diag(\bar{W}_1 \ldots \bar{W}_n) \\ 0_{r\times r} & 0_{r\times r(n)} \end{bmatrix} \\ \bar{W}_i &= \begin{bmatrix} 0_{(n)\times 1} & I_n \\ 0 & 0_{1\times(n)} \end{bmatrix} \\ \bar{M} &= \begin{bmatrix} 0_{(n)\times 1} & I_r \end{bmatrix} \\ \bar{N} &= \begin{bmatrix} I_r & 0_{r\times(n)} \end{bmatrix} \end{aligned} \tag{3.44}$$

Based on (3.42) and (3.43), one can design an extended model of the system as follows

$$\begin{cases} \dot{\bar{\chi}} = \bar{\bar{A}}\bar{\chi} + \bar{\bar{B}}u + Mz^{(n)} \\ y = \bar{\bar{C}}\bar{\chi} \end{cases} \tag{3.45}$$

where $\bar{\chi} = \begin{bmatrix} \psi \\ \chi \end{bmatrix}$. And the extended matrices are designed as below

$$\bar{\bar{A}} = \begin{bmatrix} \bar{S} & 0_{rn\times m} \\ (D\bar{N})_m \times rn & A \end{bmatrix}$$
$$\bar{\bar{B}} = \begin{bmatrix} 0_{rn\times l} \\ B \end{bmatrix}$$
$$\bar{\bar{C}} = \begin{bmatrix} 0_{rn\times s} & C \end{bmatrix}$$
$$M = \begin{bmatrix} \bar{M} \\ 0_{m\times r} \end{bmatrix} \tag{3.46}$$

The observability condition for the system states can be proven via the Lemma 3.6.

Lemma 3.6.1. *The pair $(\bar{\bar{A}}, \bar{\bar{C}})$ is observable for every integer $n > 0$, if the next conditions are hold:*

1. *(A, C) is observable;*
2. *rank $\begin{bmatrix} A & D \\ C & 0_{s\times r} \end{bmatrix}$ = m + r.*

Using the extended system (3.45), the disturbance observer is designed

$$\dot{\hat{\bar{\chi}}} = \bar{\bar{A}}\hat{\bar{\chi}} + \bar{\bar{B}}u + \bar{L}(y - \bar{\bar{C}}\bar{\bar{\chi}}) \tag{3.47}$$

where $\bar{L}$ is an observer gain which is a function of $\bar{P}$, i.e. a solution of the algebraic Riccati equation given below

$$\bar{\bar{A}}\bar{P} + \bar{P}\bar{\bar{A}}^T - \bar{P}\bar{\bar{C}}^T R_{obs}^{-1}\bar{\bar{C}}\bar{P} + Q_{obs} = 0 \tag{3.48}$$

where $Q_{obs} \geq 0$ is a symmetric matrix, $R_{obs} > 0$ is a symmetric matrix. Then the observer gain $\bar{L}$ is obtained by

$$\bar{L} = \bar{P}\bar{\bar{C}}^T R_{obs}^{-1} \tag{3.49}$$

The state error dynamics form of the designed observer can be obtained further

$$\dot{\bar{\chi}}_e = (\bar{\bar{A}} - \bar{L}\bar{\bar{C}})\hat{\bar{\chi}} + Mz^{(n)} \tag{3.50}$$

in which $\bar{\chi}_e = \bar{\chi} - \hat{\bar{\chi}}$ is state estimation error. The stability of the designed observer is guaranteed via the theorem stated below.

Theorem 3.6.1. *$\bar{\chi}_e$ converges to zero via the designed optimal observer in (3.47).*

Proof. Let us consider the Lyapunov function of the form

$$V(\bar{\chi}_e) = \bar{\chi}_e \bar{P}^{-1}\bar{\chi}_e \tag{3.51}$$

The time-derivative of the candidate Lyapunov function is

$$\dot{V}(\bar{\chi}_e) = 2\bar{\chi}_e^T(\bar{P}^{-1}\bar{\bar{A}} - \bar{P}C^T R_{obs}^{-1}C)\bar{\chi}_e + 2\bar{\chi}_e^T\bar{P}^{-1}Mz^{(n)}$$

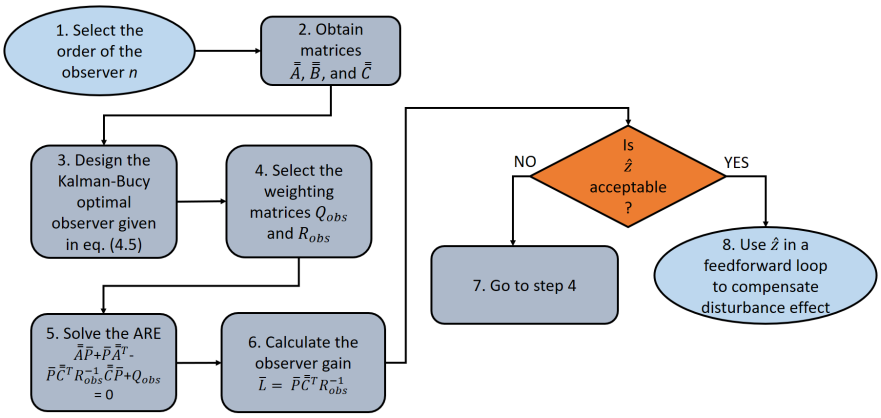

Figure 3.10: A flowchart showing design steps of the GHDO.

$$= \bar{\chi}_e^T \bar{P}^{-1}(\bar{\bar{A}}\bar{P} + \bar{P}\bar{\bar{A}}^T - 2\bar{P}\bar{\bar{C}}^T R_{obs}^{-1}\bar{\bar{C}}\bar{P})\bar{P}^{-1} + 2\bar{\chi}_e^T \bar{P}^{-1} M z^{(n)} \leq -\bar{\chi}_e^T \bar{P}^{-1} Q_{obs} \bar{P}^{-1} \bar{\chi}_e +$$
$$2\bar{\chi}_e^T \bar{P}^{-1} M z^{(n)} \leq - \parallel \bar{\chi}_e \parallel \left[\alpha \parallel \bar{\chi}_e \parallel -2 \parallel \bar{P}^{-1} M \parallel \eta\right] \tag{3.52}$$

■

where α is the minimum eigenvalue of $\bar{P}^{-1} Q_{obs} \bar{P}^{-1}$. Hence, from (3.52), it can be established that after long time properly selected Q_{obs} and R_{obs} can guarantee a bounded norm of the estimation error as

$$\parallel \bar{\chi}_e \parallel \leq \beta \tag{3.53}$$

with the bound $\beta = \frac{2\|\bar{P}^{-1} M\|\eta}{\alpha}$. It is seen that the accuracy of the estimation is dependent on the value of β. And the proper value of β can be obtained via the tuning Q_{obs} and R_{obs}, appropriately. This means that the proposed observer ensures upper boundedness and stability of a ball with randomly defined small radius with center at $\bar{\chi}_e$.

3.7 Design of the optimal DOBC

3.7.1 Problem formulation

Let us consider a system provided in (3.4). Then (3.4) can be written in the extended state space form as

$$\begin{cases} \dot{\chi}_{ext} = \bar{A}_{ext}\chi_{ext} + \bar{B}_{ext} u + \bar{E}_{ext}\dot{\epsilon} \\ y = \bar{C}_{ext}\chi_{ext} \end{cases}$$

$$\bar{A}_{ext} = \begin{bmatrix} 0 & 1 \\ 0 & 0 \end{bmatrix}$$

$$\bar{B}_{ext} = \begin{bmatrix} 1 \\ 0 \end{bmatrix}$$

$$\bar{E}_{ext} = \begin{bmatrix} 0 \\ 1 \end{bmatrix}$$

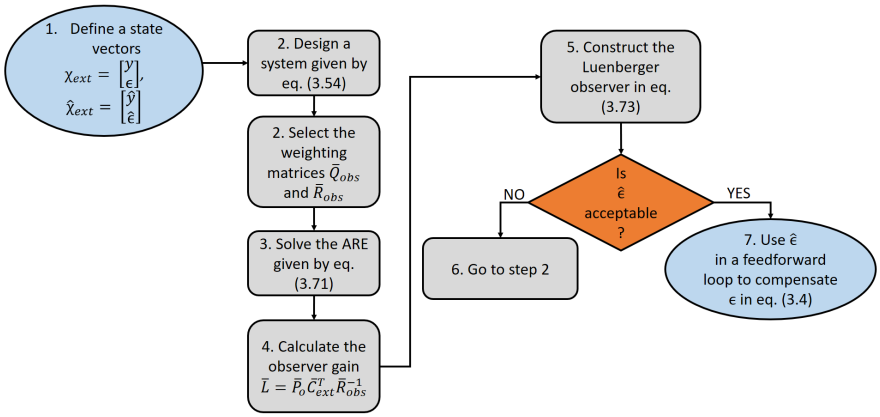

Figure 3.11: A flowchart showing design steps of the ESO with optimal parameters.

$$\bar{C}_{ext} = \begin{bmatrix} 1 & 0 \end{bmatrix} \tag{3.54}$$

where $\chi_{ext} = \begin{bmatrix} y & \epsilon \end{bmatrix}^T$ is a state vector augmented with the lumped disturbance ϵ.

Further a composite controller $u = u_{hodobc}$ is designed to compensate the disturbance effect in (3.4)

$$u_{hodobc} = \frac{1}{b_0}(u_{optPI} - \hat{\epsilon}) \tag{3.55}$$

After substitution of (3.55) into (3.4), the compensated plant is obtained

$$\dot{\chi} = u_{optPI} \tag{3.56}$$

where $\hat{\epsilon}$ is an estimation of the lumped disturbance obtained by the disturbance observer which will be designed in the next section, u_{optPI} is an optimal PI controller to be designed. Let us define an output tracking error as

$$e_y = y_{ref} - y \tag{3.57}$$

where y_{ref} is a reference command for tracking. Then the second-order derivative of (3.57) will be

$$\ddot{e}_y = -\ddot{y} \tag{3.58}$$

Since $\chi = y$, the second-order time derivative of (3.56) is

$$\ddot{y} = -\dot{u}_{optPI} \tag{3.59}$$

Taking $\bar{e} = \begin{bmatrix} e_y & \dot{e}_y \end{bmatrix}^T$ as a state vector, we can get a state-space model in the form as

$$\dot{\bar{e}} = \bar{A}_e \bar{e} + \bar{B}_e \dot{u}_{optPI} \tag{3.60}$$

where $\bar{A}_e = \begin{bmatrix} 0 & 1 \\ 0 & 0 \end{bmatrix}$, $\bar{B}_e = \begin{bmatrix} 0 \\ -1 \end{bmatrix}$. Further, the state-space model in (3.60) will be utilized to derive the optimal PI controller.

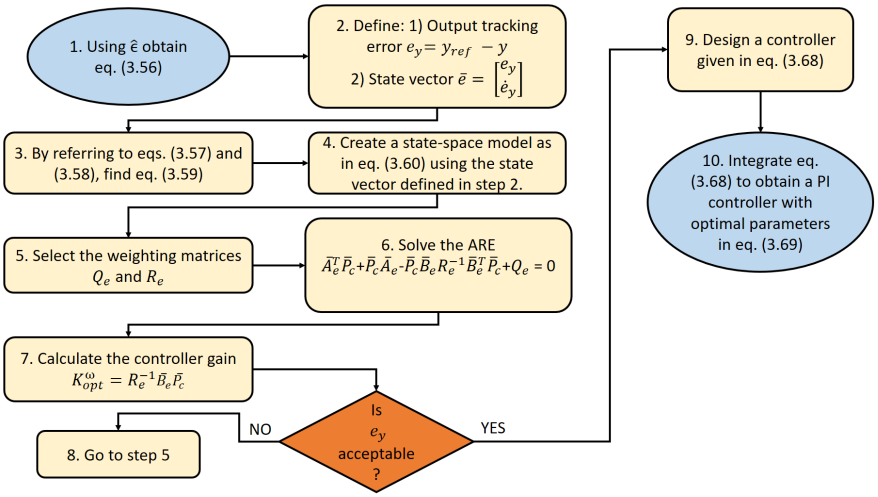

Figure 3.12: A flowchart showing design steps of the PI controller with optimal parameters.

3.7.2 Design of the optimal PI controller

The goal of the proposed controller is designing of the PI controller to improve tracking performance of the system in (2.72) via searching for the PI control with optimal parameters such that

$$\dot{u}_{optPI}(t) = min\ \bar{J}_1(\bar{e}, \dot{u}_{optPI}, t) \tag{3.61}$$

where $\bar{J}_1(\bar{e}, \dot{u}_{optPI}, t)$ is a cost function to be minimized, which is usually determined as

$$\bar{J}_1 = \bar{J}_{state} + \bar{J}_{control} + \bar{J}_{final} \tag{3.62}$$

where $\bar{J}_{state}$ represents a state cost function defined as

$$\bar{J}_{state} = \int_0^\infty \bar{e}^T(t)Q_e\bar{e}(t)dt \tag{3.63}$$

where Q_e is a positive semi-definite weight matrix, i.e. $Q_e = Q_e^T \geq 0$. $J_{control}$ is a control input cost function which has a form

$$\bar{J}_{control} = \dot{u}_{optPI}^T(t)R_e\dot{u}_{optPI}(t)dt \tag{3.64}$$

where R_e is a positive definite symmetric weight matrix, i.e. $R_e = R_e^T \geq 0$. In this study, we assume that the final error cost function is zero, i.e. $\bar{J}_{final} = 0$. Hence, the cost function $\bar{J}_1$ is determined as

$$\bar{J}_1 = \int_0^\infty [\bar{e}^T(t)Q_e\bar{e}(t) + \dot{u}_{optPI}^T(t)R_e\dot{u}_{optPI}(t)]dt \tag{3.65}$$

Then the optimal feedback control law can be designed as follows

$$\dot{u}_{optPI} = -K_{opt}\bar{e} \tag{3.66}$$

where $K_{opt} = R_e^{-1}\bar{B}_e\bar{P}_c$ and $\bar{P}_c$ is a solution of the continuous-time algebraic Riccati equation (ARE)

$$\bar{A}_e^T\bar{P}_c + \bar{P}_c\bar{A}_e - \bar{P}_c\bar{B}_eR_e^{-1}\bar{B}_e^T\bar{P}_c + Q_e = 0 \tag{3.67}$$

Giving that $K_{opt} = \begin{bmatrix} k_1 & k_2 \end{bmatrix}^T$, (3.66) can be expanded as

$$\dot{u}_{optPI} = -k_1 e_y - k_2 \dot{e}_y \tag{3.68}$$

The integration of (3.68) results in the PI controller with optimal parameters

$$u_{optPI} = k_p e_y + k_i \int_0^t e_y dt \tag{3.69}$$

where $k_p = -k_2$ and $k_i = -k_1$.

3.7.3 Design of the ESO with optimal parameters

This section presents an approach to find the parameters of the ESO shown in Chapter 4 via the LQR formulation. Let us define a quadratic cost functional in the form as

$$\bar{J}_2 = \int_0^\infty (\chi_{ext}^T(t) \bar{Q}_{obs} \chi_{ext}(t) + \dot{\bar{u}}_0{}^T \bar{R}_{obs} \dot{\bar{u}}_0) dt \tag{3.70}$$

where $\bar{Q}_{obs}$ is a positive semi-definite symmetric matrix and $\bar{R}_{obs}$ is a positive definite symmetric matrix. The continuous-time ARE in can be written as

$$\bar{A}_{ext} \bar{P}_o + \bar{P}_o \bar{A}_{ext}^T - \bar{P}_o \bar{C}_{ext}^T \bar{R}_{obs}^{-1} \bar{C}_{ext} \bar{P}_o + \bar{Q}_{obs} = 0 \tag{3.71}$$

where $\bar{P}_o$ is a solution of the continuous-time ARE given in (3.71). Then the gain of the observer system is calculated

$$\bar{L} = \bar{P}_o \bar{C}_{ext}^T \bar{R}_{obs}^{-1} = \begin{bmatrix} \bar{l}_1 & \bar{l}_2 \end{bmatrix}^T \tag{3.72}$$

Based on (3.35), (3.54), and (3.72) the Luenberger observer is synthesized as

$$\dot{\hat{\chi}}_{ext} = \bar{A}_{ext} \hat{\chi}_{ext} + \bar{B}_{ext} u_{optPI} + \bar{L}(y - \bar{C}_{ext} \hat{\chi}_{ext}) \tag{3.73}$$

where $\hat{\chi}_{ext} = \begin{bmatrix} \hat{y} & \hat{\epsilon} \end{bmatrix}^T$ is an observed state vector.

Hence in this chapter we shown details on theory of observers' design and the next chapters presents results and analysis of the proposed observer-based control schemes applied to speed control of the SPMSM. Design steps of the ESO and PI controllers with optimal parameters are summarized in the flowcharts depicted in Figures 3.11-3.12.

Part II

Applications

BLANK

Chapter 4

High-order disturbance observer-based composite control (HDOBCC)

4.1 Introduction

The traditional PI or PID controllers are widely used in motion control, robotic systems, and drive control systems. However, these controllers are highly sensitive to disturbance effect [99], hence precise speed or current tracking cannot be achieved at some operation point, especially at transient times. Fuzzy approach as one of the nonlinear approaches have been introduced to control systems with predefined dynamic models. For control of AC machines, numerous fuzzy logic-based control solutions [30, 59, 99–122] were proposed since the last two decades.

In this method, the fuzzy inference is exploited to tune the PI controller parameters in order to improve performance at transient time.

This chapter presents a generalized high-order disturbance observer-based composite control (HDOBCC), consisting of the fuzzy-PI speed controller and generalized high-order disturbance observer (GHDO). A finite-time stability of the system is provided by the fuzzy-PI speed controller, whereas the GHDO is designed to estimate lumped disturbances including parameter variations, uncertainties, and load torque effect. The negative effect of the lumped disturbance is compensated by the estimated output of the GHDO in the feedforward loop. Three different orders of the proposed observer are compared and detailed stability analysis of the proposed composite control scheme is demonstrated. The orders of the GHDO are increased gradually until the performance of two sequential orders remains unchanged. The fuzzy logic is exploited to improve transient time performance by adjusting the parameters of the PI speed controller. Two standard PI controllers are used to control i_d^r and i_q^r currents. The proposed scheme is introduced as a novel FOC approach for a 3-phase PMSM system. Results of performance analysis and comparison between standard cascaded control system, which includes a PI speed controller and two PI current controllers, and the proposed composite control scheme have been presented.

4.2 Proposed GHDO design

This section presents an application of the proposed high-order observer introduced in Section 3.6 to estimate lumped disturbances presenting in the SPMSM. Let us define $\chi = \omega_m$, $u = T_e$, and $c = \frac{1}{J_m}$, then (2.71) will have a state-space form as below

$$\begin{cases} \dot{\chi} = A\chi + Bu + Dz \\ y = C\chi \end{cases} \tag{4.1}$$

where $A = 0$, $B = c$, $C = 1$, $D = -c$. According to Assumption 3.6.1, the total disturbance needs to be continuous and its high-order derivatives are bounded. In most recent research papers on disturbance observer design, this assumption is not considered. In contrast, those papers assume that the disturbance has slow dynamics [30–39, 41, 42, 44–48] or high-order derivatives of disturbance equals to zero [40, 51]. Assumption 3.6.1 requires only the high-order derivative terms of the disturbance to be upper-bounded, which in turn, is feasible in practical applications.

Assumption 4.2.1. *1) ω_m, i_q^r, and i_d^r are measurable; 2) T_{fr}, T_v, T_{flux}, T_L, ΔJ_m, and z are unknown.*

Remark 4.2.1. *Generally, in some latest studies on control of a PMSM [30–42, 44–48, 123–126], friction torque T_{fric} is assumed to be known, whilst torque generated due to viscosity friction T_{visc} and flux effect $T_{d\phi_m}$ are bypassed during the design of observers. Consequently, only the load torque is considered as a disturbance and be estimated. Unfortunately, those ignored or bypassed disturbance terms, i.e. T_{fric}, T_{visc}, and $T_{d\phi_m}$, are hard to avoid [127], and their effect might be severe. Thus, it is reasonable to consider T_{fric}, T_{visc}, $T_{d\phi_m}$, and T_L as unknown disturbance which can be estimated by the observer.*

Hence, the following model of the disturbance can be obtained by Assumption 3.6.1

$$\begin{cases} \dot{\psi} = \bar{S}\psi + \bar{M}z^{(n+1)} \\ z = \bar{N}\psi \end{cases} \tag{4.2}$$

where $\bar{S}$, $\bar{M}$, and $\bar{N}$ are the system matrices, ψ is a vector of disturbance and its high-order derivatives. These matrices are defined in the next structures

$$\begin{aligned} \bar{S} &= \begin{bmatrix} 0 & I_n \\ 0 & 0_{1\times n} \end{bmatrix} \\ \bar{M} &= \begin{bmatrix} 0_{n\times 1} \\ 1 \end{bmatrix} \\ \bar{N} &= \begin{bmatrix} 1 & 0_{n\times 1} \end{bmatrix} \\ \psi &= \begin{bmatrix} z & z^{(1)} & \dots & z^{(n)} \end{bmatrix} \end{aligned} \tag{4.3}$$

in which I_n are $n \times n$ identity matrices and $z^{(0)} = z$.

Using (4.1) and (4.2), the extended system can be designed

$$\begin{cases} \dot{\bar{\chi}} = \bar{\bar{A}}\bar{\chi} + \bar{\bar{B}}u + Mz^{(n+1)} \\ y = \bar{\bar{C}}\bar{\chi} \end{cases} \tag{4.4}$$

in which $\bar{\chi} = \begin{bmatrix} \psi & \chi \end{bmatrix}^T$, $\bar{\bar{A}} = \begin{bmatrix} \bar{S} & 0_{n\times 1} \\ D & 0_{1\times n} \end{bmatrix}$, $\bar{\bar{B}} = \begin{bmatrix} 0_{n\times 1} \\ B \end{bmatrix}$, $\bar{\bar{C}} = \begin{bmatrix} 0_{n\times 1} & C \end{bmatrix}$, $M = \begin{bmatrix} \bar{M} \\ 0 \end{bmatrix}$.

Based on the Kalman-Bucy optimal observer, the generalized high-order disturbance observer is proposed to estimate a total disturbance and its high-order derivatives

$$\dot{\hat{\bar{\chi}}} = \bar{\bar{A}}\hat{\bar{\chi}} + \bar{\bar{B}}u + \bar{L}(y - \bar{\bar{C}}\hat{\bar{\chi}}) \tag{4.5}$$

with $\bar{L} = \bar{P}\bar{\bar{C}}^T R_{obs}^{-1}$ as an observer optimal gain; $\bar{P}$ is a solution of the ARE

$$\bar{\bar{A}}\bar{P} + \bar{P}\bar{\bar{A}}^T - \bar{P}\bar{\bar{C}}^T R_{obs}^{-1}\bar{\bar{C}}\bar{P} + Q_{obs} = 0 \tag{4.6}$$

where $Q_{obs} \geq 0$ is a $(n+2) \times (n+2)$ symmetric matrix, $R_{obs} > 0$ is a scalar number.

The algorithms of tuning the gains of the GHDO is presented in [128]. Initially, Q_{obs} is selected as a diagonal matrix, where the responsible tuning gains are located on the diagonal, and the tuning algorithm is based on the level of a measurement noise of the system, i.e. in case of high measurement noise, the value of the diagonal elements Q_{obs} are set to be small and R_{obs} is set to be large. Whereas, in case of low measurement noise, Q_{obs} and R_{obs} are to be large/small, respectively.

The stability of the proposed observer is guaranteed by Theorem 3.6.1. In the next sections, the results of application of the GHDO with different orders n are provided.

4.2.1 Design of the GHDO: n = 0

This section presents the design of the GHDO for the case of $n = 0$. This particular case of the GHDO is based on the assumption that works for disturbances with bounded first-order time derivative. Hence, the most proposed disturbance observer in literature [30–39, 41, 42, 44–48] belong to this particular case of the GHDO. In this case, the system matrices presented in (4.4) will be

$$\begin{aligned} \bar{\bar{A}} &= \begin{bmatrix} 0 & 0 \\ -c & 0 \end{bmatrix} \\ \bar{\bar{B}} &= \begin{bmatrix} 0 & c \end{bmatrix}^T \\ \bar{\bar{C}} &= \begin{bmatrix} 0 & 1 \end{bmatrix} \\ \bar{\chi} &= \begin{bmatrix} z & \omega_m \end{bmatrix}^T \end{aligned} \tag{4.7}$$

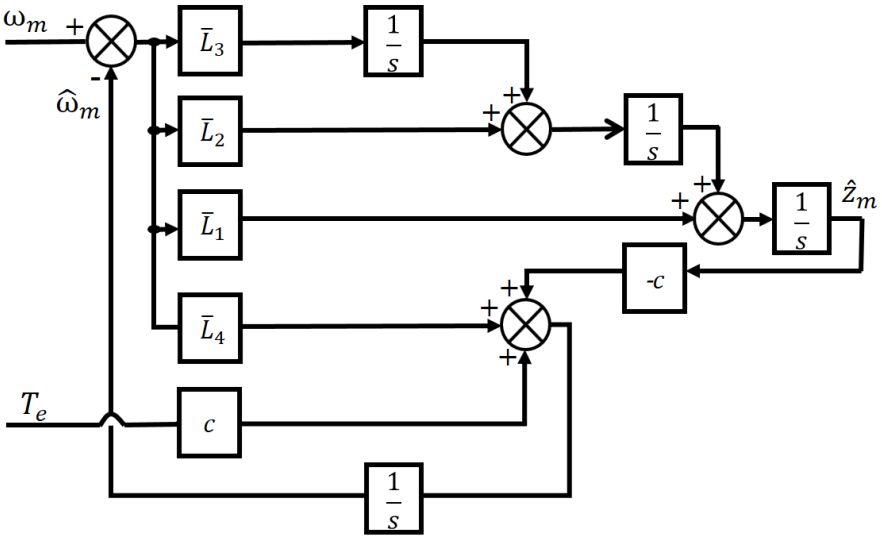

Figure 4.1: Schematic diagram of the proposed high-order disturbance observer when $n = 2$; $\bar{L} = \begin{bmatrix} \bar{L}_1 & \bar{L}_2 & \bar{L}_3 & \bar{L}_4 \end{bmatrix}^T$.

This kind of observer is sometimes called as a proportional-integral (PI) observer or PIO [129, 130].

4.2.2 Design of the GHDO: n = 1

The case $n = 1$ is based on the assumption that disturbance has bounded second-order time derivative. The observer has the matrices and vectors with the following structures

$$\begin{aligned} \bar{\bar{A}} &= \begin{bmatrix} 0 & 1 & 0 \\ 0 & 0 & 0 \\ -c & 0 & 0 \end{bmatrix} \\ \bar{\bar{B}} &= \begin{bmatrix} 0 & 0 & c \end{bmatrix}^T \\ \bar{\bar{C}} &= \begin{bmatrix} 0 & 0 & 1 \end{bmatrix} \\ \bar{\chi} &= \begin{bmatrix} z & z^{(1)} & \omega_m \end{bmatrix}^T \end{aligned} \tag{4.8}$$

4.2.3 Design of the GHDO: n = 2

Based on the literature review, this type of the high-order observer is not proposed in general form for PMSMs. Especially, the second-order observer ($n = 2$) is not designed for PMSMs so far. The matrices for the second-order observer are

$$\begin{aligned} \bar{\bar{A}} &= \begin{bmatrix} 0 & 1 & 0 & 0 \\ 0 & 0 & 1 & 0 \\ 0 & 0 & 0 & 0 \\ -c & 0 & 0 & 0 \end{bmatrix} \\ \bar{\bar{B}} &= \begin{bmatrix} 0 & 0 & 0 & c \end{bmatrix}^T \end{aligned}$$

$$\bar{\bar{C}} = \begin{bmatrix} 0 & 0 & 0 & 1 \end{bmatrix}$$
$$\bar{\chi} = \begin{bmatrix} z & z^{(1)} & z^{(2)} & \omega_m \end{bmatrix}^T \tag{4.9}$$

Despite that we propose the high-order observer to estimate the total disturbance, the observer's matrices $\bar{\bar{A}}$ and $\bar{\bar{C}}$ are spare matrices and, hence, the solution of the ARE (4.6) is obtained easily. This simplicity in design makes the proposed GHDO practical and applicable for the broad range of systems.

A schematic diagram of the SDO is shown in Figure 4.1.

4.3 Fuzzy-PI speed controller design

4.3.1 Problem formulation

This section presents an implementation of the fuzzy logic-based PI controller used to automatically tune the PI parameters to improve reference tracking ability of the speed loop particularly at the transient period of time. As inputs the fuzzy-PI speed controller takes the speed tracking error $\tilde{\omega}_m$ and time-derivative of the speed tracking error $\dot{\tilde{\omega}}_m$ and generates the reference q-axis current, $i_{q_{ref}}$, to the current controller. Note that the speed tracking is defined as

$$\tilde{\omega}_m = \omega_m - \omega_{m_{ref}} \tag{4.10}$$

Consequently, the rules of the fuzzy-PI speed controller stabilizing the speed loop based on the T-S inference model are obtained

Rule j for $C_{fuzzy-PI}$*:* IF $\tilde{\omega}_m$ $\hat{G}_j$ AND $\dot{\tilde{\omega}}_m$ is $\hat{M}_j$ THEN

$$C_{fuzzy-PI} = -k_{p_j}\tilde{\omega}_m - k_{i_j}\int_0^t \tilde{\omega}_m dt \tag{4.11}$$

where k_{p_j} and k_{i_j} are proportional and integral parameters of the PI controllers, respectively; $\hat{G}_j$ and $\hat{M}_j$ represent fuzzy sets based on which values of $\tilde{\omega}_m$ and $\dot{\tilde{\omega}}_m$ are determined; $j = 1, 2, 3$ defines number of the rules.

In this study, four different fuzzy sets are used, i.e. "ZE" for the speed tracking error, "ZDE", "PDE", and "NDE" for the time derivative of the speed tracking error. "ZE" stands for "zero speed tracking error", "ZDE", "PDE", and "NDE" stand for "zero change of the derivative of the speed tracking error", "positive change of the derivative of the speed tracking error", and "negative change of the derivative of the speed tracking error", accordingly. Hence, based on the defined sets the fuzzy rules for the speed loop control are defined as below

Rule 1:

IF $\tilde{\omega}_m$ is ZE AND $\dot{\tilde{\omega}}_m$ is PDE THEN

$$C_{fuzzy-PI} = -k_{p_1}\tilde{\omega}_m - k_{i_1}\int_0^t \tilde{\omega}_m dt \tag{4.12}$$

Rule 2:

$$\text{IF } \tilde{\omega}_m \text{ is ZE AND } \dot{\tilde{\omega}}_m \text{ is NDE THEN}$$
$$C_{fuzzy-PI} = -k_{p_2}\tilde{\omega}_m - k_{i_2}\int_0^t \tilde{\omega}_m dt \tag{4.13}$$

Rule 3:

$$\text{IF } \tilde{\omega}_m \text{ is ZE AND } \dot{\tilde{\omega}}_m \text{ is ZDE THEN}$$
$$C_{fuzzy-PI} = -k_{p_3}\tilde{\omega}_m - k_{i_3}\int_0^t \tilde{\omega}_m dt \tag{4.14}$$

The general fuzzy-PI speed controller can be written as a

$$C_{fuzzy-PI} = \sum_{j=1}^{3} \rho_j \left(\tilde{\omega}_m, \dot{\tilde{\omega}}_m\right)\left(k_{p_j}\tilde{\omega}_m + k_{i_j}\int_0^t \tilde{\omega}_m dt\right) \tag{4.15}$$

where $\rho_j = \frac{\nu_j(\tilde{\omega}_m, \dot{\tilde{\omega}}_m)}{\sum_{i=1}^{3}\nu_i(\tilde{\omega}_m, \dot{\tilde{\omega}}_m)}$ represents a normalized weight of each rules shown in (4.12)-(4.14). Sigmoid type membership functions ν_j for each fuzzy rule with the following forms are selected in this work

$$\nu_j = e^{-\bar{a}_j\tilde{\omega}_m^2 - \bar{b}_j(\dot{\tilde{\omega}}_m - \Gamma)^2} \tag{4.16}$$

where $\bar{a}_j > 0$, $\bar{b}_j > 0$ $(j = 1, 2, 3)$, and $\Gamma > 0$ are constant parameters specific for each membership function. The sigmoid type membership functions are chosen as effective and convenient functions since the fuzzy sets represent some fuzzy values in open intervals defined based on $\tilde{\omega}_m$ and $\dot{\tilde{\omega}}_m$ [131]. The parameters of the membership functions are chosen empirically to get effectively working fuzzy rules.

Remark 4.3.1. *The fuzzy-PI speed controller in (4.15) generates a torque equivalent to the difference between the electromagnetic torque T_e and lumped disturbance z_m in (2.71). To eliminate the effect of the lumped disturbance, the outputs of the proposed high-order observer and the fuzzy-PI speed controller are summed up, which is resulted in a reference torque $T_{m_{ref}} = C_{fuzzy-PI} + \hat{z}_m$.*

Further, the reference q-axis current is obtained via the relationship

$$i_{q_{ref}}^r = \frac{1}{K_T}(C_{fuzzy-PI} + \hat{z}_m) \tag{4.17}$$

4.4 Stability analysis of the HDOBCC scheme

The dynamic of the speed tracking error can be derived in the form

$$\dot{\tilde{\omega}}_m = \kappa i_q^r - (\eta_e + D_v)\omega_m - (\eta_{hys} + \eta_{fr})sign(\omega_m) - \bar{k}z_m^{'} \tag{4.18}$$

where $\kappa = K_T\bar{k}$, $\bar{k} = \frac{1}{J_{m_0}}$, $z_m^{'} = z_m - \frac{(\eta_e + D_v)}{\bar{k}}\omega_m - \frac{(\eta_{hys}+\eta_{fr})}{\bar{k}}sign(\omega_m)$. Note that $(\eta_e + D_v)\omega_m$ and $(\eta_{hys} + \eta_{fr})sign(\omega_m)$ represent T_v and T_{fr}, respectively, in (2.40).

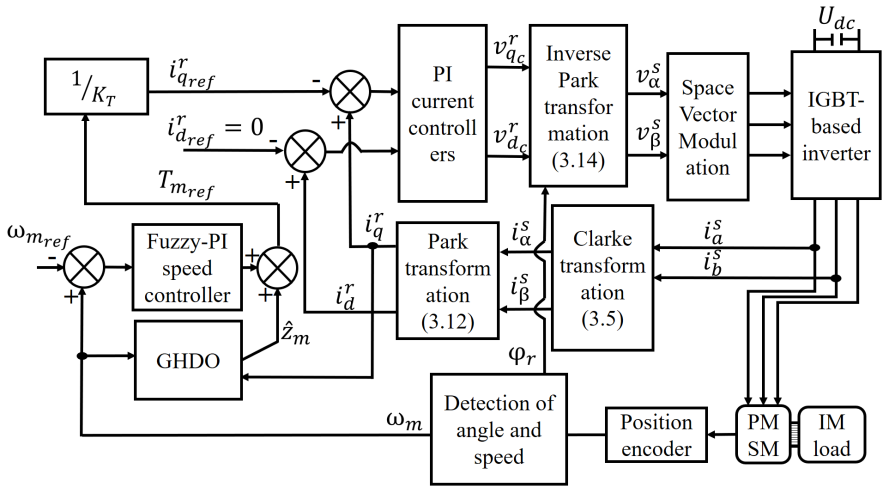

Figure 4.2: PMSM control system with the HDOBCC

Theorem 4.4.1. *From [132], the speed tracking error in* (4.18) *asymptotically goes to zero.*

To consider a stability of the closed-loop system, let us introduce an estimation error in the form

$$e_{est} = z_m^{'} - \hat{z}_m^{'} \tag{4.19}$$

Observing that $z_m^{'} - \hat{z}_m^{'} = z_m - \hat{z}_m$ gives the modified speed tracking dynamic equation in (4.18) as

$$\dot{\tilde{\omega}}_m = \kappa i_q^r - (\eta_e + D_v)\omega_m - (\eta_{hys} + \eta_{fr})sign(\omega_m) - \bar{k}\hat{z}_m^{'} - \bar{k}e_{est} \tag{4.20}$$

Next, we use the following lemma to prove the stability of the closed-loop system.

Lemma 4.4.1. *Consider a system having the form [133]*

$$\begin{cases} \dot{\zeta} = f\left(\zeta, \bar{\bar{y}}\right) \\ \dot{\bar{\bar{y}}} = \bar{r}\left(\bar{\bar{y}}\right) \end{cases} \tag{4.21}$$

in which $\dot{\bar{\bar{y}}} = \bar{r}\left(\bar{y}\right)$ *is stable at* $\bar{\bar{y}} = 0$. *If* $\dot{\zeta} = f\left(\zeta, 0\right)$ *is stable at* $\zeta = 0$, *then the system in* (4.21) *is stable at* $\left(\zeta, \bar{\bar{y}}\right) = (0, 0)$.

Theorem 4.4.2. *Speed tracking error* $\tilde{\omega}_m$ *and observer's estimation error* e_{est} *converge to zero under the proposed HDOBCC scheme.*

Proof: From Theorem 4.4.1, speed tracking error $\tilde{\omega}_m$ given in (4.18) is stable at zero. By referring to Theorem 3.6.1, the observer's estimation error e_{est} in (4.19) is also stabilizable at zero. Then, using Lemma 4.4.1, it is shown that $\tilde{\omega}_m$ and e_{est} are stabilized at zero.

Figure 4.2 depicts the overall diagram of the proposed control scheme.

Table 4.1: Parameters of the observers

Observers	**Tuning matrices Q_{obs}, R_{obs}, and observer's gain $\bar{L}$**
ZDO	$Q_{obs} = \begin{bmatrix} 1 & 0 \\ 0 & 10^6 \end{bmatrix}$, $R_{obs} = 400$, $\bar{L} = \begin{bmatrix} -0.0500 \\ 51.1978 \end{bmatrix}$
FDO	$Q_{obs} = \begin{bmatrix} 1 & 0 & 0 \\ 0 & 1.9 \times 10^8 & 0 \\ 0 & 0 & 1 \times 10^6 \end{bmatrix}$, $R_{obs} = 400$, $\bar{L} = \begin{bmatrix} -14.9645 \\ -689.2024 \\ 196.9204 \end{bmatrix}$
SDO	$Q_{obs} = \begin{bmatrix} 1 & 0 & 0 & 0 \\ 0 & 1.9 \times 10^8 & 0 & 0 \\ 0 & 0 & 7 \times 10^9 & 0 \\ 0 & 0 & 0 & 1 \times 10^6 \end{bmatrix}$, $R_{obs} = 400$, $\bar{L} = \begin{bmatrix} -15.9000 \\ -780.0000 \\ -4.1833 \\ 202.9000 \end{bmatrix}$

4.5 Experimental results

In the first study, comparative experimental validations among the different orders of the proposed GHDO as well as the standard ESO are conducted on the test stand presented in Section 2.8. The traditional PI controller is used as a stabilizing controller together with the GHDO and ESO in the first study. Further, the proposed control scheme consisting of the fuzzy-PI speed controller and the proposed GHDO is compared with the control scheme consisting of the traditional PI controller and the proposed GHDO. To test the performance of each control scheme, we use the load torque command with the shapes shown in Figure 4.3. In Figure 4.3(a) a triangular shape load torque represents Scenario 1, a rectangular form load torque in Figure 4.3(b) is considered as Scenario 2, and, finally, a sinusoidal shape load torque in Figure 4.3(c) is applied in Scenario 3. In Scenario 1 and 2, the load torque maximum value is 0.8 $N \cdot m$, whereas in Scenario 3, the maximum value of the torque is equal to the rated torque value. In the all experiments, the commanded mechanical speed of the motor is set as 2000 rpm.

4.5.1 First study: comparing different orders of the GHDO and ESO

In this stage, we construct a ZDO and obtain the optimal gains for this observer to reach satisfactory performance. Next, we increase the order observer by one to construct a FDO. Further, the ZDO and FDO are compared under the same conditions to reveal the best one. From the obtained results, the case with FDO shows better outcomes comparing to the ZDO. Hence, we design the SDO by increasing the order of the FDO by one. After tuning the gains of the SDO to optimal ones and comparing with the FDO, it shows that the newly designed SDO has performance similar to the FDO. Finally, we stop increasing the order of the observer at this point. The obtained gains and parameters of the designed observers are given in Table 4.1. Under the same conditions, we implemented the standard ESO [41, 42] in order to compare with the proposed observer. As mentioned previously, in all cases, the PI controller is responsible for the

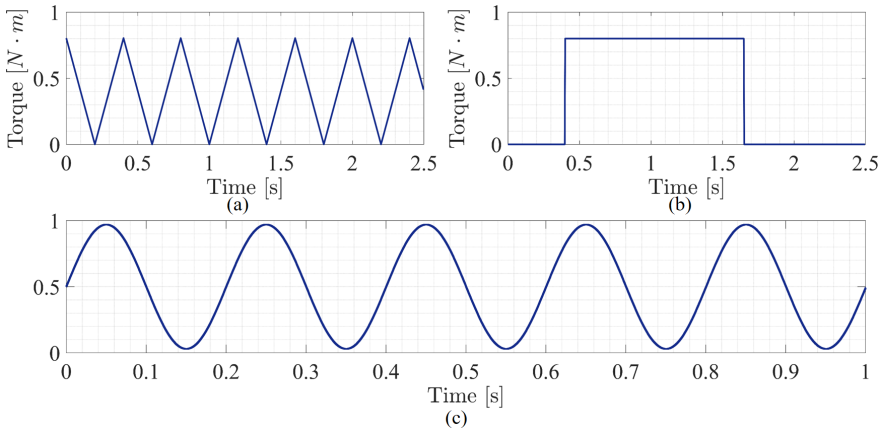

Figure 4.3: Forms of the load torque used in the tests: (a) Triangular load torque of 0.8 $N{\cdot}m$ - Scenario 1. (b) Rectangular load torque of 0.8 $N{\cdot}m$ - Scenario 2. (c) Sinusoidal load torque of 0.97 $N{\cdot}m$ - Scenario 3.

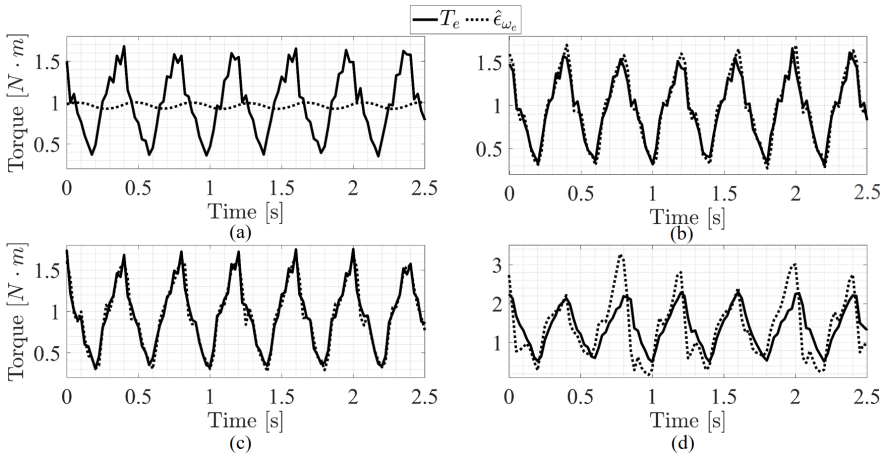

Figure 4.4: Comparison of estimation performance of each observer scheme in Scenario 1: (a) ZDO. (b) FDO. (c) SDO. (d) ESO.

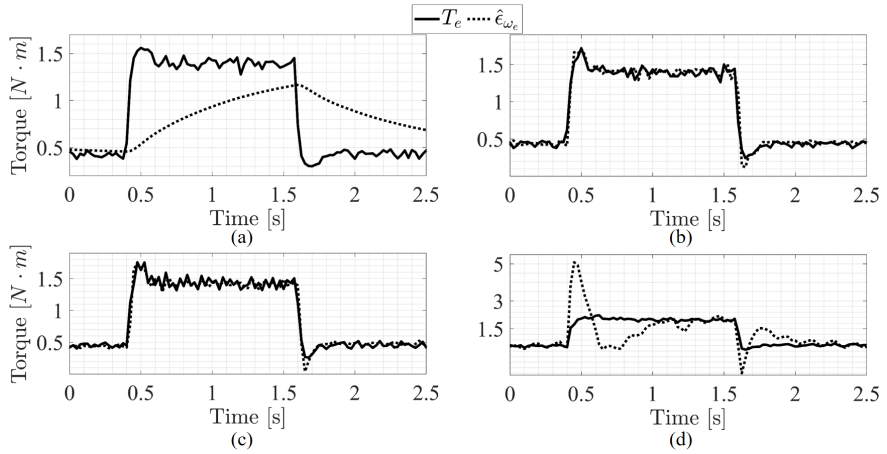

Figure 4.5: Comparison of estimation performance of each observer scheme in Scenario 2: (a) ZDO. (b) FDO. (c) SDO. (d) ESO.

stabilization of the system after compensation of disturbance. The parameters of the PI controller are obtained based on the approach described in [134].

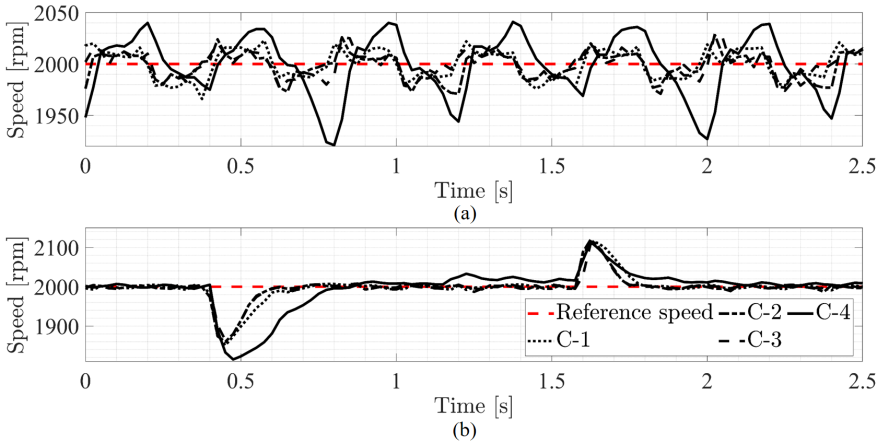

Figure 4.6: Speed response of each control scheme in Scenario 1 and 2: (a) Scenario 1. (b) Scenario 2. (where C-1 - ZDO-based PI speed controller, C-2 - FDO-based PI speed controller, C-3 - SDO-based PI speed controller, C-4 - ESO-based PI speed controller.)

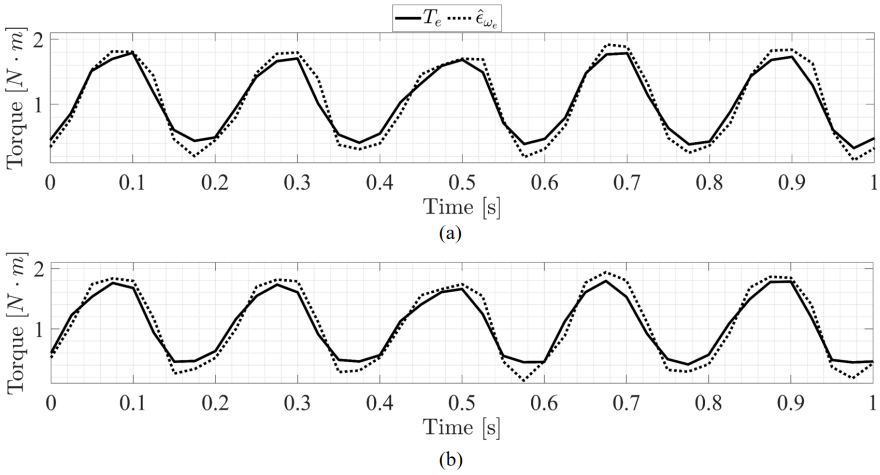

Figure 4.7: Comparison of estimation performance of each observer scheme in Scenario 3: (a) FDO-based PI speed controller. (b) SDO-based PI speed controller.

Table 4.2: Comparative results of the observers under Scenario 1

Performance index	**ZDO**	**FDO**	**SDO**	**ESO**
IAE for e_{est}	0.8252	0.1841	0.1847	1.0138
IAE for $\tilde{\omega}_m$	31.9000	27.7125	26.5625	59.0000
ITAE for e_{est}	1.0395	0.2370	0.2238	1.3323
ITAE for $\tilde{\omega}_m$	38.7231	36.4081	32.8081	75.8237

Table 4.3: Comparative results of the observers under Scenario 2

Performance index	**ZDO**	**FDO**	**SDO**	**ESO**
IAE for e_{est}	1.0468	0.1121	0.1436	1.1883
IAE for $\tilde{\omega}_m$	39.2250	32.9625	29.1500	70.7875
ITAE for e_{est}	1.3448	0.1355	0.1684	1.1711
ITAE for $\tilde{\omega}_m$	40.8994	35.1375	29.4744	71.3894

The graphs of the performance of four observers under the test in estimating of the lumped disturbance as well as their effect in the speed response of the closed-loop

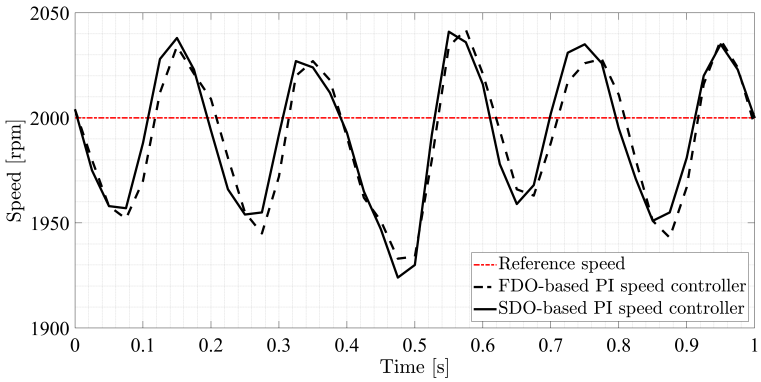

Figure 4.8: Comparison of speed response of the FDO-based PI speed controller and SDO-based PI speed controller.

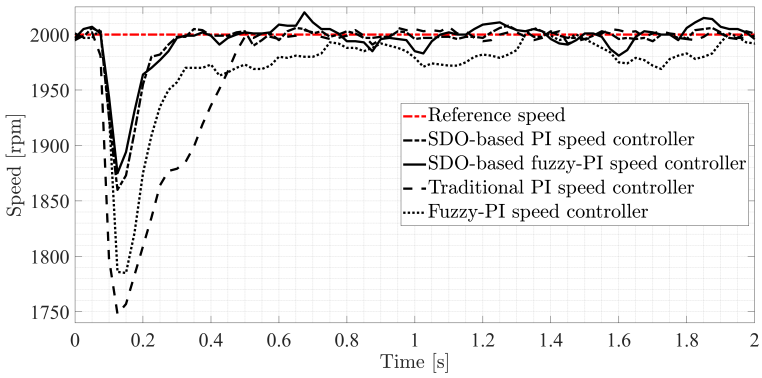

Figure 4.9: Effect of the SDO in improving the tracking performance of the traditional PI speed controller and fuzzy-PI speed controller.

system in Scenario 1 are illustrated in Figure 4.4. Since, in the steady-state, the observer estimation should converge to the electromagnetic torque, in the experiments, we set the electromagnetic torque as a reference to disturbance estimation. Hence, theoretically, the best estimation occurs when the estimated disturbance maximally follows the reference electromagnetic torque at both the transient as well as steady-state regions. In the plots, the electromagnetic torque is shown with the solid black line, while the estimated disturbance is presented with the dashed black line. The FDO and SDO show similar estimation performance and both are better comparing to the ZDO and ESO. In order to represent more detailed comparison of observers and related observer-based closed systems, we show the results in terms of the performance indices such as an integral of absolute error (IAE) and integral time absolute error (ITAE). The quantitative analysis are listed in Table 4.2. According to the results in Table 4.2, the worst performance is achieved when the ESO is utilized, whereas both the FDO and SDO are better than the ZDO in terms of estimation and reference speed tracking performance. The superiority of the FDO and SDO over the ZDO and ESO can be explained by the fact that the latter two observers are based on the conventional assumption and do not consider high-order dynamics of the disturbance during design. It is observed that the SDO (IAE: 0.1847,

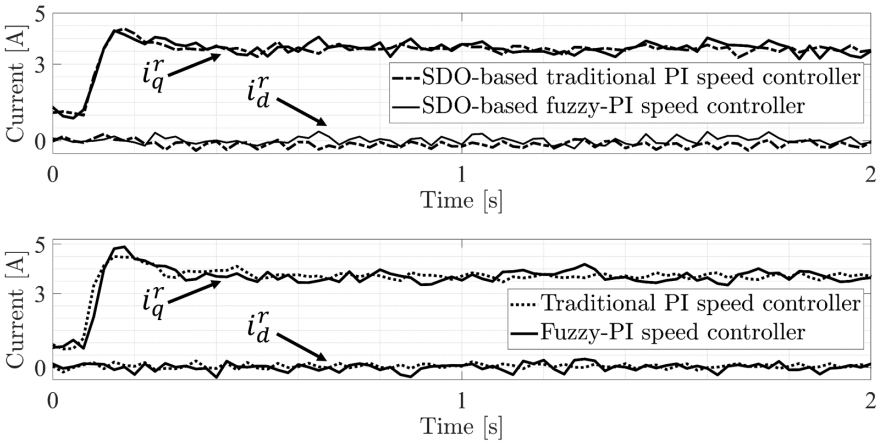

Figure 4.10: Effect of the SDO on the current performance of the traditional PI speed controller and fuzzy-PI speed controller.

Table 4.4: Comparative results of the FDO and SDO under Scenario 3

Performance index	**FDO**	**SDO**
IAE for e_{est}	0.1265	0.1521
IAE for $\tilde{\omega}_m$	29.6250	29.2750
ITAE for e_{est}	0.0652	0.0774
ITAE for $\tilde{\omega}_m$	14.7556	14.4837

ITAE: 0.2238) with similar estimation performance to the FDO (IAE: 0.1841, ITAE: 0.2370) can work better than the FDO in the closed-loop speed control system. From these results, the SDO is considered as the best choice among other observers under Scenario 1.

The results for Scenario 2 are shown in Figure 4.5 and the performance index data are depicted in Table 4.3. Rectangular shape load torque helps to test how quick a system can response to sudden load changes. From Scenario 2, it is observed that the FDO and SDO are faster and more accurate comparing to the ZDO and ESO. Especially, the FDO and SDO give precies estimation during the transient regions of the load changes, i.e. when the load suddenly increases and decreases, while the ZDO responses slowly with significant estimation error at transient time. The ESO reacts faster than the FDO, but it generates overshoots and undershoots during the load changes. Although the FDO (IAE: 0.1121, ITAE: 0.1355) slightly outperforms the SDO (IAE: 0.1436, ITAE: 0.1684) in terms of estimation accuracy, the SDO-based closed-loop speed control reveals the better performance (IAE: 29.15, ITAE: 29.47) indices in contradistinction to the FDO-based closed-loop speed control (IAE: 32.9625, ITAE: 35.1375). The phenomenon can be explained by faster dynamics of the SDO comparing to the FDO.

From Scenario 1 and 2, it is confirmed that the ZDO and ESO inferior to the FDO and SDO in terms of disturbance estimation and response time, whereas the latter two observers might have similar performance indices. To investigate further difference between the FDO and SDO, in Scenario 3, the observers are tested under the sinusoidal

Table 4.5: Gains of the traditional PI and fuzzy-PI speed controllers

Controllers	Parameters
Traditional PI speed controller	$k_p = 0.1$, $k_i = 2$
Fuzzy-PI speed controller	$k_{p_1} = 5$, $k_{i_1} = 100$, $k_{p_2} = 0.1$, $k_{i_2} = 2$, $k_{p_3} = 3$, $k_{i_3} = 3$

Table 4.6: Parameters of the membership functions in the fuzzy-PI speed controller

Membership functions	Parameters
ν_1	$\bar{a}_1 = 10^{-3}$, $\bar{b}_1 = 10^{-8}$, $\Gamma = 50$
ν_2	$\bar{a}_2 = 10^{-6}$, $\bar{b}_2 = 5\times10^{-8}$, $\Gamma = 50$
ν_3	$\bar{a}_3 = 10^{-3}$, $\bar{b}_3 = 10^{-6}$, $\Gamma = 50$

Table 4.7: Comparative tracking performance of the SDO-based traditional PI speed controller and SDO-based fuzzy-PI speed controller

Performance index	SDO-based traditional PI speed controller	SDO-based fuzzy-PI speed controller
IAE	14.0875	12.5875
ITAE	3.3350	3.0056
Mean error	20.92	18.80

load torque application (Figure 4.7 and Figure 4.8). From Table 4.4, the comparative results indicate that the FDO (IAE: 0.1265, ITAE: 0.0652) has more or less better estimation than the SDO (IAE: 0.1521, ITAE: 0.0774), and no significant difference is observed in the speed tracking of the FDO (IAE: 29.6250, ITAE: 14.7556) and SDO (IAE: 29.2750, ITAE: 14.4837) case. This fact can be justified by slower dynamics of the sinusoidal load torque comparing the load forms in Scenario 1 and 2.

4.5.2 Second study: comparison of the SDO-based traditional PI speed controller and SDO-based fuzzy-PI speed controller

In the second study, the composite controller consisting of the traditional PI controller and the SDO is compared to the composite controller consisting of the fuzzy-PI speed controller and the SDO. Here the SDO is chosen as a main proposed observer, since its results comparing to the FDO are better in terms of the speed tracking performance according to scenarios 1, 2, and 3 in the first study. The obtained parameters of the two control schemes are listed in Table 4.5. The parameters of the fuzzy-PI speed controller are given in Table 4.6. Figure 4.9 depicts speed response and i_d^r and i_q^r dynamics when an a sudden load torque of 0.8 $N \cdot m$ is applied at constant speed of 2000 rpm. To show how the observer can improve the speed response, Figure 4.9 also shows the speed response of the traditional PI speed controller and fuzzy-PI speed controller without observers. It is clear that the SDO-based composite control with either the traditional

PI speed controller or fuzzy-PI speed controller is better than the those standard control schemes in terms of the speed tracking. However, between the SDO-based traditional PI speed controller and the SDO-based fuzzy-PI speed controller, the latter one has better dynamics with reduced reference tracking error. According to Table 4.7, the improvement of the speed tracking in the SDO-based fuzzy-PI speed controller is about 11% by the IAE, whereas there is 9.9% enhancement in terms of the ITAE. The mean error is reduced by 2.12 rpm, which is 10% improvement comparing to the SDO-based traditional PI speed controller results.

4.6 Summary

A novel composite speed controller named as high-order disturbance observer-based composite controller (HDOBCC) is proposed for the SPMSM. The HDOBCC consists of the Takagi-Sugeno inference-based fuzzy controller and the generalized high-order disturbance observer (GHDOBC). The Takagi-Sugeno inference-based fuzzy controller is designed to achieve an asymptotic convergence of the speed tracking error to zero. The GHDOBC is proposed to estimate and recoup the lumped disturbance in the speed loop to enhance the robustness of the system to disturbance effect. The detailed stability analysis of the closed-loop system with the HDOBCC is provided. The rules of the fuzzy-PI speed controller are selected based on the speed tracking error and its change of the rate. Based on this, the fuzzy sets are obtained, where each fuzzy set determines whether the speed error or its rate of change is zero, positive, or negative. Using the combinations of the fuzzy sets, the PI speed controllers are constructed, accordingly. Since, the selected fuzzy sets are represented as open intervals, it is decided to define sigmoid type membership functions as effective ones. The GHDO design is based on the relaxing of the conventional assumption used to design in most recent disturbance observers. Unlike the conventional disturbance observers, where only disturbances with slow dynamics are considered, this proposed GHODO is able to estimate the disturbances with order higher than one, i.e. with fast dynamics. The experimental results present that the GHODO has advantages over the conventional observers and ESO in terms of estimation and simple practical implementation.

Chapter 5

Disturbance rejection (DR) control for SPMSM

5.1 Introduction

In this chapter, a novel speed control called disturbance rejection PI (DR-PI) scheme is presented for the SPMSM. Accurate disturbance attenuation of the PI speed control scheme augmented with a pre-filter and presenting of practicable method for tuning parameters of the PI speed control scheme based on the modified DOBC scheme are the main purpose of the current work. In contrast to the conventional DOBC scheme, in which a disturbance observer and PI controller are designed separately, in the proposed DR-PI scheme observer and controller are combined into the one compact structure. In addition, in the proposed design, an overshoot issue commonly existing in a traditional PI scheme is resolved by the augmented pre-filter design in the DR-PI scheme. The experimental outcomes show the proposed DR-PI scheme is not only more feasible than the traditional DOBC scheme, but it also guarantees satisfactory performance during the transient period.

Based on the detailed analysis, the following contributions are made: (1) Since in a traditional PI control scheme there is a lack of obvious relationship between system response and controller parameters, most recent researches use a plant model to find a PI control parameters. The Ziegler-Nichols (ZN) method as one of the popular tuning methods is used for calculation of PI parameters. Unfortunately, the ZN approach is based on the experience and knowledge of the control engineer, and sometimes PI controller tuned by the ZN method may result in unsatisfactory results. Moreover, with the ZN method it could be hard to set up stability conditions. Due to those reasons, it is affirmed in [60] that only information about an order of a plant is enough to design a controller with disturbance attenuation mechanism under the framework of the modified DOBC scheme. Consequently, this chapter presents a design of a PI controller with a pre-filter in which an explicit connection between the PI control parameters and the process is shown in terms of the parameters of a filtering element and desired closed-loop model; (2) With the proposed DR-PI scheme a tuning procedure becomes simple. Analysis on a stability and tuning gains are very straightforward due to the explicit design of the DR-PI; (3) Unlike in the traditional DOBC scheme, the proposed

DR-PI design does not require information about nominal plant model, i.e. this method introduces a desired closed-loop model of a system in order to avoid a need for nominal system parameters; (4) In the end, introduction of the pre-filter block during the DR-PI design helps to resolve an overshoot issue which is frequent in a traditional PI adjusted by the ZN method or other different methods.

5.2 Design of DR-PI scheme for SPMSMs

5.2.1 Derivation of the PI-like structure

Remark 5.2.1. *Many industrial systems are minimum phase (MP) systems with low order. Therefore, numerous researches have been proposed for such type of systems [60]. In this work, it is assumed that the current control loops are tuned properly, and the task is to propose a simple and practical speed control scheme with disturbance attenuation mechanism.*

Remark 5.2.2. *Note that most of the studies consider T_{fr} as known, hence the dynamic equation of the rotor's shaft becomes a first order system. However, we consider T_{fr} to be unknown according to Assumption 4.2.1, therefore the transfer function of the speed loop is represented in an integrator form.*

From (2.71), it is seen that we have a first order transfer function in the speed loop. The obtained transfer function has no zeros on the RHP and has a pole with real and imaginary parts both equal to zero. Hence, we consider a case when no zeros on the RHP and set m = 1, p = 1 to define a DR-PI controller in (3.30) as $\bar{C}_{DR-PI} = \frac{\rho_1}{\lambda_0\bar{\tau}} + \frac{\lambda_1}{\rho_0\bar{\tau}\bar{\alpha}s}$ with $\bar{k}_c = \frac{\rho_1}{\lambda_0\bar{\alpha}}$. Then the DR-PI controller can be written in a PI-like structure as

$$\bar{C}_{DR-PI} = K_p^{dr-pi}(1 + \frac{1}{\bar{\alpha}s}) \tag{5.1}$$

where $K_p^{dr-pi} = \frac{\rho_1}{\lambda_0\bar{\tau}}$ or $K_p^{dr-pi} = \frac{\bar{k}_c\bar{\alpha}}{\bar{\tau}}$, K_p^{dr-pi} is a proportional gain of the newly defined PI controller. The proportional gain and integal time constant of the newly defined controller are written in terms of the parameters of the compensator, time constant of the desired model, and time constant of the filtering element, i.e. $\bar{k}_c$, $\bar{\alpha}$, and $\bar{\tau}$, respectively. Although the proposed DR-PI has a simple PI-like structure, it implicitly includes functionality of the proposed desired model, filtering element, and compensator. This implicit interconnection of $\bar{W}_r(s)$, $Q_{DOB}(s)$, and $\bar{K}(s)$ leads to easy and systematic parameter tuning of the newly defined DR-PI controller.

Remark 5.2.3. *Although the proposed DR-PI design is based on the modified DOBC scheme, it does not estimate the disturbance term explicitly as in the most DOBC approaches [33, 34, 62, 67, 68, 135, 136]. It means that the DR-PI does not focus on the estimation of disturbance, but it mainly focuses on the controller tuning together*

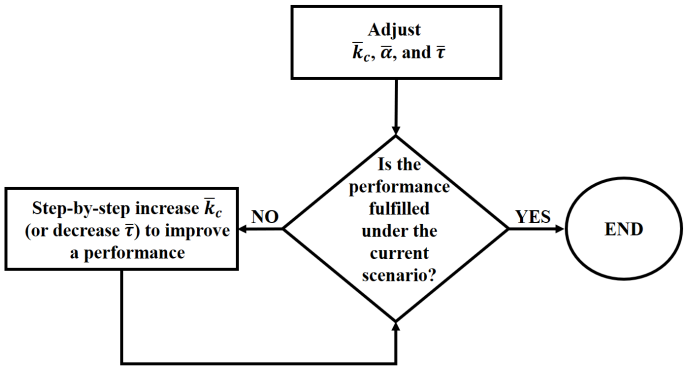

Figure 5.1: Flowchart of tuning the parameters of the DR-PI.

with disturbance rejection mechanism. Hence, the DR-PI is a controller, which designed as an implicit combination of disturbance observer and controller.

Remark 5.2.4. *Actually, the pre-filter block in the DR-PI is an important part that makes this control scheme different than other ones. As it shown, the pre-filter is derived during the design of the DR-PI itself, and its structure is determined in terms of the desired model transfer function and transfer function of the filtering element. The pre-filter helps to get faster speed response [137]. Successful application of a pre-filter can be seen in studies of [84, 138–140].*

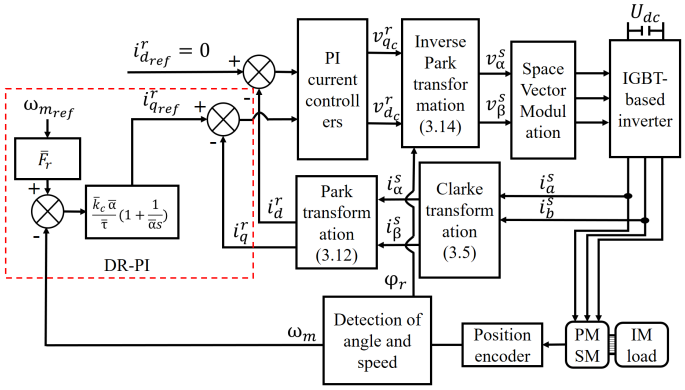

Figure 5.2: SPMSM control system with the proposed DR-PI scheme.

5.2.2 Mechanism of tuning the gains

As obtained so far, the DR-PI designed to control a system given in (2.71) has a simple PI-structure with the gains depending on the parameters of the desired model, filtering element, and compensator. Furthermore, the pre-filter is derived as a main part of the PI-like DR-PI controller. This section discusses about a mechanism of the tuning the parameters of the DR-PI.

Table 5.1: Controller parameters.

Parameter	traditional PI	DOBC	DR-PI
Proportional gain, $\bar{K}_p$	0.0045	0.0020	0.0495
Integral time constant, $\bar{T}_i$	0.3000	0.0500	0.1500
Compensator gain, $\bar{k}_c$	-	-	0.022
Time constant, $\bar{\tau}$	-	-	0.0667
Time constant, $\bar{\alpha}$	-	-	0.15

5.2.2.1 Comments on the selection the tuning parameters within the stability concern

Having the pre-filter after the reference command, the proposed DR-PI has a general PI-like structure as given in (5.1). Furthermore, it is shown that the traditional ADRC structure can be derived as a general PID controller for second-order systems [60]. This observation leads to a question on how the gains of PI(PID) can be effectively tuned to cope with disturbances.

5.2.2.2 Gain tuning in terms of stability issues

A characteristic equation of the closed-loop system with (5.1) is derived as

$$(\bar{\alpha}s + \bar{\beta})(s^2 + \frac{\bar{k}_c\bar{\alpha}}{J_m\bar{\tau}}s + \frac{\bar{k}_c}{J_m\bar{\tau}}) = 0 \tag{5.2}$$

From (5.2), one can observe that: 1) Poles of (5.2) are on the LHP, since the parameters are always positive, hence the closed-loop system is always stable; 2) A stability margin of the closed-loop system can be increased once $\frac{\bar{k}_c\bar{\alpha}}{J_m\bar{\tau}}$ is selected as high as possible, i.e. in that case, poles of (5.2) are located on the LHP and as far as possible from the origin.

5.2.2.3 Gain tuning in terms of parameters of $\bar{W}_r$ and Q_{DOB}

1) As known, the performance of the filtering element can be improved if $\bar{\tau}$ is chosen as small as possible, however, too small $\bar{\tau}$ may negatively affect to the stability of the closed-loop system; 2) Since the inverse of the parameter $\bar{\alpha}$ determines a bandwidth of the desired model, it is responsible for time response of the closed-loop system; 3) To totally eliminate overshoot, the parameter $\bar{\beta}$ is selected as 1.

Finally, the stability of the closed-loop system with the DR-PI can be easily verified, since it has a PI-like structure with the pre-filter. A general flowchart showing the tuning process of the DR-PI is presented in Figure 5.1. A closed-system with the DR-PI is illustrated in Figure 5.2. The closed-loop system of the SPMSM includes the DR-PI controller showing in the dashed region, which generates the reference for the i_q^r-current PI controller. To approach the MTPA strategy, i_d^r is maintained at zero by another PI current controller. An electrical angle and mechanical speed are obtained based on

the encoder device. Other control system blocks include the Clark transformation to transform the $d-q$ components into the $\alpha-\beta$ components, and the Park transformation to transform the $\alpha-\beta$ components into the $d-q$ components.

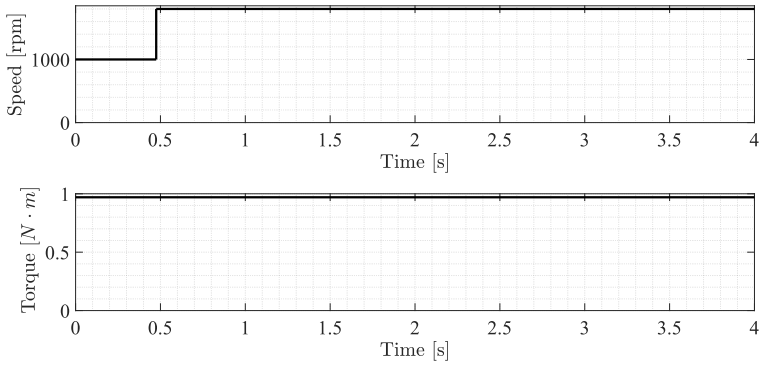

Figure 5.3: Scenario 1: a step-change of the reference speed from 1000 rpm to 1800 rpm under the rated torque.

5.3 Experimental results

5.3.1 Simulations and Experiments

Two scenarios commonly occurring in practice as shown in Figure 5.3 and 5.4 are validated in the studies. Figure 5.3 represents Scenario 1, where a speed of the motor operating under the rated torque (0.97 $N \cdot m$) steps up from 1000 rpm to 1850 rpm, and Figure 5.4 shows Scenario 2, where a sudden change of the load from 0 $N \cdot m$ to 0.97 $N \cdot m$ occurs during the operation of the motor at a constant speed of 1800 rpm.

Simulation results of the SPMSM control system with the proposed DR-PI for different $\bar{K}_p$ under Scenario 2 is shown in Figure 5.5. In this simulation study, the DR-PI with the gain obtained using the proposed scheme is compared to the DR-PI with the gains obtained via the trial-and-error. So, the calculated gain with the proposed scheme is $\bar{K}_p = 0.0495$, whereas the trial-and-error gains are selected as $\bar{K}_p = 0.01$, $\bar{K}_p = 0.02$, and $\bar{K}_p = 0.04$. Note that the time constant of the desired model $\bar{\alpha}$ is kept constant as given in Table 5.1. As shown in Figure 5.5, with increasing of $\bar{K}_p$ the performance of the speed response increases as well, the DR-PI with $\bar{K}_p = 0.01$ becomes the worst one with large speed drop and overshoot. Furthermore, its response time to disturbance effect is also the worst. Once $\bar{K}_p$ is increased to 0.02, the overshoot is eliminated and the speed drop is significantly decreased. For $\bar{K}_p = 0.04$, the control system performance is greatly improved comparing to the previous two values of $\bar{K}_p$. Among the tested values of $\bar{K}_p$, a value of 0.0495 reveals the best performance. Note that the value of 0.0495 is calculated based on the parameters of $Q_{DOB}(s)$, $\bar{W}_r$(s), and $\bar{C}_{comp}(s)$, hence its calculation has practical meaning. The superiority of the DR-PI

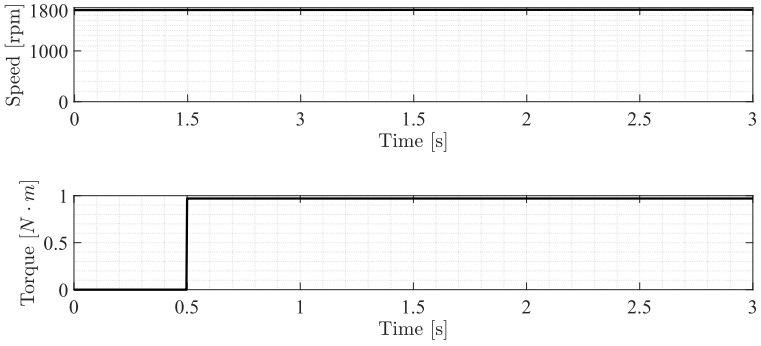

Figure 5.4: Scenario 2: step-change of the load torque from zero to rated value at a constant speed of 1800 rpm.

Table 5.2: Performance of DR-PI with different $\bar{K}_p$ and constant $\bar{T}_i$ = 0.15 in simulations.

	$\bar{K}_p = 0.01$	$\bar{K}_p = 0.02$	$\bar{K}_p = 0.04$	$\bar{K}_p = 0.0495$
Speed overshoot, %	0.5	-	-	-
Speed drop, %	8.8	5.2	3	2.5

Table 5.3: Performance of DR-PI with different $\bar{K}_p$ and constant $\bar{T}_i$ = 0.15 in experiments.

	$\bar{K}_p = 0.01$	$\bar{K}_p = 0.02$	$\bar{K}_p = 0.04$	$\bar{K}_p = 0.0495$
Speed overshoot, %	-	-	-	-
Speed drop, %	18	10	6.7	5.78

with $\bar{K}_p$ = 0.0495 is shown from the current response depicted in Figure 5.6. The controller with $\bar{K}_p$ = 0.0495 has faster i_q^r dynamics and more stable i_d^r dynamics during the transient time, i.e. when the load torque changes suddenly. The same trend as in the simulation results can be observed in the experimental outcomes presented in Figs. 5.7-5.8. But in the experiments, the speed tracking performance of each case has additional ripples at steady state comparing to the simulations. Table 5.3 shows that no overshoots occur in the experiments and the speed drop values for each controller gain has been increased for almost double times comparing to the data in Table 5.2. These differences in the results can be explained by the fact that simulation studies does not include any measurement noises and nonlinearities which may arise during the operation of power electronics components of the VSD system.

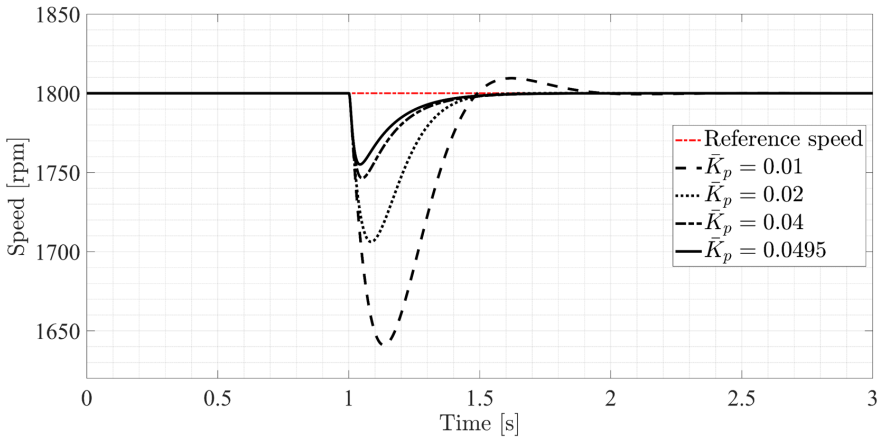

Figure 5.5: Speed response with the DR-PI scheme with various $\bar{K}_p$ and same $\bar{T}_i$ under Scenario 2. Simulation result.

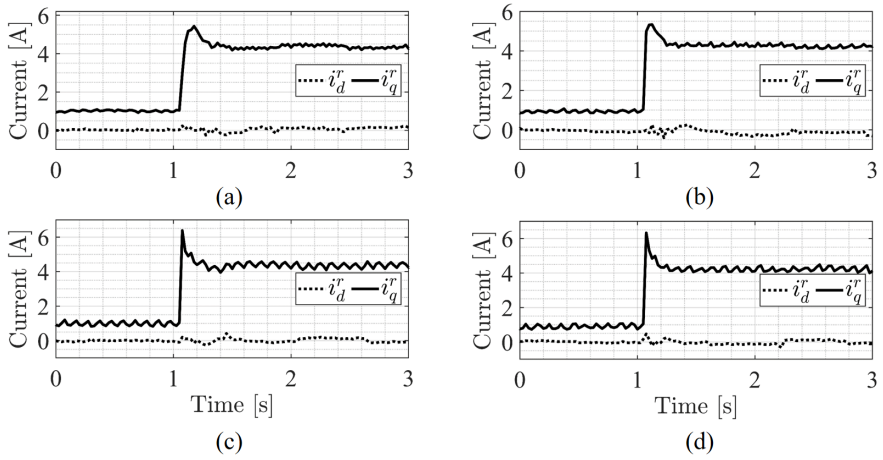

Figure 5.6: Current response with the DR-PI scheme with various $\bar{K}_p$ and constant $\bar{T}_i$ under Scenario 2. Simulation result: (a) $\bar{K}_p = 0.01$; (b) $\bar{K}_p = 0.02$; (c) $\bar{K}_p = 0.04$; (d) $\bar{K}_p = 0.0495$.

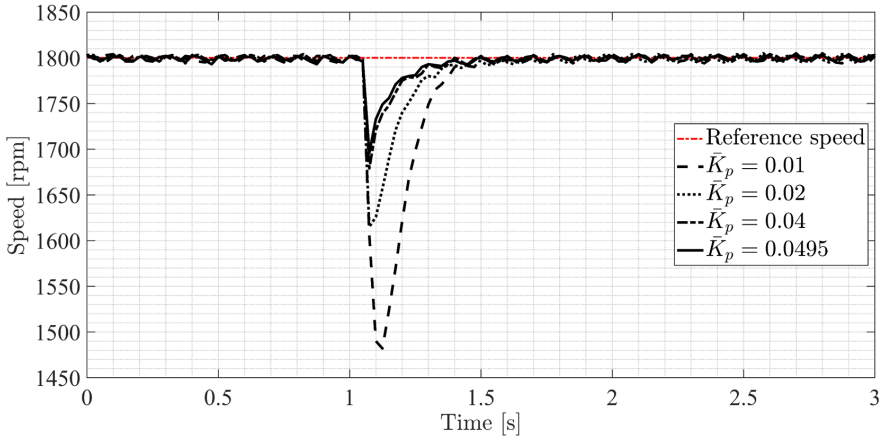

Figure 5.7: Speed response with the DR-PI scheme with various $\bar{K}_p$ and same $\bar{T}_i$ under Scenario 2. Experimental result.

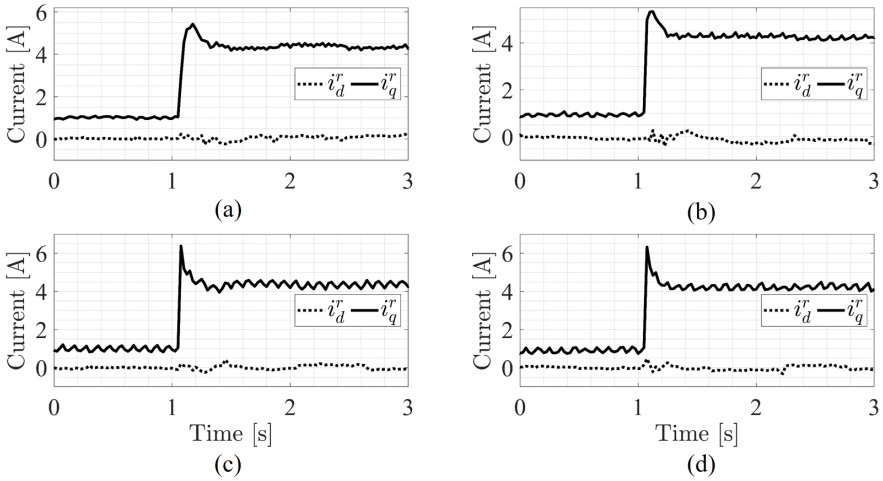

Figure 5.8: Current response with the DR-PI scheme with different $\bar{K}_p$ and constant $\bar{T}_i$ under Scenario 2. Experimental result: (a) $\bar{K}_p = 0.01$; (b) $\bar{K}_p = 0.02$; (c) $\bar{K}_p = 0.04$; (d) $\bar{K}_p = 0.0495$.

5.3.2 Comparison of the traditional PI, DOBC, and proposed DR-PI

This section presents the results of comparison of the DR-PI performance with a performance of the traditional PI and DOBC. The traditional PI parameters are tuned based on the ZN method, which is based on the step response characteristics. The parameters such as ultimate gain $\bar{K}^{ult}$, ultimate time period of oscillations $\bar{T}^{ult}$, and time delay $\bar{D}$ are used to calculate the parameters of the traditional PI based on the ZN method shown in [59], and the parameters of the PI controller and disturbance observer in the DOBC are selected according to the method provided in [134, 141]. The parameters of the step response are found as $\bar{T}^{ult} = 0.15$ s, $\bar{K}^{ult} = 303.0303$, and $\bar{D} = 0.1$ s. Hence, the ZN-based traditional PI controller parameters are defined in terms of $\bar{T}^{ult}\bar{K}^{ult}\bar{D}$ as below

$$\begin{aligned} \bar{K}_p &= \frac{0.9\bar{T}_{ult}}{\bar{K}^{ult}\bar{D}} \\ \bar{T}_i &= 3\bar{D} \end{aligned} \tag{5.3}$$

Figure 5.9 depicts the speed response of each control scheme under Scenario 1. The traditional PI and DOBC show faster response comparing to the DR-PI, but the DR-PI outperforms these two controllers in terms of settling time and level of an overshoot in the speed tracking. We note that the tolerance band is taken as $\pm$ 18 rpm or $\pm$ 1 $\%$ of 1800 rpm for determination of the settling time. The traditional PI seems faster with the settling time of 0.9 s comparing to the DOBC which has the settling time of 1.6 s, while the DR-PI has the shortest settling time of 0.575 s. Regarding the overshoot level, the DOBC scheme accomplishes the highest level of the overshoot with value of 5.56 $\%$ (100.08 rpm) with slight difference from the traditional PI (5.39 $\%$ (97.02 rpm)), and

zero overshoot level is reached with DR-PI.

The pre-filter appeared due to the modification of the DOBC helps to deal with an overshoot and increase convergence speed. Quick convergence of the pre-filter is also reported in [137, 142]. The stator currents are presented in Figure 5.10, where the i_d^r current is smooth for all controllers. With respect to current regulation, the proposed DR-PI shows more robust dynamics at transient periods of the speed. Figure 5.11 summarizes the control performance of each controller under Scenario 1.

The speed response of each controller under Scenario 2 is given in Figure 5.12. The highest speed drop is shown by the traditional PI with 32.78% (590.04 rpm). The DOBC scheme has a speed drop of 10% (180 rpm). Regarding the overshoot level, the traditional PI and DR-PI has zero overshoot comparing to the DOBC, which has an overshoot of 1.61 % (28.98 rpm). It is shown that the traditional PI and the DOBC have almost similar settling time of 0.925 s and 1.05 s, respectively. With respect to the DR-PI, it is seen that the highest speed drop is 4.33% (77.94 rpm) which is the smallest achieved value among the three controllers. Beside this, the settling time of the DR-PI is the shortest one comparing to the traditional PI and DOBC scheme. The stator current response of each controller case is shown in Figure 5.13. The i_q^r current for DOBC and DR-PI is quite similar, but the DR-PI generates sharp i_q^r dynamics at transient period. Unlike the results of two controllers, the traditional PI generates the i_q^r current with smooth dynamics. With respect to the i_d^r current in the DR-PI, at transient period, the d-axis current has the shortest oscillation time (0.2 s) after sudden torque change, whereas in the traditional PI and DOBC cases, i_d^r current oscillates longer with 1 s and 1.5 s, respectively. The performance data of three controllers are summarized in Figure 5.14.

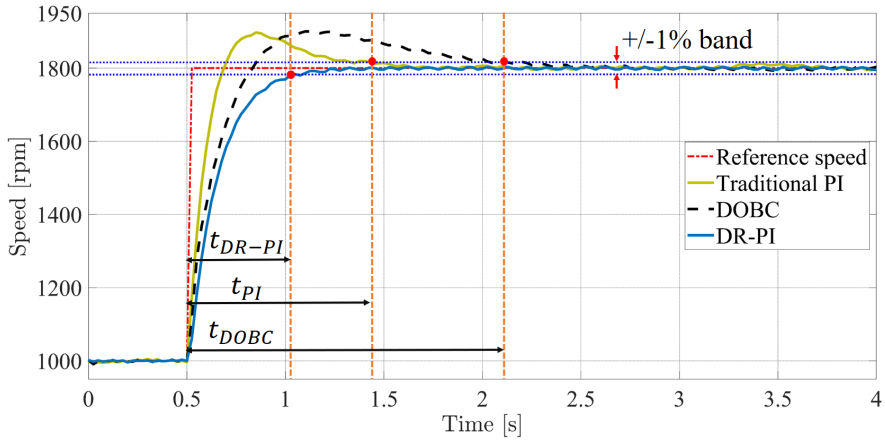

Figure 5.9: Speed responses under Scenario 1.

After the experiments conducted under Scenario 1 and 2 with three controllers, it is concluded that the DR-PI is able to show minimum variations and the fastest response at transient time.

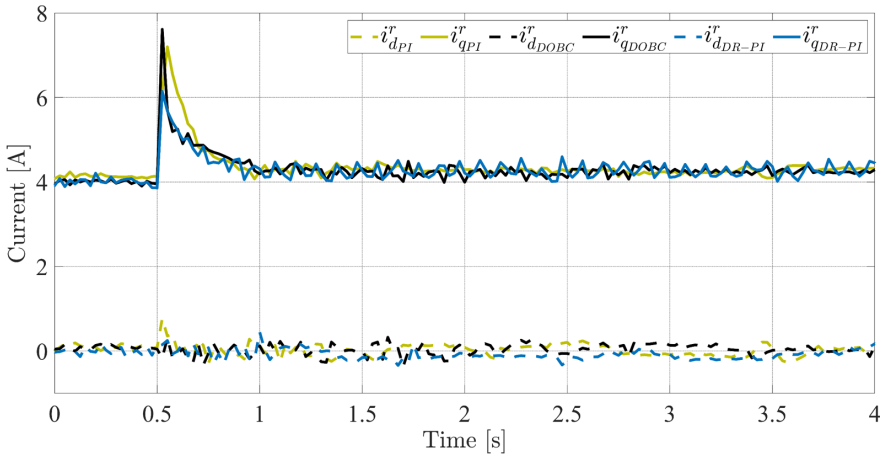

Figure 5.10: i^r_d and i^r_q response under Scenario 1.

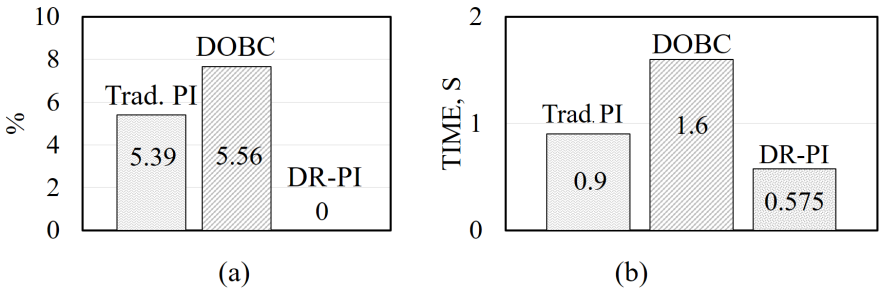

Figure 5.11: Barchart of performance comparison under Scenario 1: (a) Overshoot; (b) Settling time.

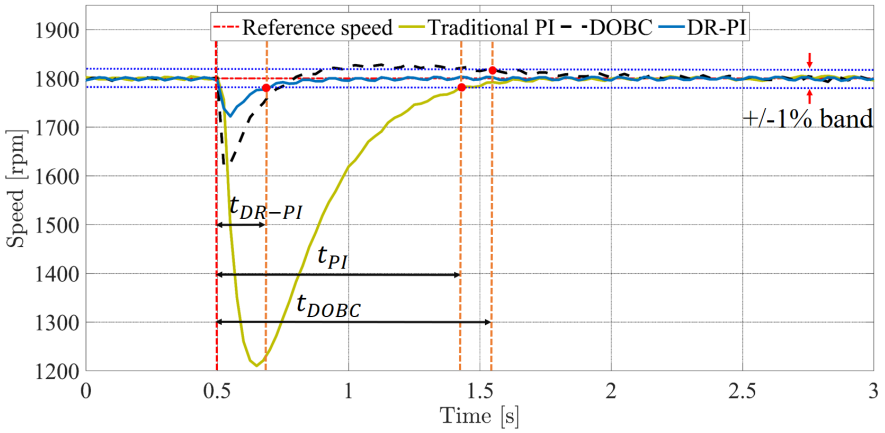

Figure 5.12: Speed responses under Scenario 2.

5.4 Summary

In this chapter, a novel speed control scheme called disturbance-rejection PI (DR-PI) is designed for control the SPMSM. The proposed DR-PI is based on the modification of the traditional DOBC scheme. This control scheme helps to solve some implementation limitations of the traditional DOBC and provide the clear and effective way of parameter tuning of the traditional PI controller. The stability analysis of the closed-loop system with the DR-PI is discussed in detail. A novel FOC method for the SPMSM

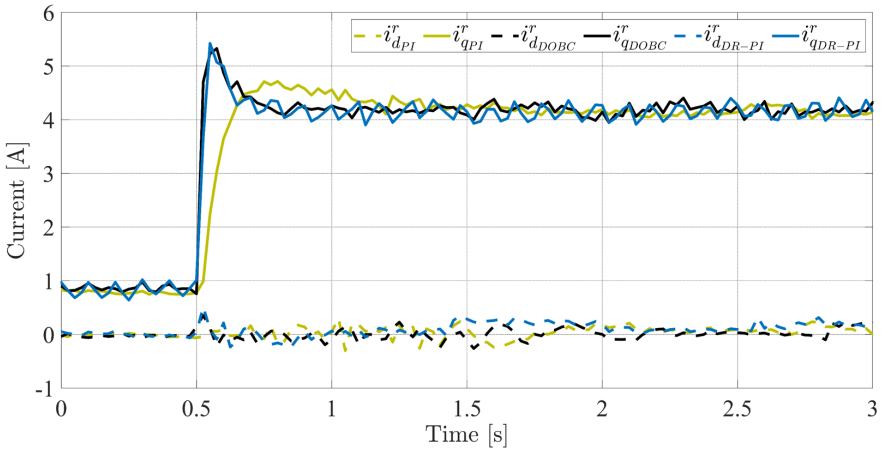

Figure 5.13: i^r_d and i^r_q response under Scenario 2.

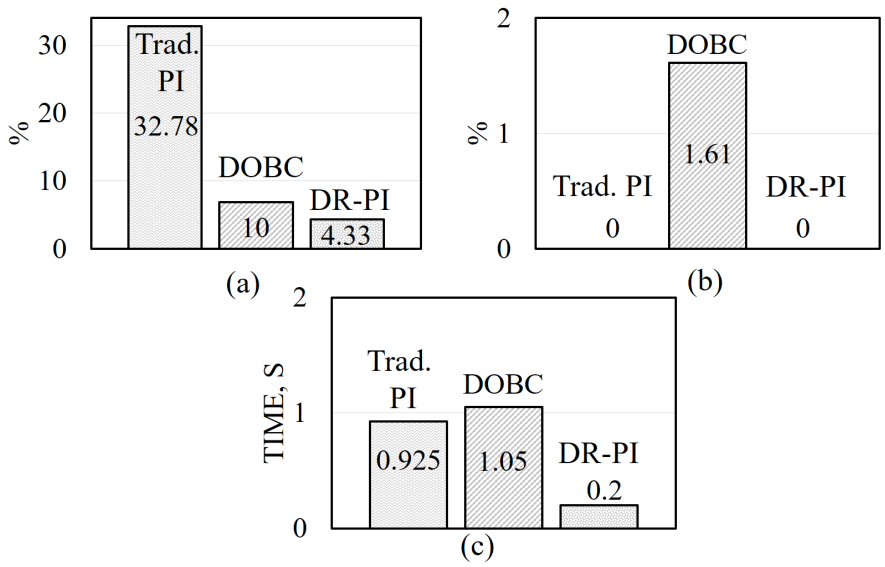

Figure 5.14: Barchart of performance comparison under Scenario 2: (a) Speed drop; (b) Overshoot; (c) Settling time.

is introduced, which consists of the proposed DR-PI to control the speed and two traditional PI controllers to control i^r_d and i^r_q currents. The aim of this work was to design a controller which is tuned systematically with better performance than that of the traditional PI controller. Comparative experiments of the traditional PI speed controller, DOBC scheme, and the proposed DR-PI speed controller are conducted on the experimental stand presented in Section 2.8. The obtained experimental data show that the DR-PI can guarantee minimal variations and fastest response at transient time comparing to other controllers. After the experiments with the DR-PI application to the SPMSM, this method can be considered as a novel practicable method to control AC drives.

BLANK

Chapter 6

Hierarchical Optimal Disturbance Observer-based Control (HODOBC) Scheme for SPMSMs Synthesized by Linear Quadratic Formulation

In this chapter, we present an optimal DOBC (HODOBC) for both speed and current control loops in which the parameters of PI controllers and disturbance observers are calculated via the linear quadratic formulation. Thanks to the well-developed theory of the linear optimal control, the gain tuning technique shown in this method is clear and simple to implement experimentally. Experimental evidences show that the HODOBC can guarantee faster and more robust response comparing to traditional PI and DOBC methods under various operation conditions of the SPMSM.

6.1 Design of the HODOBC for speed regulation of the SPMSM

6.1.1 Optimal PI derivation

Recall the dynamic equation of the rotor in (2.72), and let us adopt it to the form given in (3.4). Then the speed loop dynamic equation can be represented as

$$\dot{\omega}_e = \epsilon_{\omega_e} + b_{0_{\omega_e}} u_{\omega_e} \tag{6.1}$$

where $\epsilon = \epsilon_{\omega_e} = -\frac{p}{J_{m_0}} z_m$, $b_{0_{\omega_e}} = \frac{p}{J_{m_0}}$, $y = \omega_e$, and $u = u_{\omega_e}$.

Note that the lumped disturbance ϵ_{ω_e} in the speed loop estimated by the optimal ESO can be obtained via the relationship

$$\hat{\epsilon}_{\omega_e} = \bar{G}^{ESO}_{\omega_e} \epsilon_{\omega_e} \tag{6.2}$$

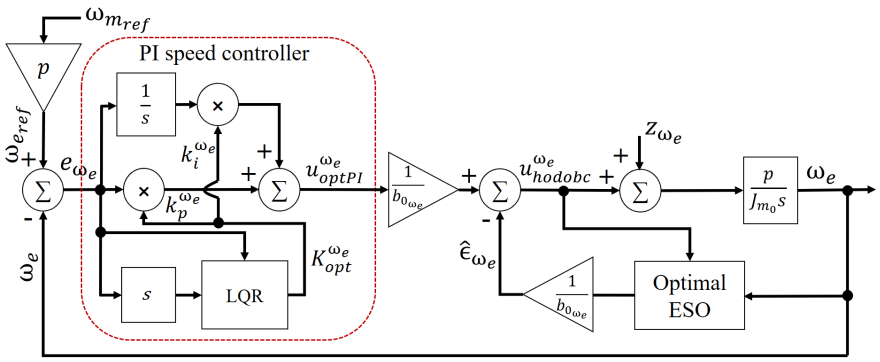

Figure 6.1: Speed control scheme with the HODOBC.

where $G_{\omega_e}^{ESO}$ represents a closed-loop transfer function of the ESO which is derived from the Luenberger observer given in (3.73) and it has a form

$$G_{\omega_e}^{ESO} = \frac{\bar{l}_2^{\omega_e}}{s^2 + \bar{l}_1^{\omega_e} s + \bar{l}_2^{\omega_e}} \tag{6.3}$$

Then the HODOBC for the speed loop can be designed as below

$$u_{hodobc} = \frac{1}{b_{0_{\omega_e}}}(u_{optPI}^{\omega_e} + b_{0_{\omega_e}} G_{\omega_e}^{ESO} \epsilon_{\omega_e}) \tag{6.4}$$

Further expanding of (6.4) gives the HODOBC in terms of parameter variations and lumped disturbance

$$u_{hodobc} = \frac{u_{optPI}^{\omega_e} - G_{\omega_e}^{ESO} \epsilon_{\omega_e}(1 - \Delta J_m J_m^{-1})}{1 + G_{\omega_e}^{ESO} \Delta J_m J_m^{-1}} \tag{6.5}$$

After the compensation of the disturbance the dynamic equation of the speed loop will be reduced to

$$\dot{\omega}_e = u_{optPI}^{\omega_e} \tag{6.6}$$

The speed tracking error is given as

$$e_{\omega_e} = \omega_{e_{ref}} - \omega_e \tag{6.7}$$

Similar to the equations (3.56) and (3.58) shown in Section 3.7.1, the second-order time derivative of (6.7) will be

$$\ddot{e}_{\omega_e} = -\dot{u}_{optPI}^{\omega_e} \tag{6.8}$$

By introducing a state vector $\bar{e}_{\omega_e} = \begin{bmatrix} e_{\omega_e} & \dot{e}_{\omega_e} \end{bmatrix}^T$, an error dynamics-based state-space model of the speed loop can be obtained

$$\dot{\bar{e}}_{\omega_e} = \bar{A}_{\omega_e} \bar{e}_{\omega_e} + \bar{B}_{\omega_e} \dot{u}_{optPI}^{\omega_e} \tag{6.9}$$

with $\bar{A}_{\omega_e} = \begin{bmatrix} 0 & 1 \\ 0 & 0 \end{bmatrix}$, $\bar{B}_{\omega_e} = \begin{bmatrix} 0 \\ -1 \end{bmatrix}$. Then the LQR is formulated for the system in (6.9) with the cost function

$$\bar{J}_{\omega_e} = \int_0^\infty \bar{e}_{\omega_e}^T(t) Q_{e_{\omega_e}} \bar{e}_{\omega_e}(t) dt + \dot{u}_{optPI}^{\omega_e{}^T}(t) R_{e_{\omega_e}} \dot{u}_{optPI}^{\omega_e}(t) dt \tag{6.10}$$

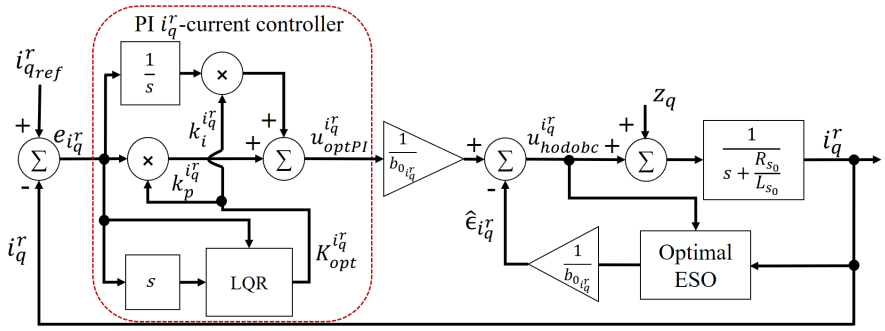

Figure 6.2: i_q^r current control scheme with the HODOBC.

where $Q_{e_{\omega_e}}$ is a positive semi-definite symmetric matrix, $R_{e_{\omega_e}}$ is a positive definite symmetric matrix. The optimal feedback controller calculated via the LQR formulation and designed for (6.9) is

$$\dot{u}_{optPI}^{\omega_e} = -K_{opt}^{\omega_e}\bar{e}_{\omega_e} = -k_1^{\omega_e}e_{\omega_e} - k_2^{\omega_e}\dot{e}_{\omega_e} \tag{6.11}$$

with the optimal gain $K_{opt}^{\omega} = R_{e_{\omega_e}}^{-1}\bar{B}_{\omega_e}\bar{P}_c^{\omega_e}$, where $\bar{P}_c^{\omega_e}$ is a solution of the continuous-time ARE given as

$$\bar{A}_{\omega_e}^T\bar{P}_c^{\omega_e} + \bar{P}_c^{\omega_e}\bar{A}_{\omega_e} - \bar{P}_c^{\omega_e}\bar{B}_{\omega_e}R_{e_{\omega_e}}^{-1}\bar{B}_{e_{\omega_e}}^T\bar{P}_c^{\omega_e} + Q_{e_{\omega_e}} = 0 \tag{6.12}$$

Further, integration both sides of (6.11) gives the PI speed controller with parameters obtained via the LQR method

$$u_{optPI}^{\omega_e} = k_p^{\omega_e}e_{\omega_e} + k_i^{\omega_e}\int_0^t e_{\omega_e}dt \tag{6.13}$$

where $k_p^{\omega_e} = -k_2^{\omega_e}$ and $k_i^{\omega_e} = -k_1^{\omega_e}$ are proportional and integral gains of the PI speed controller, respectively.

6.1.2 Design an ESO with optimal parameters for estimation of the lumped disturbance in the speed loop

In this section, the extended state-space is designed based on the dynamic equation of the rotor given in (2.71). Using the extended state vector $\chi_{ext}^{\omega} = \begin{bmatrix}\omega_e & \epsilon_{\omega_e}\end{bmatrix}^T$, the extended state-space model will be obtained as

$$\begin{cases}\dot{\chi}_{ext}^{\omega_e} = \bar{A}_{ext}^{\omega_e}\chi_{ext}^{\omega_e} + \bar{B}_{ext}^{\omega_e}u_{optPI}^{\omega_e} + \bar{E}_{ext}^{\omega_e}\dot{\epsilon}_{\omega_e} \\ y = \bar{C}_{ext}^{\omega_e}\chi_{ext}^{\omega_e}\end{cases} \tag{6.14}$$

where $\bar{A}_{ext}^{\omega_e} = \begin{bmatrix}0 & 1\\ 0 & 0\end{bmatrix}$, $\bar{B}_{ext}^{\omega_e} = \begin{bmatrix}b_0\\ 0\end{bmatrix}$, $\bar{C}_{ext}^{\omega_e} = \begin{bmatrix}1 & 0\end{bmatrix}$, and $\bar{E}_{ext}^{\omega_e} = \begin{bmatrix}0\\ 1\end{bmatrix}$. Hence, using the extended state-space model, we derive an ESO for estimation of the lumped disturbance ϵ_{ω_e} in the speed loop dynamics as follows

$$\begin{cases}\dot{\hat{\chi}}_{ext}^{\omega_e} = \bar{A}_{ext}^{\omega_e}\hat{\chi}_{ext}^{\omega_e} + \bar{B}_{ext}^{\omega_e}u_{optPI}^{\omega_e} + \bar{L}_{\omega_e}(y_{ref} - \hat{y}) \\ \hat{y} = C_{ext}^{\omega_e}\hat{\chi}_{ext}^{\omega_e}\end{cases} \tag{6.15}$$

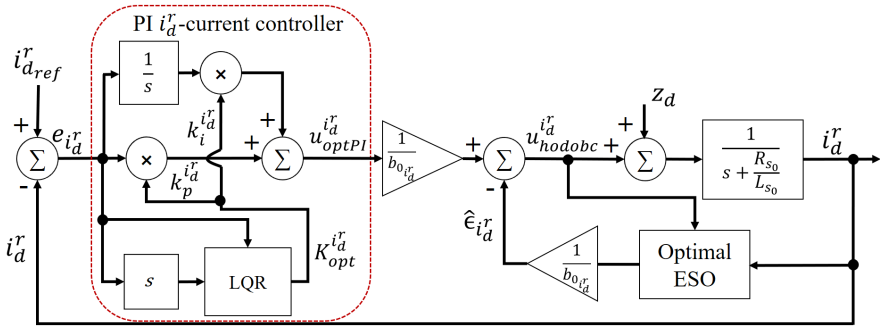

Figure 6.3: i_d^r current control scheme with the HODOBC.

with $y_{ref} = \omega_{e_{ref}}$, $\hat{y} = \hat{\omega}_e$, and the estimation vector is $\hat{\chi}_{ext}^{\omega_e} = \begin{bmatrix} \hat{\omega}_e & \hat{\epsilon}_{\omega_e} \end{bmatrix}^T$. The observer gain $\bar{L}_{\omega_e}$ is obtained via the LQR method as $\bar{L}_{\omega_e} = \bar{P}_o^{\omega_e} \bar{C}_{ext}^{\omega_e{}^T} \bar{R}_{obs}^{\omega_e{}^{-1}} = \begin{bmatrix} \bar{l}_1^{\omega_e} & \bar{l}_2^{\omega_e} \end{bmatrix}^T$ with $\bar{P}_o^{\omega_e}$ as a solution of the continuous-time ARE of the form

$$\bar{A}_{ext}^{\omega_e} \bar{P}_o^{\omega_e} + \bar{P}_o^{\omega_e} \bar{A}_{ext}^{\omega_e{}^T} - \bar{P}_o^{\omega_e} \bar{C}_{ext}^{\omega_e{}^T} \bar{R}_{obs}^{\omega_e{}^{-1}} \bar{C}_{ext}^{\omega_e} \bar{P}_o^{\omega_e} + \bar{Q}_{obs}^{\omega_e} = 0 \tag{6.16}$$

with $\bar{Q}_{obs}^{\omega_e}$ and $\bar{R}_{obs}^{\omega_e}$ are a positive semi-definite matrix and positive definite matrix, respectively. The speed loop control system with the HODOBC is depicted in Figure 6.1.

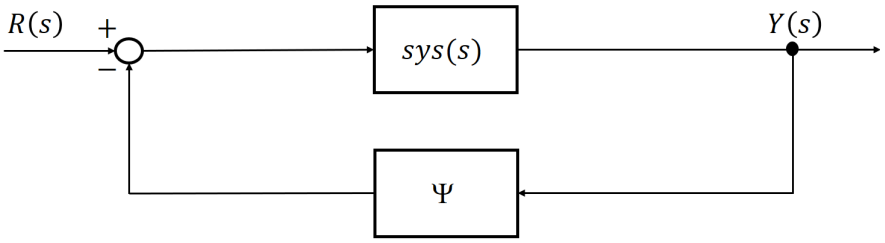

Figure 6.4: A negative unity-feedback closed-loop system with varying feedback gain $\Psi(s)$.

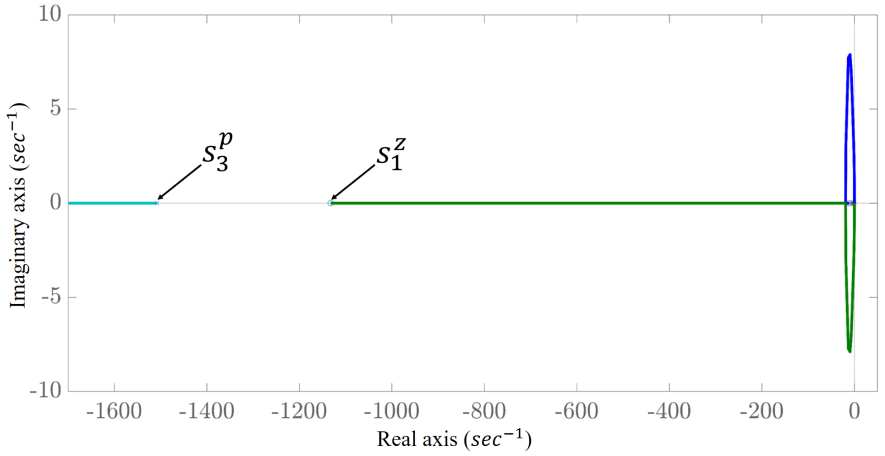

Figure 6.5: Zoomed view of the root locus: locations of s_1^z and s_3^p.

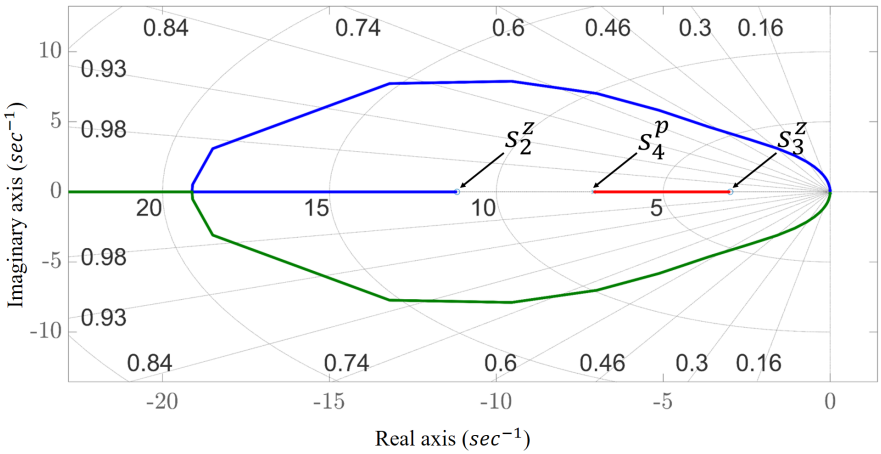

Figure 6.6: Zoomed view of the root locus: locations of s_2^z, s_3^z, and s_4^p.

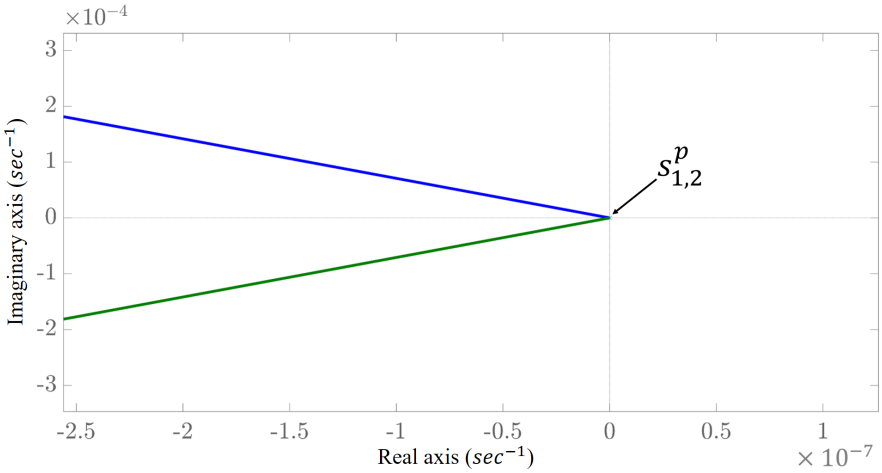

Figure 6.7: Zoomed view of the root locus: locations of s_1^p and s_2^p.

6.1.3 Stability analysis of the speed loop with the HODOBC

The stability of the proposed HODOBC for speed loop is shown using the root locus technique. Let us consider a negative unity-feedback closed-loop system transfer function shown in (3.24) with $\bar{P}(s) = \frac{1}{J_m s}$ and $\bar{C}(s) = u_{\omega_e}$. After the substitution of the plant and controller transfer functions into the equation in (3.24), we can obtain a closed-loop transfer function for the speed loop with the HODOBC as

$$G_{\omega_e} = \frac{k_p^{\omega_e} s^3 + (k_p^{\omega_e} \bar{l}_1^{\omega_e} + k_i^{\omega_e}) s^2 + \ldots}{J_m s^4 + (J_m \bar{l}_1^{\omega_e} + k_p^{\omega_e}) s^3 + \ldots} \\ \frac{\cdots + (k_p^{\omega_e} \bar{l}_2^{\omega_e} + k_i^{\omega_e} \bar{l}_1^{\omega_e}) s + k_i^{\omega_e} \bar{l}_2^{\omega_e}}{\cdots + (J_m \bar{l}_2^{\omega_e} + \Delta J_m \bar{l}_2^{\omega_e} + k_p^{\omega_e} \bar{l}_1^{\omega_e} + k_i^{\omega_e}) s^2 + (k_p^{\omega_e} \bar{l}_2^{\omega_e} + k_i^{\omega_e} \bar{l}_1^{\omega_e}) s + k_i^{\omega_e} \bar{l}_2^{\omega_e}} \quad (6.17)$$

Let us consider a characteristic equation of the closed-loop system's transfer function given in (6.17).

$$J_m s^4 + (J_m \bar{l}_1^{\omega_e} + k_p^{\omega_e}) s^3 + (J_m \bar{l}_2^{\omega_e} + \Delta J_m \bar{l}_2^{\omega_e} + k_p^{\omega_e} \bar{l}_1^{\omega_e} + k_i^{\omega_e}) s^2 + \ldots \\ \cdots + (k_p^{\omega_e} \bar{l}_2^{\omega_e} + k_i^{\omega_e} \bar{l}_1^{\omega_e}) s + k_i^{\omega_e} \bar{l}_2^{\omega_e} = 0 \quad (6.18)$$

Table 6.1: Control methods parameters.

	Traditional cascaded PI-PI	**Speed control with the traditional DOBC**	**Speed control with the HODOBC**	**Cascaded speed-current control with the HODOBC**
Gains of the speed controller	k_p = 0.0415, k_i = 0.0869		k_p = 0.0470, k_i = 0.3331	
Gains of the current controllers	$k_{p_{id}} = 20$, $k_{i_{id}} = 0.04$, $k_{p_{iq}} = 0.5073$, $k_{i_{iq}} = 22.3480$			$k_{p_{id}} = 32.19$, $k_{i_{id}} = 3162$, $k_{p_{iq}} = 0.5073$, $k_{i_{iq}} = 22.348$
Gains of the DO in the speed loop	NaN	$L_{1\omega} = 158.0385$, $L_{2\omega} = 5.3452 \times 10^3$		
Gains of the DO in the current loops	NaN	NaN	NaN	$L_{1d} = 316.2309$, $L_{2d} = 1$, $L_{1q} = 316.2309$, $L_{2q} = 1$

Then, to provide the root locus analysis the characteristic equation in (6.18) can be adopted as below

$$1 + \Psi_{\omega_e} \frac{\frac{k_p^{\omega_e}}{J_{m_0}} s^3 + (\frac{k_i^{\omega_e}}{J_{m_0}} + \frac{k_p^{\omega_e}}{J_{m_0}} \bar{l}_1^{\omega_e} - \bar{l}_2^{\omega_e}) s^2 + (\frac{k_i^{\omega_e}}{J_{m_0}} \bar{l}_1^{\omega_e} + \frac{k_p^{\omega_e}}{J_{m_0}} \bar{l}_2^{\omega_e}) s + \frac{k_i^{\omega_e}}{J_{m_0}} \bar{l}_2^{\omega_e}}{s^2(s^2 + \bar{l}_1^{\omega_e} s + 2\bar{l}_2^{\omega_e})} = 0 \quad (6.19)$$

or

$$1 + \Psi_{\omega_e} sys(s) = 0 \quad (6.20)$$

where $\Psi_{\omega_e} = \frac{J_{m_0}}{J_m}$ is a system's gain parameter and $sys(s)$ represents the open-loop transfer function having a form

$$sys(s) = \frac{\frac{k_p^{\omega_e}}{J_{m_0}} s^3 + (\frac{k_i^{\omega_e}}{J_{m_0}} + \frac{k_p^{\omega_e}}{J_{m_0}} \bar{l}_1^{\omega_e} - \bar{l}_2^{\omega_e}) s^2 + (\frac{k_i^{\omega_e}}{J_{m_0}} \bar{l}_1^{\omega_e} + \frac{k_p^{\omega_e}}{J_{m_0}} \bar{l}_2^{\omega_e}) s + \frac{k_i^{\omega_e}}{J_{m_0}} \bar{l}_2^{\omega_e}}{s^2(s^2 + \bar{l}_1^{\omega_e} s + 2\bar{l}_2^{\omega_e})} \quad (6.21)$$

Actually, the equation in (6.20) represents the characteristic equation of a unity-feedback closed-loop system (see Figure 6.4) with $\Psi = \Psi_{\omega_e}$.

Using the Matlab $rlocus(sys)$ command, one can obtain a root locus plot for the open-loop system $sys(s)$. The root locus shows the trajectories of closed-loop poles as a function of feedback gain Ψ_{ω_e}. Then the open-loop system $sys(s)$ has 4 poles as $s_{1,2}^p = 0$, $s_3^p = -1508$, and $s_4^p = -7.1$, and 3 zeros as $s_1^z = -1133$, $s_2^z = -11.2$, and $s_3^z = -3$. The locations of the open-loop zeros and poles are depicted in Figures 6.5-6.7. From Figure 6.7, it is observed that the trajectory of the closed-loop poles does not enter the RHP, the root locus starts from the open-loop poles $s_1^p = s_2^p = 0$ when $\Psi_{\omega_e} = 0$ and the closed-loop pole moves to the left toward the open-loop zero $s_2^z = -11.2$ as Ψ_{ω_e} increases up to infinity. This fact reveals that the proposed HODOBC can guarantee robust performance of the closed-loop speed control system. Design steps of the ESO and PI controller in HODOBC applied for the speed control are shown in the flowcharts depicted in Figures 6.8-6.9.

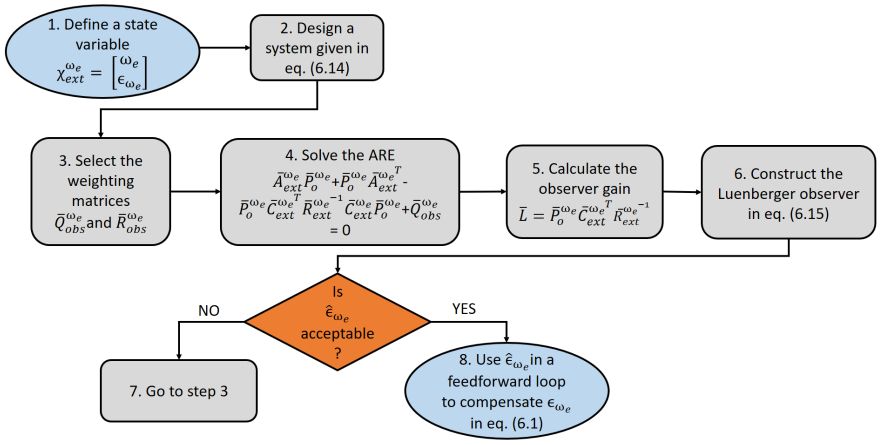

Figure 6.8: A flowchart showing design steps of the ESO with optimal parameters for the speed loop.

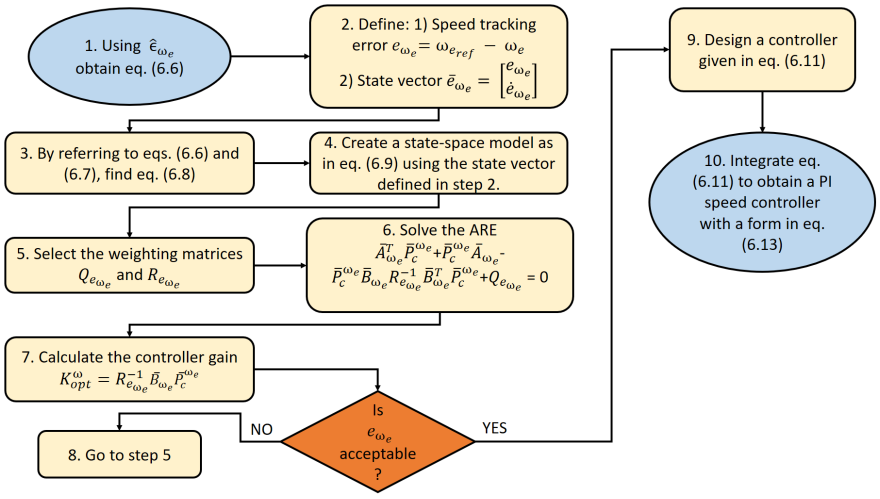

Figure 6.9: A flowchart showing design steps of the PI speed controller with optimal parameters.

6.2 Design of the HODOBC for current regulation of the SPMSM

6.2.1 The HODOBC for the current control

To design the HODOBC for the stator currents, let us consider the dynamic equations of the $d-q$-currents in (2.68). Then the dynamic equations of the i_d^r and i_q^r current can be presented as in (3.4)

$$\dot{i}_d^r = \epsilon_{i_d^r} + L_{s_0} u_{d_{ref}}^r \tag{6.22}$$

$$\dot{i}_q^r = \epsilon_{i_q^r} + L_{s_0} u_{q_{ref}}^r \tag{6.23}$$

where for the i_d^r current control loop: $y_{i_d^r} = i_d^r$, $u = u_{d_{ref}}^r$, and $\epsilon_{i_d^r} = -\frac{R_{s_0}}{L_{s_0}} i_d^r + z_d$; for the i_q^r current control loop: $y = y_{i_q^r} = i_q^r$, $u = u_{q_{ref}}^r$, and $\epsilon_{i_q^r} = -\frac{R_{s_0}}{L_{s_0}} i_q^r - \frac{1}{L_{s_0}}\omega_e \gamma_{pm} + z_q$, $b_{0_{i_d}} = b_{0_{i_q}} = \frac{1}{L_{s_0}}$, and the nonlinear coupling terms $\frac{1}{L_{s_0}}\omega_e L_s i_d^r$ and $\frac{1}{L_{s_0}}\omega_e L_s i_q^r$ are

compensated in the feedforward loop. Then the composite control laws for the i_d^r and i_q^r currents are derived as

$$\begin{aligned} u_{i_d^r} &= \frac{1}{b_{0_{i_d}}}(u_{PI}^{i_d^r} - \hat{\epsilon}_{i_d^r}) \\ u_{i_q^r} &= \frac{1}{b_{0_{i_q}}}(u_{PI}^{i_q^r} - \hat{\epsilon}_{i_q^r}) \end{aligned} \tag{6.24}$$

Noting that the estimations of $\hat{\epsilon}_{i_d^r}$ and $\hat{\epsilon}_{i_q^r}$ relate to their real values as

$$\begin{aligned} \hat{\epsilon}_{i_d^r} &= G_{i_d^r}^{ESO}\epsilon_{i_d^r} \\ \hat{\epsilon}_{i_q^r} &= G_{i_q^r}^{ESO}\epsilon_{i_q^r} \end{aligned} \tag{6.25}$$

with $G_{i_d^r}^{ESO} = \frac{\bar{l}_2^{i_d^r}}{s^2+\bar{l}_1^{i_d^r}s+\bar{l}_2^{i_d^r}}$ and $G_{i_q^r}^{ESO} = \frac{\bar{l}_2^{i_q^r}}{s^2+\bar{l}_1^{i_q^r}s+\bar{l}_2^{i_q^r}}$. Then the composite control laws for the i_d^r and i_q^r currents can be rewritten as

$$\begin{aligned} u_{i_d^r} &= u_{i_{d\,PI}^r} - \frac{1}{b_{0_{i_d^r}}}G_{i_d^r}^{ESO}\epsilon_{i_d^r} \\ u_{i_q^r} &= u_{i_{q\,PI}^r} - \frac{1}{b_{0_{i_q^r}}}G_{i_q^r}^{ESO}\epsilon_{i_q^r} \end{aligned} \tag{6.26}$$

Further expanding of (6.26) will result in composite controls for the i_d^r and i_q^r currents explicitly defined in terms of parameter variations and lumped disturbance as

$$\begin{aligned} u_{i_d^r} &= \frac{\bar{a}s^4 + \left(\bar{a}\bar{l}_1^{i_d^r} + \bar{b}\right)s^3 + \left(\bar{a}\bar{l}_2^{i_d^r} + \bar{b}\bar{l}_1^{i_d^r} + \bar{c}\right)s^2 + \left(\bar{b}\bar{l}_2^{i_d^r} + \bar{c}\bar{l}_1^{i_d^r}\right)s + \bar{c}\bar{l}_2^{i_d^r}}{\bar{d}s^4 + \bar{e}s^3 + \bar{f}s^2 + \bar{g}s} \\ u_{i_q^r} &= \frac{\bar{\bar{a}}s^4 + \left(\bar{\bar{a}}\bar{l}_1^{i_q^r} + \bar{\bar{b}}\right)s^3 + \left(\bar{\bar{a}}\bar{l}_2^{i_q^r} + \bar{\bar{b}}\bar{l}_1^{i_q^r} + \bar{\bar{c}}\right)s^2 + \left(\bar{\bar{b}}\bar{l}_2^{i_q^r} + \bar{\bar{c}}\bar{l}_1^{i_q^r}\right)s + \bar{\bar{c}}\bar{l}_2^{i_q^r}}{\bar{\bar{d}}s^4 + \bar{\bar{e}}s^3 + \bar{\bar{f}}s^2 + \bar{\bar{g}}s} \end{aligned} \tag{6.27}$$

where the coefficients for the i_d^r current controller are defined as: $\bar{a} = L_{s_0}^2 k_p^{i_d^r}(1+\Delta L_s)$, $\bar{b} = L_{s_0}^2 k_i^{i_d^r}(1+\Delta L_s) + L_{s_0}R_s k_p^{i_d^r}$, $\bar{c} = L_{s_0}R_s k_i^{i_d^r}$, $\bar{d} = L_{s_0}(1+\Delta L_s)$, $\bar{e} = L_{s_0}(1+\Delta L_s)\bar{l}_1^{i_d^r}$, $\bar{f} = L_{s_0}(1+\Delta L_s) - \Delta L_s L_{s_0}^2 \bar{l}_2^{i_d^r} + R_s\bar{l}_1^{i_d^r}$, $\bar{g} = R_s\bar{l}_2^{i_d^r}(1-L_{s_0})$; the coefficients for the i_q^r current controller are defined as: $\bar{\bar{a}} = L_{s_0}^2 k_p^{i_q^r}(1+\Delta L_s)$, $\bar{\bar{b}} = L_{s_0}^2 k_i^{i_q^r}(1+\Delta L_s) + L_{s_0}R_s k_p^{i_q^r}$, $\bar{\bar{c}} = L_{s_0}R_s k_i^{i_q^r}$, $\bar{\bar{d}} = L_{s_0}(1+\Delta L_s)$, $\bar{\bar{e}} = L_{s_0}(1+\Delta L_s)\bar{l}_1^{i_q^r}$, $\bar{\bar{f}} = L_{s_0}(1+\Delta L_s) - \Delta L_s L_{s_0}^2 \bar{l}_2^{i_q^r} + R_s\bar{l}_1^{i_q^r}$, $\bar{\bar{g}} = R_s\bar{l}_2^{i_q^r}(1-L_{s_0})$. After the lumped disturbance is eliminated in the feedforward loop, the compensated i_d^r and i_q^r dynamics will be

$$\begin{aligned} \dot{i}_d^r &= u_{PI}^{i_d^r} \\ \dot{i}_q^r &= u_{PI}^{i_q^r} \end{aligned} \tag{6.28}$$

Hence, the errors of the current tracking $e_{i_d^r}$ and $e_{i_q^r}$ for the FOC-based SPMSM system are obtained as

$$e_{i_d^r} = i_{d_{ref}}^r - i_d^r$$

$$e_{i_q^r} = i^r_{q_{ref}} - i^r_q \tag{6.29}$$

Taking the second-time derivatives of the tracking errors in (6.29) will result in

$$\begin{aligned} \ddot{e}_{i_d^r} &= \dddot{i}^r_{d_{ref}} - \dddot{i}^r_d \\ \ddot{e}_{i_q^r} &= \dddot{i}^r_{q_{ref}} - \dddot{i}^r_q \end{aligned} \tag{6.30}$$

Since the reference currents for the current loops can be considered as constants, the equations in (6.30) can be reduced to

$$\begin{aligned} \ddot{e}_{i_d^r} &= -\dddot{i}^r_d \\ \ddot{e}_{i_q^r} &= -\dddot{i}^r_q \end{aligned} \tag{6.31}$$

Selecting $e_{i_d^r}$ and $\dot{e}_{i_d^r}$ as states for the d-axis current tracking error system, and $e_{i_q^r}$ and $\dot{e}_{i_q^r}$ as states for the q-axis current tracking error system, the following error dynamics-based state-space models can be derived

$$\begin{aligned} \dot{\bar{e}}_{i_d^r} &= \bar{A}_{i_d^r}\bar{e}_{i_d^r} + \bar{B}_{i_d^r}u^{i_d^r}_{PI} \\ \dot{\bar{e}}_{i_q^r} &= \bar{A}_{i_q^r}\bar{e}_{i_q^r} + \bar{B}_{i_q^r}u^{i_q^r}_{PI} \end{aligned} \tag{6.32}$$

where $\bar{e}_{i_d^r} = \begin{bmatrix} e_{i_d^r} & \dot{e}_{i_d^r} \end{bmatrix}^T$ and $\bar{e}_{i_q^r} = \begin{bmatrix} e_{i_q^r} & \dot{e}_{i_q^r} \end{bmatrix}^T$ are the state vectors of the error-dynamics based i_d^r and i_q^r control systems, respectively; $\bar{A}_{i_d^r} = \bar{A}_{i_q^r} = \begin{bmatrix} 0 & 0 \\ 0 & 0 \end{bmatrix}$, $\bar{B}_{i_d^r} = \bar{B}_{i_q^r} = \begin{bmatrix} 0 \\ -1 \end{bmatrix}$. Subsequently, the LQR is designed for each system in (6.32) with the performance functions as

$$\begin{aligned} \bar{J}_{i_d^r} &= \int_0^\infty \bar{e}^T_{i_d^r}(t)Q_{e_{i_d^r}}\bar{e}_{i_d^r}(t)dt + \dot{u}^{i_d^r T}_{PI}(t)R_{e_{i_d^r}}\dot{u}^{i_d^r}_{PI}(t)dt \\ \bar{J}_{i_q^r} &= \int_0^\infty \bar{e}^T_{i_q^r}(t)Q_{e_{i_q^r}}\bar{e}_{i_q^r}(t)dt + \dot{u}^{i_q^r T}_{PI}(t)R_{e_{i_q^r}}\dot{u}^{i_q^r}_{PI}(t)dt \end{aligned} \tag{6.33}$$

where $Q_{e_{i_d^r}}$ and $Q_{e_{i_q^r}}$ are positive semi-definite symmetric matrices responsible for the state cost function of each system, respectively, whereas $R_{e_{i_d^r}}$ and $R_{e_{i_q^r}}$ are positive definite symmetric matrices responsible for the control input cost function of each system, respectively.

Then the optimal control laws for the i_d^r and i_q^r are synthesized as follows

$$\begin{aligned} \dot{u}^{i_d^r}_{optPI} &= -K^{i_d^r}_{opt}\bar{e}_{i_d^r} = -k_1^{i_d^r}e_{i_d^r} - k_2^{i_d^r}\dot{e}_{i_d^r} \\ \dot{u}^{i_q^r}_{optPI} &= -K^{i_q^r}_{opt}\bar{e}_{i_q^r} = -k_1^{i_q^r}e_{i_q^r} - k_2^{i_q^r}\dot{e}_{i_q^r} \end{aligned} \tag{6.34}$$

where $K^{i_d^r}_{opt} = R^{-1}_{e_{i_d^r}}\bar{B}_{i_d^r}\bar{P}^c_{i_d^r}$, $K^{i_q^r}_{opt} = R^{-1}_{e_{i_q^r}}\bar{B}_{i_q^r}\bar{P}^c_{i_q^r}$ in which $\bar{P}^c_{i_d^r}$ and $\bar{P}^c_{i_q^r}$ are solutions of the continuous ARE, respectively

$$\begin{aligned} \bar{A}^T_{i_d^r}\bar{P}^c_{i_d^r} + \bar{P}^c_{i_d^r}\bar{A}_{i_d^r} - \bar{P}^c_{i_d^r}\bar{B}_{i_d^r}R^{-1}_{e_{i_d^r}}\bar{B}^T_{e_{i_d^r}}\bar{P}^c_{i_d^r} + Q_{e_{i_d^r}} = 0 \\ \bar{A}^T_{i_q^r}\bar{P}^c_{i_q^r} + \bar{P}^c_{i_q^r}\bar{A}_{i_q^r} - \bar{P}^c_{i_q^r}\bar{B}_{i_q^r}R^{-1}_{e_{i_q^r}}\bar{B}^T_{e_{i_q^r}}\bar{P}^c_{i_q^r} + Q_{e_{i_q^r}} = 0 \end{aligned} \tag{6.35}$$

After the integration of (6.34), the PI current regulators with parameters found via the LQR approach are designed

$$\begin{aligned} u_{optPI}^{i_d^r} &= k_p^{i_d^r} e_{i_d^r} + k_i^{i_d^r} \int_0^t e_{i_d^r} dt \\ u_{optPI}^{i_q^r} &= k_p^{i_q^r} e_{i_q^r} + k_i^{i_q^r} \int_0^t e_{i_q^r} dt \end{aligned} \tag{6.36}$$

where $k_p^{i_d^r} = -k_2^{i_d^r}$ and $k_i^{i_d^r} = -k_1^{i_d^r}$, $k_p^{i_q^r} = -k_2^{i_q^r}$ and $k_i^{i_q^r} = -k_1^{i_q^r}$ are the proportional and integral gains of the PI i_d^r and i_q^r current controllers, respectively.

6.2.2 Design of ESO with optimal parameters for estimation of the lumped disturbance in the current loop

Let us introduce extended vectors for the i_d^r and i_q^r current control systems as $\chi_{ext}^{i_d^r} = \begin{bmatrix} i_d^r \\ \epsilon_{i_d^r} \end{bmatrix}$ and $\chi_{ext}^{i_q^r} = \begin{bmatrix} i_q^r \\ \epsilon_{i_q^r} \end{bmatrix}$ and define extended state-space models as follows

$$\begin{aligned} \dot{\chi}_{ext}^{i_d^r} &= \bar{A}_{ext}^{i_d^r} \chi_{ext}^{i_d^r} + \bar{B}_{ext}^{i_d^r} u_{i_d^r} + E_{ext}^{i_d^r} \epsilon_{i_d^r} \\ \dot{\chi}_{ext}^{i_q^r} &= \bar{A}_{ext}^{i_q^r} \chi_{ext}^{i_q^r} + \bar{B}_{ext}^{i_q^r} u_{i_q^r} + E_{ext}^{i_q^r} \epsilon_{i_q^r} \end{aligned} \tag{6.37}$$

where $\bar{A}_{ext}^{i_d^r} = \bar{A}_{ext}^{i_q^r} = \begin{bmatrix} 0 & 1 \\ 0 & 0 \end{bmatrix}$, $\bar{B}_{ext}^{i_d^r} = \bar{B}_{ext}^{i_q^r} = \begin{bmatrix} b_{0_{i_d^r}} \\ 0 \end{bmatrix}$, $\bar{C}_{ext}^{i_d^r} = \bar{C}_{ext}^{i_q^r} = \begin{bmatrix} 1 & 0 \end{bmatrix}$, and $\bar{E}_{ext}^{i_d^r} = \bar{E}_{ext}^{i_q^r} = \begin{bmatrix} 0 \\ 1 \end{bmatrix}$. Based on the extended state-space models in (6.37), the ESO for the current loops can be designed in (6.38)

$$\begin{cases} \dot{\hat{\chi}}_{ext}^{i_d^r} = \bar{A}_{ext}^{i_d^r} \hat{\chi}_{ext}^{i_d^r} + \bar{B}_{ext}^{i_d^r} u_{i_d^r} + L_{i_d^r} (i_d^r - \hat{i}_d^r) \\ \hat{y}_{i_d^r} = \bar{C}_{ext}^{i_d^r} \hat{\chi}_{ext}^{i_d^r} \end{cases}$$
$$\begin{cases} \dot{\hat{\chi}}_{ext}^{i_q^r} = \bar{A}_{ext}^{i_q^r} \hat{\chi}_{ext}^{i_q^r} + \bar{B}_{ext}^{i_q^r} u_{i_q^r} + L_{i_q^r} (i_q^r - \hat{i}_q^r) \\ \hat{y}_{i_q^r} = \bar{C}_{ext}^{i_q^r} \hat{\chi}_{ext}^{i_q^r} \end{cases} \tag{6.38}$$

with $\hat{\chi}_{ext}^{i_d^r} = \begin{bmatrix} \hat{i}_d^r \\ \hat{\epsilon}_{i_d^r} \end{bmatrix}$ and $\hat{\chi}_{ext}^{i_d^r} = \begin{bmatrix} \hat{i}_q^r \\ \hat{\epsilon}_{i_q^r} \end{bmatrix}$ are the estimation vectors of the ESO designed for the i_d^r and i_q^r current control systems, respectively; $L_{i_d^r} = \begin{bmatrix} l_1^{i_d^r} \\ l_2^{i_d^r} \end{bmatrix}$ and $L_{i_q^r} = \begin{bmatrix} l_1^{i_q^r} \\ l_2^{i_q^r} \end{bmatrix}$ are the gains of the ESO designed for the i_d^r and i_q^r current control loops, respectively. Two HODOBC laws for control the i_d^r and i_q^r currents are presented in Figs. 6.2-6.3.

6.2.3 Stability analysis of the current control loops with the HODOBC

The root locus method is utilized to analyze the stability of the current loops with the proposed control schemes. Let us consider the unity-feedback closed-loop transfer

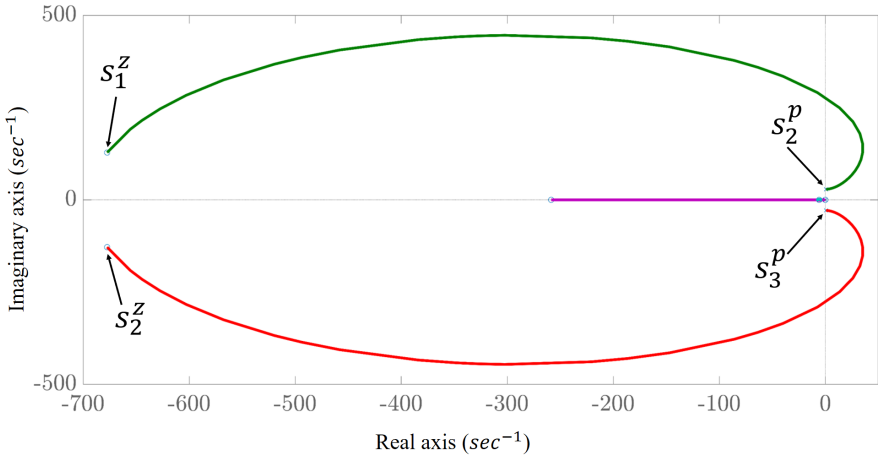

Figure 6.10: Zoomed root locus plot for the closed-loop i_d current control: locations of $s^z_{1,2}$ and $s^p_{2,3}$.

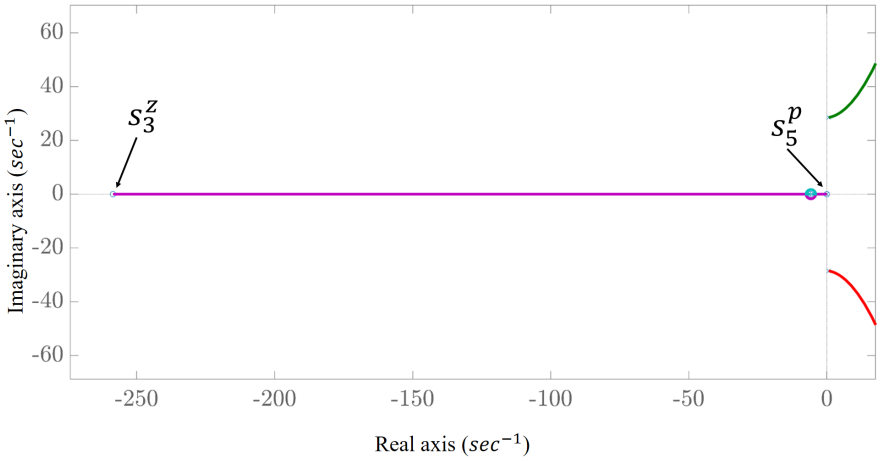

Figure 6.11: Zoomed root locus plot for the closed-loop i_d current control: locations of s^z_3 and s^p_5.

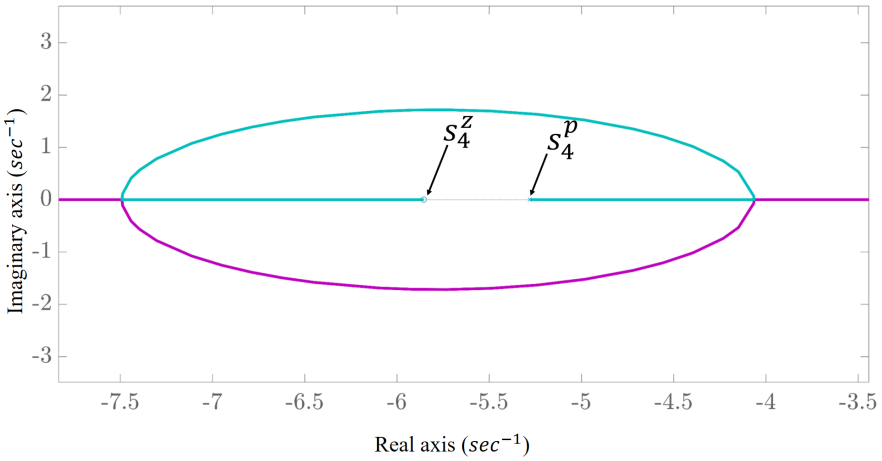

Figure 6.12: Zoomed root locus plot for the closed-loop i_d current control: locations of s^z_4 and s^p_4.

function given in (3.24) for each current control loop. Hence, we consider two plants as $\bar{P}_{i_d^r}(s) = \bar{P}_{i_q^r}(s) = \frac{\frac{1}{L_{s_0}}}{s+\frac{R_{s_0}}{L_{s_0}}}$ and two composite controllers $u_{i_d^r}$ and $u_{i_q^r}$. Then the

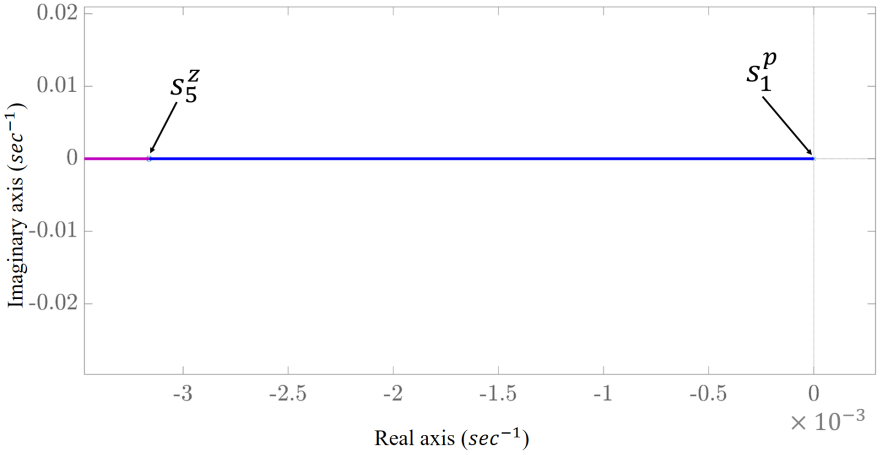

Figure 6.13: Zoomed root locus plot for the closed-loop i_d current control: locations of s_5^z and s_1^p.

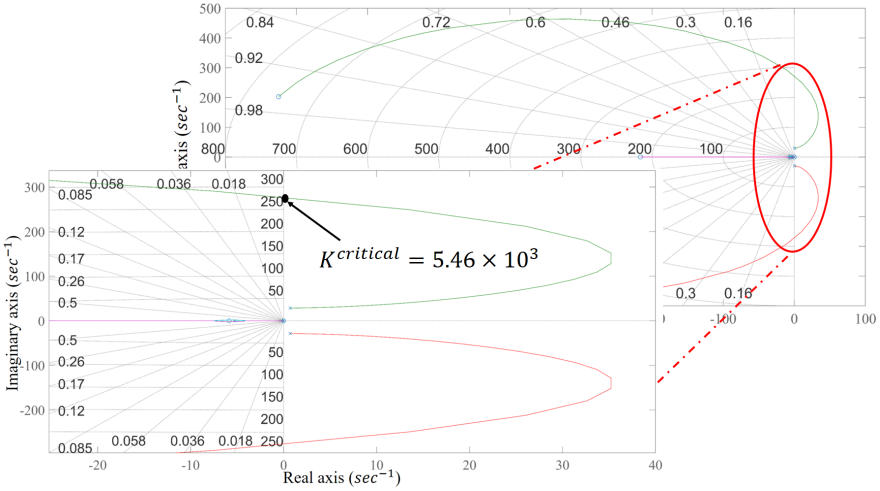

Figure 6.14: Zoomed root locus plot for the closed-loop i_d current control with the proposed controller.

closed-loop transfer functions for the i_d^r current control loop can be derived in (6.39)

$$G_{i_d^r} = \frac{\bar{a}L_{s_0}s^4 + \left(\bar{a}l_1^{i_d^r} + \bar{b}\right)L_{s_0}s^3 + \left(\bar{a}l_2^{i_d^r} + \bar{b}l_1^{i_d^r} + \bar{c}\right)L_{s_0}s^2 + \ldots}{\bar{d}L_{s_0}s^5 + \left((\bar{a}+\bar{e})L_{s_0} + \bar{d}R_{s_0}\right)s^4 + \left(\left(\bar{a}l_1^{i_d^r} + \bar{b}\right)L_{s_0} + \bar{f}L_{s_0} + \bar{e}R_{s_0}\right)s^3 + \ldots}$$
$$= \frac{\cdots + \left(\bar{b}l_2^{i_d^r} + \bar{c}l_1^{i_d^r}\right)L_{s_0}s + \bar{c}L_{s_0}l_2^{i_d^r}}{\cdots + \left(\left(\bar{a}l_2^{i_d^r} + \bar{b}l_1^{i_d^r} + \bar{c}\right)L_{s_0} + \bar{g}L_{s_0} + \bar{f}R_{s_0}\right)s^2 + \left(\left(\bar{b}l_2^{i_d^r} + \bar{c}l_1^{i_d^r}\right)L_{s_0} + \bar{g}R_{s_0}\right)s + \bar{c}L_{s_0}l_2^{i_d^r}} \tag{6.39}$$

The closed-loop transfer function for the i_q^r current control loop is given as

$$G_{i_q^r} = \frac{\bar{\bar{a}}L_{s_0}s^4 + \left(\bar{\bar{a}}l_1^{i_q^r} + \bar{\bar{b}}\right)L_{s_0}s^3 + \left(\bar{\bar{a}}l_2^{i_q^r} + \bar{\bar{b}}l_1^{i_q^r} + \bar{\bar{c}}\right)L_{s_0}s^2 + \ldots}{\bar{\bar{d}}L_{s_0}s^5 + \left((\bar{\bar{a}}+\bar{\bar{e}})L_{s_0} + \bar{\bar{d}}R_{s_0}\right)s^4 + \left(\left(\bar{\bar{a}}l_1^{i_q^r} + \bar{\bar{b}}\right)L_{s_0} + \bar{\bar{f}}L_{s_0} + \bar{\bar{e}}R_{s_0}\right)s^3 + \ldots}$$

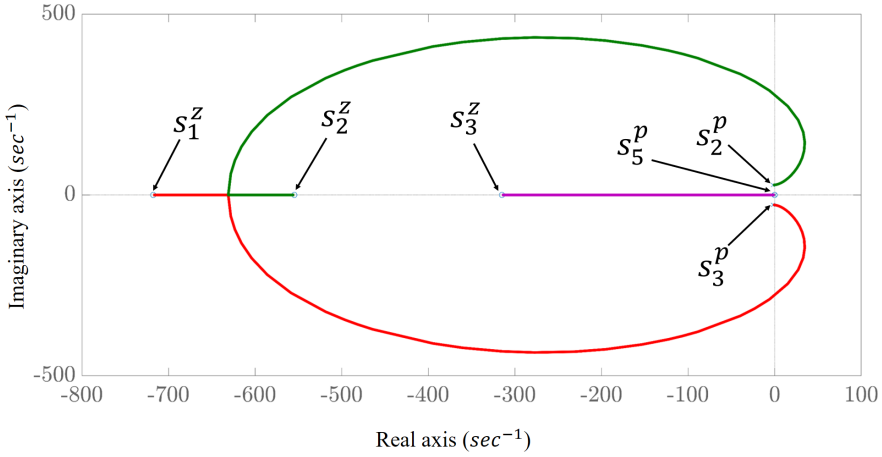

Figure 6.15: Zoomed root locus plot for the closed-loop i_q current control: locations of s_1^z and s_3^p, s_2^z and s_2^p, s_3^z and s_5^p.

$$= \frac{\cdots + \left(\bar{\bar{b}} l_2^{i_q^r} + \bar{\bar{c}} l_1^{i_q^r}\right) L_{s_0} s + \bar{\bar{c}} L_{s_0} l_2^{i_q^r}}{\cdots + \left(\left(\bar{\bar{a}} l_2^{i_q^r} + \bar{\bar{b}} l_1^{i_q^r} + \bar{\bar{c}}\right) L_{s_0} + \bar{\bar{g}} L_{s_0} + \bar{\bar{f}} R_{s_0}\right) s^2 + \left(\left(\bar{\bar{b}} l_2^{i_q^r} + \bar{\bar{c}} l_1^{i_q^r}\right) L_{s_0} + \bar{\bar{g}} R_{s_0}\right) s + \bar{\bar{c}} L_{s_0} l_2^{i_q^r}} \tag{6.40}$$

From (6.39), the characteristic equation of $G_{i_d^r}$ is

$$\begin{aligned} &\bar{d} L_{s_0} s^5 + \left((\bar{a} + \bar{e}) L_{s_0} + \bar{d} R_{s_0}\right) s^4 + \left(\left(\bar{a} l_1^{i_d^r} + \bar{b}\right) L_{s_0} + \bar{f} L_{s_0} + \bar{e} R_{s_0}\right) s^3 + \ldots \\ &\cdots + \left(\left(\bar{a} l_2^{i_d^r} + \bar{b} l_1^{i_d^r} + \bar{c}\right) L_{s_0} + \bar{g} L_{s_0} + \bar{f} R_{s_0}\right) s^2 + \left(\left(\bar{b} l_2^{i_d^r} + \bar{c} l_1^{i_d^r}\right) L_{s_0} + \bar{g} R_{s_0}\right) s + \bar{c} L_{s_0} l_2^{i_d^r} = 0 \end{aligned} \tag{6.41}$$

Similarly, from (6.40), the characteristic equation of $G_{i_q^r}$ is

$$\begin{aligned} &\bar{\bar{d}} L_{s_0} s^5 + \left((\bar{\bar{a}} + \bar{\bar{e}}) L_{s_0} + \bar{\bar{d}} R_{s_0}\right) s^4 + \left(\left(\bar{\bar{a}} l_1^{i_q^r} + \bar{\bar{b}}\right) L_{s_0} + \bar{\bar{f}} L_{s_0} + \bar{\bar{e}} R_{s_0}\right) s^3 + \ldots \\ &\cdots + \left(\left(\bar{\bar{a}} l_2^{i_q^r} + \bar{\bar{b}} l_1^{i_q^r} + \bar{\bar{c}}\right) L_{s_0} + \bar{\bar{g}} L_{s_0} + \bar{\bar{f}} R_{s_0}\right) s^2 + \left(\left(\bar{\bar{b}} l_2^{i_q^r} + \bar{\bar{c}} l_1^{i_q^r}\right) L_{s_0} + \bar{\bar{g}} R_{s_0}\right) s + \bar{\bar{c}} L_{s_0} l_2^{i_q^r} = 0 \end{aligned} \tag{6.42}$$

Further adoptions of the characteristic equations lead to (6.43) and (6.44) which are used in the root locus analysis

$$1 + \Psi_{i_d^r} \frac{\bar{A}_0 s^5 + \bar{A}_1 s^4 + \bar{A}_2 s^3 + \bar{A}_3 s^2 + \bar{A}_4 s + \bar{A}_5}{\bar{B}_0 s^5 + \bar{B}_1 s^4 + \bar{B}_2 s^3 + \bar{B}_3 s^2 + \bar{B}_4 s} = 0 \tag{6.43}$$

$$1 + \Psi_{i_q^r} \frac{\bar{\bar{A}}_0 s^5 + \bar{\bar{A}}_1 s^4 + \bar{\bar{A}}_2 s^3 + \bar{\bar{A}}_3 s^2 + \bar{\bar{A}}_4 s + \bar{\bar{A}}_5}{\bar{\bar{B}}_0 s^5 + \bar{\bar{B}}_1 s^4 + \bar{\bar{B}}_2 s^3 + \bar{\bar{B}}_3 s^2 + \bar{\bar{B}}_4 s} = 0 \tag{6.44}$$

where $\Psi_{i_d^r} = \frac{1}{L_s L_{s_0}}$ and $\Psi_{i_q^r} = \frac{1}{L_s L_{s_0}}$ are the gain parameters of the $d-$ and $q-$ axis closed-loop current control loops, respectively. The coefficients $\bar{A}_0 - \bar{A}_5$ and $\bar{B}_0 - \bar{B}_4$

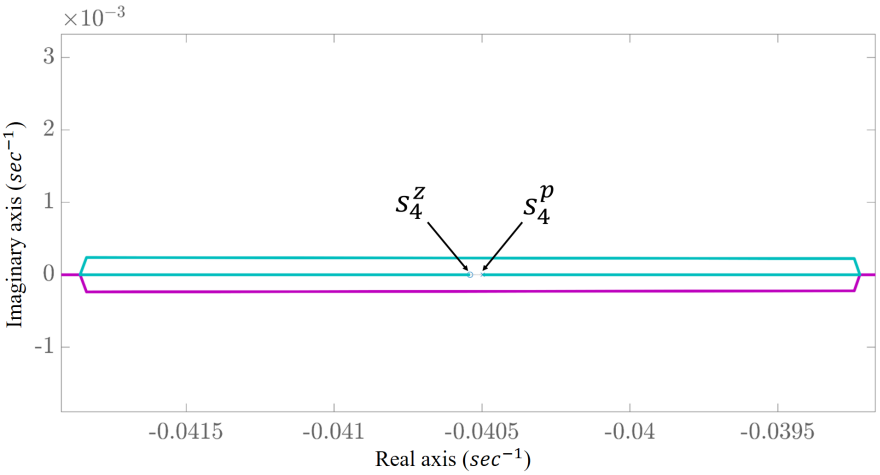

Figure 6.16: Zoomed root locus plot for the closed-loop i_q current control: locations of s_4^z and s_4^p.

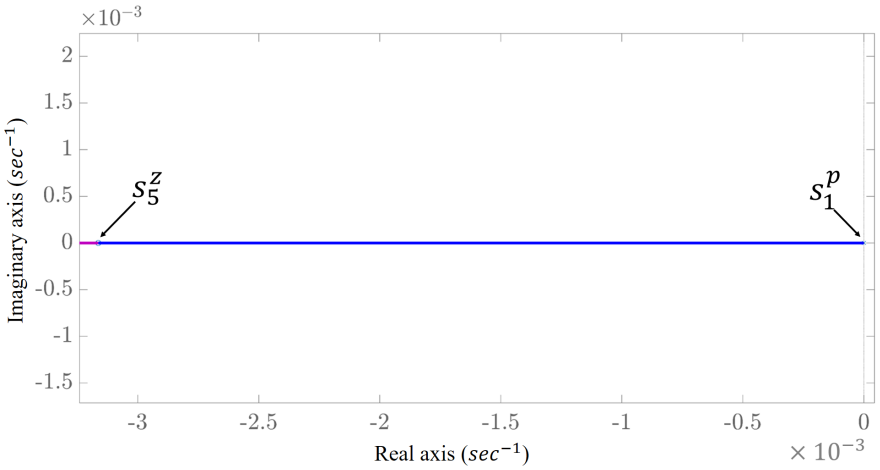

Figure 6.17: Zoomed root locus plot for the closed-loop i_q current control: locations of s_1^p and s_5^z.

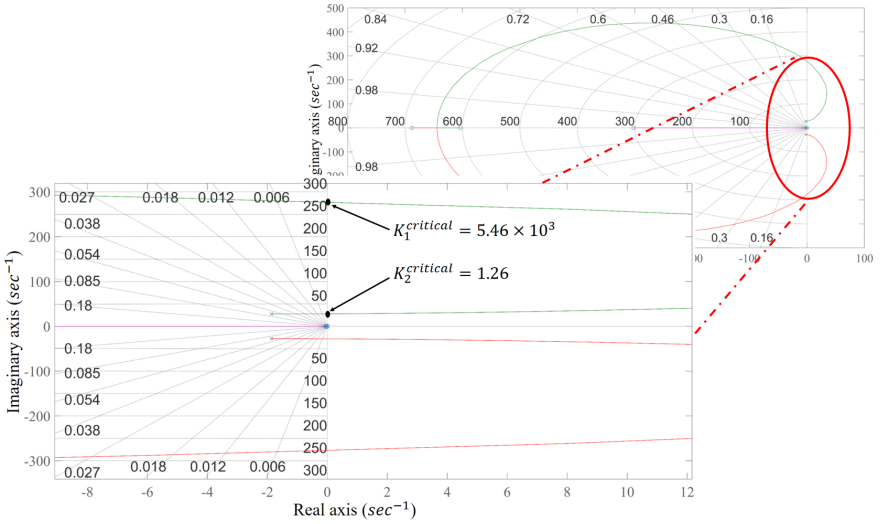

Figure 6.18: Root locus plot for the closed-loop i_q current control with the proposed controller.

are given below

$$\begin{gathered}
\bar{A}_0 = L_{s_0}^2 \left(1 - L_{s_0}\right) \\
\bar{A}_1 = L_{s_0}\left(L_{s_0}\left(k_p^{i_d^r} + l_1^{i_d^r}\right)\left(1 - L_{s_0}\right) + R_s + R_{s_0} - L_{s_0}R_{s_0}\right) \\
\bar{A}_2 = L_{s_0}k_p^{i_d^r}\left(L_{s_0}l_1^{i_d^r} + R_s\right) + \dots \\
\cdots + \left(L_{s_0}^2 k_i^{i_d^r} + L_{s_0}R_{s_0}l_1^{i_d^r} + L_{s_0}^2 l_2^{i_d^r}\right)\left(1 - L_{s_0}\right) + \dots \\
\cdots + L_{s_0}^4 l_2^{i_d^r} + R_s l_1^{i_d^r} L_{s_0} + R_s R_{s_0} \\
\bar{A}_3 = L_{s_0}^2 k_p^{i_d^r} l_2^{i_d^r}\left(1 - L_{s_0}\right) + L_{s_0}^2 k_i^{i_d^r} l_1^{i_d^r}\left(1 - L_{s_0}\right) + L_{s_0}R_s\left(k_p^{i_d^r} l_1^{i_d^r} + k_i^{i_d^r}\right) + \dots \\
\cdots + L_{s_0} l_2^{i_d^r}\left(R_s + R_{s_0}\right) + L_{s_0}R_s k_i^{i_d^r} + L_{s_0}R_{s_0} l_2^{i_d^r}\left(1 - L_{s_0} + L_{s_0}^2\right) \\
\bar{A}_4 = L_{s_0} l_2^{i_d^r}\left(L_{s_0}k_i^{i_d^r}\left(1 - L_{s_0}\right) + R_s\left(k_p^{i_d^r} - R_{s_0}\right)\right) + R_s\left(L_{s_0}k_i^{i_d^r} l_1^{i_d^r} + R_{s_0} l_2^{i_d^r}\right) \\
\bar{A}_5 = L_{s_0}R_s k_i^{i_d^r} l_2^{i_d^r} \\
\bar{B}_0 = 1 \\
B_1 = L_{s_0}\left(k_p^{i_d^r} + l_1^{i_d^r}\right) + R_{s_0} \\
\bar{B}_2 = L_{s_0}k_p^{i_d^r} l_1^{i_d^r} + L_{s_0}k_i^{i_d^r} + L_{s_0} l_2^{i_d^r} - L_{s_0}^2 l_2^{i_d^r} + R_{s_0} l_1^{i_d^r} \\
\bar{B}_3 = L_{s_0}k_p^{i_d^r} l_2^{i_d^r} + L_{s_0}k_i^{i_d^r} l_1^{i_d^r} + R_{s_0} l_2^{i_d^r} - L_{s_0}R_{s_0} l_2^{i_d^r} \\
\bar{B}_4 = L_{s_0}k_i^{i_d^r} l_2^{i_d^r}
\end{gathered} \tag{6.45}$$

and the coefficients $\bar{\bar{A}}_0 - \bar{\bar{A}}_5$ and $\bar{\bar{B}}_0 - \bar{\bar{B}}_4$ are defined as

$$\begin{gathered}
\bar{\bar{A}}_0 = L_{s_0}^2 \left(1 - L_{s_0}\right) \\
\bar{\bar{A}}_1 = L_{s_0}\left(L_{s_0}\left(k_p^{i_q^r} + l_1^{i_q^r}\right)\left(1 - L_{s_0}\right) + R_s + R_{s_0} - L_{s_0}R_{s_0}\right) \\
\bar{\bar{A}}_2 = L_{s_0}k_p^{i_q^r}\left(L_{s_0}l_1^{i_q^r} + R_s\right) + \dots \\
\cdots + \left(L_{s_0}^2 k_i^{i_q^r} + L_{s_0}R_{s_0}l_1^{i_q^r} + L_{s_0}^2 l_2^{i_q^r}\right)\left(1 - L_{s_0}\right) + \dots \\
\cdots + L_{s_0}^4 l_2^{i_q^r} + R_s l_1^{i_q^r} L_{s_0} + R_s R_{s_0} \\
\bar{\bar{A}}_3 = L_{s_0}^2 k_p^{i_q^r} l_2^{i_q^r}\left(1 - L_{s_0}\right) + L_{s_0}^2 k_i^{i_q^r} l_1^{i_q^r}\left(1 - L_{s_0}\right) + L_{s_0}R_s\left(k_p^{i_q^r} l_1^{i_q^r} + k_i^{i_q^r}\right) + \dots \\
\cdots + L_{s_0} l_2^{i_q^r}\left(R_s + R_{s_0}\right) + L_{s_0}R_s k_i^{i_q^r} + L_{s_0}R_{s_0} l_2^{i_q^r}\left(1 - L_{s_0} + L_{s_0}^2\right) \\
\bar{\bar{A}}_4 = L_{s_0} l_2^{i_q^r}\left(L_{s_0}k_i^{i_q^r}\left(1 - L_{s_0}\right) + R_s\left(k_p^{i_q^r} - R_{s_0}\right)\right) + R_s\left(L_{s_0}k_i^{i_q^r} l_1^{i_q^r} + R_{s_0} l_2^{i_q^r}\right) \\
\bar{\bar{A}}_5 = L_{s_0}R_s k_i^{i_q^r} l_2^{i_q^r} \\
\bar{\bar{B}}_0 = 1 \\
B_1 = L_{s_0}\left(k_p^{i_q^r} + l_1^{i_q^r}\right) + R_{s_0} \\
\bar{\bar{B}}_2 = L_{s_0}k_p^{i_q^r} l_1^{i_q^r} + L_{s_0}k_i^{i_q^r} + L_{s_0} l_2^{i_q^r} - L_{s_0}^2 l_2^{i_q^r} + R_{s_0} l_1^{i_q^r} \\
\bar{\bar{B}}_3 = L_{s_0}k_p^{i_q^r} l_2^{i_q^r} + L_{s_0}k_i^{i_q^r} l_1^{i_q^r} + R_{s_0} l_2^{i_q^r} - L_{s_0}R_{s_0} l_2^{i_q^r} \\
\bar{\bar{B}}_4 = L_{s_0}k_i^{i_q^r} l_2^{i_q^r}
\end{gathered} \tag{6.46}$$

Let us consider d- and q- axis current control loops as unity-feedback closed-loop systems which have general scheme as in Figure 6.4, where $sys(s)$ represents an open-

loop transfer function for either d- or q- axis current control. If we denote the open-loop transfer function for the d-axis current control as $sys(s) = sys_{id}(s)$, then from (6.43) it has a form

$$sys_{id}(s) = \frac{\bar{A}_0 s^5 + \bar{A}_1 s^4 + \bar{A}_2 s^3 + \bar{A}_3 s^2 + \bar{A}_4 s + \bar{A}_5}{\bar{B}_0 s^5 + \bar{B}_1 s^4 + \bar{B}_2 s^3 + \bar{B}_3 s^2 + \bar{B}_4 s} \tag{6.47}$$

Similarly, the open-loop transfer function $sys_{iq}(s)$ for the q-axis current control can be expressed as

$$sys_{iq}(s) = \frac{\bar{\bar{A}}_0 s^5 + \bar{\bar{A}}_1 s^4 + \bar{\bar{A}}_2 s^3 + \bar{\bar{A}}_3 s^2 + \bar{\bar{A}}_4 s + \bar{\bar{A}}_5}{\bar{\bar{B}}_0 s^5 + \bar{\bar{B}}_1 s^4 + \bar{\bar{B}}_2 s^3 + \bar{\bar{B}}_3 s^2 + \bar{\bar{B}}_4 s} \tag{6.48}$$

$sys_{id}(s)$ has 5 poles as $s_1^p = 0$, $s_{2,3}^p = 0.7075 \pm 28.5272i$, $s_4^p = -5.2801$, and $s_5^p = -0.0032$, and 5 zeros as $s_{1,2}^z = -677.37 \pm 1.2815i$, $s_3^z = -258.59$, $s_4^z = -5.86$, and $s_5^z = 0$. At the same time, $sys_{iq}(s)$ has 5 poles as $s_1^p = 0$, $s_{2,3}^p = -1.8442 \pm 27.3257i$, $s_4^p = -0.0405$, and $s_5^p = -0.0032$, and 5 zeros as $s_1^z = -717.7694$, $s_2^z = -554.7425$, $s_3^z = -314.9514$, $s_4^z = -0.0405$, and $s_5^z = -0.0032$. The root loci plots for the d-axis current control are given in Figures 6.10-6.13 and the root loci for the q-axis current control are given in Figures 6.15-6.17.

The root locus plots of the $d-$ and $q-$ axis current control loops with critical gain region are shown in Figure 6.14 and Figure 6.18, respectively. As shown, the parameters of the closed-loop current control systems, $\Psi_{i_d^r}$ and $\Psi_{i_q^r}$, depend on the actual value of the inductance, L_s, and its nominal value, L_{s_0}. In Figure 6.14, at $\Psi_{i_d^r} = K^{critical} = 5.46 \times 10^3$ the parametric variation is very high, i.e. the actual inductance is 9.91 times from the nominal value. Similarly, in Figure 6.18 the root locus shows two critical gains for the $q-$ axis current control loop. These gains are achieved when the inductance increases 9.91 times (when $K_1^{critical} = 5.46 \times 10^3$) or1 233 times (when $K_2^{critical} = 1.26$) from the nominal value. We note that the root locus plots for the d- and q-axis current control loops are obtained based on the HODOBC parameters listed in Table 6.1. The closed-loop system becomes more stable and robust to parametric uncertainty at large values of the gain parameters $\Psi_{i_d^r}$ and $\Psi_{i_q^r}$, and this is reasonable, since $\Psi_{i_d^r}$ and $\Psi_{i_q^r}$ are defined as reciprocals of $L_s L_{s_0}$. The variations in the inductance obtained from the root locus are not feasible in practical cases, hence it shows that the current control system with the HODOBC can provide stable and robust system performance for the $d-$ and $q-$ axis current loops.

6.3 Experimental Results

The experimental validations are performed using the experiment stand described in Chapter 2.8. The proposed FOC strategy is compared to the traditional PI-controller-based and traditional DOB-based FOC strategies. The sampling frequency of the DSP hardware is set to 8 kHz. Comparative tests are conducted based on Scenario 1, 2, and

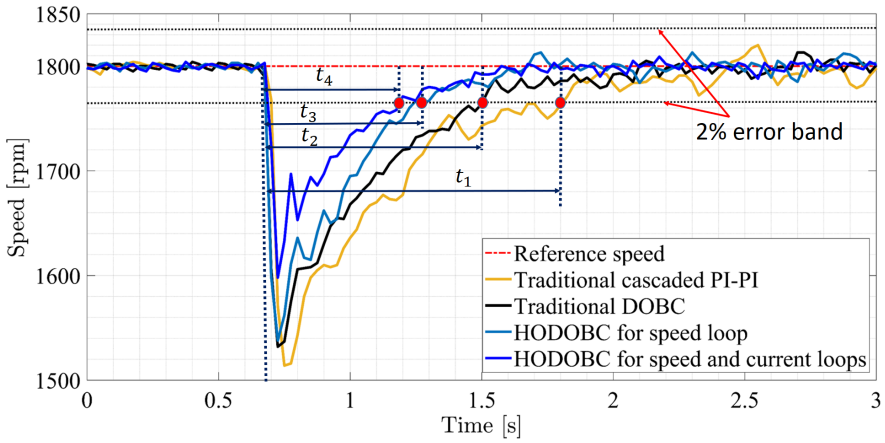

Figure 6.19: Comparative study of the traditional controllers with the proposed controller under Scenario 1 - Speed response.

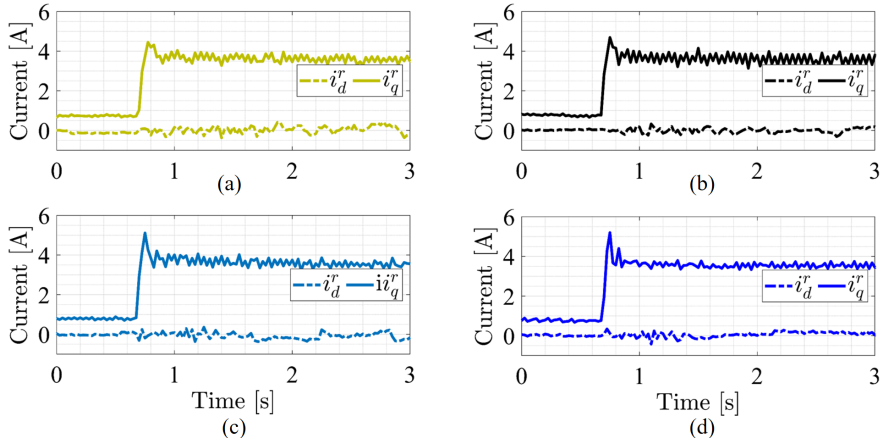

Figure 6.20: Comparative study of the traditional controllers with the proposed controller under Scenario 1 - Current response: (a) Controller-1 (Traditional PI-PI); (b) Controller-2 (Traditional DOBC); (c) Controller-3 (HODOBC for speed loop); (d) Controller-4 (HODOBC for speed and current loops).

3. Four different control schemes named as Controller-1, Controller-2, Controller-3, and Controller-4 are tested in the experiments. The parameters of the controllers are shown in Table 6.1. The SPMSM control system with the cascaded HODOBC is given in Figure 6.21. Controller-1's structure consists of the traditional PI controller in the speed loop, and two traditional PI current controllers. Controller-2 represents a traditional DOBC scheme in a speed control loop and two traditional PI regulators in the current control loops. Controller-3 is a structure in which a speed control is achieved by the HODOBC scheme and $d-q$ currents are controlled by two traditional PI controllers. Finally, Controller-4 is designed using the HODOBC scheme for the speed loop and two HODOBC schemes for the $d-q$ currents regulations. To evaluate performance of each controller a settling time-based criterion is used. To determine the settling time-based criterion, an error band of 2% is chosen.

In Scenario 1, the ability of each controller under sudden change in the load torque has been tested. The load torque in this scenario suddenly increases from 0 $N \cdot m$ to 0.8

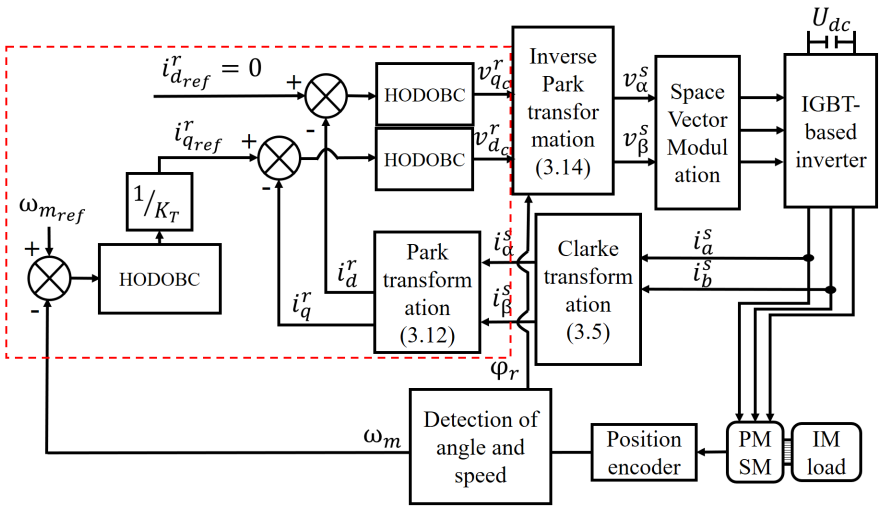

Figure 6.21: A SPMSM control system with the HODOBC.

$N \cdot m$, and the motor speed is regulated at 1800 rpm. Figure 6.19 shows the responses of the rotor speed with each controller, while Figure 6.20 presents current responses with each FOC strategy. From the speed response, it is seen that Controller-1 showing the longest settling time and highest overshoot is the worst among four controllers. Controller-2 is the next controller with shorter settling time and smaller overshoot comparing to Controller-1. The settling is reduced further when Controller-3 is tested, however it is not able to reduce the overshoot showing value similar to Controller-2. Finally, the smallest overshoots and shortest settling time in the speed response are obtained with Controller-4. From Figure 6.20, it is observed that Controller-4 generates the smoothest i^r_q current with less oscillations and the i^r_d current fluctuating around the reference with the smallest error. Furthermore, the i^r_d current generated by Controller-4 is able to quickly recover after the sudden load torque change. Referring to the current responses of other three controllers, the i^r_d current generated by those controllers takes longer time to recover after the load torque change, whereas the i^r_q current becomes oscillating under the applied load torque. To conclude Scenario 1, it can be stated that in comparison with Controller-1, Controller-2, and Controller-3, Controller-4 is able to achieve the smallest transient and steady-state tracking errors and shortest settling time for both speed and current tracking regulation under the load torque change.

In Scenario 2, the reference mechanical speed $\omega_{m_{ref}}$ rises up from 1000 rpm to 1800 rpm, whereas the load torque is kept at 0.8 $N \cdot m$. The tracking performance of the reference speed and $d-q$-current responses of each tested FOC schemes are given in Figure 6.22 and Figure 6.23, respectively. From Figure 6.22 it is seen that the speed performances of Controller-1, Controller-2, and Controller-3 are without much difference at the steady-state. Based on the results, Controller-1 has the worst dynamic with longest settling time, while with the small difference from Controller-1 Controller-2 shows the second worst result. Considering the current performances reveals that each

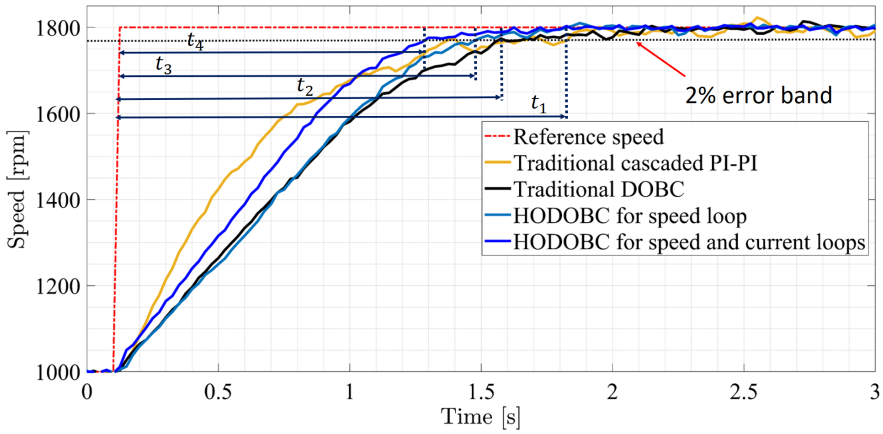

Figure 6.22: Comparative study of the traditional controllers with the proposed controller under Scenario 2 - Speed response.

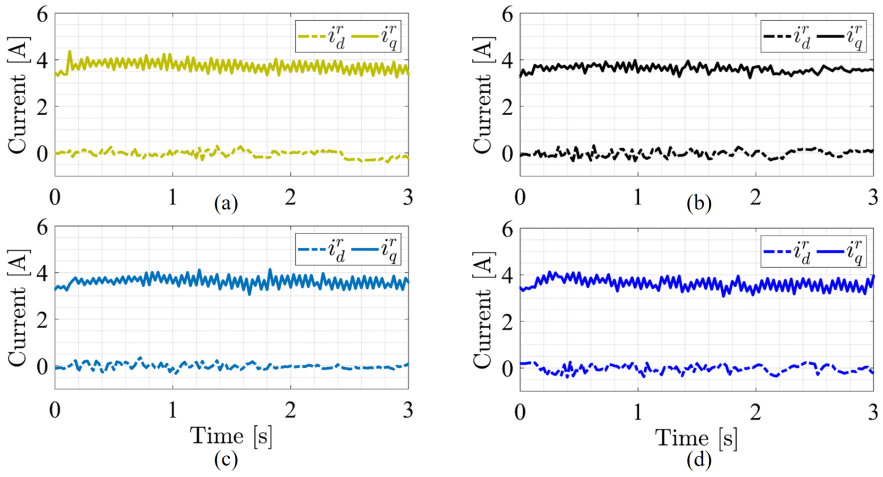

Figure 6.23: Comparative study of the traditional controllers with the proposed controller under Scenario 2 - Current response: (a) Controller-1 (Traditional PI-PI); (b) Controller-2 (Traditional DOBC); (c) Controller-3 (HODOBC for speed loop); (d) Controller-4 (HODOBC for speed and current loops).

controller is able to generate intensive i_q^r during in the transient region. However, the Controller-4 becomes the best in regulating the i_d^r current comparing to others. The i_d^r current generated by Controller-4 has less oscillations and smaller tracking error, whereas other three control schemes cannot suppress oscillations and generate the larger steady-state tracking error. Comparing Controller-3 and Controller-4, it reveals that although both controllers are not different in terms of settling time criteria of the speed response, Controller-4 still performs better in regulating the i_d^r and i_q^r currents under the load torque.

In Scenario 3, the performances of the controllers are tested during the ramp increase of the reference mechanical speed $\omega_{m_{ref}}$ from 1000 rpm to 2000 rpm with a sudden step increase of the load torque from 0 $N \cdot m$ to 0.8 $N \cdot m$ during the ramp change of the speed reference. The speed and current response of each FOC strategy are depicted in Figure 6.24 and Figure 6.25, accordingly. The worst controller is Controller-1 showing

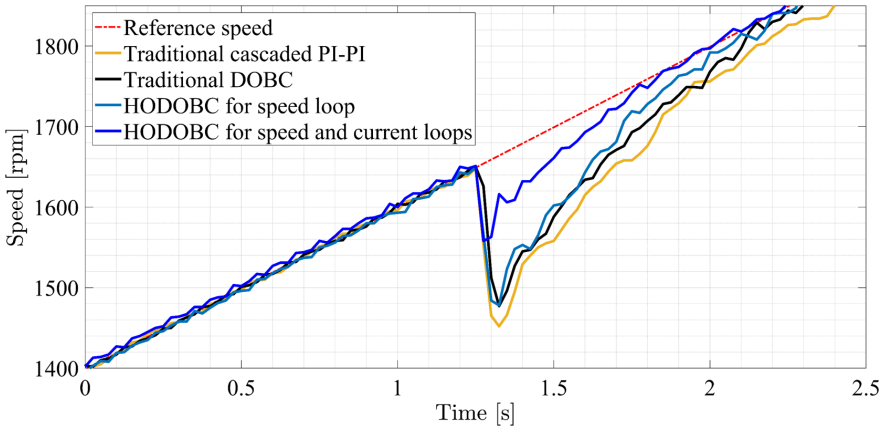

Figure 6.24: Comparative study of the traditional controllers with the proposed controller under Scenario 3 - Speed response.

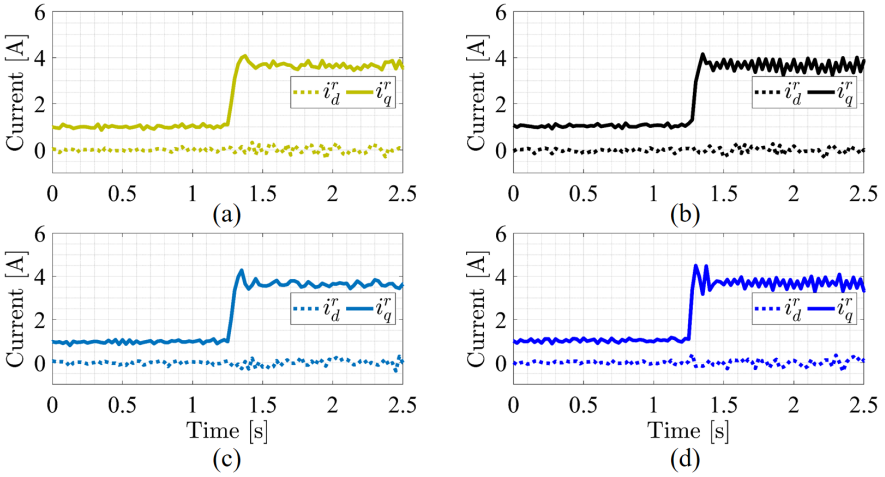

Figure 6.25: Comparison of current responses of the traditional controllers and the proposed controller under Scenario 3: (a) Traditional cascaded PI-PI; (b) Traditional DOBC; (c) HODOBC for the speed loop; (d) HODOBC for the speed and current loops.

the largest speed drop and longest time to recover. Controller-2 and Controller-3 result in the same speed drop, but Controller-3 is faster in converging to the reference speed. Since during the ramp increase of the speed the motor is not at steady-state anymore, the obtained speed performance of Controller-4 in Figure 6.24 substantiates that it is able to accomplish the fastest convergence rate to the reference speed with smallest speed drop during the transient mode comparing to others. The i_d^r dynamics is similar in each controller's case. Referring to the i_q^r current, it is more intensive in the case of Controller-4 and less intensive in the case of Controller-1. The high intensity of the i_q^r generated by Controller-4 can be explained by the resultant fast dynamics of the controller in tracking the reference ramp speed under the load torque change.

6.4 Summary

This chapter presents a composite controller named as the HODOBC proposed to control both speed and current loops in the SPMSM. Generally, the HODOBC's scheme includes a traditional PI controller and traditional ESO with parameters derived via the LQR formulation. Hence, this chapter is more about the technique of tuning the PI controller as well ESO in the traditional ADRC approach. The derivation of the HODOBC for the speed and current control loops takes parameter variations into account as well. Since the i_d^r and i_q^r have nonlinear dynamics the ESO blocks with optimal parameters are integrated to the PI controllers to improve robustness of the current tracking control. The stability analysis of the speed and current tracking controllers are performed using the well-known root locus technique. The obtained experimental outcomes show that the proposed controller is able to guarantee better speed and current tracking performance and high robustness under the disturbance changes comparing to the traditional cascaded PI-PI control and traditional DOBC schemes. The results also show that the integration of the ESO to the current control greatly improves the disturbance rejection ability and overall response of the SPMSM control system. The design steps of the HODOBC for the speed control is illustrated in Figures 6.8-6.9, and we note that one can use the same steps to apply the proposed method to control d- and q- axis currents as well.

BLANK

Chapter 7

Unification of dynamic delay of DOBC and ADRC: SPMSM example

7.1 Introduction

In the original DOBC scheme, the disturbance observer includes a nominal plant model and the filtering element, in most cases, represented by low-pass filter (LPF). In the original ADRC scheme, the bounded total disturbance is taken as an extra state variable. Based on this, the ESO is designed to estimate disturbance. Previously, different studies are conducted to compare the DOBC and ADRC schemes. In [143], the DOBC and ADRC are compared during the application for drive position control system, and it is concluded that the ADRC scheme is better in terms of performance and robustness comparing to the DOBC scheme. The study in [144] reveals that, in the DOBC, if a nominal plant is taken as an integrator (series of integrators) then the disturbance observer in the DOBC scheme becomes as a linear case of the ESO. Relation between the DOBC scheme and ADRC scheme is investigated, and combination of the DOBC and ADRC is proposed for a PMSM in [145]. Preliminary results on comparison of the DOBC and ADRC schemes to control a PMBLDC are shown in [146]. Unfortunately, dynamical delays of these two schemes are not considered.

Based on the provided literature review, two main points should be figured out: 1) there is no detailed assessment on dynamical delays of the disturbance estimation in the DOBC and ADRC schemes. Such detailed analysis on the dynamic delay of the estimation might help for an engineer to establish an accurate formula of estimation during the design of a control system in a time domain; 2) There is no such study that unifies the DOBC and ADRC schemes. The unification of these schemes might help for an engineer to receive benefits of both approaches while synthesizing a controller. It means that one can select the delay estimation of the LPF in the DOBC scheme and, further, design an ADRC-based control system to overcome the effect of derivative operation existing in the DOBC.

In this chapter, results of the study on unification of dynamical delays of DOBC and ADRC schemes with detailed formulas of the delays are presented. The explicit formulas

of disturbance estimation identifies the components as follows: external disturbance (mainly load torque change), disturbance due to parameter uncertainties, and dynamical delay of disturbance estimation. Via the simulations and experiments, it is proved that the DOBC and ADRC can be unified.

7.2 Traditional Control Scheme

7.2.1 Traditional speed control scheme

Recall that the traditional PI controller applied to the rotor's speed control of the SPMSM have a form as:

$$T_{e_{ref}}^{PI} = \left(k_p^{\omega_e} + \frac{k_i^{\omega_e}}{s}\right)\left(\omega_{e_{ref}} - \omega_e\right) \tag{7.1}$$

where $k_p^{\omega_e}$ and $k_i^{\omega_e}$ are the proportional and integral parameters of the controller, accordingly. $\omega_{e_{ref}}$ and ω_e are the reference and actual electrical speed of the motor, respectively. Using (7.1) and inversion of the electromechanical relationship in (2.57) the reference q-axis current ($i_{q_{ref}}^r$) is calculated, while the reference d-axis current ($i_{d_{ref}}^r$) is set to zero.

Remark 7.2.1. *The d-q currents are also regulated by two PI controllers which are designed based on the electrical equations given in (2.71), the output of the current controllers are the reference voltage commands v_d^r and v_q^r served as inputs to the PWM block. The decoupling of the back-EMF terms, inverse reference frame transformations, and PWM are implemented.*

The described traditional PI control scheme is utilized as a base to describe disturbance observer-based control schemes analyzed in the further sections.

7.3 Structure of the traditional DOBC and ADRC schemes

7.3.1 DOBC scheme

Let us consider a structure of the traditional DOB scheme presented in Figure 3.1. The output $Y(s)$ is affected by the control input $U_c(s)$ and external disturbance $Z(s)$. The control input $U_c(s)$ consists of two parts such as control signal $U_b(s)$ which responsible for stabilizing a system performance and the estimated lumped disturbance $\hat{\epsilon}_0(s)$ as a output of the DO. Note that $\hat{\epsilon}_0(s)$ is considered as a sum of the external disturbance $Z(s)$ and parametric uncertainty. From the input-output relationship in Figure 3.1 which is

shown in (3.5), the external disturbance can be expressed by

$$Z(s) = -(U_c(s) - P(s)^{-1}Y(s)). \tag{7.2}$$

Where $P^{-1}(s)$ is an inverse of the actual plant. In theory, the external disturbance $Z(s)$ can be exactly calculated. However, in practice, a precise plant model is hard to achieve. Hence, it is possible to use a nominal model $P_n(s)$ to replace the actual plant in calculation of the inverse in (7.2). However, the inverse of the nominal plant belong to a category of non-causal systems. Therefore, a filter $Q_{DOB}(s)$ is added to resolve the lack of the causality such that the inverse of the nominal plant becomes causal. Adding of the filter creates a delay in the observer system. To equate delay time of the observer, the same filter is integrated to the path of $U_c(s)$. The disturbance observer results in the estimation of the lumped disturbance which is a sum of the external disturbance and parametric uncertainty created due to the difference between the actual plant $P(s)$ and nominal plant $P_n(s)$. From Figure 3.1, the estimation of the lumped disturbance $\hat{\epsilon}_0$ can be deduced as

$$\hat{\epsilon}_0(s) = Q_{DOB}(s)(P_n^{-1}(s)Y(s) - U_c(s)) \tag{7.3}$$

Also from Figure 3.1, the control input and plant output are derived respectively as $U_c(s) = U_b(s) - \hat{\epsilon}(s)$ and $Y(s) = P(s)(U_b(s) - \hat{\epsilon}(s) + Z(s))$. Hence (7.3) can modified as

$$\hat{\epsilon}(s) = \frac{Q_{DOB}(s)P_n^{-1}(s)P(s)Z(s) - Q_{DOB}(s)U_b(s)(1 - P_n^{-1}(s)P(s))}{1 - Q_{DOB}(s)(1 - P_n^{-1}(s)P(s))} \tag{7.4}$$

Then the control signal $U_c(s)$ is designed

$$U_c(s) = \frac{U_b(s) - Q_{DOB}(s)P_n^{-1}P(s)Z(s)}{1 - Q_{DOB}(s)(1 - P_n^{-1}(s)P(s))} \tag{7.5}$$

From (7.5) it follows that the disturbance rejection mechanism could perfectly work when $Q_{DOB}(s) = 1$, and this would lead to the simplified control signal $U_c(s)$ as

$$U_c(s) = \frac{U_b(s)}{P_n^{-1}(s)P(s)} - Z(s) \tag{7.6}$$

where the plant's parameter uncertainties could be compensated by the term $\frac{U_b(s)}{P_n^{-1}(s)P(s)}$ and hence the external disturbance could be eliminated by the term $-Z(s)$.

7.3.2 ADRC scheme

Design of the ADRC scheme is based on the state-space model of the plant $P(s)$, where the lumped disturbance is considered as an extra state variable. Note that unlike the DO in the DOBC scheme, the ESO used as a part of the ADRC scheme is able to estimate both matched and unmatched disturbances. As in the DOBC scheme, the stabilization

of the compensated plant is achieved by the baseline controller usually implemented as a PI scheme. In this work, the first-order ADRC which is used to control a first-order plant or a plant of an integral form is presented.

Recall a SISO system in (3.1) presented as

$$\begin{cases} \dot{\chi} = a + bu \\ y = \chi \end{cases} \tag{7.7}$$

Then taking into account parameter variations, the system in (7.7) can be written as

$$\begin{cases} \dot{\chi} = \epsilon + b_0 u \\ y = \chi \end{cases} \tag{7.8}$$

where a_0 and b_0 are nominal system parameters, Δa and Δb are parameter variations, respectively. A term $\epsilon = a_0 + \Delta a + \Delta b u$ represents a generalized disturbance or lumped disturbance which consists of the external disturbance z and parameter uncertainties Δa and Δb.

Considering ϵ as an extra state variable, the given plant $P(s)$ can be presented in the state-space form with state vector $\chi_{ext} = \begin{bmatrix} \chi \\ \epsilon \end{bmatrix}$ as

$$\begin{cases} \dot{\chi}_{ext} = \bar{A}_{ext}\chi_{ext} + \bar{B}_{ext}u + \bar{E}_{ext}\dot{\epsilon} \\ y = \bar{C}_{ext}\chi_{ext} \end{cases} \tag{7.9}$$

where $\bar{A}_{ext} = \begin{bmatrix} 0 & 1 \\ 0 & 0 \end{bmatrix}$, $\bar{B}_{ext} = \begin{bmatrix} b_0 \\ 0 \end{bmatrix}$, $\bar{C}_{ext} = \begin{bmatrix} 1 & 0 \end{bmatrix}$, and $\bar{E}_{ext} = \begin{bmatrix} 0 \\ 1 \end{bmatrix}$. Based on (7.9), the ESO is designed via the Luenberger observer

$$\begin{cases} \dot{\hat{\chi}}_{ext} = \bar{A}_{ext}\hat{\chi}_{ext} + \bar{B}_{ext}u + L(y - \bar{C}_{ext}\hat{\chi}_{ext}) \\ \hat{y} = \hat{\chi}_{ext} \end{cases} \tag{7.10}$$

in which $L = \begin{bmatrix} l_1 \\ l_2 \end{bmatrix}$ is the ESO gain to be designed, $\hat{\chi}_{ext} = \begin{bmatrix} \hat{y} \\ \hat{\epsilon} \end{bmatrix}$ is the estimation of the extended state vector. A transfer function of the closed-loop Luenberger observer model in (7.10) is

$$G^{ESO} = \frac{l_2}{s^2 + l_1 s + l_2} \tag{7.11}$$

where $G^{ESO} = \frac{\hat{\epsilon}}{\epsilon}$. As it is seen from (7.11), the ESO gains l_1 and l_2 are the poles of the closed-loop transfer function of the observer, hence these gains should be chosen properly. According to the separation principle, the observer can be synthesized separately from the feedback stabilizing controller. Once the ESO is designed, the composite control law under the ADRC framework is presented as

$$u = u_b - \frac{1}{b_0}\hat{\epsilon} \tag{7.12}$$

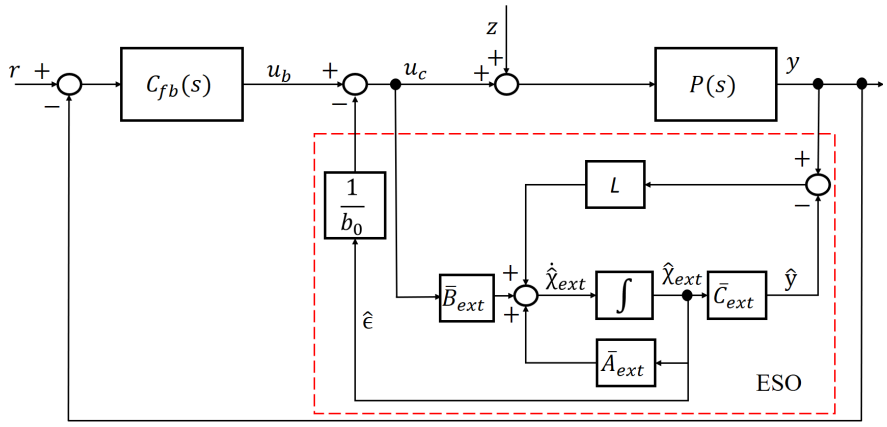

Figure 7.1: ADRC scheme

where u_b is a feedback stabilizing control law.

After substitution of (7.12) into (7.8) gives

$$\dot{\chi} = (\epsilon - \hat{\epsilon}) + b_0 u_b \tag{7.13}$$

From (7.13), it is seen that the generalized disturbance can be eliminated in the case when $G^{ESO} = 1$ or when $\epsilon = \hat{\epsilon}$. Once ϵ is compensated, the plant model is simplified as

$$\begin{cases} \dot{\chi} = b_0 u_b \\ y = \chi \end{cases} \tag{7.14}$$

The traditional scheme of the ADRC is displayed in Figure 7.1, where $u = u_c$.

7.4 Disturbance estimation: analogy of the DOBC and ADRC

This section provides comparison of estimation of the lumped disturbance by the disturbance observers in the traditional DOBC and ADRC schemes. It is noted that two schemes are utilized the same PI controller for the feedback stabilization. This means that comparison of the DOBC and ADRC leads to comparison of the disturbance observer (DO) and ESO.

Since we consider a speed control loop, the actual plant model $P(s)$, control input $U_c(s)$, the system output $Y(s)$, and the external disturbance $Z(s)$ are $\frac{1}{J_m s}$, $T_e(s)$, $\omega_e(s)$, and $z_m(s)$, respectively. The nominal plant model is $P_n(s) = \frac{1}{J_{m_0} s}$. Here, the variation in the parameter is expressed by the difference $\Delta J = J_m - J_{m_0}$. Since the current control is usually ten time faster than the speed loop, it is assumed that $T_e(s) = T_{e_{ref}}(s)$, where $T_{e_{ref}}(s)$ is a torque command generated by the DO-based control schemes (DOBC or ADRC). Furthermore, the design of the DO requires the electromagnetic torque as an input, hence the DO in the DOBC and ESO in the ADRC use the estimation of the

electromagnetic torque, i.e. $T_{e_{est}}(s)$. Thus, $U_c(s)$ in these two DO-based schemes can be denoted as $U_c(s) = T_e(s) = T_{e_{ref}}(s) = T_{e_{est}}(s)$. The feedback stabilizing controller $C_{fb}(s)$ is represented by the control signal $U_b(s) = T^{PI}_{e_{ref}}(s)$ which in turn represented by the PI controller given in (7.1).

We shall notice that in this work variations in mechanical part represented as parametric uncertainties in J_m and frictions parameters shown in (2.40) are addressed. Variations in electrical parameters such as stator resistance R_s and inductances in the $d-q$-frame, i.e. L_d and L_q, are neglected. Hence, this study assumes that the inner current control loop is designed properly, and only the outer speed control loop needs to be adjusted.

7.4.1 Calculations for the DOBC scheme

From Figure 3.1, the estimated lumped disturbance $\hat{\epsilon}$ can be derived as

$$\hat{\epsilon}^{DOBC}(s) = Q_{DOB}(s)\left(T_{e_{est}}(s) - J_{m_0} s\omega_{m_e}(s)\right) \tag{7.15}$$

where $T_{e_{est}(s)}$ as the first input to the DO is obtained as

$$T_{e_{est}}(s) = T^{DOBC}_{e_{ref}} = T^{PI}_{e_{ref}}(s) + \hat{\epsilon}^{DOBC}(s) \tag{7.16}$$

and rotor's speed $\omega_e(s)$ as the second input to the DO is given as

$$\omega_e(s) = \frac{1}{J_m s}(T^{PI}_{e_{ref}}(s) + \hat{\epsilon}^{DOBC}(s) - z_m(s)) \tag{7.17}$$

Once, after substitution of $T_{e_{est}}(s)$ and $\omega_e(s)$ into (7.15), the explicit formulation of the lumped disturbance estimation is resulted as

$$\hat{\epsilon}^{DOBC}(s) = \frac{Q_{DOB}(s)(1 - J_{m_0}J_m^{-1})T^{PI}_{m_{ref}(s)} + Q_{DOB}(s)J_{m_0}J_m^{-1}z_m(s)}{1 - Q_{DOB(s)}(1 - J_{m_0}J_m^{-1})} \tag{7.18}$$

Hence, from the explicit expression of $\hat{\epsilon}^{DOBC}(s)$, one can see that it is defined in terms of the external disturbance $z_m(s)$ and variations in parameter expressed as $(1-J_{m_0}J_m^{-1})$.

Finally, the torque command of the motor $T^{DOBC}_{e_{ref}}(s)$ in (7.16) can be defined in the explicit form

$$T^{DOBC}_{e_{ref}}(s) = \frac{T^{PI}_{e_{ref}}(s) + Q_{DOB}(s)J_{m_0}J_m^{-1}z_m(s)}{1 - \frac{Q_{DOB}(s)}{p}(1 - J_{m_0}J_m^{-1})} \tag{7.19}$$

7.4.2 Calculations for the ADRC scheme

Let us consider the rotor's dynamic equation in (2.69) in terms of the electrical speed

$$\dot{\omega}_e = \frac{p}{J_m}(T_e - T_{friction}) \tag{7.20}$$

where $T_{friction} = T_{fr} - T_v - T_{flux} - T_L$. Further, (7.20) can be modified as follows

$$\dot{\omega}_e = \frac{p}{J_{m_0}} T_e + \left(\frac{p(J_{m_0} - J_m)}{J_{m_0} J_m} T_e - \frac{p}{J_m} T_{friction} \right) \tag{7.21}$$

Hence, the lumped disturbance ϵ^{ADRC} is defined in terms of the parameter variation and friction torque $T_{friction}$ as

$$\epsilon^{ADRC} = \left(\frac{p(J_{m_0} - J_m)}{J_{m_0} J_m} T_e - \frac{p}{J_m} T_{friction} \right) \tag{7.22}$$

The estimation of the lumped disturbance is obtained via the closed-loop transfer function of the ESO

$$\hat{\epsilon}^{ADRC} = G^{ADRC} \epsilon^{ADRC} = G^{ADRC} \left(\frac{p(J_{m_0} - J_m)}{J_{m_0} J_m} T_{e_{est}} - \frac{p}{J_m} T_{friction} \right) \tag{7.23}$$

Recall that the ϵ^{ADRC} is used as an extended state $\chi_{ext} = \begin{bmatrix} \omega_e \\ \epsilon^{ADRC} \end{bmatrix}$ in the ESO design which is based on the Luenberger observer given in (7.10) with $b_0 = \frac{p}{J_{m_0}}$.

The torque command in the ADRC scheme is deduced as

$$T_{e_{ref}}^{ADRC} = T_{e_{ref}}^{PI} - \frac{1}{b_0} \hat{\epsilon}^{ADRC} = T_{e_{ref}}^{PI} - \frac{1}{b_0} G^{ADRC} \left(\frac{p(J_{m_0} - J_m)}{J_{m_0} J_m} T_{e_{est}} - \frac{p}{J_m} T_{friction} \right) \tag{7.24}$$

By recalling that $T_{e_{est}} = T_{e_{ref}}^{ADRC}$, the torque command in (7.24) is shown in the form

$$T_{e_{ref}}^{ADRC} = \frac{T_{e_{ref}}^{PI} + G^{ESO} J_{m_0} J_m^{-1} T_{friction}}{1 - \frac{G^{ESO}}{p} (1 - J_{m_0} J_m^{-1})} \tag{7.25}$$

The effectiveness of two considered composite control schemes mainly relies on the efficiency of the observers used in each scheme. Note that when the filtering element of the DO in the DOBC scheme has same dynamics as the closed-loop transfer function of the ESO in the ADRC scheme, i.e. $Q_{DOB} = G^{ESO}$, the delays in dynamics of both observers will be unified. This condition results in the sameness of the torque commands in (7.19) and (7.25), i.e. $T_{e_{ref}}^{DOBC} = T_{e_{ref}}^{ADRC}$. Consequently, it means that the DOBC and ADRC schemes are able to show same performance in the speed control of motor drives.

To show the veracity of the observations provided above, in this work, the filtering element of the DOBC Q_{DOB} and the closed-loop transfer function of the ESO G^{ESO} are chosen as a second-order transfer function with the form given in (7.11). The transfer function parameters l_1 and l_2 are obtained such that to have observers with dynamics faster than that of the dynamics of the speed feedback control.

Remark 7.4.1. *Note that the motor torque commands provided in (7.19) and (7.25) are reasonable, i.e. the denominator of each control law never becomes zero. This fact can be shown as follows:*

Let us examine the denominators of both (7.19) and (7.25)

$$1 - \frac{G^{observer}}{p}(1 - J_{m_0}J_m^{-1}) = 1 - \frac{1}{p}\frac{l_2}{s^2 + l_1 s + l_2}(1 - J_{m_0}J_m^{-1}) \tag{7.26}$$

where $G^{observer} = G^{DO} = G^{ESO}$*. Hence, the next three cases referring to the difference* $1 - J_{m_0}J_m^{-1}$ *can guarantee the non-zero denominator:*

1. *Case when* $J_{m_0} = J_m$*, then the denominator becomes one, i.e.* $1 - \frac{G^{observer}}{p}(1 - J_{m_0}J_m^{-1}) = 1$

2. *Case when* $J_{m_0} > J_m$*, then the denominator is larger than one, i.e.* $1 - \frac{G^{observer}}{p}(1 - J_{m_0}J_m^{-1}) > 1$*, since* $1 - J_{m_0}J_m^{-1} < 0$ *and* $G^{observer} > 0$ *for every* $l_1 \geq 0$ *and* $l_2 \geq 0$*.*

3. *Case when* $J_{m_0} < J_m$*, then the denominator is larger than zero, i.e.* $1 - \frac{G^{observer}}{p}(1 - J_{m_0}J_m^{-1}) > 0$*, since* $1 - J_{m_0}J_m^{-1} < 1$ *and* $G^{observer} < 1$ *for every* $l_1 \geq 0$ *and* $l_2 \geq 0$*.*

It is seen that all possible cases with J_{m_0} *and* J_m *guarantee that the synthesized control laws in (7.19) and (7.25) are reasonable.*

Recommendation on a process of control design: Owing to unified dynamic delay of the DOBC and ADRC schemes, some recommendations on the process of controller design are presented below:

- Using the information of the low-pass filter (LPF) $Q_{DOB}(s)$ used in the DOBC scheme one can determine the desirable dynamical delay of estimation. The LPF should be capable to eliminate unwanted noise in the system. Furthermore, the designed DO should have faster response time than that of the feedback stabilizing controller $C_{fb}(s)$.

- Once the desirable dynamical delay of estimation is obtained, the closed-loop poles of the ESO transfer function G^{ESO} can be selected. Hence, this dynamical delay unification serves as a link between the filtering element in the DOBC scheme and obtaining poles of the ESO in the ADRC design.

- Next, the vector of gains of the ESO is calculated. Eventually, a composite controller as an ADRC depicted in Figure 7.1 is designed. Note that comparing to the DOBC scheme, the ADRC scheme is less susceptible to noise of the system, since its implementation does not require a derivative action.

7.4.3 Stability analysis of the DO-based closed-loop schemes

The stability of the DOBC and ADRC schemes are analyzed using the root locus approach. The output of the DO-based control system can be represented as

$$\omega_e(s) = G^{\omega_e}_{\omega_{e_{ref}}}(s)\omega_{e_{ref}}(s) + G^{\omega_e}_{z}(s)T_{friction}(s) \tag{7.27}$$

where $G^{\omega_e}_{\omega_{e_{ref}}}(s) = \frac{\omega_e}{\omega_{e_{ref}}}\Big|_{T_{friction}=0} = \frac{(s^2+l_1s+l_2)(k_p^{\omega_e}s+k_i^{\omega_e})}{(s^2+l_1s+l_2)(k_p^{\omega_e}s+k_i^{\omega_e})+s^2(J_ms^2+l_1J_ms+l_2J_{m_0})}$ and $G^{\omega_e}_{z} = \frac{\omega_e}{T_{friction}}\Big|_{\omega_{e_{ref}}=0} = \frac{-s(s^2+l_1s)}{(s^2+l_1s+l_2)(k_p^{\omega_e}s+k_i^{\omega_e})+s^2(J_ms^2+l_1J_ms+l_2J_{m_0})}$.

The characteristic equation of the closed-loop DO-based control system is

$$(s^2 + l_1s + l_2)(k_p^{\omega_e}s + k_i^{\omega_e}) + s^2(J_ms^2 + l_1J_ms + l_2J_{m_0}) = 0 \tag{7.28}$$

Based on (7.28), the modified characteristic equation in terms of the system gain parameter Ψ_{gain} can be obtained as follows

$$1+\Psi_{gain}\frac{\frac{1}{J_{m_0}}k_p^{\omega_e}s^3 + \left(\frac{1}{J_{m_0}}(k_p^{\omega_e}l_1 + k_i^{\omega_e}) + l_2\right)s^2 + \frac{1}{J_{m_0}}\left(k_p^{\omega_e}l_2 + k_i^{\omega_e}l_1\right)s + \frac{1}{J_{m_0}}k_i^{\omega_e}l_2}{s^4 + l_1s^3} = 0 \tag{7.29}$$

The gain parameter Ψ_{gain} in (7.29) is defined in terms of the nominal and actual inertia values, i.e. $\Psi_{gain} = \frac{J_{m_0}}{J_m}$. Based on the modified characteristic equation in (7.29), a root locus of the closed-loop DO-based system can be plotted as in Figure 7.2. From the root locus plot, it is observed that the closed-loop DO-based system may remain to be stable for sufficiently large parameter variation. The system becomes unstable when $\Psi_{gain} = 0.591$, i.e. when the actual moment of inertia J_m increases 1.69 times from the nominal value J_{m_0}. In fact, this amount of variation in inertia value is rare in practice. Consequently, according to the root locus analysis, the stability and robustness of the DO-based closed-loop system can be safely ensured.

7.4.4 Discrete-time implementation

Experiments on the hardware require a discrete model of the observers. This study uses a Tustin method to approximate a continuous time variable s to discrete one as the following

$$s = \frac{2(z-1)}{\bar{T}_s(z+1)} \tag{7.30}$$

where $\bar{T}_s$ represents a sampling period specified by the hardware setup. Hence, with using of (7.30) the discrete-time versions of the DOBC and ADRC can be represented

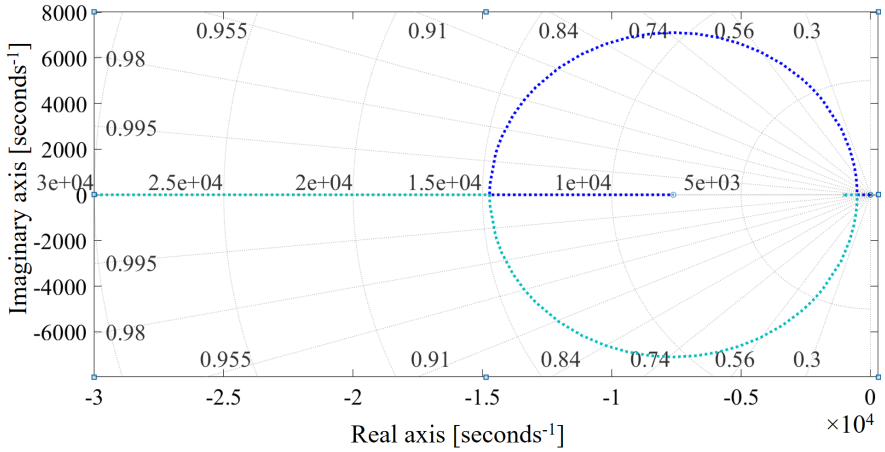

(a) Root locus diagram for the system (7.27)

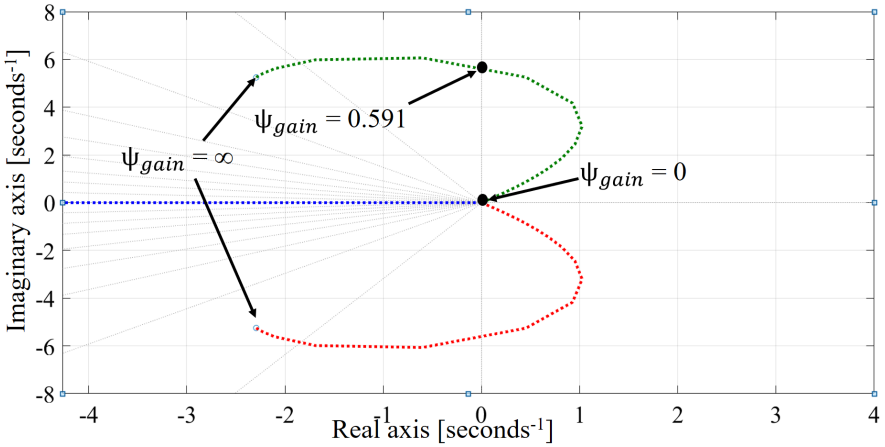

(b) Zoomed root locus diagram

Figure 7.2: Root locus analysis of the system in (7.27)

in Figure 7.3 and Figure 7.4, accordingly. The parameters used in the discretization are

$$\begin{aligned} \bar{n} &= \frac{4}{\bar{T}_s^2 l_2} \\ \bar{m} &= \frac{2l_1}{\bar{T}_s l_2} \\ b_0 &= \frac{1}{J_{m_0}} \end{aligned} \tag{7.31}$$

Based on the discrete-time implementation, it is shown that the ADRC scheme has more handy structure to implement since its discrete form contains only discrete-time integrators and some algebraic manupilations on the observer's inputs. Therefore, due to the dynamical unification of the DOBC and ADRC schemes, it would be favorable to obtain the gains of the observer under the DOBC framework, and afterwards implement the ADRC to cancel out disturbance effect.

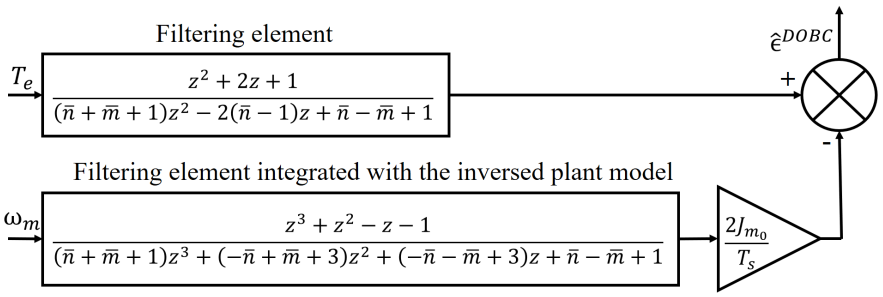

Figure 7.3: Discrete-time implementation of the DOBC scheme

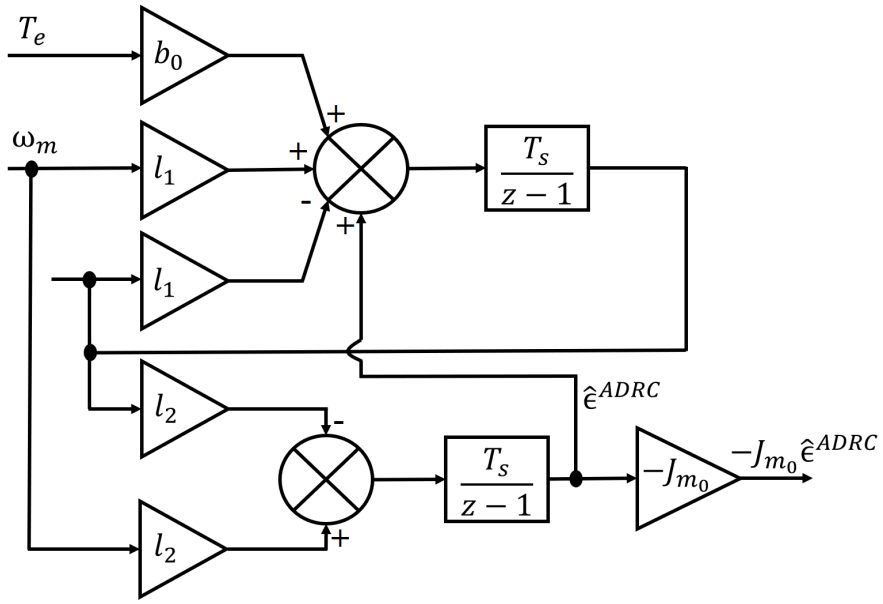

Figure 7.4: Discrete-time implementation of the ADRC scheme

Table 7.1: Controller and Observers Design

PI Controller	**Disturbance Observers**
$k_p^{\omega_e} = 0.005$	$l_1 = 1000$
$k_i^{\omega_e} = 0.125$	$l_2 = 10000$

7.5 Simulation results

In the simulation studies, the SPMSM runs at a constant reference speed of 2500 rpm without any load, and a step load torque is applied at steady-state operation of the motor. One of the advantages of the simulation is that it allows us to check a performance of a scheme in the ideal case where the friction torque $T_{friction}$ is totally available and can be directly eliminated in the feedforward scheme. Hence, two controllers such as the traditional PI controller and the ideal case controller serve as a base for the two DO-based control schemes. Figure 7.5a shows performances of the DOBC and ADRC schemes which proves the dynamical unification of both methods. In Figure 7.5a, a

sudden load torque is applied at 0.1 s, and both observer converge to the value shown by the dashed-dot red line. Note that this dashed red line represents a lumped disturbance to be estimated. The performance of the DOBC (black solid line) and ADRC (the blue dashed line) are same, since they show identical convergence time of 0.4 s, and this happens due to $Q_{DOB} = G^{ESO}$. The estimation of the DO $\hat{\epsilon}^{DOBC}$ in the DOBC is equal to the estimation of the ESO $\hat{\epsilon}^{ADRC}$ in the ADRC after its multiplication by $-\frac{1}{b_0}$, which results in $-J_{m_0}\hat{\epsilon}^{ADRC}$.

It is accentuated that the convergent time of 0.4 s is not accidental outcome, i.e. it is determined due to the observer parameters listed in Table 7.1.

Due to the equal performance of the DOBC and ADRC schemes, the motor speed response for both control schemes is indistinguishable as shown in Figure 7.5b. Consequently, the unification of two schemes is proven. In the mean time, the traditional PI scheme (the golden solid line) shows the largest speed drop comparing to the DOBC and ADRC working under the same conditions. The $d-q$ current responses plotted in Figure 7.5c and Figure 7.5d reveal the advantage of the disturbance attenuation control schemes. From those plots, it is seen that under the load torque change the DOBC and ADRC generate currents with faster dynamics and with less amplitude comparing to the traditional PI scheme.

In order to affirm the performance of each tested control methods under the critical condition, a step load torque of 0.5 $N \cdot m$ is applied when the motor accelerates from 1700 rpm to 2000 rpm. As in the previous condition, the DOBC and ADRC have quicker response and show smaller speed drop in contrast to the tradition PI scheme (Figure 7.6). It is notable that this condition in which the motor examines a sudden load change during its acceleration is severe and presented seldom in previous research studies.

7.6 Experimental results

Two DO-based control techniques are tested using the experimental stand presented in Section 2.8. The mechanical speed of the motor is regulated at 2500 rpm. In the first experiment, a sudden step load torque is applied to the motor running at the steady state speed of 2500 rpm. Figure **??** depicts the speed response of the motor controlled by each tested control schemes. From this plot, both DOBC and ADRC ensure the similar efficiency in attenuating of an effect of the external disturbance and parameter change in the speed control. This indistinguishable effectiveness of the two DO-based schemes is resulted due to the unification of the dynamical delays of observer in the DOBC and ESO in the ADRC, respectively. Generally, without consideration of delay in dynamics of observers it is hard to exactly compare DO-based control schemes.

Even if the DOBC and ADRC schemes show similar speed response, the ADRC is

preferable than the DOBC in terms of implementation point of view. Since, the DOBC requires a derivative action in its implementation, this scheme is highly susceptible to undesired measurement noises. With respect to the ADRC scheme, it has easier discretization process comparing to the DOBC for high-order systems. From Figure 7.7a, two DO-based schemes show the smallest speed drop of 2%, whereas the traditional PI controllers is the worst one with the speed drop of 8%.

The dynamics of the $d-q$ currents are shown in Figure 7.7b and Figure 7.7c for the traditional PI and DO-based control schemes, respectively. Since the experiments are conducted at speed below the rated speed of the SPMSM, the d-axis current is regulated at zero reference value. The current dynamics in Figure 7.7c are same for each DO-based control scheme, which in turn verifies that motor torque commands shown by (7.19) and (7.25) are similar with unified dynamical delays of the observers.

Finally, Figure 7.8 presents the experimental outcomes for the motor accelerating its speed from 1700 rpm to 2000 rpm and suddenly imposed by step load torque of 0.5 $N \cdot m$. It is observed that the traditional PI controller shows higher speed drop in the experiment comparing to the simulation test in Figure 7.6. This phenomenon is justified by the uncertainties in the model which create such difference. Unlike the traditional PI scheme, the DOBC and ADRC schemes almost replicate the results shown by simulations. This fact establishes the superiority of the DO-based control schemes to cope with uncertainties in a model. In overall, the experimental studies confirm again that the DOBC and ADRC scheme can be unified due to the identical efficiency in disturbance attenuation, speed tracking performance, and stator current dynamics.

The performance data for the constant speed and accelerating speed operations of the motor are given in Figure 7.9 and Figure 7.10, respectively. The provided data show the superiority of the DO-based control techniques over the traditional PI and affirm again the similar peformance of the DOBC and ADRC scheme.

7.7 Summary

This chapter presents an analysis of performances of two popular disturbance observer based control schemes, DOBC and ADRC, in the speed control application of the SPMSM. The transparent formulas for the disturbance estimation of the DO and ESO are derived for the first time. Using the transparent formulas of the observers dynamical delays of each observer are shown. Consequently, via using the identical dynamical delays of the observers, the DOBC and ADRC schemes are unified. The theoretical knowledge is validated via the extensive simulation and experimental outcomes. According to the results, the DOBC and ADRC schemes have similar performance under the effect of external torque and mismatch in the parameter.

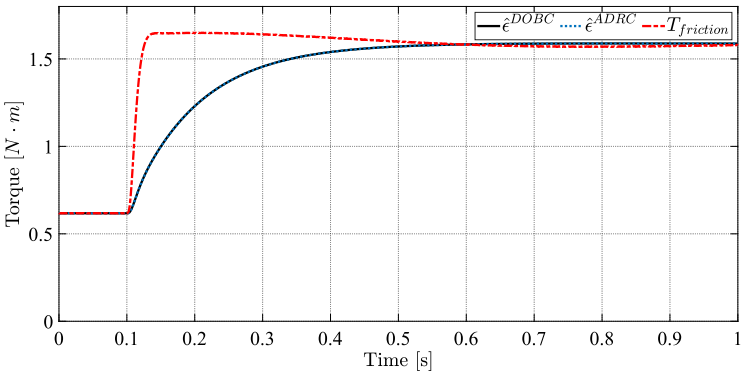

(a) Estimated disturbance

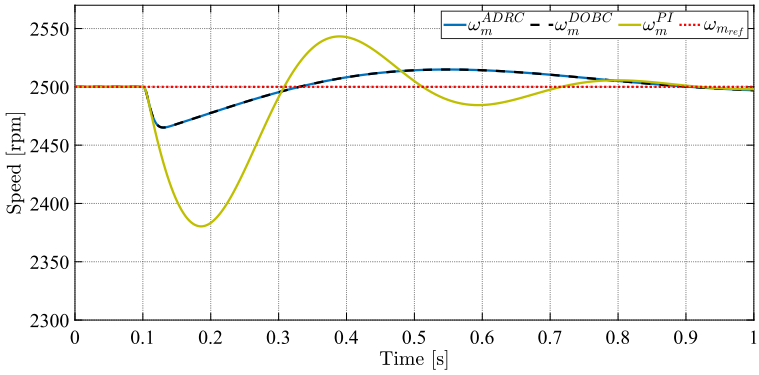

(b) Motor speed response

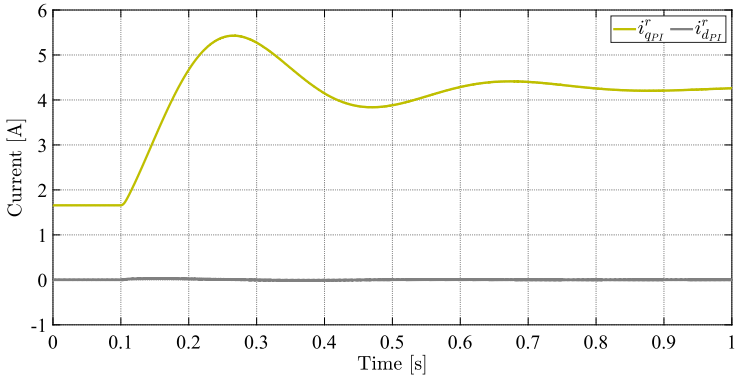

(c) Motor currents with PI speed controller

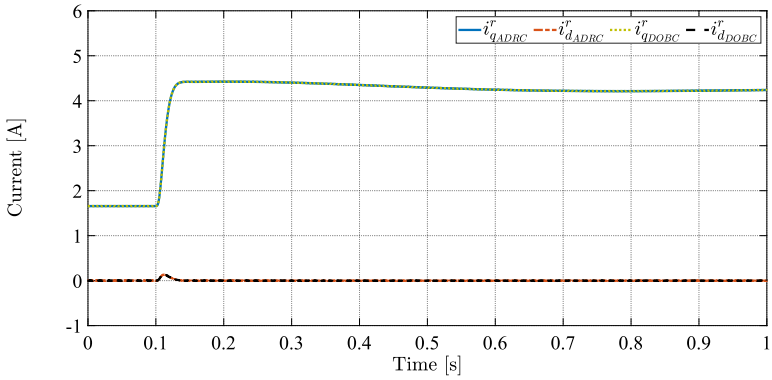

(d) Motor currents with DOBC and ADRC speed controllers

Figure 7.5: Simulation results during the sudden load change at constant speed.

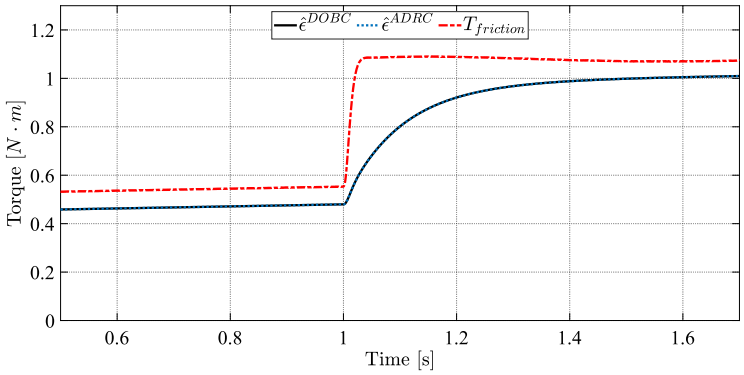

(a) Disturbance estimation in the DOBC and ADRC schemes

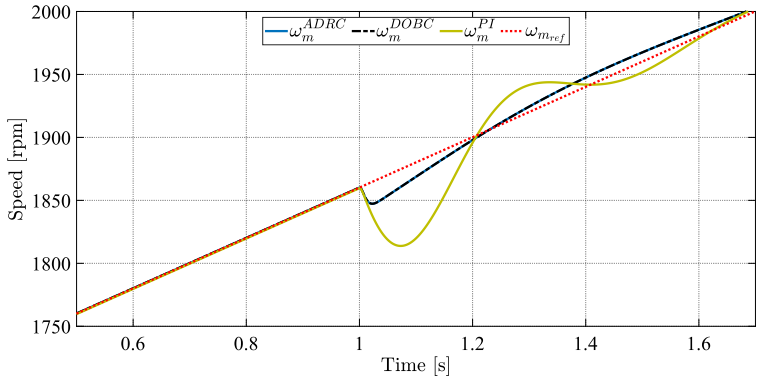

(b) Speed response

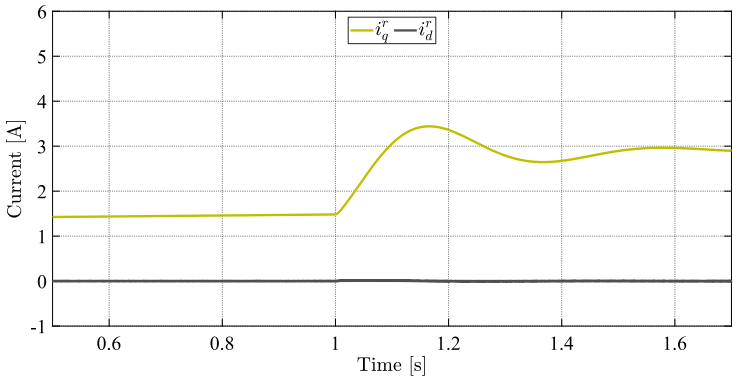

(c) Current response for the PI scheme

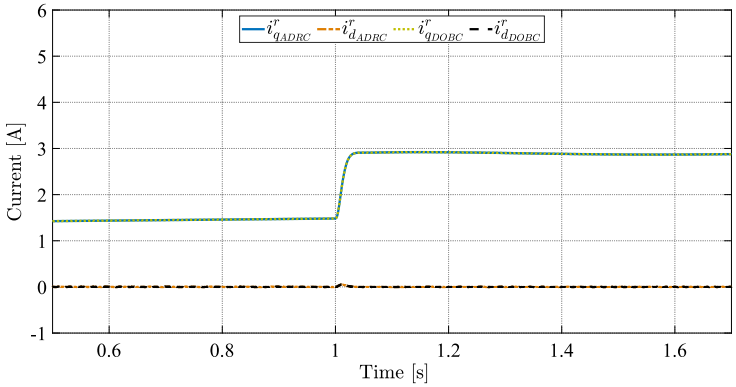

(d) Current response for the DOBC and ADRC schemes

Figure 7.6: Simulation results of the sudden load torque change during the motor acceleration.

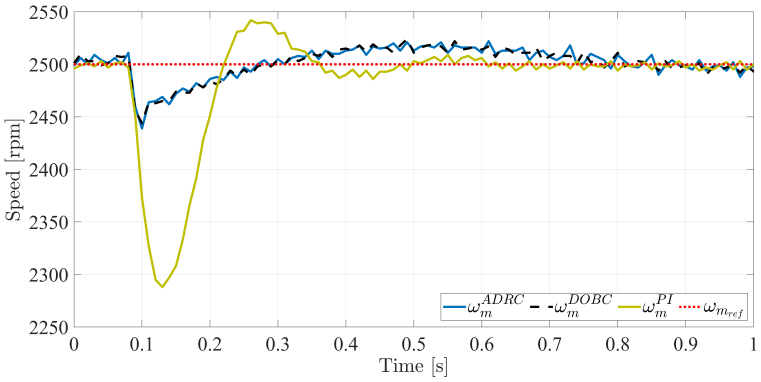

(a) Speed response

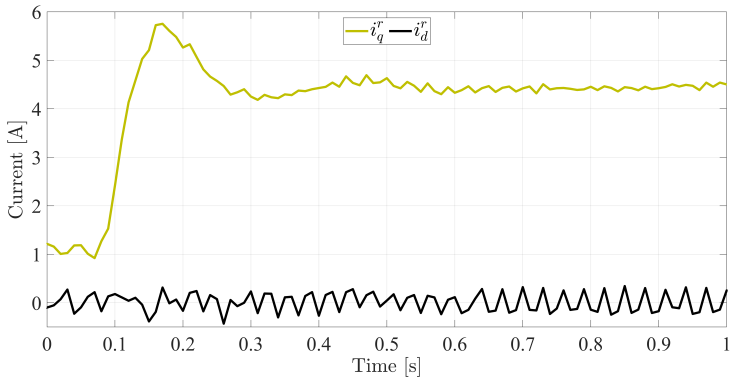

(b) Current response for the PI scheme

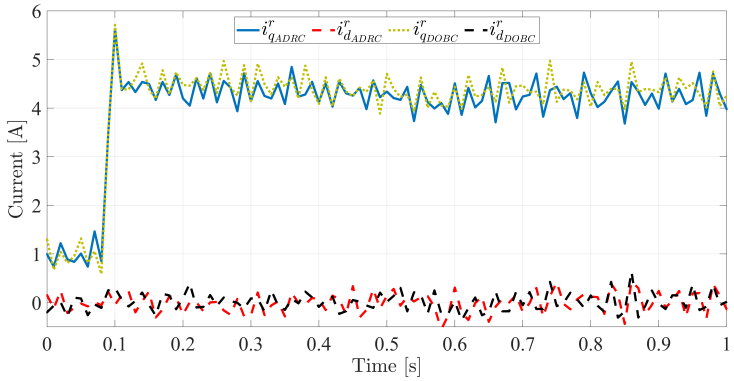

(c) Current response for the DOBC and ADRC schemes

Figure 7.7: Experimental results of the sudden load torque change during the constant speed operation.

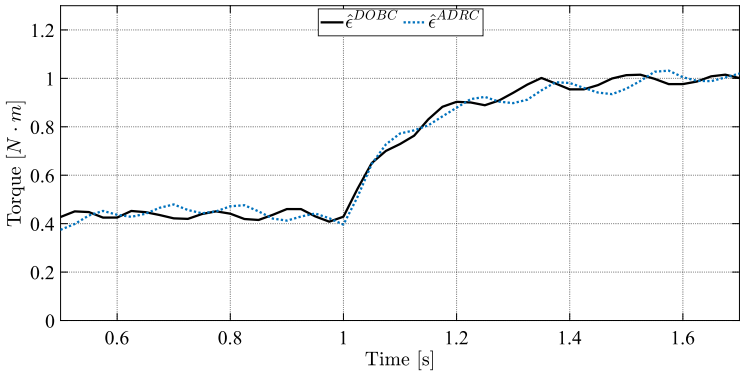

(a) Disturbance estimation in the DOBC and ADRC schemes

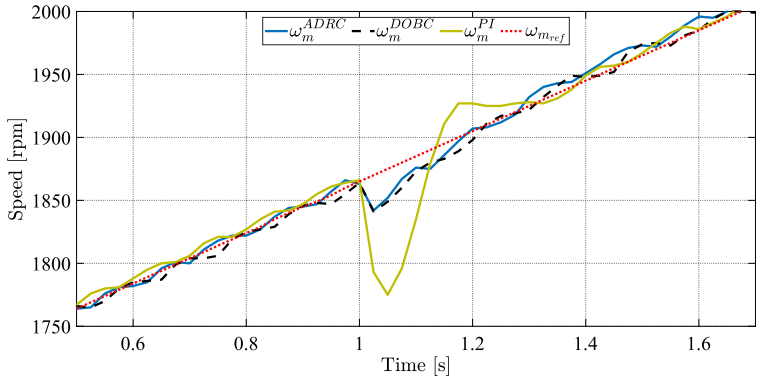

(b) Speed response

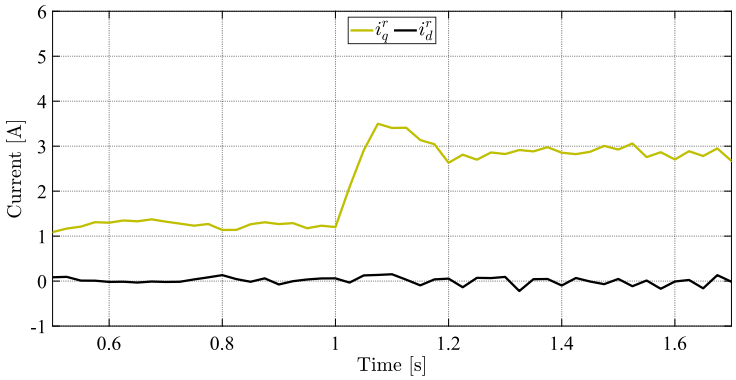

(c) Current response for the PI scheme

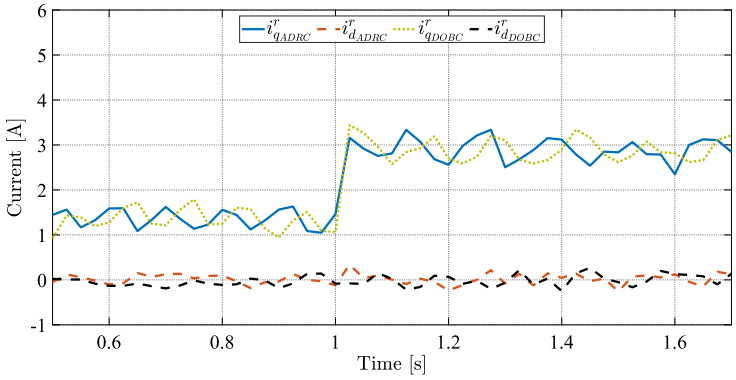

(d) Current response for the DOBC and ADRC schemes

Figure 7.8: Experimental results of the sudden load torque change during the motor acceleration.

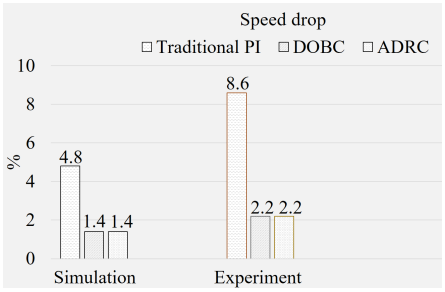

(a)

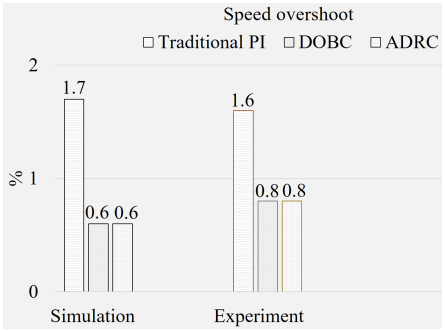

(b)

Figure 7.9: Speed drop and overshoot percentage under the load torque change at constant speed

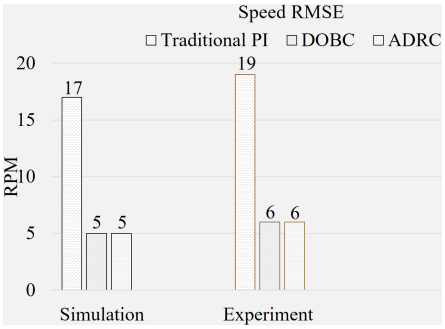

Figure 7.10: Reference speed tracking RMSE when the motor accelerates.

Chapter 8

Conclusions and Future work

8.1 Summary of the contribution

This thesis presents three different methods for control the SPMSM based on the FOC strategy. The analysis and comparison of the traditional DOBC and ADRC schemes are also presented in this thesis. It should be noted that those three methods have similar objectives such that to achieve accurate speed tracking performance and enhance robustness of the SPMSM control system in presence of different uncertainties. However, they are different in terms of design and contributions.

The first method is called as HDOBCC, which is a composite controller consisting of a fuzzy-PI speed controller and generalized high-order disturbance observer (GHDO). The fuzzy-PI speed controller is utilized to stabilize speed control loop of the SPMSM, once disturbance is compensated via the feedforward loop. The GHDO is designed to estimate lumped disturbance represented by uncertainties due to external load, parameter mismatch, and modelling errors. The detailed stability analysis of the proposed composite control method is performed and performances of the three different orders of the proposed GHDO are compared. The order of the proposed observer is increased little by little until the efficiency of two consecutive orders remains unchanged. The transient time dynamics of the rotor's speed is improved by utilizing fuzzy logic to calculate parameters of the PI controller. The i_d^r and i_q^r currents are regulated by two traditional PI controllers. During the design of the speed controller, it is assumed that the current controls loop are well-designed. The comparative experimental studies between the traditional cascaded control system, consisting of one PI speed controller and two PI current controllers, and the proposed HDOBCC are presented.

The second proposed controller called as DR-PI is designed based on the modified DOBC scheme. The proposed method is represented by a PI-like form, where a pre-filter is used to eliminate an overshoot which is typical for the traditional PI controller. Comparing to the traditional DOBC scheme where the disturbance observer and PI controller are designed apart, in the DR-PI scheme the controller and observer are not separated. In this method, information about an order of a plant is enough for controller design, and no need to know nominal parameters of the plant as it is required in the traditional DOBC design. Thanks to the simple PI-like form, a tuning procedure of the DR-PI and stability analysis of the closed loop system become straightforward. Experimental results show that the proposed DR-PI scheme is able to provide better

performance comparing to the traditional DOBC during transient period of operation of the motor.

The third proposed controller called as HODOBC is designed based on the theory of optimal control. This control scheme consists of the PI controller which is used to regulate reference tracking performance and the ESO to estimate lumped disturbance and compensate it in the feedforward loop. The optimal control approach is used to calculate the parameters of the PI controllers in the speed and current loops. The performance of the PMSM is studied when the HODOBC is applied for speed control and for speed-current control under the FOC strategy. The experimental results show that the SPMSM operates better when both speed and current control loops are regulated with the HODOBC, and its reference tracking performance and robustness to parameter mismatches become superior comparing to the cases with the traditional cascaded PI control and DOBC schemes. The stability of the HODOBC-based closed system is shown using the root locus method.

Finally, we present analysis of the traditional DOBC and ADRC schemes with application to speed control of the SPMSM. Transparent formulas of estimated disturbance via the DOBC and ADRC are derived. From the transparent formulas of the estimated disturbance, it is possible to identify components such as external disturbance, disturbance due to parameter mismatch, and dynamical delay due to disturbance estimation. The unification of these well-known disturbance rejection schemes may help for engineers to get benefits while designing of a controller. After unification of the methods, designer can select estimation delay of the LPF of the DOBC scheme, and use it to design an ADRC method to resolve issues with derivative operation typical for the DOBC scheme. Stability of both control schemes is analysed in the frequency domain via the root locus method.

To conclude, in this thesis we studied techniques of disturbance estimation of PMSMs. We have studied recent work on disturbance estimation techniques proposed for PMSMs. Among the methods proposed in this thesis, the HDOBCC method is more about designing of novel disturbance observer for PMSM that estimates not only disturbance but also its high order derivatives. Hence, the HDOBCC can be considered as another version of disturbance observer-based technique improved via the combination of the fuzzy-PI and GHDO. The proposed DR-PI method is more about improvement on the traditional PI controller where disturbance rejection mechanism is integrated into the structure of the PI controller. Furthermore, it helps to explicitly tune the parameters of the controller by taking into account the parameters of the filtering element and desired closed-loop system. The HODOBC method is also proposed to show a novel method of designing of the disturbance observer-based composite controller where the PI controller and observer have optimal parameters. On the basis of the SPMSM setup, all the proposed solutions are compared experimentally with the

well-known traditional methods as PI controller, DOBC, and ADRC, and in all tests the proposed methods show better reference tracking performance and robustness under different form of external disturbance. Lastly, a research on the performance analysis of the DOBC and ADRC is conducted to unify these two methods. Unification of these methods can be beneficial for control engineers while designing proper disturbance rejection controller.

8.2 Limitations of the research

Although several control schemes were proposed to speed control of the SPMSM, there are still some important limitations need to be considered and studied.

1. During the design of the speed controllers, the current control loops are regulated by the traditional PI controllers and it is assumed that the controllers are well-tuned. As shown from the simulation and experimental results, the traditional PI controllers may degrade at some operating points of a system. The performance analysis of the current control loops are omitted during the design of speed controller.

2. Although the proposed HDOBCC method shows quite good performance in disturbance estimation, the question about the size of upper bound of disturbance derivatives remains to be open.

3. The DR-PI control design in this thesis is proposed for minimum-phase system, and further analysis on extending its application to control non-minimum phase systems might be required. Furthermore, the DR-PI is proposed for systems with maximum relative degree of 2. Since the proposed DR-PI has an integrator term in its structure, potential anti-windup issue may arise in case of current saturation. Furthermore, the proposed DR-PI method is designed in continuous-time domain, while most control systems require discretized version of a control algorithm, performance of discretized DR-PI scheme remains to be further studied. Lastly, the speed and accuracy of disturbance estimation of the DR-PI is not investigated in the current research, and these questions could be considered as a next step of research.

4. The traditional DOBC scheme is able to estimate and compensate only matched disturbance, whereas the traditional ADRC schemes is capable to estimate and compensate both matched and unmatched type of disturbance. In the current research, the delay unification of these two DO-based techniques are achieved in terms of estimation of matched type disturbance, which means that the proposed theory is limited to systems working under matched type disturbance.

5. Finally, all designed methods in this thesis require exact model of a plant to be available, which could limit application of these methods for systems with unknown models.

8.3 Future work

As future work we can mention the following directions:

1. In the proposed methods provided in this thesis, the speed and current control loops are designed separately under the FOC strategy. It is interesting and promising to analyze relationship of time constants of the inner current loop and outer speed loop in order to systematically choose parameters of controller and observer as well.

2. In the GHDOB and DR-PI methods, the proposed methods are applied to control only speed loop, hence it would be next research studies to apply these methods to the current loop as well.

Bibliography

[1] S. Vaez-Zadeh, *Control of permanent magnet synchronous motors*. Oxford University Press, 2018.

[2] S. Manias, *Power electronics and motor drive systems*. Academic Press, 2016.

[3] K. H. Nam, *AC motor control and electric vehicle applications*. CRC press, 2017.

[4] L. Wang, S. Chai, D. Yoo, L. Gan, and K. Ng, *PID and predictive control of electrical drives and power converters using MATLAB/Simulink*. John Wiley & Sons, 2015.

[5] S.-K. Sul, *Control of electric machine drive systems*. John Wiley & Sons, 2011.

[6] Y. Liu, *Contributions to Disturbance-Observer-Based Control: Application to Synchronous Motor-Based Variable Speed Drive Systems*. PhD thesis, Bourgogne Franche-Comté, 2020.

[7] D. Mohanraj, J. Gopalakrishnan, B. Chokkalingam, and L. Mihet-Popa, "Critical aspects of electric motor drive controllers and mitigation of torque ripple-review," *IEEE Access*, 2022.

[8] K. Suleimenov and T. D. Do, "Design and analysis of a generalized high-order disturbance observer for pmsms with a fuzy-pi speed controller," *IEEE Access*, vol. 10, pp. 42252–42260, 2022.

[9] K. Suleimenov and T. D. Do, "A practical disturbance rejection control scheme for permanent magnet synchronous motors," *Symmetry*, vol. 14, no. 9, p. 1873, 2022.

[10] S. Li, J. Yang, W.-H. Chen, and X. Chen, *Disturbance observer-based control: methods and applications*. CRC press, 2014.

[11] J. Yang, W.-H. Chen, S. Li, L. Guo, and Y. Yan, "Disturbance/uncertainty estimation and attenuation techniques in pmsm drives—a survey," *IEEE Transactions on Industrial Electronics*, vol. 64, no. 4, pp. 3273–3285, 2016.

[12] E. Sariyildiz, "A guide to design disturbance observer-based motion control systems in discrete-time domain," in *2021 IEEE International Conference on Mechatronics (ICM)*, pp. 1–6, IEEE, 2021.

[13] H. Kobayashi, S. Katsura, and K. Ohnishi, "An analysis of parameter variations of disturbance observer for motion control," *IEEE Transactions on Industrial Electronics*, vol. 54, no. 6, pp. 3413–3421, 2007.

[14] S. Komada, N. Machii, and T. Hori, "Control of redundant manipulators considering order of disturbance observer," *IEEE Transactions on Industrial Electronics*, vol. 47, no. 2, pp. 413–420, 2000.

[15] C. Zhongyi, S. Fuchun, and C. Jing, "Disturbance observer-based robust control of free-floating space manipulators," *IEEE Systems journal*, vol. 2, no. 1, pp. 114–119, 2008.

[16] Y. Oh and W. K. Chung, "Disturbance-observer-based motion control of redundant manipulators using inertially decoupled dynamics," *IEEE/ASME transactions on mechatronics*, vol. 4, no. 2, pp. 133–146, 1999.

[17] K. Yang, Y. Choi, and W. K. Chung, "On the tracking performance improvement of optical disk drive servo systems using error-based disturbance observer," *IEEE Transactions on Industrial Electronics*, vol. 52, no. 1, pp. 270–279, 2005.

[18] K. K. Tan, T. H. Lee, H. F. Dou, S. J. Chin, and S. Zhao, "Precision motion control with disturbance observer for pulsewidth-modulated-driven permanent-magnet linear motors," *IEEE Transactions on Magnetics*, vol. 39, no. 3, pp. 1813–1818, 2003.

[19] E. Sariyildiz, S. Hangai, T. Uzunovic, T. Nozaki, and K. Ohnishi, "Stability and robustness of the disturbance observer-based motion control systems in discrete-time domain," *IEEE/ASME Transactions on Mechatronics*, vol. 26, no. 4, pp. 2139–2150, 2020.

[20] X. Zhou, W. Zhong, Y. Ma, K. Guo, J. Yin, and C. Wei, "Control strategy research of d-statcom using active disturbance rejection control based on total disturbance error compensation," *IEEE Access*, vol. 9, pp. 50138–50150, 2021.

[21] X. Zhou, Q. Liu, Y. Ma, and B. Xie, "Dc-link voltage research of photovoltaic grid-connected inverter using improved active disturbance rejection control," *IEEE Access*, vol. 9, pp. 9884–9894, 2021.

[22] J. Yang, H. Cui, S. Li, and A. Zolotas, "Optimized active disturbance rejection control for dc-dc buck converters with uncertainties using a reduced-order gpi observer," *IEEE Transactions on Circuits and Systems I: Regular Papers*, vol. 65, no. 2, pp. 832–841, 2017.

[23] M. Li, J. Zhao, Y. Hu, and Z. Wang, "Active disturbance rejection position servo control of pmslm based on reduced-order extended state observer," *Chinese Journal of Electrical Engineering*, vol. 6, no. 2, pp. 30–41, 2020.

[24] H. Sira-Ramírez, J. Linares-Flores, C. García-Rodríguez, and M. A. Contreras-Ordaz, "On the control of the permanent magnet synchronous motor: An active disturbance rejection control approach," *IEEE Transactions on Control Systems Technology*, vol. 22, no. 5, pp. 2056–2063, 2014.

[25] W. Zhang, H. Zhu, Y. Xu, and M. Wu, "Direct control of bearingless permanent magnet slice motor based on active disturbance rejection control," *IEEE Transactions on Applied Superconductivity*, vol. 30, no. 4, pp. 1–5, 2020.

[26] C. Sun, C. Liu, X. Feng, and X. Jiao, "Visual servoing of flying robot based on fuzzy adaptive linear active disturbance rejection control," *IEEE Transactions on Circuits and Systems II: Express Briefs*, vol. 68, no. 7, pp. 2558–2562, 2021.

[27] S. Gu, J. Zhang, S. Zou, K. Zhao, and Z. Ma, "Trajectory tracking control for delta parallel manipulators: A variable gain adrc approach," *IEEE Robotics and Automation Letters*, vol. 7, no. 3, pp. 7747–7754, 2022.

[28] V.-T. Nguyen, C.-Y. Lin, S.-F. Su, W. Sun, and M. J. Er, "Global finite time active disturbance rejection control for parallel manipulators with unknown bounded uncertainties," *IEEE Transactions on Systems, Man, and Cybernetics: Systems*, vol. 51, no. 12, pp. 7838–7849, 2020.

[29] W. Xue, R. Madonski, K. Lakomy, Z. Gao, and Y. Huang, "Add-on module of active disturbance rejection for set-point tracking of motion control systems," *IEEE Transactions on Industry Applications*, vol. 53, no. 4, pp. 4028–4040, 2017.

[30] H. H. Choi, N. T.-T. Vu, and J.-W. Jung, "Design and implementation of a takagi–sugeno fuzzy speed regulator for a permanent magnet synchronous motor," *IEEE Transactions on Industrial Electronics*, vol. 59, no. 8, pp. 3069–3077, 2011.

[31] L. Li, G. Pei, J. Liu, P. Du, L. Pei, and C. Zhong, "2-dof robust h_∞ control for permanent magnet synchronous motor with disturbance observer," *IEEE Trans. Power Electron.*, vol. 36, no. 3, pp. 3462–3472, 2021.

[32] Z. Kuang, B. Du, S. Cui, and C. C. Chan, "Speed control of load torque feedforward compensation based on linear active disturbance rejection for five-phase pmsm," *IEEE Access*, vol. 7, pp. 159787–159796, 2019.

[33] P. Lin, Z. Wu, K.-Z. Liu, and X.-M. Sun, "A class of linear-nonlinear switching active disturbance rejection speed and current controllers for pmsm," *IEEE Transactions on Power Electronics*, 2021.

[34] A. Apte, U. Thakar, and V. Joshi, "Disturbance observer based speed control of pmsm using fractional order pi controller," *IEEE/CAA Journal of Automatica Sinica*, vol. 6, no. 1, pp. 316–326, 2019.

[35] S. K. Kommuri, Y. Park, and S. B. Lee, "Online compensation of mechanical load defects with composite control in pmsm drives," *IEEE/ASME Transactions on Mechatronics*, vol. 26, no. 3, pp. 1392–1400, 2020.

[36] E. Lu, W. Li, X. Yang, and Y. Liu, "Anti-disturbance speed control of low-speed high-torque pmsm based on second-order non-singular terminal sliding mode load observer," *ISA transactions*, vol. 88, pp. 142–152, 2019.

[37] C. Lian, F. Xiao, S. Gao, and J. Liu, "Load torque and moment of inertia identification for permanent magnet synchronous motor drives based on sliding mode observer," *IEEE Trans. Power Electron.*, vol. 34, no. 6, pp. 5675–5683, 2019.

[38] C. Gong, Y. Hu, K. Ni, J. Liu, and J. Gao, "Sm load torque observer-based fcs-mpdsc with single prediction horizon for high dynamics of surface-mounted pmsm," *IEEE Trans. Power Electron.*, vol. 35, no. 1, pp. 20–24, 2020.

[39] B. Xu, L. Zhang, and W. Ji, "Improved non-singular fast terminal sliding mode control with disturbance observer for pmsm drives," *IEEE Trans. Transport. Electrific.*, vol. 7, no. 4, pp. 2753–2762, 2021.

[40] M. S. Rafaq, A. T. Nguyen, H. H. Choi, and J.-W. Jung, "A robust high-order disturbance observer design for sdre-based suboptimal speed controller of interior pmsm drives," *IEEE Access*, vol. 7, pp. 165671–165683, 2019.

[41] P. Gao, G. Zhang, H. Ouyang, and L. Mei, "An adaptive super twisting nonlinear fractional order pid sliding mode control of permanent magnet synchronous motor speed regulation system based on extended state observer," *IEEE Access*, vol. 8, pp. 53498–53510, 2020.

[42] K. Choi, Y. Kim, S.-K. Kim, and K.-S. Kim, "Current and position sensor fault diagnosis algorithm for pmsm drives based on robust state observer," *IEEE Trans. Ind. Electron.*, vol. 68, no. 6, pp. 5227–5236, 2021.

[43] Y. Yan, J. Yang, Z. Sun, C. Zhang, S. Li, and H. Yu, "Robust speed regulation for pmsm servo system with multiple sources of disturbances via an augmented

disturbance observer," *IEEE/ASME Transactions on Mechatronics*, vol. 23, no. 2, pp. 769–780, 2018.

[44] H. Aschemann, B. Haus, and P. Mercorelli, "Second-order smc with disturbance compensation for robust tracking control in pmsm applications," *IFAC-PapersOnLine*, vol. 53, no. 2, pp. 6225–6231, 2020.

[45] T. D. Do, H. H. Choi, and J.-W. Jung, "Sdre-based near optimal control system design for pm synchronous motor," *IEEE Trans. Ind. Electron.*, vol. 59, no. 11, pp. 4063–4074, 2012.

[46] T. D. Do, H. H. Choi, and J.-W. Jung, "θ-d approximation technique for nonlinear optimal speed control design of surface-mounted pmsm drives," *IEEE/ASME Trans. Mechatron.*, vol. 20, no. 4, pp. 1822–1831, 2015.

[47] Y. Wang, H. Yu, and Y. Liu, "Speed-current single-loop control with overcurrent protection for pmsm based on time-varying nonlinear disturbance observer," *IEEE Trans. Ind. Electron.*, vol. 69, no. 1, pp. 179–189, 2022.

[48] Y. Dai, S. Ni, D. Xu, L. Zhang, and X.-G. Yan, "Disturbance-observer based prescribed-performance fuzzy sliding mode control for pmsm in electric vehicles," *Engineering Applications of Artificial Intelligence*, vol. 104, p. 104361, 2021.

[49] T. Li, X. Liu, and H. Yu, "Backstepping nonsingular terminal sliding mode control for pmsm with finite-time disturbance observer," *IEEE Access*, vol. 9, pp. 135496–135507, 2021.

[50] X. Liu and H. Yu, "Continuous adaptive integral-type sliding mode control based on disturbance observer for pmsm drives," *Nonlinear dynamics*, vol. 104, no. 2, pp. 1429–1441, 2021.

[51] B. Sarsembayev, K. Suleimenov, and T. D. Do, "High order disturbance observer based pi-pi control system with tracking anti-windup technique for improvement of transient performance of pmsm," *IEEE Access*, vol. 9, pp. 66323–66334, 2021.

[52] F. Wang and L. He, "Fpga-based predictive speed control for pmsm system using integral sliding-mode disturbance observer," *IEEE Trans. Ind.l Electron.*, vol. 68, no. 2, pp. 972–981, 2021.

[53] Y. Wang, Y. Feng, X. Zhang, J. Liang, and X. Cheng, "New reaching law control for permanent magnet synchronous motor with extended disturbance observer," *IEEE Access*, vol. 7, pp. 186296–186307, 2019.

[54] L. Li, J. Xiao, Y. Zhao, K. Liu, X. Peng, H. Luan, and K. Li, "Robust position anti-interference control for pmsm servo system with uncertain disturbance," *CES Transactions on Electrical Machines and Systems*, vol. 4, no. 2, pp. 151–160, 2020.

[55] Q. Hou and S. Ding, "Gpio based super-twisting sliding mode control for pmsm," *IEEE Transactions on Circuits and Systems II: Express Briefs*, vol. 68, no. 2, pp. 747–751, 2020.

[56] C. Xia, N. Liu, Z. Zhou, Y. Yan, and T. Shi, "Steady-state performance improvement for lqr-based pmsm drives," *IEEE Transactions on Power Electronics*, vol. 33, no. 12, pp. 10622–10632, 2018.

[57] J.-W. Choi and S.-C. Lee, "Antiwindup strategy for pi-type speed controller," *IEEE Transactions on Industrial Electronics*, vol. 56, no. 6, pp. 2039–2046, 2009.

[58] R. Errouissi, A. Al-Durra, and S. Muyeen, "Experimental validation of a novel pi speed controller for ac motor drives with improved transient performances," *IEEE Transactions on Control Systems Technology*, vol. 26, no. 4, pp. 1414–1421, 2017.

[59] A. V. Sant, K. Rajagopal, and N. K. Sheth, "Permanent magnet synchronous motor drive using hybrid pi speed controller with inherent and noninherent switching functions," *IEEE Transactions on Magnetics*, vol. 47, no. 10, pp. 4088–4091, 2011.

[60] Z.-Y. Nie, C. Zhu, Q.-G. Wang, Z. Gao, H. Shao, and J.-L. Luo, "Design, analysis and application of a new disturbance rejection pid for uncertain systems," *ISA transactions*, vol. 101, pp. 281–294, 2020.

[61] Z.-Y. Nie, Z. Li, Q.-G. Wang, Z. Gao, and J. Luo, "A unifying ziegler–nichols tuning method based on active disturbance rejection," *International Journal of Robust and Nonlinear Control*, 2021.

[62] C. Dai, T. Guo, J. Yang, and S. Li, "A disturbance observer-based current-constrained controller for speed regulation of pmsm systems subject to unmatched disturbances," *IEEE Transactions on Industrial Electronics*, vol. 68, no. 1, pp. 767–775, 2020.

[63] L. Qu, W. Qiao, and L. Qu, "An enhanced linear active disturbance rejection rotor position sensorless control for permanent magnet synchronous motors," *IEEE Transactions on Power Electronics*, vol. 35, no. 6, pp. 6175–6184, 2019.

[64] Q. Chen, Y. Tan, J. Li, and I. Mareels, "Decentralized pid control design for magnetic levitation systems using extremum seeking," *IEEE Access*, vol. 6, pp. 3059–3067, 2017.

[65] F. Meng, S. Liu, and K. Liu, "Design of an optimal fractional order pid for constant tension control system," *IEEE Access*, vol. 8, pp. 58933–58939, 2020.

[66] Y. Liu, J. Gao, Y. Zhong, and L. Zhang, "Extended state observer-based imc-pid tracking control of pmlsm servo systems," *IEEE Access*, vol. 9, pp. 49036–49046, 2021.

[67] Z. Hao, Y. Yang, Y. Gong, Z. Hao, C. Zhang, H. Song, and J. Zhang, "Linear/nonlinear active disturbance rejection switching control for permanent magnet synchronous motors," *IEEE Transactions on Power Electronics*, vol. 36, no. 8, pp. 9334–9347, 2021.

[68] A. A. Alfehaid, E. G. Strangas, and H. K. Khalil, "Speed control of permanent magnet synchronous motor with uncertain parameters and unknown disturbance," *IEEE Transactions on Control Systems Technology*, 2020.

[69] J.-W. Jung, V. Q. Leu, T. D. Do, E.-K. Kim, and H. H. Choi, "Adaptive pid speed control design for permanent magnet synchronous motor drives," *IEEE Transactions on Power Electronics*, vol. 30, no. 2, pp. 900–908, 2014.

[70] Z. Che, H. Yu, S. Mobayen, M. Ali, C. Yang, and A. Bartoszewicz, "An improved extended state observer-based composite nonlinear control for permanent magnet synchronous motor speed regulation systems," *Energies*, vol. 15, no. 15, p. 5699, 2022.

[71] F. F. El-Sousy, M. M. Amin, and A. Al-Durra, "Adaptive optimal tracking control via actor-critic-identifier based adaptive dynamic programming for permanent-magnet synchronous motor drive system," *IEEE Transactions on Industry Applications*, vol. 57, no. 6, pp. 6577–6591, 2021.

[72] T. D. Do, H. H. Choi, and J.-W. Jung, "θ-d approximation technique for nonlinear optimal speed control design of surface-mounted pmsm drives," *IEEE/ASME Transactions on Mechatronics*, vol. 20, no. 4, pp. 1822–1831, 2014.

[73] Y. Zheng, H. Zhao, S. Zhen, and C. He, "Designing robust control for permanent magnet synchronous motor: fuzzy based and multivariable optimization approach," *IEEE Access*, vol. 9, pp. 39138–39153, 2021.

[74] M. Liu, K. W. Chan, J. Hu, W. Xu, and J. Rodriguez, "Model predictive direct speed control with torque oscillation reduction for pmsm drives," *IEEE Transactions on Industrial Informatics*, vol. 15, no. 9, pp. 4944–4956, 2019.

[75] S. Li, H. Won, X. Fu, M. Fairbank, D. C. Wunsch, and E. Alonso, "Neural-network vector controller for permanent-magnet synchronous motor drives: Simulated and hardware-validated results," *IEEE transactions on cybernetics*, vol. 50, no. 7, pp. 3218–3230, 2019.

[76] F. F. El-Sousy and F. A. Alenizi, "Optimal adaptive super-twisting sliding-mode control using online actor-critic neural networks for permanent-magnet synchronous motor drives," *IEEE Access*, vol. 9, pp. 82508–82534, 2021.

[77] L. N. Tan and T. C. Pham, "Optimal tracking control for pmsm with partially unknown dynamics, saturation voltages, torque, and voltage disturbances," *IEEE Transactions on Industrial Electronics*, vol. 69, no. 4, pp. 3481–3491, 2021.

[78] C. Grimholt and S. Skogestad, "Optimal pi and pid control of first-order plus delay processes and evaluation of the original and improved simc rules," *Journal of Process Control*, vol. 70, pp. 36–46, 2018.

[79] H. A. Hussain, "Tuning and performance evaluation of 2dof pi current controllers for pmsm drives," *IEEE Transactions on Transportation Electrification*, vol. 7, no. 3, pp. 1401–1414, 2020.

[80] A. M. Diab, S. Bozhko, M. Galea, and C. Gerada, "Stable and robust design of active disturbance-rejection current controller for permanent magnet machines in transportation systems," *IEEE Transactions on Transportation Electrification*, vol. 6, no. 4, pp. 1421–1433, 2020.

[81] L. Li, G. Pei, J. Liu, P. Du, L. Pei, and C. Zhong, "2-dof robust h_∞ control for permanent magnet synchronous motor with disturbance observer," *IEEE Transactions on Power Electronics*, vol. 36, no. 3, pp. 3462–3472, 2020.

[82] R. Krishnan, *Permanent magnet synchronous and brushless DC motor drives*. CRC press, 2017.

[83] S.-M. Lu, "A review of high-efficiency motors: Specification, policy, and technology," *Renewable and Sustainable Energy Reviews*, vol. 59, pp. 1–12, 2016.

[84] L. Liu, S. Leonhardt, and B. J. Misgeld, "Design and control of a mechanical rotary variable impedance actuator," *Mechatronics*, vol. 39, pp. 226–236, 2016.

[85] L. Guzzella, A. Sciarretta, *et al.*, *Vehicle propulsion systems*, vol. 1. Springer, 2007.

[86] E. Kabalci, *Multilevel Inverters: Control Methods and Advanced Power Electronic Applications*. Academic Press, 2021.

[87] N. P. Quang, J.-A. Dittrich, *et al.*, *Vector control of three-phase AC machines*, vol. 2. Springer, 2008.

[88] Y. Zheng, *Robust Nonlinear Control for Speed Regulation of PMSMs with Various Uncertainties*. PhD thesis, Swinburne University of Technology Melbourne, Australia, 2022.

[89] B. Bose, "Modern power electronics and ac drives prentice hall," *Inc, Publication*, pp. 70–74, 2002.

[90] T. Tarczewski, R. Szczepanski, K. Erwinski, X. Hu, and L. M. Grzesiak, "A novel sensitivity analysis to moment of inertia and load variations for pmsm drives," *IEEE Transactions on Power Electronics*, vol. 37, no. 11, pp. 13299–13309, 2022.

[91] C.-J. Wu, M.-C. Tsai, and L.-J. Cheng, "Design and implementation of position-based repetitive control torque observer for cogging torque compensation in pmsm," *Applied Sciences*, vol. 10, no. 1, p. 96, 2019.

[92] G. Ellis, *Observers in control systems: a practical guide*. Elsevier, 2002.

[93] S. Skogestad and I. Postlethwaite, *Multivariable feedback control: analysis and design*. john Wiley & sons, 2005.

[94] E. Sariyildiz, *Advanced Robust Control via Disturbance Observer: Implementations in the Motion Control Framework*. PhD thesis, Keio University, 2014.

[95] Z.-Y. Nie, Q.-G. Wang, J. She, R.-J. Liu, and D.-S. Guo, "New results on the robust stability of control systems with a generalized disturbance observer," *Asian Journal of Control*, vol. 22, no. 6, pp. 2463–2475, 2020.

[96] A. Castillo, P. García, R. Sanz, and P. Albertos, "Enhanced extended state observer-based control for systems with mismatched uncertainties and disturbances," *ISA transactions*, vol. 73, pp. 1–10, 2018.

[97] Y. Huang and W. Xue, "Active disturbance rejection control: Methodology and theoretical analysis," *ISA transactions*, vol. 53, no. 4, pp. 963–976, 2014.

[98] J. Yang, S. Li, and X. Yu, "Sliding-mode control for systems with mismatched uncertainties via a disturbance observer," *IEEE Transactions on industrial electronics*, vol. 60, no. 1, pp. 160–169, 2012.

[99] M. M. I. Chy and M. N. Uddin, "Development and implementation of a new adaptive intelligent speed controller for ipmsm drive," *IEEE Transactions on Industry Applications*, vol. 45, no. 3, pp. 1106–1115, 2009.

[100] L. Qu, W. Qiao, and L. Qu, "Active-disturbance-rejection-based sliding-mode current control for permanent-magnet synchronous motors," *IEEE Transactions on Power Electronics*, vol. 36, no. 1, pp. 751–760, 2020.

[101] M. N. Uddin and M. A. Rahman, "Fuzzy logic based speed control of an ipm synchronous motor drive," in *Engineering Solutions for the Next Millennium. 1999 IEEE Canadian Conference on Electrical and Computer Engineering (Cat. No. 99TH8411)*, vol. 3, pp. 1259–1264, IEEE, 1999.

[102] M. N. Uddin, M. Abido, and M. A. Rahman, "Development and implementation of a hybrid intelligent controller for interior permanent-magnet synchronous motor drives," *IEEE Transactions on Industry Applications*, vol. 40, no. 1, pp. 68–76, 2004.

[103] C. B. Butt, M. A. Hoque, and M. A. Rahman, "Simplified fuzzy-logic-based mtpa speed control of ipmsm drive," *IEEE Transactions on industry applications*, vol. 40, no. 6, pp. 1529–1535, 2004.

[104] M. N. Uddin, M. Abido, and M. Rahman, "Real-time performance evaluation of a genetic-algorithm-based fuzzy logic controller for ipm motor drives," *IEEE Transactions on Industry Applications*, vol. 41, no. 1, pp. 246–252, 2005.

[105] E. Kim and S. Lee, "Output feedback tracking control of mimo systems using a fuzzy disturbance observer and its application to the speed control of a pm synchronous motor," *IEEE Transactions on Fuzzy Systems*, vol. 13, no. 6, pp. 725–741, 2005.

[106] M. Cheng, Q. Sun, and E. Zhou, "New self-tuning fuzzy pi control of a novel doubly salient permanent-magnet motor drive," *IEEE Transactions on Industrial Electronics*, vol. 53, no. 3, pp. 814–821, 2006.

[107] F.-J. Lin and P.-H. Shen, "Adaptive fuzzy-neural-network control for a dsp-based permanent magnet linear synchronous motor servo drive," *IEEE Transactions on Fuzzy Systems*, vol. 14, no. 4, pp. 481–495, 2006.

[108] M. N. Uddin and M. A. Rahman, "High-speed control of ipmsm drives using improved fuzzy logic algorithms," *IEEE transactions on industrial electronics*, vol. 54, no. 1, pp. 190–199, 2007.

[109] J.-S. Yu, S.-H. Kim, B.-K. Lee, C.-Y. Won, and J. Hur, "Fuzzy-logic-based vector control scheme for permanent-magnet synchronous motors in elevator drive applications," *IEEE transactions on Industrial Electronics*, vol. 54, no. 4, pp. 2190–2200, 2007.

[110] Y.-S. Kung, C.-C. Huang, and M.-H. Tsai, "Fpga realization of an adaptive fuzzy controller for pmlsm drive," *IEEE Transactions on Industrial Electronics*, vol. 56, no. 8, pp. 2923–2932, 2009.

[111] S. Li and Z. Liu, "Adaptive speed control for permanent-magnet synchronous motor system with variations of load inertia," *IEEE transactions on industrial electronics*, vol. 56, no. 8, pp. 3050–3059, 2009.

[112] F.-J. Lin, S.-Y. Chen, L.-T. Teng, and H. Chu, "Recurrent functional-link-based fuzzy neural network controller with improved particle swarm optimization for a linear synchronous motor drive," *IEEE Transactions on magnetics*, vol. 45, no. 8, pp. 3151–3165, 2009.

[113] A. V. Sant and K. Rajagopal, "Pm synchronous motor speed control using hybrid fuzzy-pi with novel switching functions," *IEEE Transactions on Magnetics*, vol. 45, no. 10, pp. 4672–4675, 2009.

[114] M. N. Uddin and M. M. I. Chy, "A novel fuzzy-logic-controller-based torque and flux controls of ipm synchronous motor," *IEEE Transactions on Industry Applications*, vol. 46, no. 3, pp. 1220–1229, 2010.

[115] H. Chaoui and P. Sicard, "Adaptive fuzzy logic control of permanent magnet synchronous machines with nonlinear friction," *IEEE Transactions on Industrial Electronics*, vol. 59, no. 2, pp. 1123–1133, 2011.

[116] S. Li and H. Gu, "Fuzzy adaptive internal model control schemes for pmsm speed-regulation system," *IEEE Transactions on Industrial Informatics*, vol. 8, no. 4, pp. 767–779, 2012.

[117] H. H. Choi and J.-W. Jung, "Discrete-time fuzzy speed regulator design for pm synchronous motor," *IEEE Transactions on Industrial Electronics*, vol. 60, no. 2, pp. 600–607, 2012.

[118] H. H. Choi, H. M. Yun, and Y. Kim, "Implementation of evolutionary fuzzy pid speed controller for pm synchronous motor," *IEEE Transactions on Industrial Informatics*, vol. 11, no. 2, pp. 540–547, 2013.

[119] Y.-C. Chang, C.-H. Chen, Z.-C. Zhu, and Y.-W. Huang, "Speed control of the surface-mounted permanent-magnet synchronous motor based on takagi–sugeno fuzzy models," *IEEE Transactions on Power Electronics*, vol. 31, no. 9, pp. 6504–6510, 2015.

[120] C. Wang and Z. Zhu, "Fuzzy logic speed control of permanent magnet synchronous machine and feedback voltage ripple reduction in flux-weakening

operation region," *IEEE Transactions on Industry Applications*, vol. 56, no. 2, pp. 1505–1517, 2020.

[121] J. Yang, B. Huang, H. Shen, D. Xie, F. Xiong, S. Lu, and H. Chen, "Ekf based fuzzy pi controlled speed sensorless power optimal control of a direct drive power system," *IEEE Access*, vol. 7, pp. 61610–61619, 2019.

[122] Z. Wang, A. Yu, X. Li, G. Zhang, and C. Xia, "A novel current predictive control based on fuzzy algorithm for pmsm," *IEEE Journal of Emerging and Selected Topics in Power Electronics*, vol. 7, no. 2, pp. 990–1001, 2019.

[123] S. Li and Z. Liu, "Adaptive speed control for permanent-magnet synchronous motor system with variations of load inertia," *IEEE trans. ind. electron.*, vol. 56, no. 8, pp. 3050–3059, 2009.

[124] H. Chaoui and P. Sicard, "Adaptive fuzzy logic control of permanent magnet synchronous machines with nonlinear friction," *IEEE Trans. Ind.Electron.*, vol. 59, no. 2, pp. 1123–1133, 2011.

[125] H. H. Choi and J.-W. Jung, "Discrete-time fuzzy speed regulator design for pm synchronous motor," *IEEE Trans. Ind. Electron.*, vol. 60, no. 2, pp. 600–607, 2012.

[126] H. H. Choi, H. M. Yun, and Y. Kim, "Implementation of evolutionary fuzzy pid speed controller for pm synchronous motor," *IEEE Trans. Ind. Informat.*, vol. 11, no. 2, pp. 540–547, 2013.

[127] Y. Wu, G. Li, Z. Zuo, X. Liu, and P. Xu, "Practical fixed-time position tracking control of permanent magnet dc torque motor systems," *IEEE/ASME Transactions on Mechatronics*, vol. 26, no. 1, pp. 563–573, 2020.

[128] T. D. Do and H. T. Nguyen, "A generalized observer for estimating fast–varying disturbances," *IEEE Access*, vol. 6, pp. 28054–28063, 2018.

[129] I. H. Kim and Y. I. Son, "Regulation of a dc/dc boost converter under parametric uncertainty and input voltage variation using nested reduced-order pi observers," *IEEE Trans. Ind. Electron.*, vol. 64, no. 1, pp. 552–562, 2017.

[130] Y. I. Son, I. H. Kim, D. S. Choi, and H. Shim, "Robust cascade control of electric motor drives using dual reduced-order pi observer," *IEEE Trans. Ind. Electron.*, vol. 62, no. 6, pp. 3672–3682, 2015.

[131] F. Qiu and J. Jensen, "Opening the black box of neural networks for remote sensing image classification," *International Journal of Remote Sensing*, vol. 25, no. 9, pp. 1749–1768, 2004.

[132] H.-B. Shin, "New antiwindup pi controller for variable-speed motor drives," *IEEE Trans. ind. electron.*, vol. 45, no. 3, pp. 445–450, 1998.

[133] A. Isidori, E. Sontag, and M. Thoma, *Nonlinear control systems*, vol. 3. Springer, 1995.

[134] B.-H. Nguyễn and J. P. F. Trovão, "Practical linear controllers for power electronics and drives," 2023.

[135] P. Cui, F. Zheng, X. Zhou, and W. Li, "Current harmonic suppression for permanent magnet synchronous motor based on phase compensation resonant controller," *Journal of Vibration and Control*, vol. 0, no. 0, p. 1077546320982466, 2020.

[136] Z. Rongyun, G. Changfu, S. Peicheng, Z. Linfeng, and Z. Changsheng, "Research on chaos control of permanent magnet synchronous motor based on the synthetical sliding mode control of inverse system decoupling," *Journal of Vibration and Control*, vol. 27, no. 9-10, pp. 1009–1019, 2021.

[137] R. Errouissi, M. Ouhrouche, W.-H. Chen, and A. M. Trzynadlowski, "Robust cascaded nonlinear predictive control of a permanent magnet synchronous motor with antiwindup compensator," *IEEE Transactions on Industrial Electronics*, vol. 59, no. 8, pp. 3078–3088, 2011.

[138] P. M. Oliveira and D. Vrančić, "Underdamped second-order systems overshoot control," *IFAC Proceedings Volumes*, vol. 45, no. 3, pp. 518–523, 2012.

[139] N. Singh, B. Pratap, and A. Swarup, "Design of robust control for wind turbine using quantitative feedback theory," *IFAC-PapersOnLine*, vol. 49, no. 1, pp. 718–723, 2016.

[140] P. Vogt, E. Lenz, A. Klug, H. Westerfeld, and U. Konigorski, "Robust two-degree-of-freedom wheel slip controller structure for anti-lock braking," *IFAC-PapersOnLine*, vol. 52, no. 5, pp. 431–437, 2019.

[141] H. V. Nguyen, K. Suleimenov, B.-H. Nguyen, T. Vo-Duy, M. C. Ta, and T. D. Do, "Dynamical delay unification of disturbance observation techniques for pmsm drives control," *IEEE/ASME Transactions on Mechatronics*, vol. 27, no. 6, pp. 5560–5571, 2022.

[142] M. Aguilar-Orduña, E. Zurita-Bustamante, H. Sira-Ramírez, and Z. Gao, "Disturbance observer based control design via active disturbance rejection control: A pmsm example," *IFAC-PapersOnLine*, vol. 53, no. 2, pp. 1343–1348, 2020. 21st IFAC World Congress.

[143] W. Wang, S. Pan, and F. Wang, "A comparison study of two disturbance rejection control strategies for hydraulic position servo systems," in *30th Annual Conference of IEEE Industrial Electronics Society, 2004. IECON 2004*, vol. 3, pp. 1993–1996 Vol. 3, 2004.

[144] W. Xue and Y. Huang, "Comparison of the DOB based control, a special kind of PID control and ADRC," in *Proceedings of the 2011 American Control Conference*, pp. 4373–4379, 2011.

[145] M. Aguilar-Orduña, E. Zurita-Bustamante, H. Sira-Ramírez, and Z. Gao, "Disturbance observer based control design via active disturbance rejection control: A pmsm example," *IFAC-PapersOnLine*, vol. 53, no. 2, pp. 1343–1348, 2020. 21st IFAC World Congress.

[146] H. V. Nguyen, T. Vo-Duy, and M. C. Ta, "Comparative Study of Disturbance Observer-Based Control and Active Disturbance Rejection Control in Brushless DC Motor Drives," in *2019 IEEE Vehicle Power and Propulsion Conference (VPPC)*, pp. 1–6, 2019.